Stony Brook University

Measurement of the Inclusive Charged Current ν_e Interaction rate on Water with the T2K π^0 Detector

A Dissertation presented

by

Jay Hyun Jo

to

The Graduate School

in Partial Fulfillment of the

Requirements

for the Degree of

Doctor of Philosophy

in

Physics and Astronomy

Stony Brook University

August 2015

Stony Brook University

The Graduate School

Jay Hyun Jo

We, the dissertation committee for the above candidate for the

Doctor of Philosophy degree, hereby recommend

acceptance of this dissertation

Chang Kee Jung - Dissertation Advisor
Professor, Physics and Astronomy

Clark McGrew - Chairperson of Defense
Associate Professor, Physics and Astronomy

Dmitri Kharzeev
Professor, Physics and Astronomy

Brett Viren
Physicist, Brookhaven National Laboratory

This dissertation is accepted by the Graduate School

Charles Taber
Dean of the Graduate School

Abstract of the Dissertation

Measurement of the Inclusive Charged Current ν_e Interaction rate on Water with the T2K π^0 Detector

by

Jay Hyun Jo

Doctor of Philosophy

in

Physics and Astronomy

Stony Brook University

2015

The T2K (Tokai to Kamioka) experiment is a long-baseline neutrino experiment designed to measure ν_μ disappearance and ν_e appearance from the ν_μ beam. The T2K experimental setup consists of the J-PARC (Japan Proton Accelerator Research Complex) accelerator, a near detector complex (ND280) and a far detector (Super-Kamiokande). With the recent firm establishment of ν_e appearance by T2K, future precision ν_e appearance measurements can be used to explore CP-violation in neutrino interactions. However such an exploration requires detailed understanding of the ν_e interactions, as well as contamination of ν_e in the ν_μ beam. The presence of the ν_e component in the beam accounts for 1.2% of the beam, which is the main background in the ν_e appearance measurement. Moreover, as Super-Kamiokande is a large water Cherenkov detector, neutrino interaction measurements on water are important to constrain the neutrino cross-section systematic uncertainty. To this end, the T2K off-axis π^0 detector (PØD), a component of ND280, has been used to measure ν_e charged current interaction rates on water. The details of the analysis including the selection criteria and the systematic uncertainties are presented in this thesis. In addition, prospects for the charged current $\bar{\nu}_e$ interaction rate measurement with the PØD is be discussed. These are pioneering measurements of the ν_e interaction rate, particularly on water, which will become crucial in future CP-violation searches.

Dedication Page

To my dearest family and friends

Contents

List of Figures

List of Tables

Chapter 1

Introduction

"I have done something very bad today in proposing a particle that cannot be detected; it is something no theorist should ever do."

—W. Pauli

The neutrino is one of the elementary particles of nature with spin 1/2 and no electric charge. Because they only interacts with matter through the weak nuclear force and the gravity, neutrinos are extremely difficult to detect and study. As a result there remain many questions unanswered about neutrino's properties. In this chapter, the history of neutrinos will be discussed, theoretical and experimental background of the neutrino physics, and the overview of the T2K experiment. Finally, the motivation for the topics discussed in this thesis will be described.

1.1 History of neutrino

The history of the neutrino begins with the discovery of radioactivity by Henri Becquerel in 1896. In the β-decay, a type of radioactive decay, an electron or a positron is emitted from the decaying nucleus A at rest into a lighter nucleus B. The emitted electron would naively be expected to have a constant energy which coincides with the total energy released in the decay. However, In 1914, Chadwick found that the electron did not carry all the energy that had been lost by the nucleus A. The measured electrons had a continuous energy spectrum, up to the expected maximum value, as shown in the Fig. 1.1. Since no other particle was observed, the decay seemed to violate the energy conservation law.

It was Wolfgang Pauli in 1930 [1], who postulated the existence of an undetected neutral particle which carries the missing energy and Enrico Fermi named this particle neutrino (which, in Italian, means "the small neutral one") a few years later.

Pauli was skeptic about the detection of the neutrino, and it took 25 years for the neutrino to be observed experimentally. In 1955, Frederick Reines and Clyde Cowan detected electron

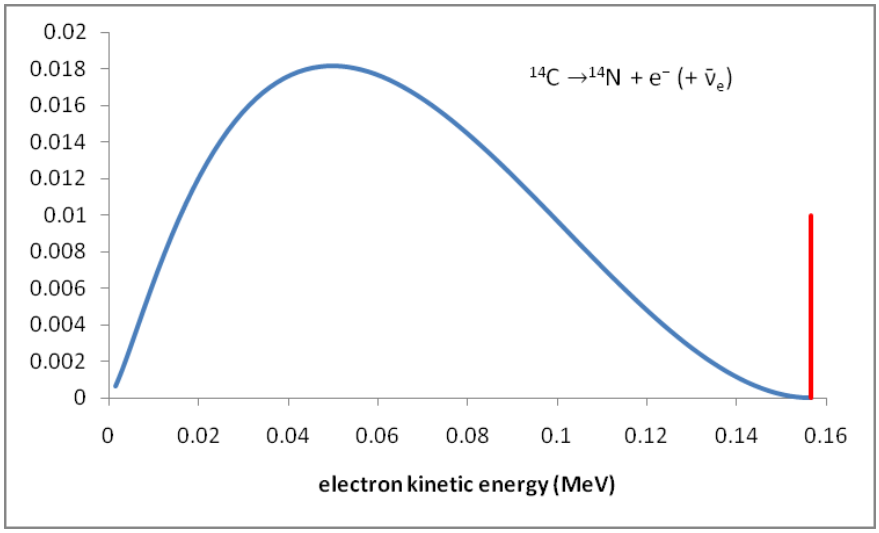

Figure 1.1: Example distribution of the energy carried by the electron in the nuclear β decay. The red line coincides with the expected spectrum for a two-body decay, without any other particles than electron.

antineutrinos ($\bar{\nu}_e$) from a nuclear reactor via the inverse β-decay reaction

$$\bar{\nu}_e + p \rightarrow e^+ + n. \tag{1.1}$$

Reines and Clyde observed the positron by detecting 511 KeV photons from positron-electron annihilation, and the neutron when it was captured by an atomic nucleus [2] (Fig. 1.2).

In 1963, Leon Lederman, Melvin Schwartz, and Jack Steinberger discovered the existence of more than one species of neutrinos at the Brookhaven National Laboratory (BNL) [3]. They used the Brookhaven AGS (Alternating Gradient Synchrotron) to detect muon neutrino (ν_μ) from pion decays.

The electroweak theory, formulated by Glashow, Weinberg and Salam, predicted that there should be another type of neutrino interaction via the exchange of the Z boson. In 1973, this prediction was verified by Gargamelle experiment at CERN [4]. In 1975, the tau lepton was discovered which suggested the existence of a third type of neutrino, tau neutrino (ν_τ). The tau neutrino was directly detected in 2000 by the DONUT Collaboration at Fermi National Accelerator Laboratory [5]. The number of light neutrino types was limited to be three by studying the decay of Z^0 produced in e^+e^- collisions at LEP [6].

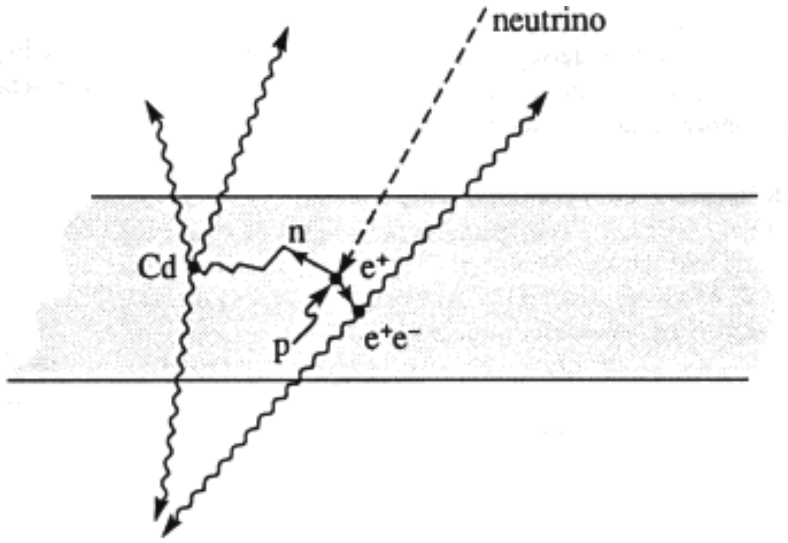

Figure 1.2: Schematic picture of the neutrino detector of Reines and Cowan.

1.2 Neutrinos in the Standard Model

The Standard Model of particle physics is the phenomenological framework that describes the interaction of the fundamental particles in terms of the strong and electroweak forces, with gravity being excluded. It was developed in the 1970s and provided an excellent description of most of phenomena of particle physics until now. With the discovery of the Higgs boson in 2012 [7, 8], the existence of all the elementary particles predicted by the Standard Model was confirmed. Figure 1.3 shows the particles that make up the Standard Model.

In the Standard Model there are 3 generations of massless neutrinos, ν_e, ν_μ, and ν_τ, corresponding to the electron, muon and tau leptons. Neutrinos do not have electric or color charges, hence they do not interact through the electromagnetic or strong interactions. Neutrinos only interact via the weak interaction by exchanging the weak gauge bosons W and Z, mediating charged and neutral current interactions, respectively.

The helicity of neutrinos was measured by M. Goldhaber *et al.* in 1957 [9]. The experiment used ^{152m}Eu, which undergoes β capture, and the direction of the spin of the neutrinos was deduced by measuring the polarization of the outgoing photon in the process. Goldhaber *et al.* concluded that the neutrinos have left-handed helicity.

1.3 Neutrino Mass and Mixing

The Standard Model assumes neutrinos to be massless: As neutrino being a spin-1/2 particle obeys the Dirac equation, both left and right-handed helicity states are required in order to produce a mass term. With Goldhaber's experiment result telling us the neutrinos have only left-handed helicity, the simplest solution is to have massless neutrinos. A non-zero neutrino

mass, therefore, would be a clear sign of new physics beyond the Standard Model.

1.3.1 Neutrino Oscillation

The idea of neutrino oscillation was first suggested by B. Pontecorvo in 1957 [10, 11]. He proposed an oscillation between neutrino and anti-neutrino states as an analogy with K^0 or B^0 mixing. The possible transformation of a neutrino of a given flavor into a different flavor was proposed later. In 1962, Z. Maki, M. Nakagawa, and S. Sakata formulated the idea of the neutrino flavor mixing [12].

Quantum mechanics allows us to express the flavor eigenstates $|\nu_\alpha\rangle$ ($\alpha = e, \mu, \tau$) as linear combinations of the mass eigenstates $|\nu_i\rangle$ ($i = 1, 2, 3$),

$$|\nu_\alpha\rangle = \sum_i U_{\alpha i} |\nu_i\rangle, \tag{1.2}$$

where $U_{\alpha i}$ is the 3×3 unitary matrix. This matrix is known as the Pontecorvo-Maki-Nakagawa-Sakata (PMNS) matrix, and it can be parameterized as

$$U = \begin{pmatrix} 1 & 0 & 0 \\ 0 & c_{23} & s_{23} \\ 0 & -s_{23} & c_{23} \end{pmatrix} \begin{pmatrix} c_{13} & 0 & s_{13}e^{i\delta_{CP}} \\ 0 & 1 & 0 \\ -s_{13}e^{i\delta CP} & 0 & c_{13} \end{pmatrix} \begin{pmatrix} c_{12} & s_{12} & 0 \\ -s_{12} & c_{12} & 0 \\ 0 & 0 & 1 \end{pmatrix} \tag{1.3}$$

$$= \begin{pmatrix} c_{12}s_{13} & s_{12}c_{13} & s_{13}e^{i\delta_{CP}} \\ -s_{12}c_{23} - c_{12}s_{13}s_{23}e^{i\delta_{CP}} & c_{12}c_{23} - s_{12}s_{13}s_{23}e^{i\delta_{CP}} & c_{13}s_{23} \\ s_{12}s_{23} - c_{12}s_{13}c_{23}e^{i\delta_{CP}} & c_{12}s_{23} - s_{12}s_{13}c_{23}e^{i\delta_{CP}} & c_{13}c_{23} \end{pmatrix}, \tag{1.4}$$

where $c_{ij} = \cos\theta_{ij}$ and $s_{ij} = \sin\theta_{ij}$. The possibility of CP violation in the lepton sector is introduced by a phase parameter, δ_{CP}, the value of which is presently unknown.

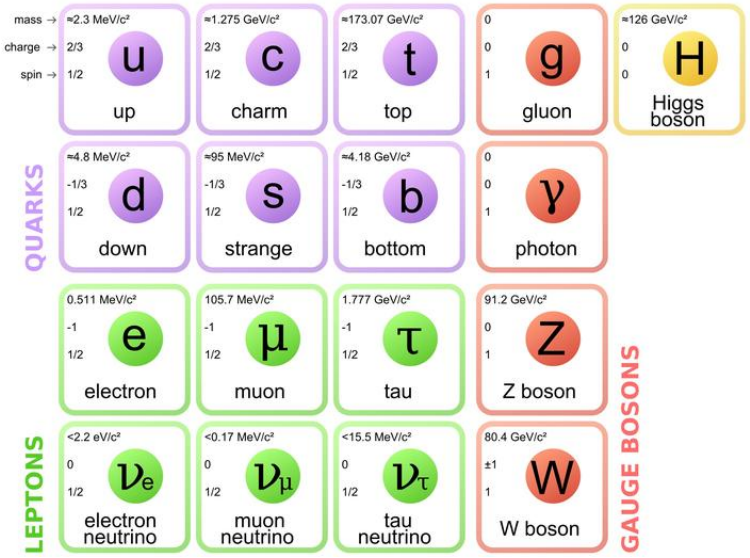

Figure 1.3: Elementary particles in the Standard Model.

In vacuum, the mass eigenstates $|\nu_i\rangle$ propagates independently with time-dependent Schrödinger equation,

$$|\nu_i(t)\rangle = \exp(-iE_i t)\,|\nu_i\rangle\,. \tag{1.5}$$

Inserting this result into Eq. 1.2 gives us

$$|\nu_\alpha(t)\rangle = \sum_i U_{\alpha i}\exp(-iE_i t)\,|\nu_i\rangle\,. \tag{1.6}$$

As neutrino masses are small, we can approximate the energy E_i by following:

$$E_i = \sqrt{p^2+m_i^2} \simeq p + \frac{m_i^2}{2p} \simeq p + \frac{m_i^2}{2E}. \tag{1.7}$$

where p and m_i are the momentum and mass of the mass eigenstate. With this approximation, Eq. 1.6 is written as:

$$\begin{aligned} |\nu_\alpha(t)\rangle &= \sum_i U_{\alpha i}\exp(-ipt)\exp(-\frac{im_i^2 t}{2E})\,|\nu_i\rangle & (1.8)\\ &= \sum_{i,\alpha} U_{\alpha i}\exp(-ipt)\exp(-\frac{im_i^2 t}{2E})U^\dagger_{\beta i}\,|\nu_\beta\rangle\,. & (1.9)\end{aligned}$$

The probability for a transition of a neutrino in flavor state α to flavor state β is given by

$$\begin{aligned} P(\nu_\alpha\to\nu_\beta) &= |\,\langle\nu_\beta|\nu_\alpha(t)\rangle\,|^2\\ &= |\sum_{i,\beta} U_{\alpha i}\exp(-ipt)\exp(-\frac{im_i^2 t}{2E})U^\dagger_{\beta j}|^2\\ &= \sum_{i,j} U^\dagger_{\alpha i}U_{\beta i}U_{\alpha j}U^\dagger_{\beta j}\exp(-\frac{i(m_i^2-m_j^2)t}{2E})\\ &= \sum_{i,j} U^\dagger_{\alpha i}U_{\beta i}U_{\alpha j}U^\dagger_{\beta j}\exp(-\frac{i\Delta m_{ij}^2 L}{2E})\\ &= \delta_{\alpha\beta} - 4\sum_{i>j}\mathrm{Re}(U^\dagger_{\alpha i}U_{\beta i}U_{\alpha j}U^\dagger_{\beta j})\sin^2(\frac{\Delta m_{ij}^2 L}{4E})\\ &+ 2\sum_{i>j}\mathrm{Im}(U^\dagger_{\alpha i}U_{\beta i}U_{\alpha j}U^\dagger_{\beta j})\sin(\frac{\Delta m_{ij}^2 L}{2E}). \end{aligned} \tag{1.10}$$

where $\Delta m_{ij}^2 = m_i^2 - m_j^2$, and time t was replaced with the travel distance $L = ct$ since neutrinos are relativistic.

From the experimental measurements, we know that one of the mass differences is much smaller than the others, namely

$$|\Delta m_{13}^2| \sim |\Delta m_{23}^2| \gg |\Delta m_{12}^2|. \tag{1.11}$$

Then the probability of short oscillation can be approximated by

$$P(\nu_\alpha \to \nu_\beta) = 4|U_{\alpha 3}|^2|U_{\beta 3}|^2 \sin^2(\frac{\Delta m^2_{13}}{4E}L). \tag{1.12}$$

Now the amplitude probabilities only depend on the elements of the third column of the mixing matrix U. The probability of ν_e appearance from ν_μ and ν_μ survival probability can be written as

$$P(\nu_\mu \to \nu_e) \simeq \sin^2 2\theta_{13} \sin^2 \theta_{23} \sin^2(\frac{\Delta m^2_{32}L}{4E}) \tag{1.13}$$

and

$$P(\nu_\mu \to \nu_\mu) \simeq 1 - (\cos^4 \theta_{13} \sin^2 2\theta_{23} + \sin^2 2\theta_{13} \sin^2 \theta_{23}) \sin^2(\frac{\Delta m^2_{32}L}{4E}). \tag{1.14}$$

1.3.2 Recent Results from Neutrino Oscillation Experiments

Depending on sources of neutrinos, one can categorize the neutrino oscillation experiments into four: Atmospheric, solar, reactor and accelerator neutrino experiments. Atmospheric neutrinos come from the interaction of comic rays with atomic nuclei in the Earth's atmosphere, creating showers of secondary particles, many of which are unstable and produce neutrinos when they decay. Solar neutrinos result from the nuclear fusion powering the Sun. Reactor neutrinos are anti-electron neutrinos generated in the β-decay of neutron-rich daughter fragments in the fission process in nuclear reactors. Finally, accelerator neutrinos are produced as decay products of charged pions or kaons generated by slamming the accelerated protons into a fixed production target. Best fit values of the oscillation parameters from Particle Data Group (PDG) 2014 [13] are summarized in Table 1.1.

The parameters θ_{12} and Δm^2_{12} have been mainly measured by solar neutrino experiments and confirmed by reactor neutrino experiments. Measurements of these parameters can be made by looking at the disappearance of electron neutrinos from the Sun, where a large flux of ν_e is produced as a byproduct of the *pp* fusion chain and the CNO cycle [14, 15]. It was Ray Davis and his collaborators in late 1960s [16] who observed a deficit of ν_e from the Sun with respect to the prediction of the Standard Solar Model (SSM). This discrepancy was

Table 1.1: Best fit values of the neutrino oscillation parameters.

Parameter	Best fit value
Δm^2_{12}	$(7.53 \pm 0.18) \times 10^{-5}$ eV^2
Δm^2_{32}	$(0.00232^{+0.00012}_{-0.00008})$ eV^2
$\sin^2 2\theta_{12}$	0.857 ± 0.024
$\sin^2 2\theta_{23}$	> 0.95
$\sin^2 2\theta_{13}$	0.095 ± 0.010

confirmed by several other experiments (Gallex, Super-Kamiokande, etc.), and was called the 'solar neutrino problem' [17]. In 2001 the SNO experiment measured flavor specific charged current (CC) and flavor blind neutral current (NC) interactions of solar neutrinos [18] in heavy water. All types of neutrinos participate in the NC interactions where the CC interaction is only sensitive to electron flavor neutrino. The SNO experiment measured the flux ratio

$$\frac{\phi_{CC}}{\phi_{NC}} = 0.301 \pm 0.033, \tag{1.15}$$

which clearly indicates that the solar electron neutrinos change flavor on the way to the Earth, and the measurement constrains the ν_e flavor content of ν_2 as well as the value of Δm^2_{12}.

The parameters θ_{23} and Δm^2_{32} have been measured by atmospheric neutrino and long-baseline accelerator neutrino experiments. Super-Kamiokande measured the disappearance of atmospheric muon neutrinos [19] which gave one of the first evidence for neutrino oscillations.

Finally, θ_{13} has been measured by reactor neutrino experiments and long-baseline accelerator neutrino experiments. Only the upper limit on θ_{13} was known given until 2011, but an indication of the non-zero θ_{13} was first reported by T2K experiment [20] by observing the appearance of electron neutrinos in a muon neutrino beam. In 2012, the Daya Bay experiment [21] along with the RENO [22] and Double Chooz [23] experiments measured θ_{13} precisely via the disappearance of anti-electron neutrinos from reactors.

1.4 Neutrino Interactions

1.4.1 Weak Interactions

The weak interaction is one of the four known fundamental interactions of nature, alongside the strong interaction, electromagnetism, and gravitation. Neutrinos interacts via only the weak interaction (and gravitation), mediated by the weak gauge bosons $W^{\pm}$ and Z^0. There are two types of weak interaction: The first type is the charged current interaction, as it is mediated by $W^{\pm}$ bosons that carry an electric charge. The second type is called the neutral current interaction because it is mediated by a neutral particle, Z^0 boson. Figure 1.4 shows Feynman diagrams of these interactions.

The propagation term for the massive boson is $1/(M^2_{W,Z} - q^2)$ and for small q^2, the propagator is then a constant, $1/M^2_{W,Z}$. Weak coupling constant can be identified as

$$\frac{G_F}{\sqrt{2}} = \frac{g_w^2}{8M_W^2}, \tag{1.16}$$

where the Fermi constant has been measured to be [24]

$$G_F = (1.16632 \pm 0.00004)^{-5}\text{GeV}^{-2}, \tag{1.17}$$

which is different from QED and QCD. Here g_w is dimensionless. For the case of the neutral current interaction, plugging the mass of the W boson as 80.4 GeV, we get a weak coupling

factor of $g_w = 0.65$. Remembering that the electromagnetic interaction coupling factor is the square root of the fine structure constant, we can compare the strength of electromagnetic and weak interaction:

$$\alpha_{EM} = \frac{1}{137}, \tag{1.18}$$

$$\alpha_W = \frac{g_w^2}{4\pi} \sim \frac{1}{30}. \tag{1.19}$$

This means the weak interaction is about 4 times stronger than the electromagnetic interaction, and the reason is the large mass of the relevant gauge bosons. At very high energy, where $q^2 \sim M_W^2$, the weak interaction is comparable in strength to the electromagnetic interaction.

This thesis investigates the interaction rate of the ν_e and $\bar{\nu}_e$, which will be extended to the measurement of ν_e and $\bar{\nu}_e$ cross section on water. It is conventional to write the effective Lagrangian of the leptonic weak interaction as a product of charged currents, where the charged currents can be expressed as:

$$j_\mu^{\pm} = \bar{u}\frac{-ig_W}{2\sqrt{2}}\gamma^\mu(1-\gamma^5)u \tag{1.20}$$

where u and $\bar{u}$ are Dirac spinors, γ^μ are the four Dirac gamma matrices, $\gamma^5 = u\gamma^0\gamma^1\gamma^2\gamma^3$, and g_W is the coupling constant as defined in Eq.1.17. With Eq. 1.17, the effective Lagrangian for νe scattering is then:

$$\mathcal{L}_{eff} = -\frac{G_F}{\sqrt{2}}\bar{\nu}\gamma_\mu(1-\gamma_5)e\bar{e}\gamma^\mu(1-\gamma_5)\nu. \tag{1.21}$$

Note that the Dirac spinors are replaced with neutrino and electron. The cross section for $\nu_e e$ and $\bar{\nu}_e e$ scattering are then given by

$$\frac{d\sigma}{dy}(\nu_e e) = \frac{2mE}{\pi}G_F^2, \tag{1.22}$$

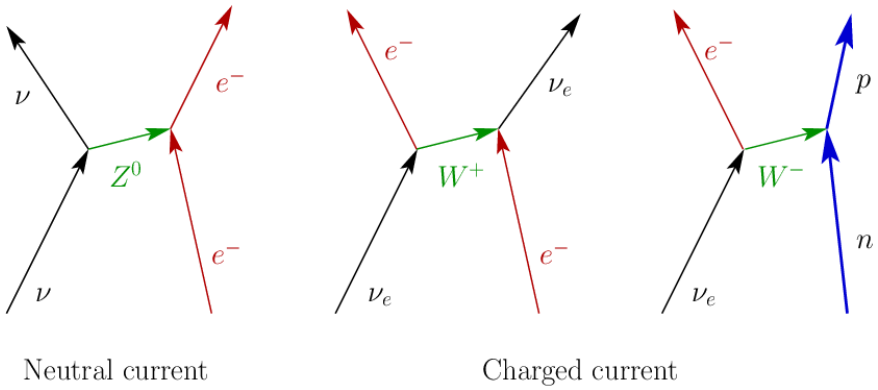

Figure 1.4: Feynman diagram of neutrino interactions in the case of the neutral current interaction and the charged current interactions.

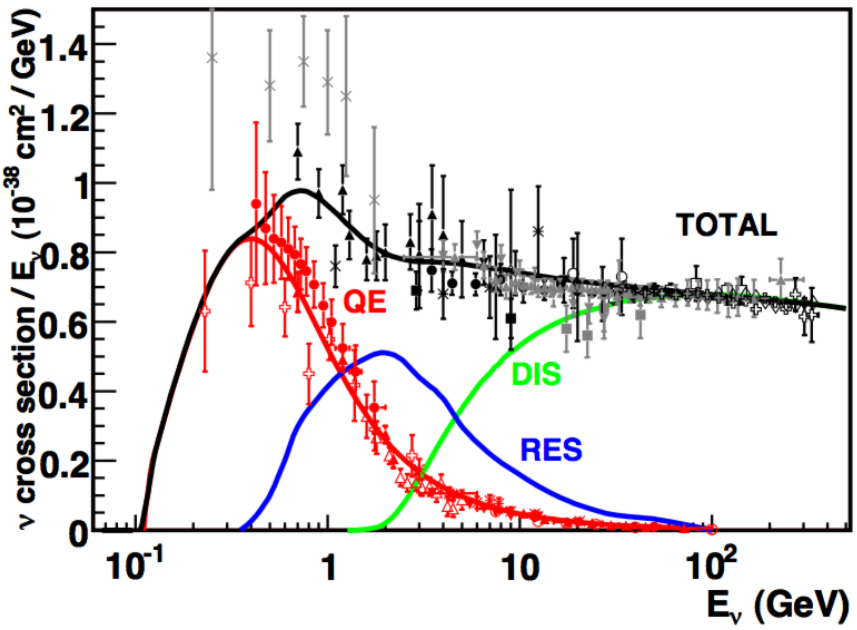

Figure 1.5: Existing muon neutrino charged current cross section measurements and predictions as a function of neutrino energy.

$$\sigma(\nu_e e) = \frac{2mE}{\pi} G_F^2 \sim 1.72 \times 10^{-41} \mathrm{cm}^2 (\frac{E}{1\mathrm{GeV}}), \tag{1.23}$$

$$\frac{d\sigma}{dy}(\bar{\nu}_e e) = \frac{2mE}{\pi} G_F^2 (1-y)^2, \tag{1.24}$$

$$\sigma(\bar{\nu}_e e) = \frac{2mE}{3\pi} G_F^2 \sim 0.574 \times 10^{-41} \mathrm{cm}^2 (\frac{E}{1\mathrm{GeV}}). \tag{1.25}$$

where m is the electron mass and yE is the energy of the recoiling electron. This shows that the cross sections for ν_e and $\bar{\nu}_e$ are extremely small, but not completely unmeasurable by experiment. Also it is noteworthy to see that the $\bar{\nu}_e$ cross section is 3 times smaller than that of ν_e. It is due to the fact that all the neutrinos are left-handed where the anti-neutrinos are right-handed, hence backward anti-neutrino scattering is forbidden to preserve the angular momentum conservation.

1.4.2 Neutrino-Nucleus Interactions

In the neutrino energy region of a few GeV, which is the energy region of the long baseline neutrino experiments, neutrino-nucleus interactions are predominant. The neutrino nucleon scattering can be broadly divided into following three processes, as shown in Fig. 1.6. Figure 1.5 shows existing muon neutrino charged current cross section measurements [25] and predictions [26] as a function of neutrino energy.

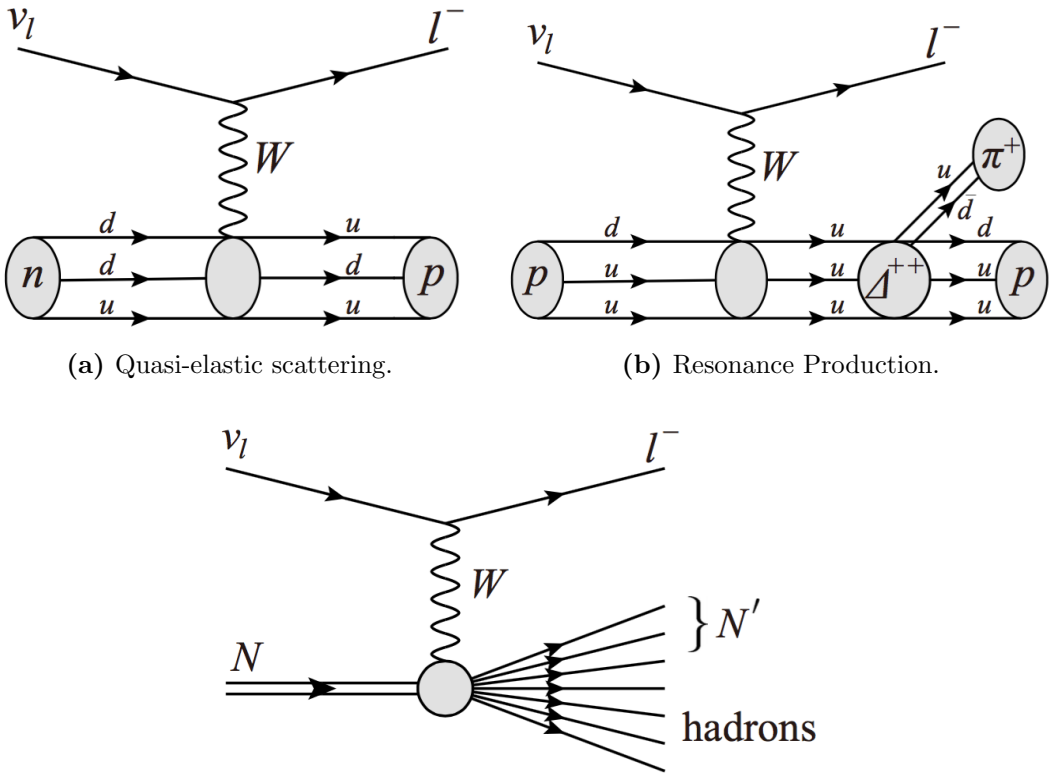

(a) Quasi-elastic scattering.

(b) Resonance Production.

(c) Deep Inelastic Scattering.

Figure 1.6: Feynman diagram of charged current neutrino-nucleus scattering.

(Quasi)Elastic Scattering (QE)

The dominant neutrino-nucleus interaction in the low energy region (less than few GeV) is a two body quasi-elastic scattering. This interaction represents a large fraction of the signal samples in many neutrino oscillation experiment. There are two types of scatterings, the charged current quasi-elastic (CCQE) scattering and the neutral current elastic scattering:

$$\text{CC: } \nu + N \rightarrow l + N' \tag{1.26}$$
$$\text{NC: } \nu + N \rightarrow \nu + N, \tag{1.27}$$

where l is the charged lepton and N is the nucleon. In the CCQE process, N is the neutron where N' is the proton.

Resonance Production (RES)

In addition to such elastic processes, neutrinos can also inelastically scatter producing a nucleon excited state (Δ, $N*$) in the intermediate energy region (1˜10 GeV). Such baryonic resonances subsequently decays mostly into a nucleon and single pion final state:

$$\text{CC: } \nu + N \rightarrow l + R \tag{1.28}$$
$$\text{NC: } \nu + N \rightarrow \nu + R, \tag{1.29}$$

where l is the charged lepton and R is a nucleon excited state, such as Δ.

Deep Inelastic Scattering (DIS)

In the high energy region (>5 GeV), the neutrino interaction is dominated by the deep inelastic scattering (DIS) where neutrinos scatter off the quarks inside the nucleon:

$$\text{CC: } \nu + N \rightarrow l + X \tag{1.30}$$
$$\text{NC: } \nu + N \rightarrow \nu + X, \tag{1.31}$$

where l is charged lepton and X is hadrons, resulted from the strong force between the quarks.

1.5 Overview of the T2K Experiment

The T2K (Tokai to Kamioka) experiment is a long-baseline neutrino experiment, located in Japan [27]. A beam of almost pure muon neutrinos is produced at the J-PARC (Japan Proton Accelerator Research Complex) in Tokai, Japan [28]. At 280m downstream from the production target, near detector complex (ND280) [29, 30, 31, 32, 33, 34] measures the properties of the neutrino beam prior to oscillation. Then neutrinos travel 295km across

the Japan to the far detector, Super-Kamiokande (SK) [35], a 50 kiloton water Cherenkov detector in Kamioka, Japan. Figure 1.7 shows an overview of T2K experiment. A more detailed description of T2K will be given in Chap. 2.

The main goal of T2K is the precise measurement of the neutrino oscillation parameters. It can be achieved by following two neutrino oscillation modes.

Discovery of $\nu_\mu \to \nu_e$ oscillation
The primary goal of the T2K was to measure the finite θ_{13} with a discovery of the $\nu_\mu \to \nu_e$ oscillation. With Eq. 1.13 and previously measured parameters θ_{23} and Δm^2_{32}, T2K could provide the first indication of ν_e appearance.

Precision measurements of $\nu_\mu \to \nu_\mu$ oscillation
In addition to the primary goal of measuring ν_e appearance, T2K also aims to measure θ_{23} and Δm^2_{32} precisely via muon neutrino disappearance (Eq. 1.14). With the reactor θ_{13} measurements, θ_{23} is the parameter with the largest uncertainty among the three mixing angles.

The results of these two measurements has been performed and published [20, 36, 37, 37, 38]. In addition, T2K also provides measurement of neutrino interaction cross sections, one of which is the subject of this thesis.

1.6 Motivation for the CCν_e Measurement

With the recent firm establishment of ν_e appearance by T2K, future precision ν_e appearance measurement can be used to explore CP violation in neutrino interactions. However such an exploration requires detailed understanding of the ν_e interactions, as well as contamination of ν_e in the ν_μ beam. The presence of the ν_e component in the beam accounts for 1.2% of the beam [39], which is the main background in the ν_e appearance measurement. T2K has observed the appearance of 28 ν_e candidate events at the far detector with 7.3σ significance over a background expectation of 4.92 ± 0.55 events for $\theta_{13} = 0$ [36]. The largest irreducible background for the appearance measurement comes from the predicted 3.2 intrinsic ν_e beam events.

Moreover, as shown in Tab. 1.2, the largest systematic uncertainty in T2K ν_e appearance observation comes from neutrino cross section error [40]. This uncertainty comes from model

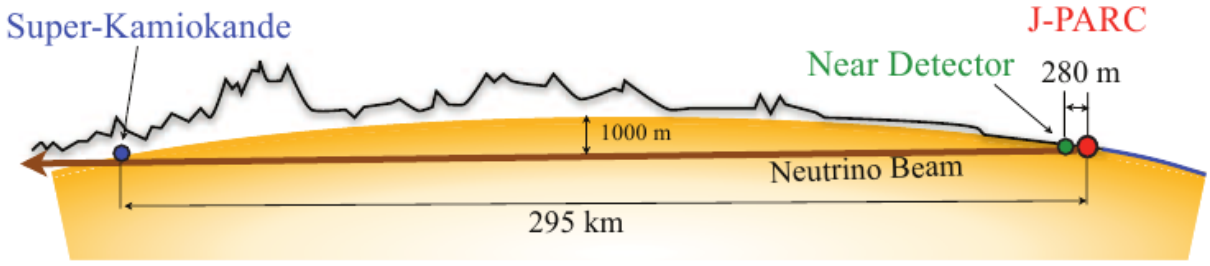

Figure 1.7: Overview of the T2K experiment.

Table 1.2: Systematic uncertainties in 2013 T2K ν_e appearance analysis.

Error source [%]	$\sin^2 2\theta_{13} = 0.1$	$\sin^2 2\theta_{13} = 0$
Beam flux and near detector	2.9	4.8
(w/o ND280 constraint)	(25.9)	(21.7)
Uncorrelated ν interaction	7.5	6.8
Far detector and FSI+SI+PN	3.5	7.3
Total	8.8	11.1

uncertainties in the meson exchange current for C versus for O, as the far detector of T2K has water target where the near detector constraints for the T2K oscillation analysis has been using the measurements only on C. To reduce the this uncertainties, better cross section measurements on carbon and water are needed. The only measurements of ν_μ neutrino interactions on water were reported by the K2K experiment for quasi-elastic interactions [41], and for reactions resulting in pions in the final state [42, 43, 44, 45].

Chapter 2

The T2K Experiment

The T2K experiment is a long-baseline accelerator neutrino experiment [27]. An overview of the experiment was given in Chap. 1. In this chapter, the details of the experiment, including neutrino beamline, the near detector facility, and the Super-Kamiokande detector will be given.

2.1 Off-axis Beam Configuration

One of the important features of the T2K experiment is that the T2K neutrino beamline is configured such that the far detector is 2.5° off the beamline axis. At fixed off-axis angles, unlike directly along the beam axis, a beam with a narrower energy spectrum is obtained as shown in Fig. 2.1. This gives T2K two advantages: first, the peak of an off-axis spectrum is lower in energy than for an on-axis beam, allowing T2K to tune the peak energy to the oscillation maximum energy of ~ 0.6 GeV, giving higher statistics where it is most important. Hence, the angle 2.5° was chosen which maximizes the neutrino oscillation probabilities at 295 km. The second advantage comes from the removal of a large flux of higher energy neutrinos, which do not contribute to the oscillation signal at SK but will generate background interactions. For oscillation analyses, an off-axis beam delivers higher statistic with lower backgrounds.

2.2 J-PARC Accelerators

An overview of the J-PARC [28] facility is shown in Fig. 2.2. J-PARC consists of three accelerators.

The Linear Accelerator (LINAC) accelerates H^- beam up to 400 MeV and converts it to H^+ beam by charge-stripping foils at the end of the LINAC, before injection into the RCS. Then the Rapid Cycling Synchrotron (RCS) accelerates the beam up to 3 GeV in 2 bunches with 25 Hz cycle. Lastly, the Main Ring Synchrotron (MR) takes 5% of the proton bunches and accelerates it up to 30 GeV, in bunches of 8 (6 prior to a 2010 Summer upgrade)

For each cycle, the beam is extracted from the MR to the neutrino beamline as a "spill". One spill contains 8 (6 prior to 2010 Summer upgrade) bunches in 4.1 μs.

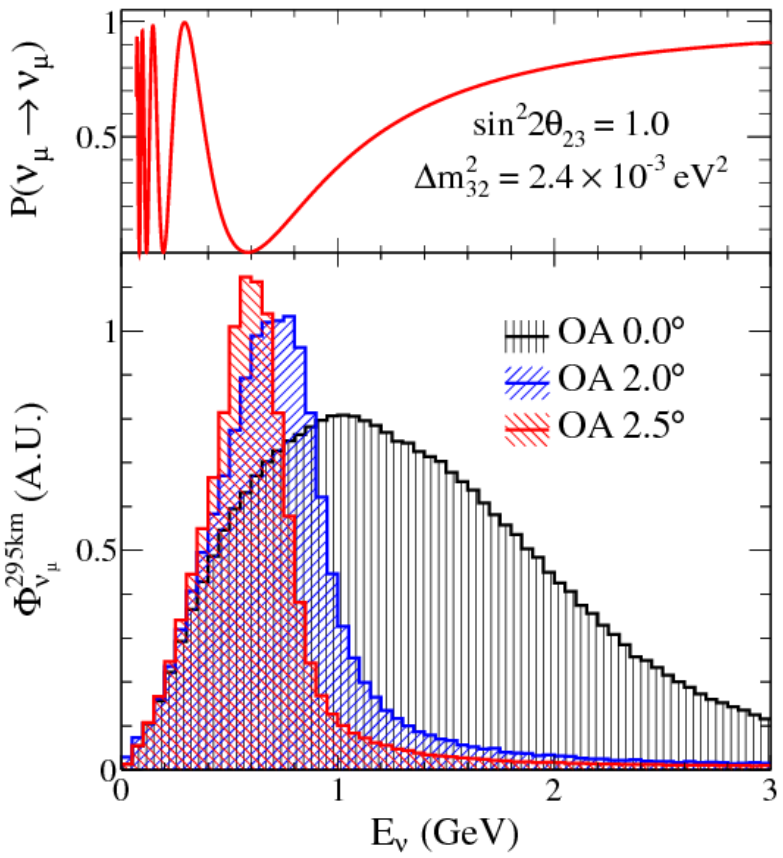

Figure 2.1: The top plot shows the muon neutrino survival probability expected at SK. The bottom plot shows the effect of moving off-axis on the ν_μ energy spectrum with the off-axis of 0.0°, 2.0° and 2.5°.

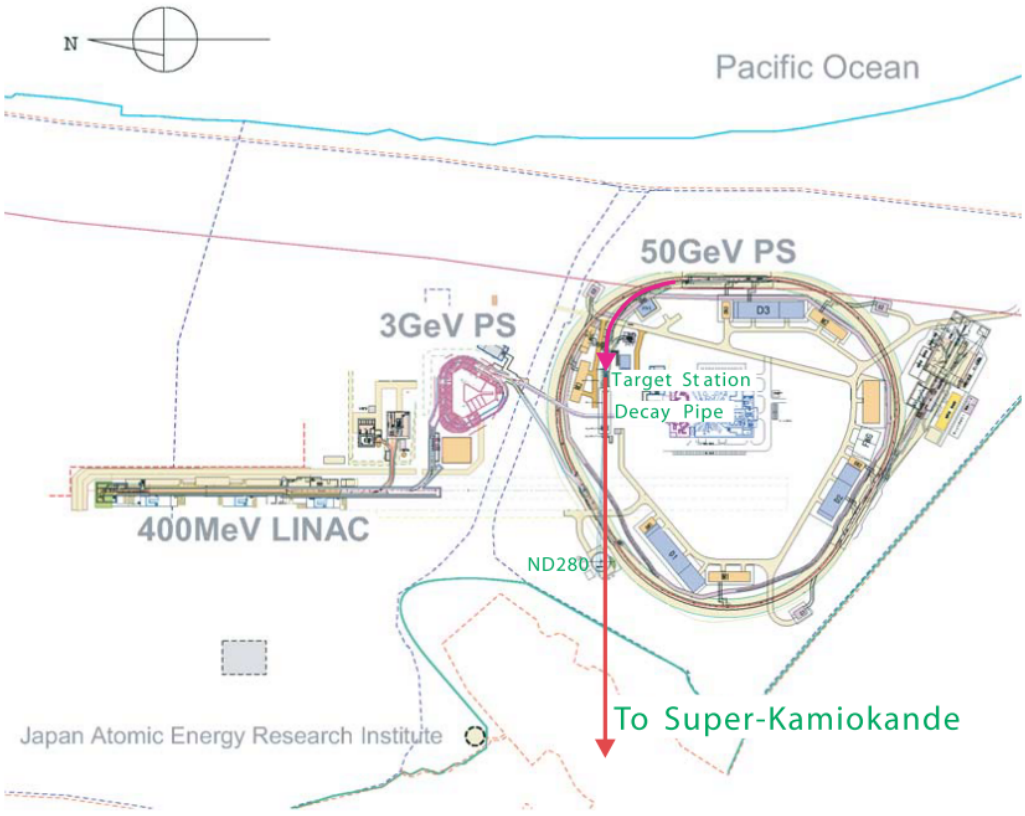

Figure 2.2: Overview of the J-PARC facility

2.3 T2K Neutrino Beamline

The T2K neutrino beamline is composed with two sub-beamlines: the primary and secondary beamlines. The proton beam is extracted from the MR in a single turn in the primary beamline, and bend in the direction of the far detector, Super-Kamiokande. In the secondary beamline, the proton beam illuminates a a graphite target, producing secondary particles consisting mostly of charged pions and kaons. These particles are focused in the forward direction by the magnetic horns, then decay into muons and muon neutrinos during travel along a decay volume. The overview of the T2K neutrino beamline is shown in Fig. 2.3.

2.3.1 Primary beamline

As shown in Fig. 2.3, the primary beamline is comprised of three sections: the preparation section (54 m long), the arc section (147 m), and final focusing section (37 m). In the preparation section, the extracted proton beam from the MR is tuned with a series of 11 normal-conducting magnets so that the beam can be accepted by the arc section. In the arc section, the beam is bent towards Kamioka by 80.7°, using 14 doublets of superconducting magnets. In the final focusing section, ten normal conducting magnets guide and focus the

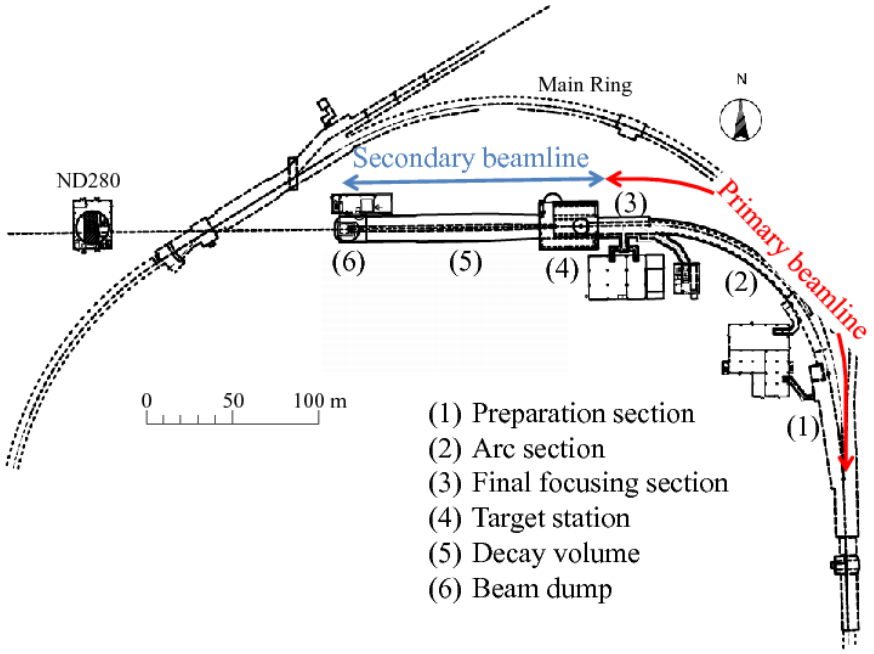

Figure 2.3: Overview of the T2K neutrino beamline

beam onto the target.

2.3.2 Secondary beamline

The secondary beamline consists of three sections: the target station, decay volume, and beam dump. A side view of the secondary beamline is shown in Fig. 2.4.

The target station contains: a baffle which collimates the beam to protect the magnetic horns; an optical transition radiation monitor (OTR) to monitor the proton beam profile just upstream of the target; the target to generate secondary pions; and three magnetic horns excited by current pulse to focus the pions. The produced charged pions enter the decay volume and decay mainly into muons and muon neutrinos. All the hadrons, as well as muons below $\sim$ 5 GeV/c, are stopped by the beam dump. The neutrinos pass through the beam dump and are used for physics experiments. Muons with momentum above $\sim$ 5 GeV/c that pass through the beam dump are monitored by a muon monitor (MUMON) which is used to characterize the neutrino beam. The MUMON is placed at the end of the beam dump, and monitors the beam stability including the overall flux and beam position.

2.4 Near Detector Complex

The T2K experiment measures the neutrino energy spectrum, flavor content, and interaction rates of the unoscillated neutrino beam with a set of detectors located 280 m from the production target. The measurements are used to predict the neutrino interactions at Super-Kamiokande. In this near detector complex, there are two detectors: the on-axis neutrino

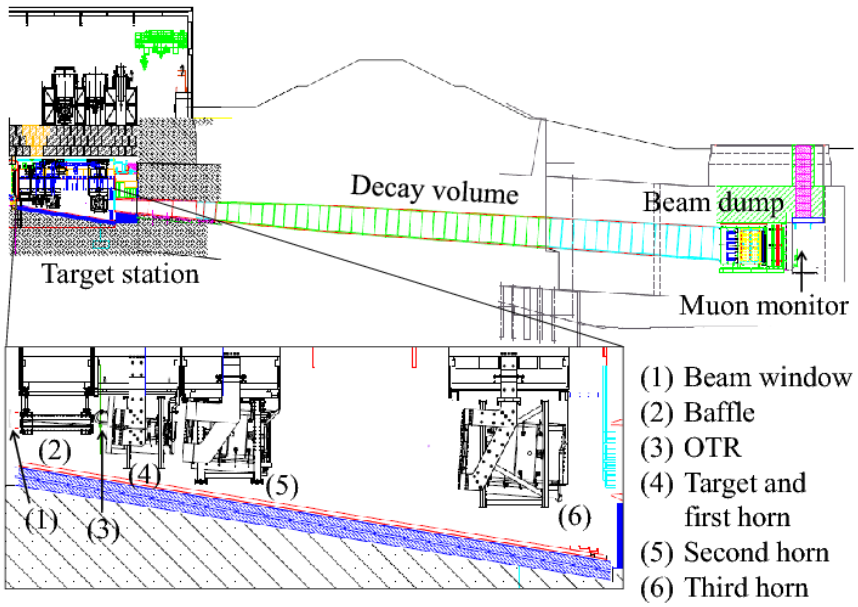

Figure 2.4: Side view of the secondary beamline.

beam monitor (INGRID), and the off-axis neutrino spectrometer (ND280). A schematic of the near detector complex is shown in Fig. 2.5, with the ND280 and the magnet on the upper level and the INGRID located on the level below.

2.4.1 On-axis Detector: INGRID

INGRID (Interactive Neutrino GRID) is a neutrino detector centered on the neutrino beam axis [34]. This on-axis detector was designed to monitor directly the neutrino beam direction and intensity by means of neutrino interactions in iron, with sufficient statistics to provide daily measurements at nominal beam intensity. The INGRID modules consist of a sandwich structure of nine iron plates and 11 tracking scintillator planes as shown in Fig. 2.6. The modules are surrounded by veto scintillator planes to reject interactions outside the module. Iron provides a dense target for the neutrinos and increases the rate of observed events. The scintillator bars contain wave length shifting (WLS) fibers that collect the scintillation light and direct it towards a Multi-Pixel Photon Counter (MPPC) [46].

2.4.2 Off-axis Detector: ND280

The off-axis detector, ND280, serves to measure the flux, energy spectrum and electron neutrino contamination in the direction of the far detector, along with measuring rates for exclusive neutrino reactions. These measurements are used to characterize signals and backgrounds in the Super-Kamiokande detector. ND280 is composed of sub-detectors as shown in Fig. 2.7.

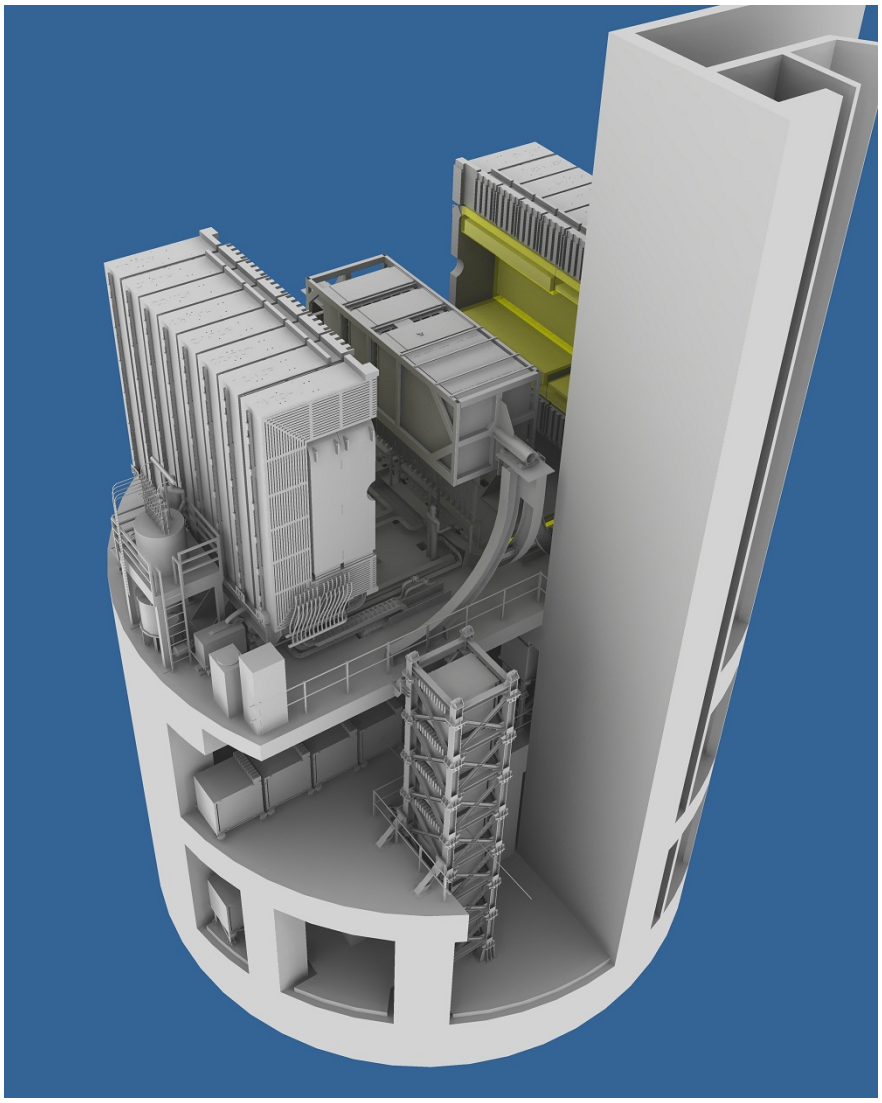

Figure 2.5: A diagram of the near detector complex. The off-axis detector, ND280, and the magnet are located on the upper level and the on-axis detector, INGRID, is located on the level below.

π^0 Detector (PØD)

The PØD is placed at the upstream end of the ND280. Its purpose is to measure the neutral current π^0 production rate ($\nu + N \rightarrow \nu + \pi^0 + N'$) and intrinsic ν_e and $\bar{\nu}_e$ component of the beam. PØD [29] will be explained in detail in the next chapter, as it is the primary detector for the analyses of this thesis.

Time Projection Chamber (TPC)

Each TPC consists of an inner box that holds an argon-based drift gas. A diagram of the general construction of the TPC is shown in Fig. 2.8 [30]. An electric field is applied to the gas volume, so that charged particles passing through the TPCs produce

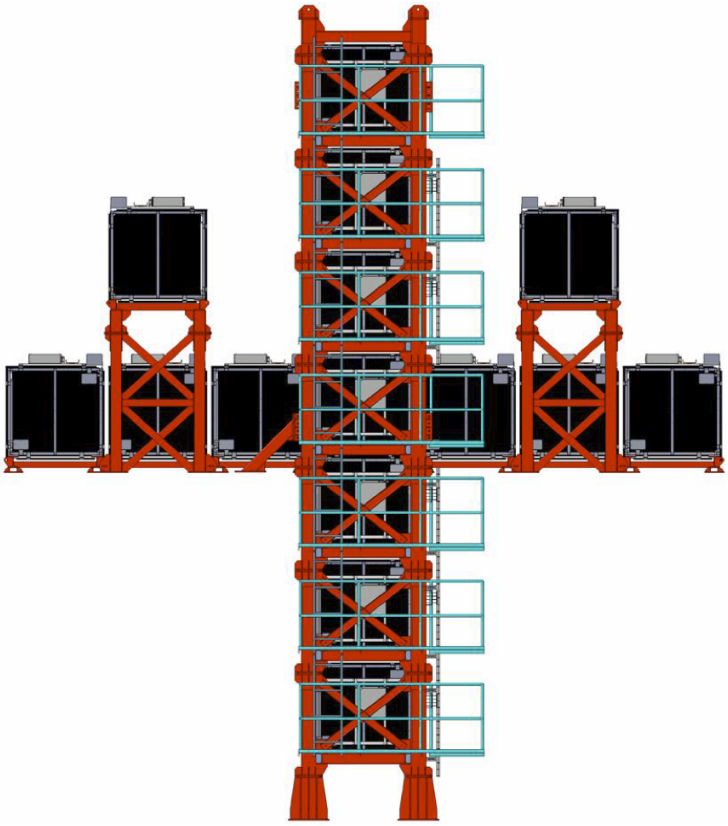

Figure 2.6: A diagram of INGRID. The beam direction is into the page at the intersection of the vertical and horizontal modules.

ionization electrons in the gas that drift away from the central cathode and toward the anodic readout planes at each end of the chambers. TPCs measure the momentum of charged particles from the track curvature in the magnetic field, as well as the density of ionization left by each particle to identify the types of charged particles.

Fine Grained Detector (FGD)

Two FGDs [31] provide target mass for neutrino interactions as well as tracking of the charged particles coming from the interaction vertex. The FGDs are constructed from polystyrene scintillator.

Electromagnetic Calorimeter (ECal)

The ECal [32] is a sampling electromagnetic calorimeter surrounding the inner detectors (PØD, TPCs, FGDs). It uses layers of plastic scintillator bars as active material with lead radiator/absorber sheets between layers, and provides near-hermetic coverage for all particles exiting the inner detector volume.

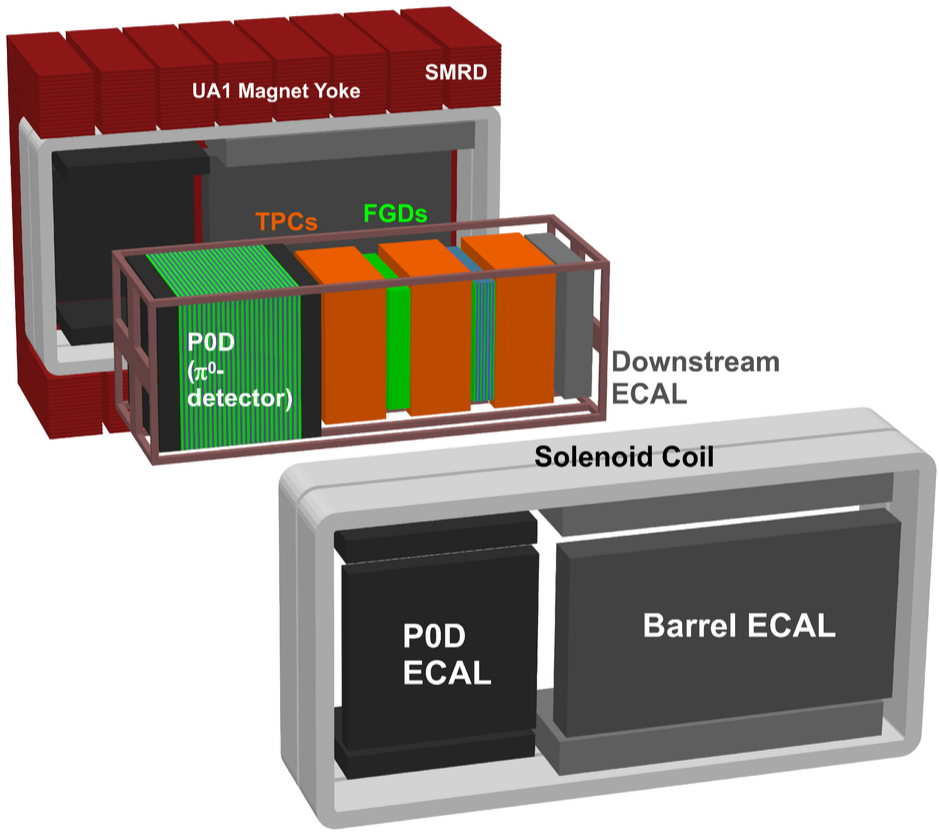

Figure 2.7: A diagram of ND280 Detector.

UA1 Magnet

The CERN UA1/NOMAD magent is reused in ND280, providing a dipole magnetic field of 0.2 T, to measure with good resolution momenta of charged particles produced by neutrino interactions and determine the signs of their charges.

Side Muon Range Detector (SMRD)

The SMRD [33] records muons escaping with high angles with respect to the beam direction and measures their momenta. It is also used to tag cosmic ray muons that penetrate the ND280 detector. It consists of scintillator modules with steel plates.

2.5 Far Detector: Super-Kamiokande

Super-Kamiokande (SK) [35], which serves as the far detector in the T2K experiment, is a large water Cherenkov detector located 295 km west of J-PARC, 1 km deep under Mount Ikenoyama. SK is a stainless steel water tank filled with 50 kton of ultra-pure water in a large cavern. Inside there are roughly 13,000 photomultiplier tubes (PMTs) image neutrino

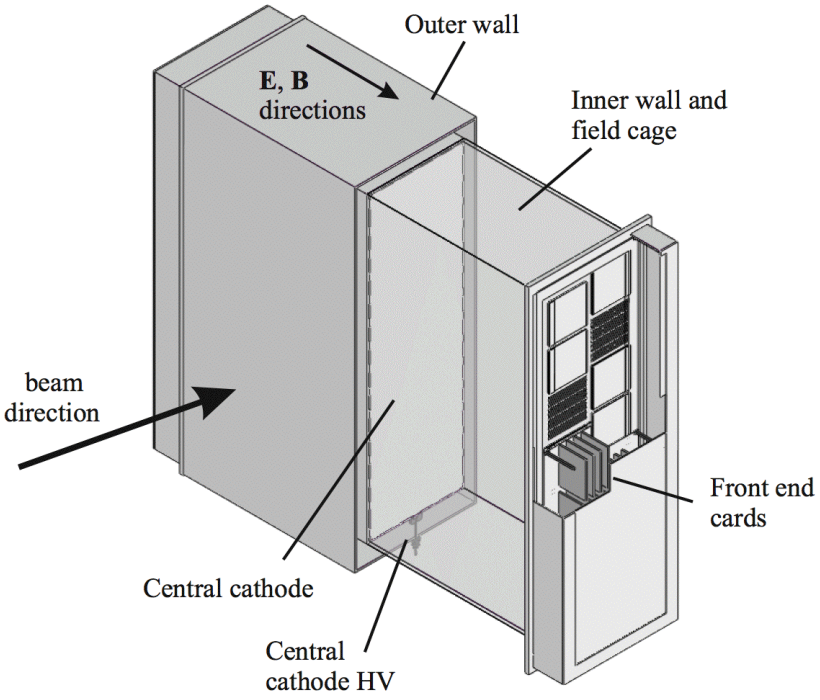

Figure 2.8: Simplified cut-away drawing of the TPC.

interactions. Figure 2.9 shows a diagram of SK in the Mozumi mine at Kamioka, Japan. The tank comprised two regions, the inner and outer detector. The inner detector (ID) is a cylindrical shell of 33.8 m in diameter and 36.2 m in height. It houses 11,129 inward-facing 50 cm diameter PMTs along it's inner walls, covering 40% of the surface. The outer detector (OD) is a 2 m thick cylindrical shell enclosing the inner detector. It contains 1,885 outward-facing 20 cm diameter PMTs along its inner walls. It is only sparsely instrumented, but is capable of nearly 100% rejection efficiency of cosmic ray muon backgrounds. The inner and outer detectors are optically separated by a light tight membrane provided by Tyvek sheets.

The fiducial volume of SK is defined as a virtual cylinder of 29.8 m diameter and 32.2 m in height, enclosing 22.5 kton of pure water. Neutrinos are detected with the PMTs by measuring the Cherenkov light emitted by charged particles from the neutrino interactions in the water. The particle's vertex, energy, direction are reconstructed from the timing and position of the Cherenkov light.

Cherenkov light is emitted when a particle travels faster than the speed of light in a dielectric medium. As a particle travels, a cone of Cherenkov light is emitted, and a collection of the Cherenkov photons creates a ring signature on the walls equipped with the PMTs at SK. When a muon travels, it does not produce an electromagnetic shower in the detector and creates a ring with very sharp edge. However, when a high energy electron/positron goes through the detector, it produces an electromagnetic shower, creating a collection of electrons that travel in generally in the same direction. This collection of electrons creates fuzzy ring signature, as many rings overlap, which shows different characteristic compared to

the ring shape of muon particle. The particle identification is performed based this feature. Figure 2.10 shows typical event displays of electron and muon.

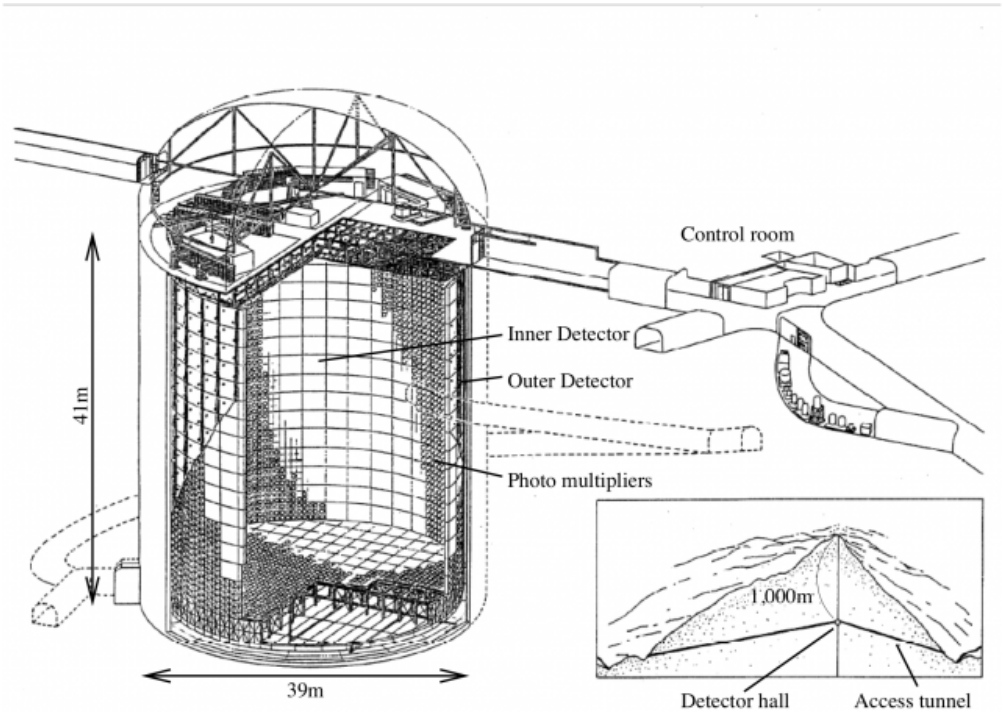

Figure 2.9: Diagram of the Super-Kamiokande Detector.

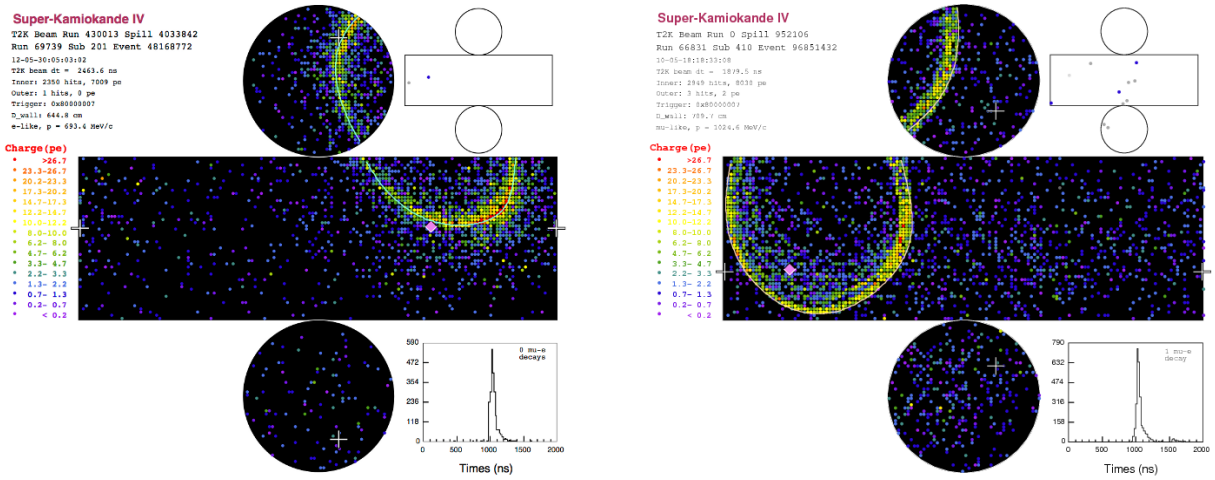

Figure 2.10: Event displays from T2K beam interactions in SK. The edge of the Cherenkov ring from an electron (left) is fuzzier than the one from a muon (right).

2.6 T2K Data Set

The result of this thesis are based on four physics runs of the T2K experiment: Run 1 (January 2010 – June 2010), Run 2 (November 2010 – March 2011), Run 3 (March 2012 – June 2012), and Run 4 (October 2012 – May 2013). Run 2 and Run 4 period is divided into two sub periods, according to the PØD configuration, using water (water-in) and air (water-out) as the main interaction target. More details on the PØD configurations will be discussed in Chap. 3. A very small fraction of Run 3 data is not used, due to the magnetic horn current decrease, which caused a failure in good spill pre-selection. The summary of the run periods, configurations and accumulated protons on target (POT) are shown in Tab. 2.1.

For the $\bar{\nu}_e$ analysis, two physics runs are used: Run 5 (May 2014 – Jun 2014) and Run 6 (Nov 2014 – Jun 2015), both in PØD air configuration. Run 5 data is composed with both neutrino and anti-neutrino runs, and only the anti-neutrino run is considered in this thesis. The summary of the these run periods are shown in Tab. 2.2.

The total accumulated POT and the averaged beam power per hour of the T2K experiment over time, is shown in Fig. 2.11.

Table 2.1: Summary of T2K neutrino runs and the number of protons on target (POT) used in the analysis

T2K Run	PØD Config.	Beam Power (kW)	POT ($\times 10^{19}$)
Run 1	Water	50	2.96
Run 2	Water	120	6.96
Run 2	Air	120	3.59
Run 3	Air	178	13.5
Run 4	Water	178	16.5
Run 4	Air	178	17.8
Total	Water		26.4
	Air		34.9

Table 2.2: Summary of T2K anti-neutrino runs and the number of protons on target (POT) used in the analysis

T2K Run	PØD Config.	Beam Power (kW)	POT ($\times 10^{19}$)
Run 5	Air	220	4.32
Run 6	Air	240	24.0
Total	Air		28.3

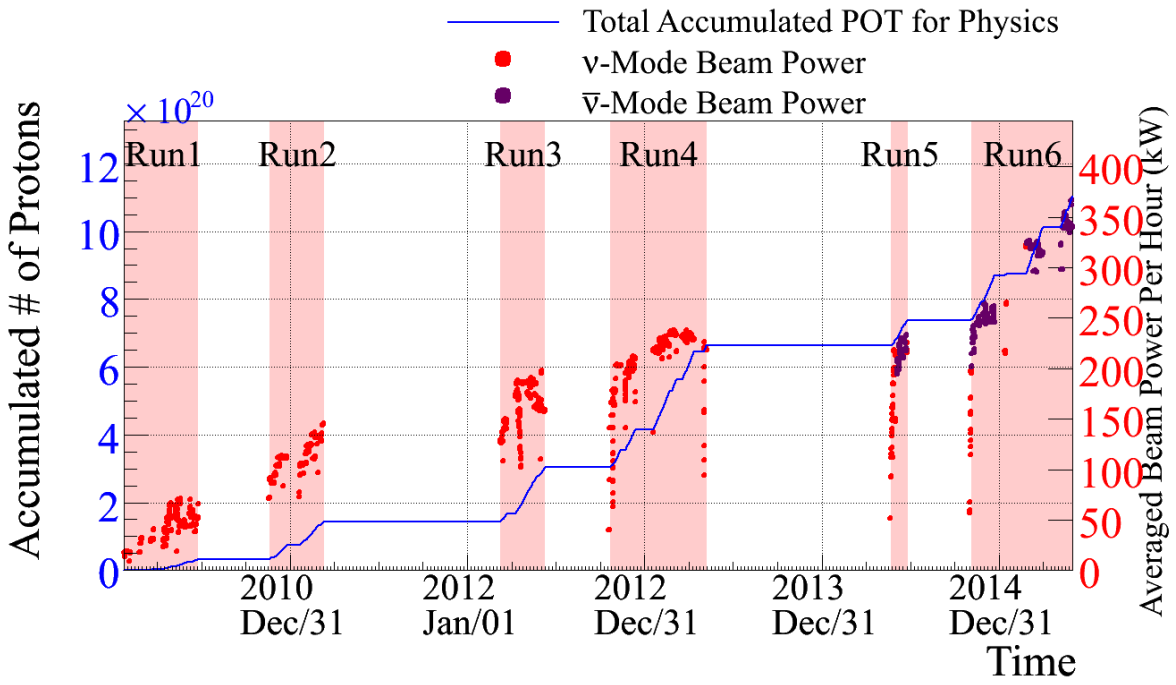

Figure 2.11: Total accumulated POT and averaged beam power per hour over time.

Chapter 3

The π^0 Detector: PØD

The π^0 detector [29], PØD, is the main detector used in this analysis. The primary physics goal of PØD is the measurement of the neutral current π^0 rate and intrinsic ν_e content of the beam flux. In this chapter, the general description of the detector along with software process, reconstruction algorithms, and the energy calibration result will be provided.

3.1 Detector Description

Figure 3.1 shows a schematic of the active regions of the PØD. The central region, composed of the "upstream water target" and "central water target", is made from alternating scintillator planes, water bags, and brass sheets. The front and rear regions, the "upstream ECal" and "central ECal" respectively, use alternating scintillator planes and lead sheets. This layout provides effective containment of electromagnetic showers and a veto region before and after the water target region to provide rejection of particle interactions that enter from outside the PØD.

There are a total of 40 scintillator modules in the PØD. Each PØD module, or PØDule, had two perpendicular arrays of triangular scintillator bars, forming a plane. There are 134 horizontal bars (y-axis) and 126 vertical bars (x-axis) in each PØDule. Each bar has a single coaxial hole through which is threaded a wavelength-shifting (WLS) fiber. Each fiber has a mirrored coating applied on one end while the other end is optically coupled to a Hamamatsu multi-pixel photon counter (MPPC) for readout, as shown in Fig. 3.2. Each photodetector is read out with Trip-t Front-end electronics. There are a total of 10,400 channels for the entire PØD.

The PØDules were assembled into four units called Super-PØDules. The two ECal Super-PØDules each consist of a sandwich of seven PØDules alternating with seven stainless steel-clad lead sheets. The water target is formed from two units, the upstream and central water target Super-PØDules. The upstream (central) water target Super-PØDule comprises 13 PØDules alternating with 13 (12) water bag layers (each of which is 28 mm thick), and 13 (12) brass sheets (1.28 mm thick), as shown in Fig. 3.3. This water bag can be filled and drained with water to give analyzers access to a mass subtraction to find on-water cross sections.

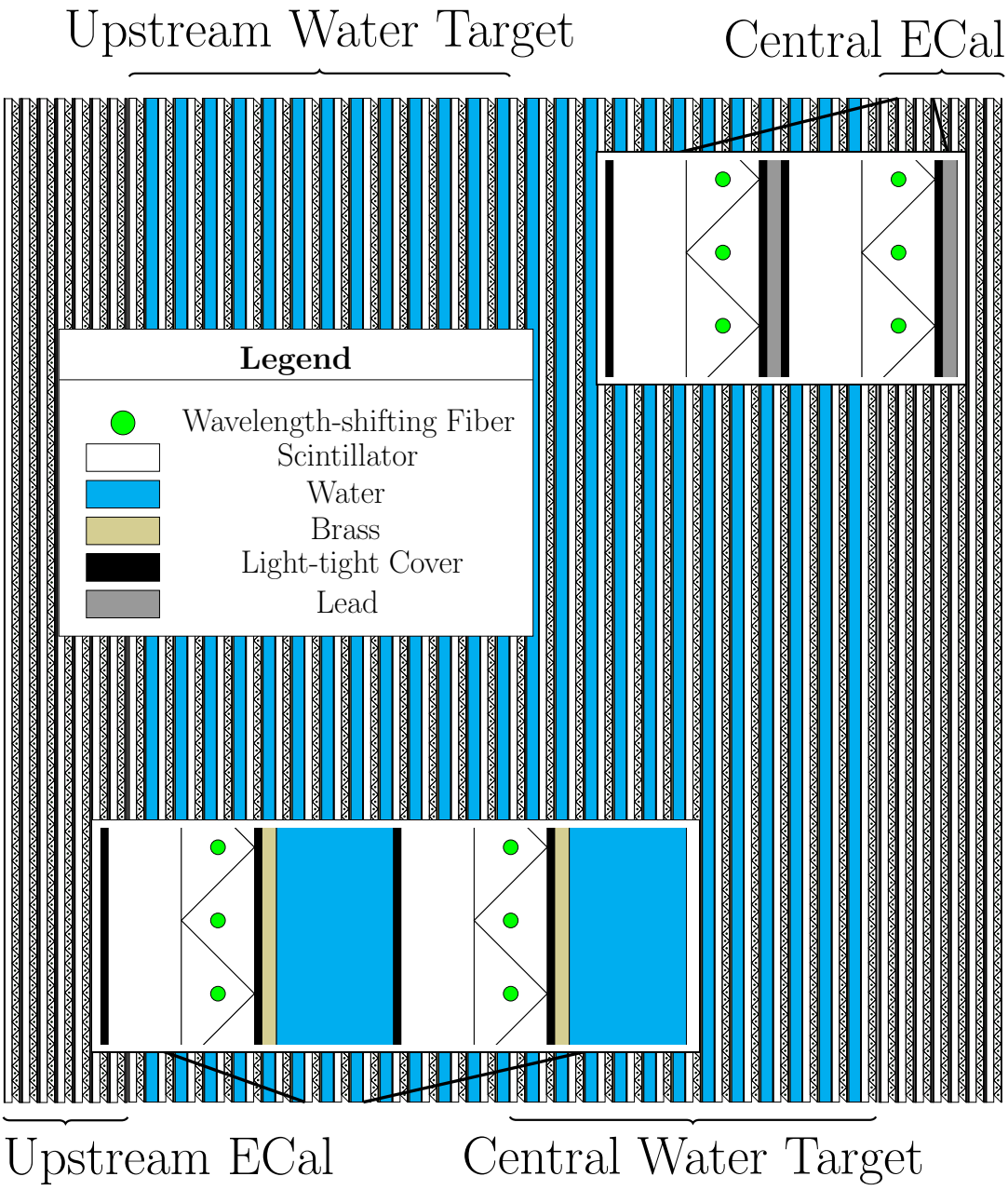

Figure 3.1: A schematic of the PØD.

The dimensions of the entire PØD active target are 2013 mm × 2239 mm × 2400 mm (width × height × length) and the mass of the detector with and without water is 15,800 kg and 12,900 kg respectively. The PØD is housed inside a detector basket structure that supports the central off-axis detectors inside the magnet.

The detector was optimized for the fiducial volume to be within 25 cm from the edge of the active area. However, the position of the detector changes when alignment correction

is applied. Current fiducial volume is defined to be: within the water target, length in x of 1600 mm, length in y of 1740 mm, length in z of 1705 mm, centered around the active center of the PØD. Table 3.1 shows the summary of the fiducial volume coordinates.

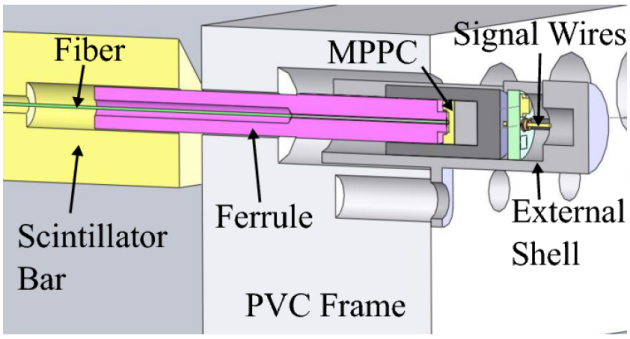

Figure 3.2: A close-up view of the edge of a PØDule showing WLS fibers and MPPCs.

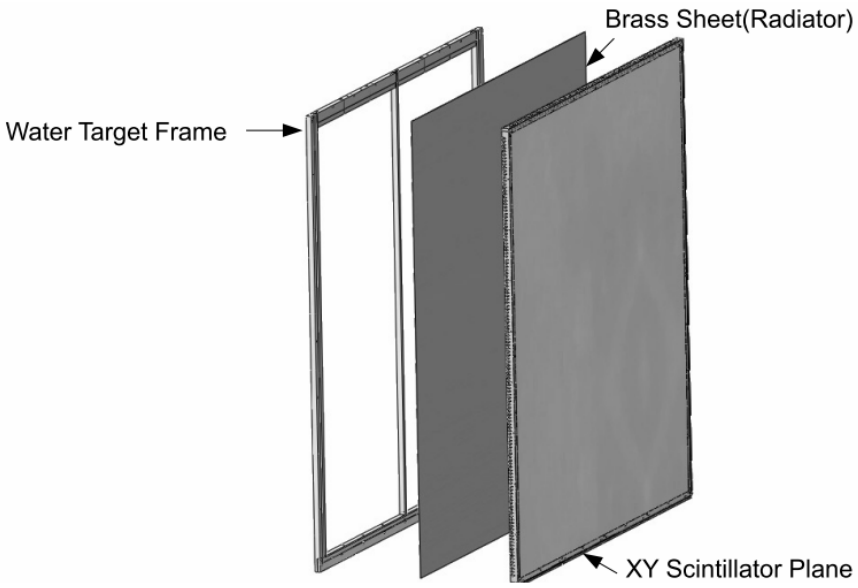

Figure 3.3: Expanded view of water target PØDule, brass radiator and water bladder containment frame.

Table 3.1: Definition of the PØD fiducial volume.

Coordinate	Center (mm)	Half-width (mm)	Minimum (mm)	Maximum (mm)
x	-36	800	-836	764
y	-1	870	-871	869
z	-2116	852.5	-2969	-1264

Table 3.2: The as-built PØD fiducial volume masses for Run 1 and 2 as well as the PØD fiducial volume mass used in MC are listed for water and air configuration.

	PØD Water Configuration (kg)	PØD Air Configuration (kg)
As-Built Run 1	5460.86 ± 37.78	3558.86 ± 34.23
As-Built Run 2	5480.30 ± 37.40	3578.30 ± 33.80
MC	5393.22 ± 0.56	3469.14 ± 0.55

The mass of the PØD fiducial volume can be calculated by adding up masses of each component: PØDules, brass, and lead layers, for both the water and air configuration. The obtained as-built masses for Run 1 and 2 as well as the PØD mass in Monte Carlo (with Production 5 and 6, version of ND280 software used in this analysis) are listed in Tab.3.2. The PØD mass is different for Run 1 and Run 2 because the entire water sensor system was replaced between those runs. As the information about the fiducial mass of the water for Run 4 is not available yet, it is therefore assumed to be the same as in Run 2. Most of the discrepancy between as-built mass and the mass in the Monte Carlo (MC) is caused by the water target dead material which is not modeled in the MC.

3.2 Software Process

The general structure of the software suite is indicated in Fig. 3.4.

The library "oaEvent" defines the file format for the offline software, which is used from the point that the raw MIDAS data files are converted for offline use, up to the production of summarized format files at the end of the chain of processing. "oaRawEvent" interfaces with the readout data format that is provided by the DAQ group, and allows the raw MIDAS files to be read directly by the offline software. Calibration constants for the detectors are stored on a centralized MySQL database, and are applied by "oaCalib" and its sub-packages at processing time. The access routines for the database are based on those developed for the MINOS experiment.

A representation fo the geometry of the detectors is constructed in GEANT4 code, and is converted to ROOT TGeoManager format and stored in version-controlled files. These are retrieved from a central repository to be used in the interpretation of raw data.

The Monte Carlo simulation starts with the neutrino interaction generator. T2K primarily uses two generators, GENIE and NEUT. The neutrino fluxes estimated from beam MC are passes through the detector geometries, and neutrino cross sections specific to the nuclei present in the geometries are used to generate interactions that are appropriate for the distribution of materials in the detector.

As an output of the generator, a list of interactions with the energies and positions of all the particles is created. Then it is passed onto `nd280mc` package which places the interactions in the geometrical volume of ND280 and propagates the particles. The electronics simulation, `elecSim`, package then simulates the response of the active detectors such as electronic noises,

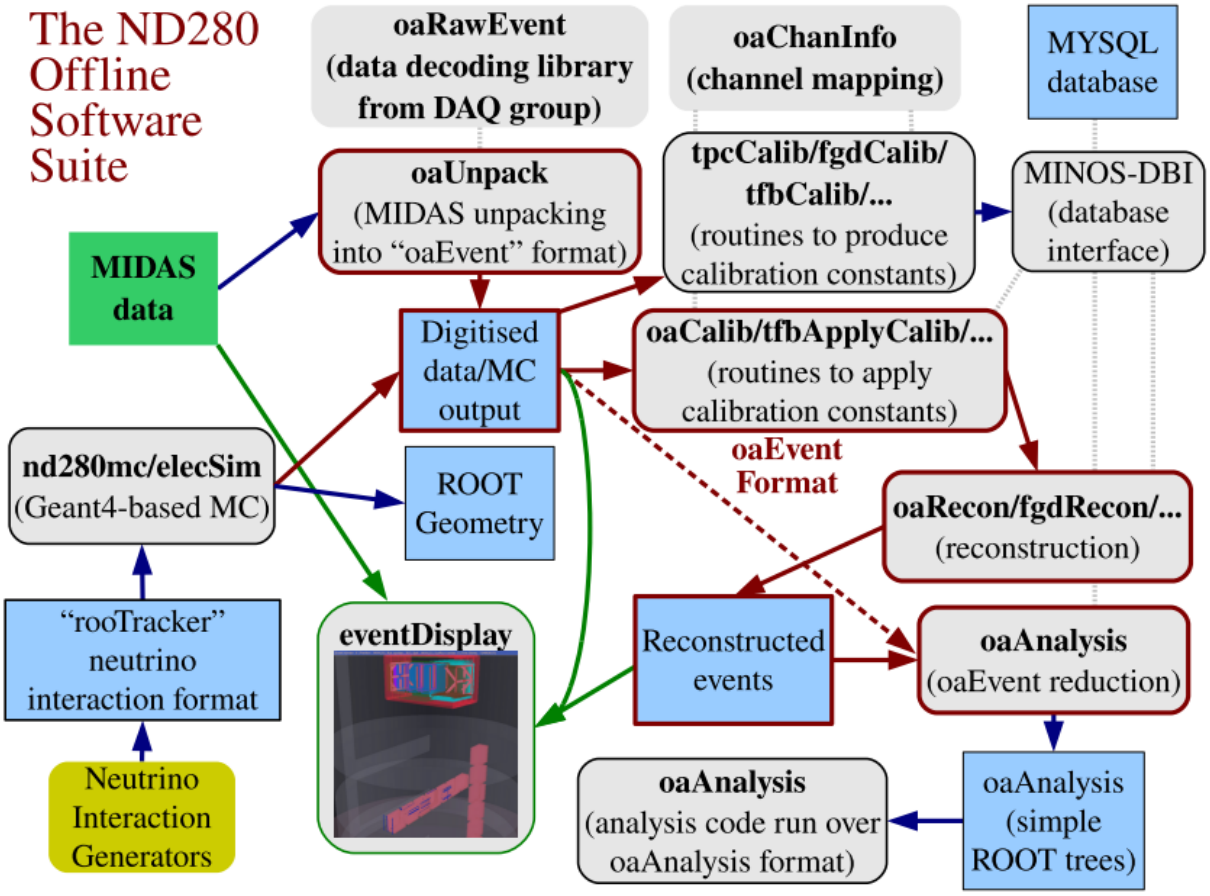

Figure 3.4: Schematic of the package structure of the ND280 Software Suite. Only the most representative packages are included.

and add to the Monte Carlo files. The output is passed to "oaCalib" which controls the calibration of all subdetectors. The next step is the reconstruction, "oaRecon". Individual subdetectors have dedicated packages designed to reconstruct event information internal to them. Then the reconstructed files is reduced to a simplified file format, "oaAnalysis", because the original reconstructed files are generally very large. The oaAnalysis files will contain all the important and necessary information in them, and they can be accessed via ROOT program.

3.3 PØD Reconstruction

The PØD reconstruction, PØDRecon is divided into two main sequential algorithm chains; track reconstruction followed by a shower reconstruction. Figure 3.5 shows the logical flow of the two chains.

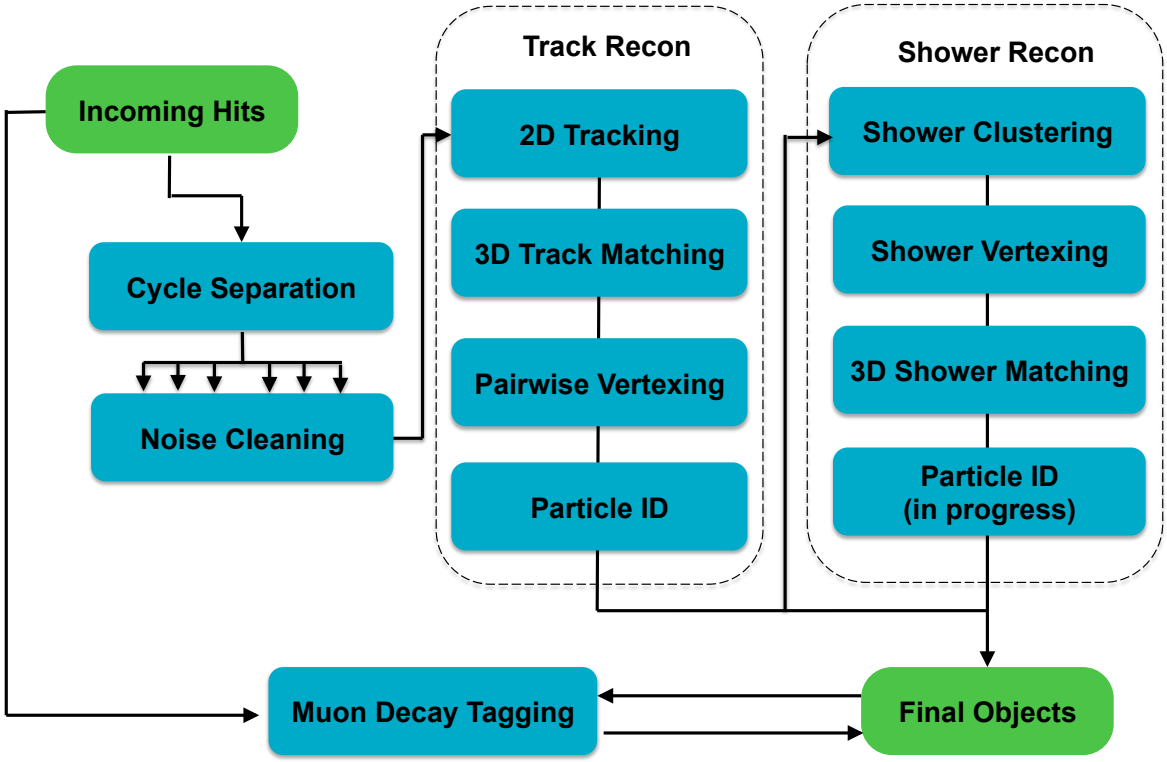

Figure 3.5: Flowchart showing the sequential algorithm chain of the PØD reconstruction. Most algorithms consider each cycle as a separate entity, and the chain can be subdivided into: preparation, track reconstruction and shower reconstruction.

3.3.1 Preparation

The input to the reconstruction is a single collection of PØD hits, which will have come from either; the calibration for data hits or the electronics simulation (`elecSim`) for MC simulated hits. As the PØD electronics produces hits subdivided into 23 cycles, and the cycles are predominantly independent, the first stage of the reconstruction is to separate hits into cycles. Only one vertex per cycle is reconstructed, then the track and shower reconstructions run on each cycle. Only the muon decay search spans the cycle objects.

Noise Cleaning

The first algorithm in the chain is noise cleaning. Noise hits are low in charge and uncorrelated to the higher charge hits from particle interactions. Therefore, a hit is retained if any of the following three conditions are true:

- It has charge $Q > 15$ pe, and has a neighbor in the same view within 30 ns in time and 20 cm in space.

- It has charge $Q > 7$ pe, and has a neighbor in the same view within 30 ns in time and 10 cm in space.
- It has a neighbor within 30 ns in time and 3.5 mm in space (with no charge requirement).

Hits failing all of these conditions are excluded from the rest of the reconstruction. Only cycles with at least 5 cleaned hits continue in the reconstruction.

3.3.2 Track Reconstruction

2D Tracking

The cleaned hits are then passed to a 2D tracking algorithm. Each of the two 2D views, xz and yz, are considered separately. Track seeds are constructed from a Hough Transform, which selects hits that conform to a straight line. The transform is constructed with bin sizes of 1.8° and 25 mm, and seeds must have a minimum of four hits.

Once a seed has been constructed, it is extended layer-by-layer using a road following algorithm, which adds hits within a 60 mm wide road, allowing for scattering of up to 1.5 rad. Once a layer has been added, up to three extra adjacent hits within the layer are also included.

Finally, the 2D track is extended non-exclusively at the end, so that hits near the vertex can be shared between multiple tracks. A maximum of 4 extra hits are included, using a 40 mm wide road, with no scattering allowed.

3D Track Matching

Once the 2D tracks are fully reconstructed, they are matched between the two views. The intention is to match as many tracks as possible, allowing for one-to-many matchings if required, as there is a good chance that tracks overlap in one view, but can still be distinguished in the other.

Each 2D track is considered in turn, comparing it with 2D tracks from the other view or 3D tracks already constructed from another pair. Each pair is weighted, based on an algorithm that accounts for: the number of overlapping layers, the relative disparity between the charges of the two tracks, and whether a track has already been matched. The best possible pairing is selected, and then the algorithm runs again over the remaining 2D tracks, until no possible pairing scores above a set threshold.

The 3D tracks are then fit with one of two algorithms: a 'Kalman' filter using the xz and yz scintillator layers as successive measurements, or a 'Parametric' fitter for high angle or short tracks where the Kalman method will not work.

For the Kalman method, the filter starts at the downstream end of the track, progresses to the upstream end of the track, and then reverses direction, returning to the downstream end. Each scintillator layer is stored as a TReconNode.

The parametric method produces a TReconNode for each hit. The rough direction of the track is determined, the hits are sorted based on that direction and each hit is fit, using

a linear method for hits within a 25 cm window. A minimum of 10 hits in each view is required, so the window is extended if necessary.

3D Vertexing

The full set of 2D and 3D tracks are then passed to a pairwise vertexing algorithm. Each pair of tracks (including a track paired with itself) provides a potential vertex. Both tracks must have either an x or y component, and they are projected back to a point of closest approach. This point is used as the vertex, with a position variance assigned based on the position and direction variances of the two tracks. Vertices are rejected if: the times of the two tracks are inconsistent ($\Delta t > 40ns$), the x or y position uncertainty is greater than 50 cm, or the z position uncertainty is greater than 50 cm.

The selection of candidate vertices are then clustered, as long as the times are consistent ($\Delta t < 40ns$), and they are not separated by more than 20 cm. Each time, the best matching pair is clustered and removed, being reintroduced as a single vertex, until all vertices have been clustered or no more matchings are possible.

Track PID

One vertices have been constructed, each constituent track is passed through particle identification algorithms, and stored as TReconPID's, contained in a copy of the vertex. The algorithm is based on the energy deposit of the tracks within PØDule layers.

The four possible hypotheses considered by the PID are `kEM` (electrons and photons), `kHeavyTrack` (protons), `kLightTrack` (muons) and `kOther`. All hits associated with a track that is classified as `kLightTrack` and `kHeavyTrack` are not forwarded to the PØDRecon shower stage and cannot be reconstructed as shower. For each track four variables are considered: the charge asymmetry between xz and yz layers in a PØDule, the charge asymmetry between neighboring PØDule, the number of layers with no charge deposit, and the fraction of charge deposited in the last five layers. A likelihood is constructed, by comparing the calculated variable to particle gun muons and electrons. The absolute charge scale of the PØD was unknown, including the agreement between the data and MC, so the variables are all intended to be independent of the charge scale.

3.3.3 Shower Reconstruction

The shower reconstruction is based on the results from the track reconstruction. Each vertex is reconstructed in turn, with showers constructed from hits from `kEM` and `kOther` TReconPID's and any hits unused in the tracking reconstruction result. The first vertex (which were ordered based on number of tracks, then z coordinate), is reconstructed with `kEM` and `kOther` TReconPID's from all vertices, any further vertices only include hits from their own TReconPID's.

The shower search works on the knowledge that all hits from a shower will fall in a cone when viewed from the interaction vertex. If the track vertex included `kLightTrack` or

`kHeavyTrack`, then the vertex location is loosely constrained by the track vertex, and any `kLightTrack` or `kHeavyTrack` TReconPID's are copied to the shower vertex.

Otherwise, the boundaries for the search are determined based on the results from an initial clustering algorithm, looking for shower seeds.

A grid search is run within the boundaries, looking for the location which best clusters hits into angular bins. This is determined with a likelihood function, with terms to penalize vertex locations with: a lot of unassigned charge, a large number of clusters (1 and 2 cluster solutions having no penalty), a long way from the first hits in the clusters, or clusters with a wide angular width.

The location with the best likelihood is selected, the clusters are then reconstructed as showers, with no further PID attempted, and the vertex uncertainty is based on the shape of the likelihood distribution near the best fit point.

3.3.4 Muon Decay Search

The final step of the PØD reconstruction is to run a muon decay search on all final vertices, from both track and shower stages. The search looks for clusters of hits, more than 200 ns after the vertex, in the same location. Clusters with more than 500 p.e. of energy are rejected, as being more likely to be later neutrino interactions or cosmic ray muons.

3.4 Energy Calibration[1]

In order to provide an accurate energy of reconstructed electron, the relationship between the reconstructed charge (PE) and the true energy (MeV) of electron need to be studied. The Monte Carlo (MC) energy calibration study compares the reconstructed charge of tracks and showers of MC events with the corresponding true electron energy, then extracts the energy calibration constants. Since absorber materials for PØD water target (WT) and electromagnetic calorimeter (ECal) are different, we need to derive each constant separately using following equations,

$$E_e = k_{\mathrm{Ecal}} \sum_{i \in \mathrm{ECal}} Q_i + k_{\mathrm{Water,WT}} \sum_{i \in \mathrm{WT}} Q_i \tag{3.1}$$

$$E_e = k_{\mathrm{Ecal}} \sum_{i \in \mathrm{ECal}} Q_i + k_{\mathrm{Air,WT}} \sum_{i \in \mathrm{WT}} Q_i \tag{3.2}$$

where E_e is true electron energy and Q is the charge of the reconstructed object , and the sums run over the charges Q of the nodes in that part of the detector.

There are three calibration constants k_{Ecal}, $k_{\mathrm{Water,WT}}$, and $k_{\mathrm{Air,WT}}$ for the ECal, the water target for PØD water configuration, and the water target for PØD air configuration, respectively. As explained later, the event selections are based on reconstructed tracks and

[1]Energy calibration constants can vary for different software and selection criteria used for each analysis. In this thesis, there are three different analyses with two different softwares. For this section, the result with the newest analysis is presented, ν_e interaction rate on water with full energy spectrum, Chap.5.

showers in the PØD for all analyses discussed in this thesis. Therefore, two sets of energy calibration constants, one for reconstructed tracks and one for reconstructed showers, need to be evaluated.

In order to find these constants, electron particle gun MC samples are used in different geometries and energy regions. 10,000 electrons with energy uniformly distributed from 1 MeV to 3 GeV are created. For the water target, a sample of electrons starting at the upstream water target and going downstream, and all of the charge of the particle is required to be inside the water target to investigate that piece of the PØD; for the ECal, nd280mc configuration is modified to fill water target region with ECal layer. After running through `nd280mc`, `elecSim`, oaCalib and PØDRecon, the outputs are used to extract true electron energies E_e and charges Q from reconstructed track/shower. It was required that at least 90% of the true energy deposit must be in the PØD, to ensure that the particle is mostly contained inside the PØD. Then the distributions of Q/E_e are plotted and peak regions fitted with Gaussian.

For the sanity check, the 2D plots of Q vs. E_e, with track/shower reconstruction and water-in WT configuration were checked. As shown in Fig. 3.6, both plots are showing clear linear relationships, which gives us justification of using calibration constants for energy region of interest.

Figure 3.7 are the plots of Q/E_e with track and shower reconstruction, for Water WT, Air WT, and ECal configurations. The distributions are fitted with Gaussian, where the fit range is restricted from the 30th to the 70th Quantiles, and the result was required to have at least one degree of freedom. In addition the maximum of the function must be within 50% of the maximum of the histogram. The final calibration constants are inverse of mean values of the fit, and are summarized in Tab. 3.3.

Figure 3.8 shows plots of relative reconstructed electron energy to true energy, with different geometry and reconstruction. Reconstructed electron energy were evaluated using

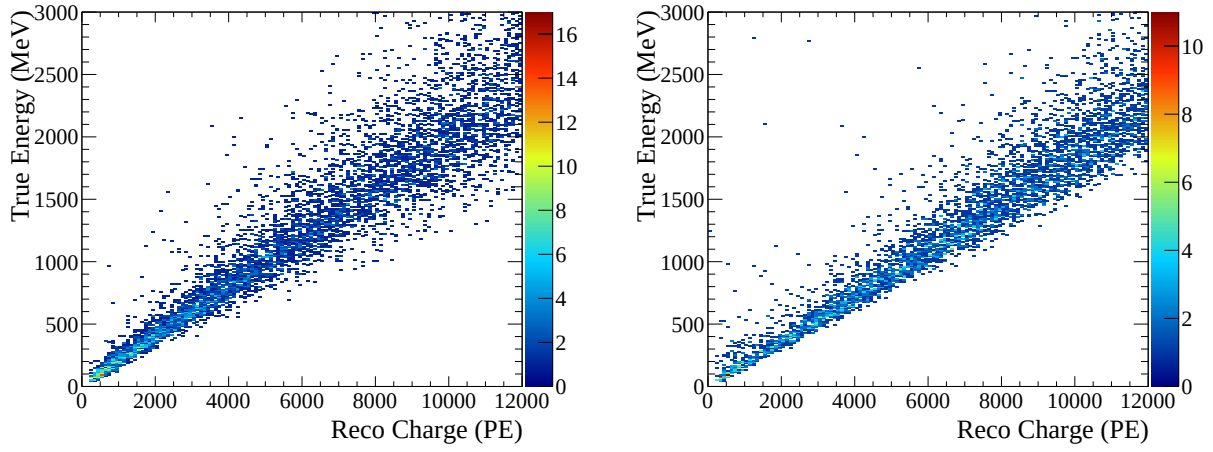

(a) E vs. Q, WT Water with Track Information **(b)** E vs. Q, WT Water with Shower Information

Figure 3.6: 2D plot of reconstructed charge Q vs. true electron energy E_e, with track and shower reconstruction.

Table 3.3: Energy calibration constants k, true energy/reconstructed charge ratio, with different geometry and reconstruction.

(MeV/PE)	Water WT	Air WT	ECal
Track Recon	0.1847 ± 0.0130	0.1340 ± 0.0207	0.1845 ± 0.0144
Shower Recon	0.1667 ± 0.0064	0.1158 ± 0.0125	0.1701 ± 0.0130

calibration constants in Table 3.3. For shower reconstruction, plots show good agreement between shower reconstructed and true energy over all energy region, most of the events aligned at 0 relative energy. Track reconstructed energy is showing little more dispersion at low/high true energy region. Nonetheless, most events are still concentrated at 0 relative energy.

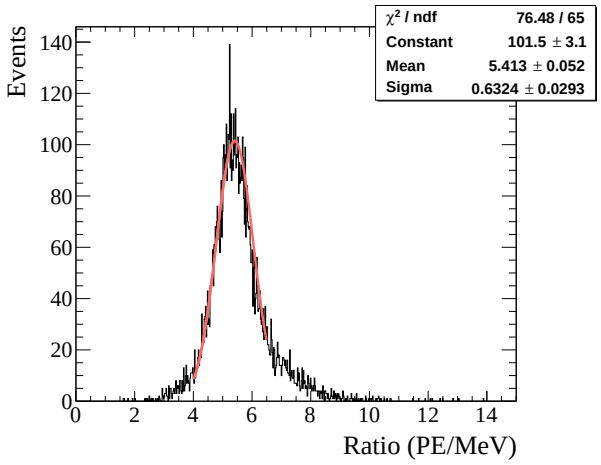

(a) Q/E, WT Water with Track Information

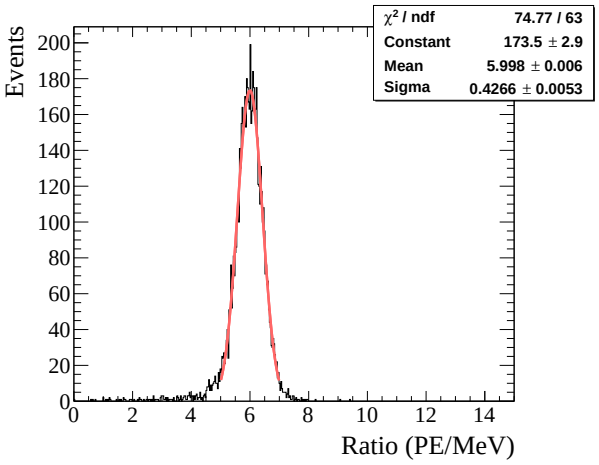

(b) Q/E, WT Water with Shower Information

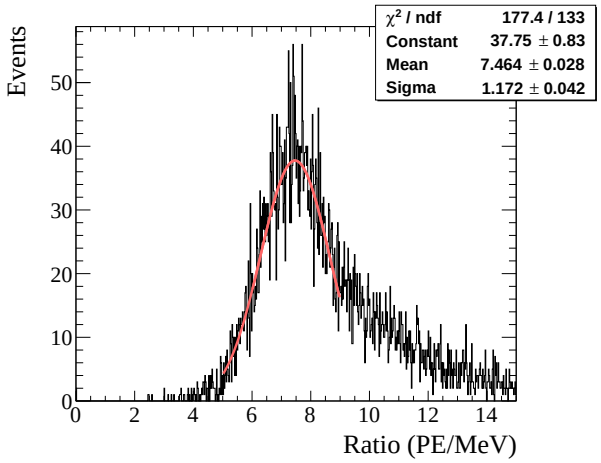

(c) Q/E, WT Air with Track Information

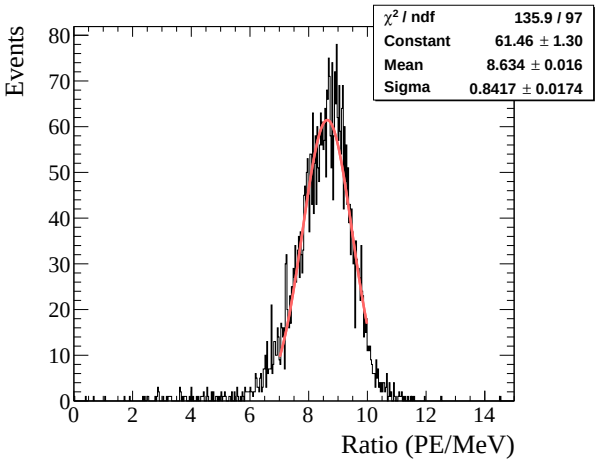

(d) Q/E, WT Air with Shower Information

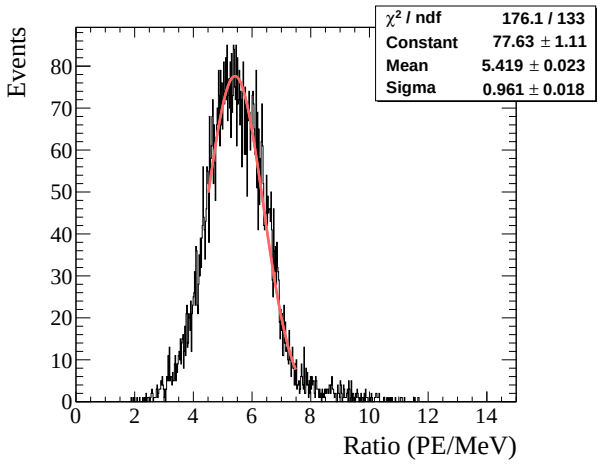

(e) Q/E, ECal with Track Information

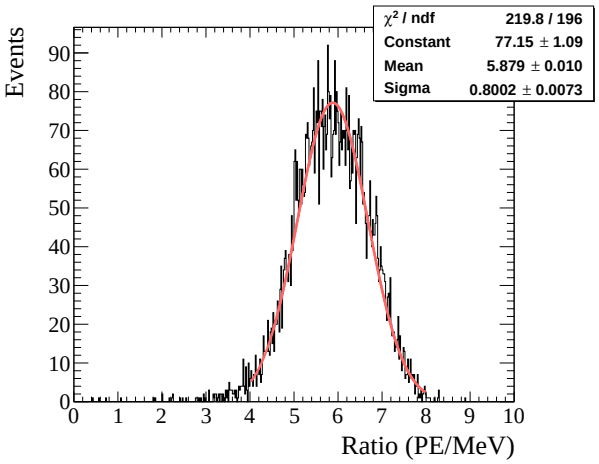

(f) Q/E, ECal with Shower Information

Figure 3.7: Reconstructed charge Q/true electron energy E_e for Water WT, Air WT, and ECal configurations, for track reconstruction and shower reconstruction. Peak regions are fitted with Gaussian.

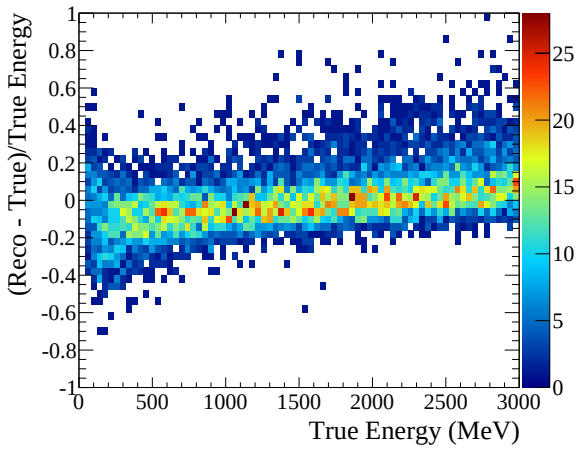

(a) WT Water with Track Information

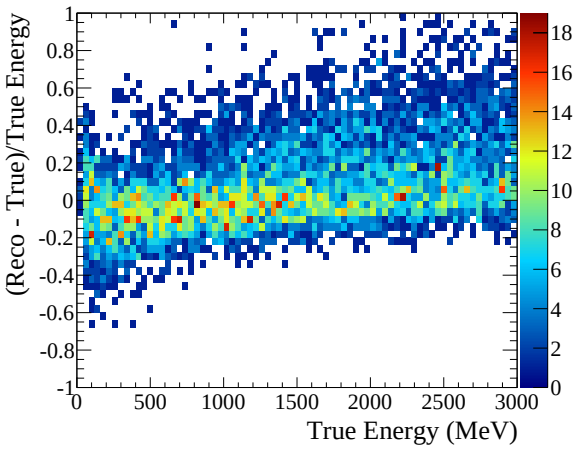

(b) WT Air with Track Information

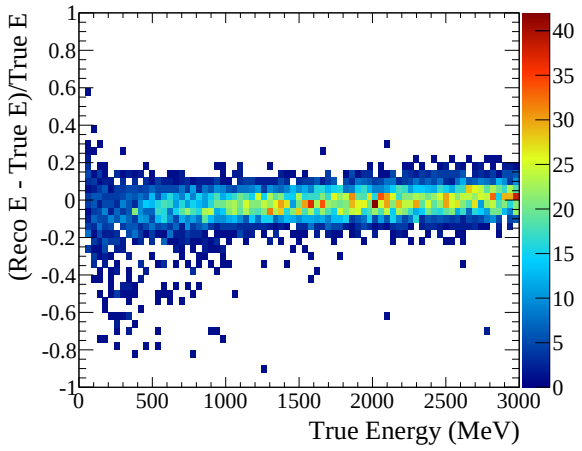

(c) WT Water with Shower Information

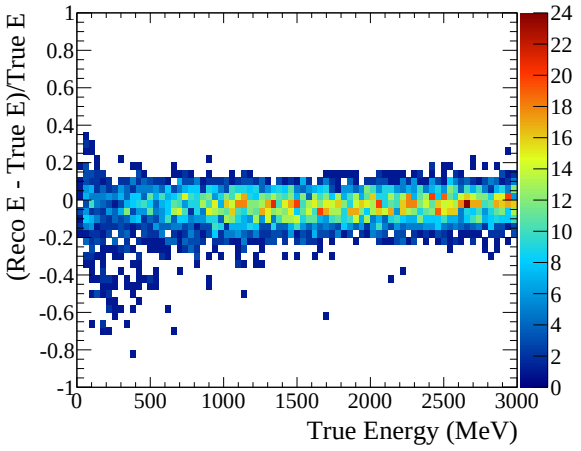

(d) WT Air with Shower Information

Figure 3.8: Relative reconstructed electron energy to true energy, for Water/Air WT configuration with track and shower reconstruction.

Chapter 4

High Energy CCν_e Interaction Rate Measurement

As stated in Sec. 1.6, the detailed understanding of CCν_e interaction rate measurement on water is crucial in future CP-violation searches in the lepton sector. This chapter describes the measurement of the high energy inclusive CCν_e interaction rate on water with the PØD. The measurement in full energy spectrum will be studied in Chap. 5.

4.1 Analysis Overview

As Fig. 4.1 shows the ν_e flux prediction at ND280 [39], the ν_e contamination is predominantly from kaon decay in the neutrino energy region $E_\nu > 1.5$ GeV. The ν_e contamination from this energy region will not directly effect T2K oscillation analysis, where it only study below 1.2 GeV. However, it would still be valuable to investigate this high energy region to cross check if the ν_e flux simulation agrees well with the data, also because the kaon flux prediction is less constrained compared to the muon flux prediction [39]. To this end, a cross check of the high energy ν_e component of the T2K beam as well as the measurement of the ν_e on-water interactions are performed.

All the data collected between January 2010 and May 2013 except for very small fraction of Run 3 data, are used as shown in Table 2.1. The Monte Carlo used in this analysis corresponds to ten times the Protons on Target (POT) of the data, and reproduces the various experimental conditions of the different data-taking periods.

Neutrino interactions in ND280 are simulated with the NEUT [47] event generator, version 5.1.4.2. Simulation of products of the neutrino interactions in the PØD is done using a GEANT 4.9.4 simulation [48, 49, 50, 51]. The standard GEANT physics list for electromagnetic interactions is used in the simulation.

For the neutrino flux reweighting, version 11b-v3.2 was used which was released by the beam group.

The signal events for the analysis are the charged current ν_e interactions in the PØD. Unless specified otherwise, the MC plots shown in this analysis are split in eight different

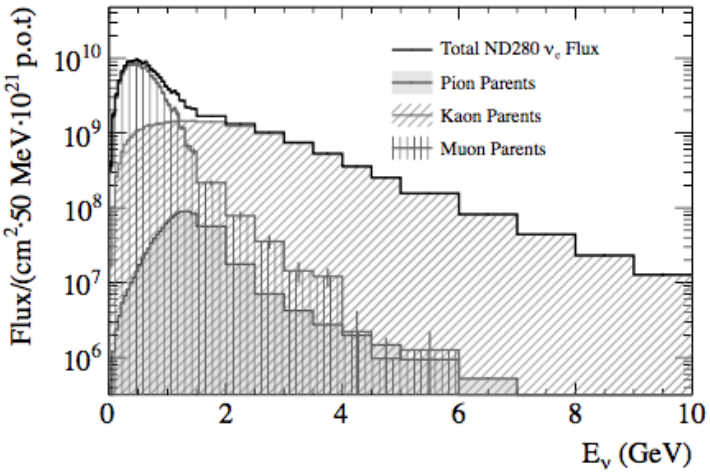

Figure 4.1: The flux prediction for the ND280 near detector broken down by the neutrino parent particle type

event type categories based on the true MC information:

Signal	Electron neutrino interaction with an electron in the final state
μ and π^0	A muon and a π^0 in the final state
μ no π^0	A muon but no π^0 in the final state
π^0 no μ	No muon but a π^0 in the final state
No μ/π^0	Neither a muon nor a π^0 in the final state
Outside P0D	True vertex of the interaction is outside the PØD detector
Multi Vertex	Several true vertices in the PØD
Noise	No true vertex

Most of the MC event type categories are based on final state particles[1]. The current PØD ν_e analysis does not distinguish between quasi-elastic (QE) or non-quasi-elastic (nonQE) electron neutrino interactions. Therefore, a signal event is defined as electron neutrino interaction with an electron and any number of other particles in the final state. However, the event selection used for the PØD ν_e analysis favors QE interactions resulting in a selected event sample with mostly single electrons in the final state as it is presented later in this thesis. In addition to the final state event categories, there are three separated categories: Outside P0D, Multi Vertex, and Noise. First, this analysis uses the reconstruction information only from the PØDRecon with the consequence that events with the vertex outside of the PØD detector cannot be reconstructed correctly, such events are therefore summarized in the "Outside P0D" category. Second, the PØDRecon framework reconstructs only one vertex in a cycle so that events with several true vertices in the PØD cannot be reconstructed and are therefore listed in the "Multi Vertex" category. Finally, it is possible that the PØDRecon output contains reconstructed objects even if there was no true vertex. As

[1]This analysis does not distinguish between neutrino and anti-neutrino interactions, therefore mentioning a certain particle always includes also its anti-particle.

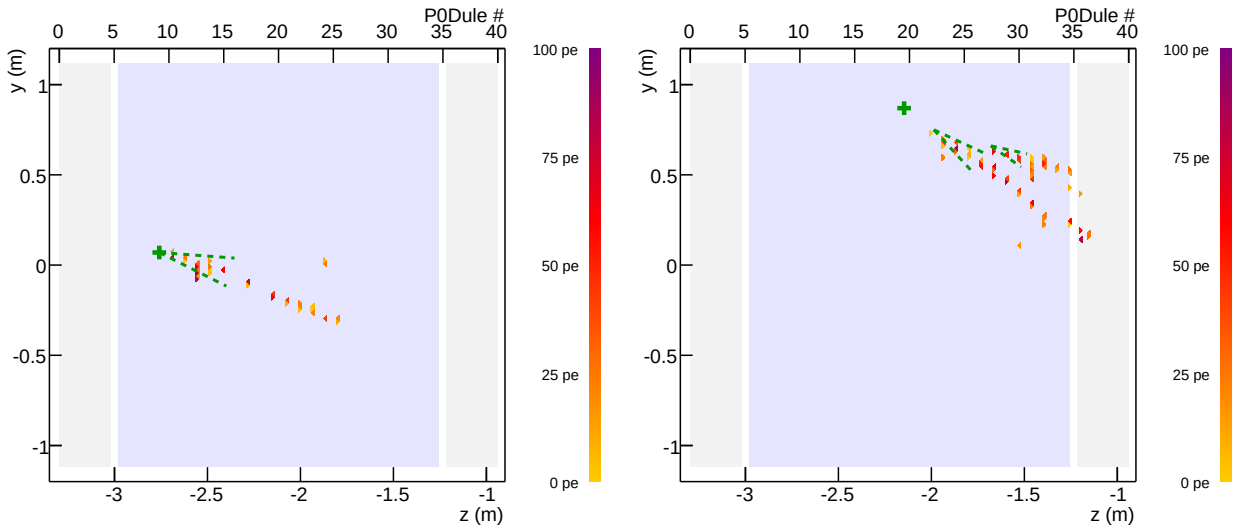

Figure 4.2: Side view of a CCν_e event (left) and a π^0 background event (right) reconstructed in the PØD. Triangles are hits colored by the charge deposited, the green cross symbol shows the reconstructed shower vertex, and the green dashed lines show the cones of reconstructed showers.

those reconstructed objects are most probably caused by noise, they are summarized in the "Noise" category.

A cut-based event selection using known reconstruction characteristics was tuned to maximize $S/\sqrt{B}$ where S is the number of MC signal events and B is the number of MC background events. To avoid bias of tuning selections based on data-MC agreement, the selection strategy was developed based on MC samples. Event displays of a typical CCν_e candidate and a π^0 background event selected in the analysis are shown in Fig. 4.2.

4.2 Reconstruction Resolution

The general description of the reconstruction algorithm in the PØD, PØDRecon, is given in Sec. 3.3.

While an event goes through the PØDRecon, muon-like tracks and their properties are copied to the final result container of the PØDRecon output. A shower reconstruction runs over hits that are associated with electromagnetic-like tracks and reconstructs three dimensional showers and the interaction vertex. The reconstructed objects after track and shower reconstruction are stored in the final container of the PØDRecon output. In the following, reconstructed objects and their properties after the track reconstruction are referred as results of the "track stage" at which only tracks are reconstructed. Reconstructed objects and their properties after track and shower reconstruction are referred as results of the "shower stage". At this stage, the result container contains both muon-like tracks and showers.

4.2.1 Vertex Resolution

The MC reconstruction resolutions of the vertex position are obtained by selecting MC events passing all selection cuts described later in Sec. 4.3 and comparing the true vertex position with the reconstructed vertex position. The study is done separately for the water and air PØD configuration as well as the X, Y, and Z coordinate. As the reconstructed vertex position at the track and the shower stage are not necessarily identical, the MC vertex position resolution is determined for both cases. The distributions obtained with the track PØDRecon information are shown in Fig. 4.3 together with the 16 % and 84 % quantiles. The irregular structure in the event distributions as a function of the Z coordinate is a consequence of the non-uniform longitudinal density profile of the PØD detector. The reconstructed vertex is placed at the center of the scintillator layer longitudinally but the true vertex might be in the water layer, brass, or scintillator. The spike at -40 mm is caused by events in the brass layer.

The MC reconstruction resolution is found by taking half the distance from the 16 % and 84 % quantiles which is equivalent to 1σ of a Gaussian fit of the distribution. The resolutions obtained from both the track and shower reconstruction stage are summarized in Tab. 4.1. The table shows that the vertex position resolution obtained by using track reconstruction information is slightly better compared to the resolutions obtained by using shower stage information. As a consequence, vertex information coming from the track reconstruction is used for vertex related selection criteria (described in Sec. 4.3).

Table 4.1: MC resolutions for the vertex position reconstruction if using vertex reconstruction information from the track stage or the shower stage. The tables show the shift (obtained from the median value) and the resolutions (obtained from the 16 % and 84 % quantiles) for all three dimensions and for the PØD configurations water and air.

(a) Vertex Resolutions with Track Stage Information

	Vertex Position X (cm)		Vertex Position Y (cm)		Vertex Position Z (cm)	
	Shift	Resolution	Shift	Resolution	Shift	Resolution
Water	0.0	1.5	0.1	1.7	-0.1	3.5
Air	0.0	2.4	0.1	2.4	0.4	4.9

(b) Vertex Resolutions with Shower Stage Information

	Vertex Position X (cm)		Vertex Position Y (cm)		Vertex Position Z (cm)	
	Shift	Resolution	Shift	Resolution	Shift	Resolution
Water	-0.1	2.1	0.0	2.3	0.1	3.9
Air	-0.1	2.8	0.1	3.0	0.4	4.1

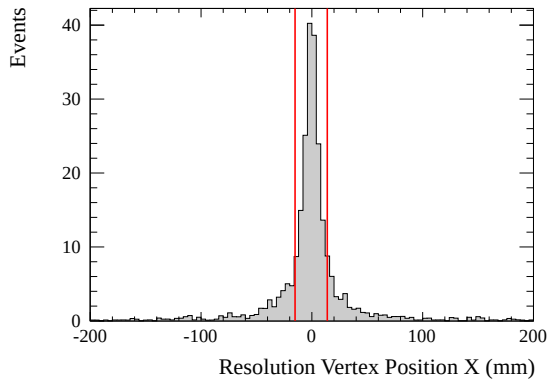

(a) Vertex Position X Water Configuration

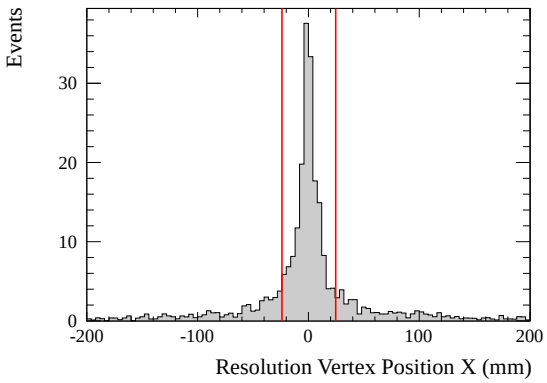

(b) Vertex Position X Air Configuration

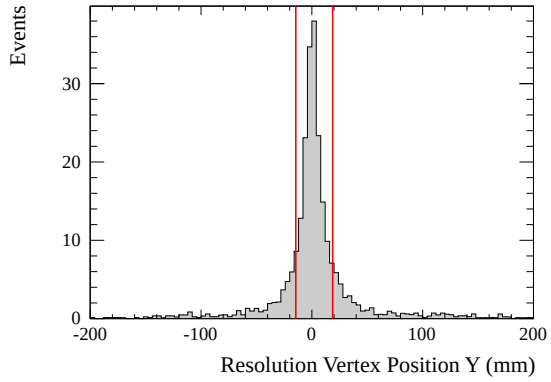

(c) Vertex Position Y Water Configuration

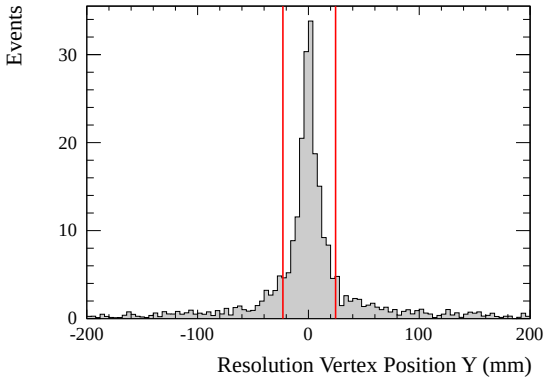

(d) Vertex Position Y Air Configuration

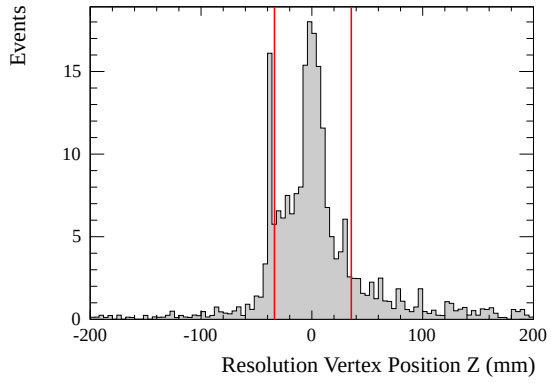

(e) Vertex Position Z Water Configuration

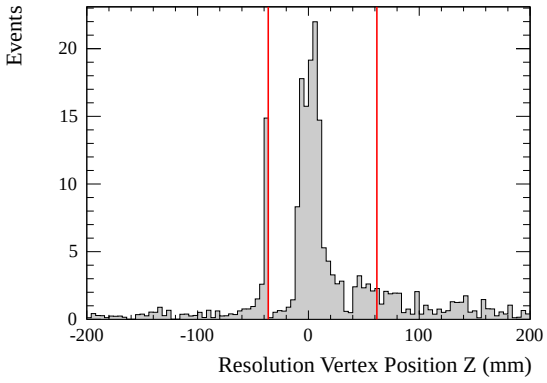

(f) Vertex Position Z Air Configuration

Figure 4.3: MC vertex position resolutions for the PØD configurations water and air for all dimensions. Reconstruction information from the track stage of PØDRecon is used for these plots. The vertical lines correspond to the 16 % and 84 % quantiles.

4.2.2 Neutrino Energy Resolution

In addition to the vertex position resolution, the MC reconstruction resolutions of the electron are examined. For that purpose, MC signal events that pass all selection criteria described in Sec. 4.3 are studied.

The reconstructed neutrino energy is calculated from the reconstructed electron energy E_e and the reconstructed electron angle θ_e using the quasi-elastic approximation

$$E_\nu = \frac{(m_n - E_b)E_e + (m_p^2 - (m_n - E_b)^2 - m_e^2)/2}{(m_n - E_b) - E_e + p_e \cos(\theta_e)} \tag{4.1}$$

where m_n is the neutron mass, E_b is the binding energy, m_p is the proton mass, m_e is the electron mass, and p_e is the electron momentum.

The distribution of the difference between true and reconstructed electron angle (scattering angle with respect to the direction of the neutrino beam) in units of π for both water and air PØD configuration, as well as the distribution of the relative difference between reconstructed and true electron/neutrino energy for the water and air PØD configuration is shown in Fig. 4.4. All those plots are obtained by using reconstruction information from the PØDRecon shower stage and are shown together with the 16 % and 84 % quantiles.

The resolutions are found by taking half the distance from those quantiles which is equivalent to 1σ of a Gaussian fit. The MC resolutions obtained from both the track and shower reconstruction stage are summarized in Tab. 4.2. The table shows that both the electron energy resolution and the angular resolution is better if it is obtained from the PØDRecon shower stage. As a consequence, the particle angle and energy related selection cuts are applied to reconstruction information coming from the shower stage of the PØDRecon.

4.3 Event Selection

4.3.1 Basic Selection

As described in Sec. 4.2, reconstructed object and their properties of both the track and the shower PØDRecon stage are used for the PØD ν_e analysis. For each reconstructed event, the track with the highest energy deposit in the PØD detector is selected from the track stage and shower with the highest energy deposit in the PØD detector is selected from the shower stage resulting in the candidate track and the candidate shower. To ensure a good reconstruction quality, it is required that the vertex, the candidate track, and the candidate shower are reconstructed in all three space dimensions (valid 3D vertex, valid 3D track, valid 3D shower).

As the reconstruction performance is reduced at the edge of the PØD detector, it is required furthermore that the reconstructed vertex must be located within the PØD fiducial volume. The definition of the fiducial volume is shown in Tab. 3.1. Both the track and the shower reconstruction return a vertex. As shown in Sec. 4.2, the MC reconstruction resolutions for the vertex position are slightly better at the track reconstruction stage than at the shower reconstruction stage. The valid 3D vertex and the fiducial volume selection cut

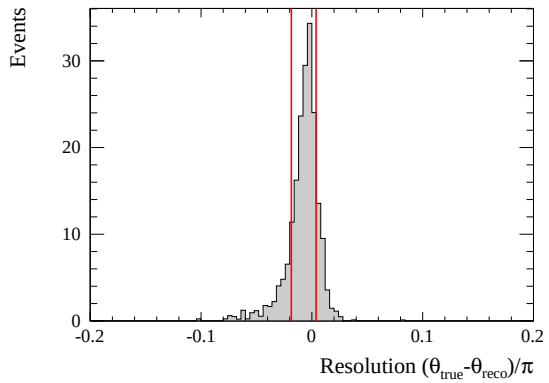

(a) Electron Angle Water Configuration

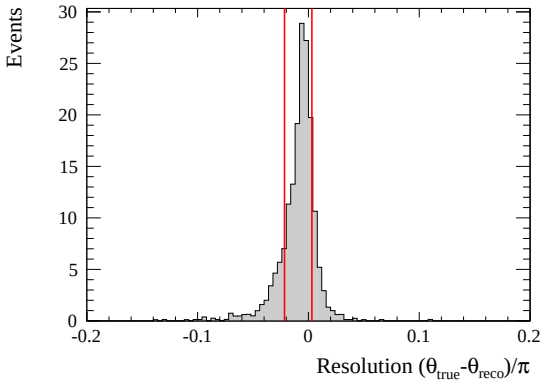

(b) Electron Angle Air Configuration

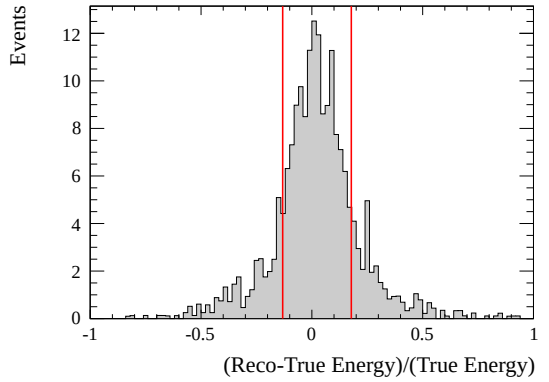

(c) Electron Energy Water Configuration

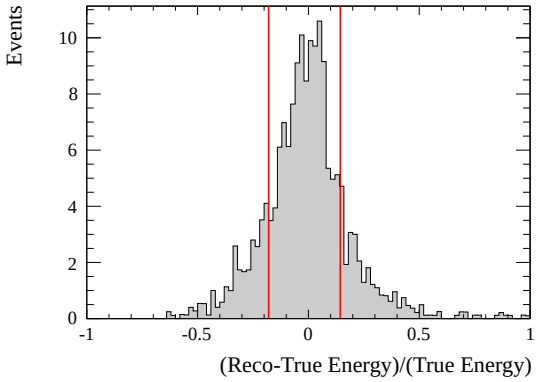

(d) Electron Energy Air Configuration

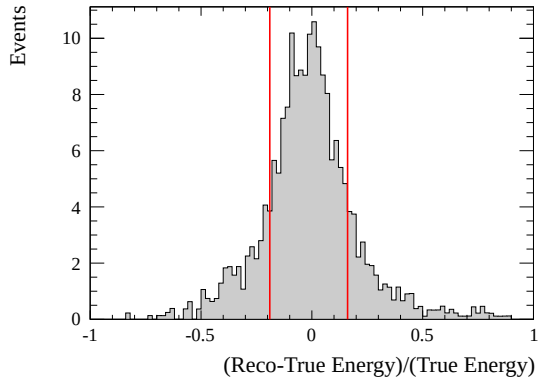

(e) Neutrino Energy Water Configuration

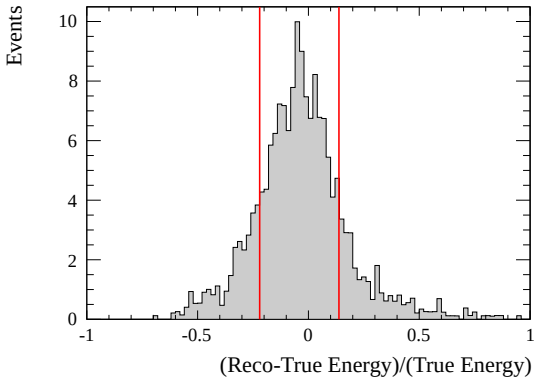

(f) Neutrino Energy Air Configuration

Figure 4.4: MC reconstruction resolutions for the electron angle, the electron energy, and the neutrino energy for the PØD configurations water and air. Reconstruction information from the shower stage of the PØDRecon is used for these plots. The vertical lines correspond to the 16 % and 84 % quantiles.

Table 4.2: MC reconstruction resolutions for the electron angle, the electron energy, and the neutrino energy if using reconstruction information from the track stage or the shower stage. The tables show the shift (obtained from the median value) and the resolutions (obtained from the 16 % and 84 % quantiles) for the PØD configurations water and air.

(a) Electron and Neutrino Resolutions with Track Stage Information

	Electron Angle (π)		Relative Electron Energy		Relative Neutrino Energy	
	Shift	Resolution	Shift	Resolution	Shift	Resolution
Water	-0.010	0.024	0.035	0.169	0.015	0.228
Air	-0.011	0.024	-0.005	0.169	-0.022	0.219

(b) Electron and Neutrino Resolutions with Shower Stage Information

	Electron Angle (π)		Relative Electron Energy		Relative Neutrino Energy	
	Shift	Resolution	Shift	Resolution	Shift	Resolution
Water	-0.005	0.011	0.019	0.155	-0.014	0.175
Air	-0.006	0.012	-0.007	0.162	-0.041	0.179

are therefore applied to the vertex obtained from the track stage. Figure 4.5 shows the area-normalized N-1 plot (plot of events passing all the selection criteria except the cut concerned here) of the fiducial volume selection cut for the water and air configuration. The plot shows the distance of the reconstructed vertex from the nearest fiducial volume edge. Events with a positive distance are inside the fiducial volume and pass therefore this selection cut. The plot clearly shows that most of the background events coming from vertices outside the PØD detector are removed with the fiducial volume cut. It also shows that there is an excess of the data events compared to the MC prediction approximately 350 mm away from the fiducial volume edge for both the water and air PØD configurations. In order to understand this data excess, the fiducial volume selection is split into separate cuts for the reconstructed vertex position in X, Y, and Z direction. Figure 4.6 shows the N-1 plots for the separated vertex position cuts for the water and air configuration. The vertical lines represent the location of the fiducial volume boundaries defined in Tab. 3.1. In each plot, the fiducial volume requirement has been applied to the other two dimensions. Compared to Fig. 4.5, the MC shown in Fig. 4.6 is normalized to the data POT. The plots clearly show that the event distributions in both the X and Y direction show very good agreement between the data and MC while there is a data excess at the upstream end of the PØD in Z direction. This excess is caused by sand muons (muons originating from beam neutrino interactions in the magnet and surrounding concrete and sand) which are not simulated in the MC used for the PØD ν_e analysis. However, using the fiducial volume selection removes those sand muon events from the selected sample.

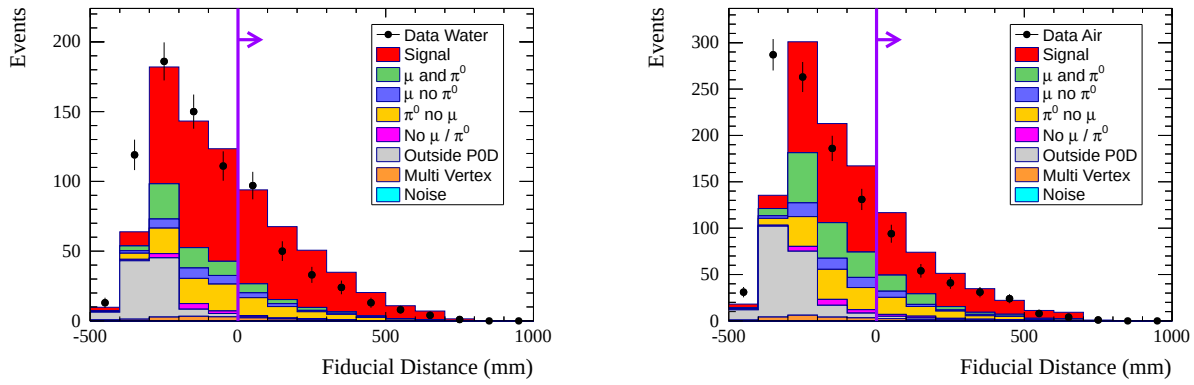

(a) Water Configuration **(b)** Air Configuration

Figure 4.5: The N-1 plot of the fiducial distance for the water (a) and air (b) configuration. The plots are area-normalized to emphasize shape differences between the data and MC. The first and last bin contain the underflow and overflow bin, respectively. The cut value is set at 0 mm for both water and air configuration.

4.3.2 Hit Matching

As discussed before, the analysis analysis uses information from both the track and the shower stage of the PØDRecon. As a candidate track and a candidate shower is selected, it is necessary for this analysis to confirm that the selected track and the shower belong to the same particle. This can be done by looking at the hits in the PØD detector that are associated with the reconstructed objects. Comparing the hits associated with the candidate track and the hits associated with the candidate shower results in the number of matching hits. Figure 4.7 shows the fraction of matching hits out of the candidate track hits for the water and air configuration when all other cuts described in this section are applied (the plots are area-normalized). The plots clearly show that almost all events passing the selection used for this analysis have an excellent hit matching between candidate track and shower. The hit matching cut is chosen to be 0.8 for both water and air configuration to ensure that the reconstructed track and shower belong to the same particle. It is not recommended to choose a tight cut value such as 0.99 as noise effects could include a systematic difference between the data and MC.

4.3.3 Particle Direction

The scintillator bars of the PØD detector have a triangular profile with angles of approximately 45°. Particles with an angle of more than 45° with respect to the beam axis would therefore hit more than two adjacent bars in a layer. As the PØDRecon is designed to deal with two adjacent bar hits in a layer, such events would cause reconstruction failures. This is the reason why only events are selected where the candidate shower has a smaller angle than 45°. As shown in Sec. 4.2, the MC angular resolution for the candidate shower is

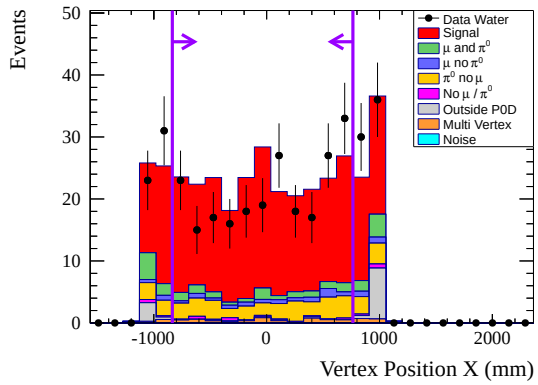

(a) Vertex Position X Water Configuration

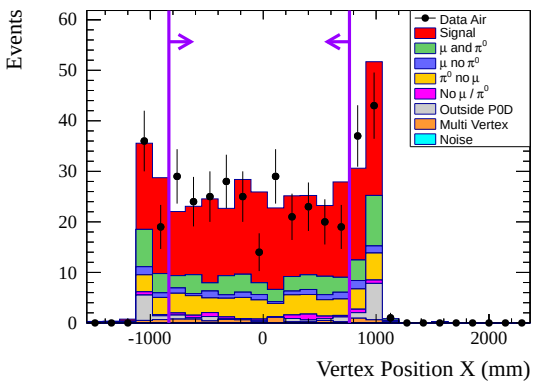

(b) Vertex Position X Air Configuration

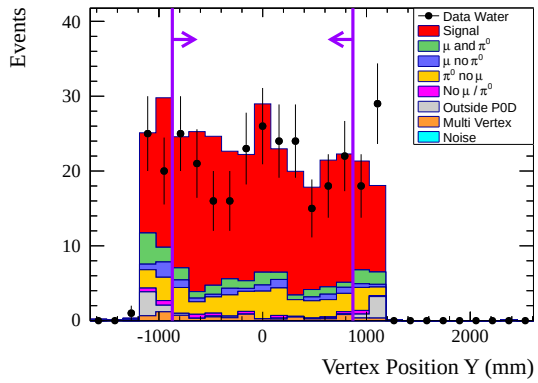

(c) Vertex Position Y Water Configuration

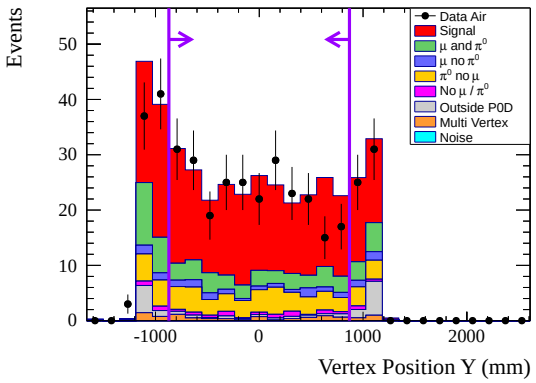

(d) Vertex Position Y Air Configuration

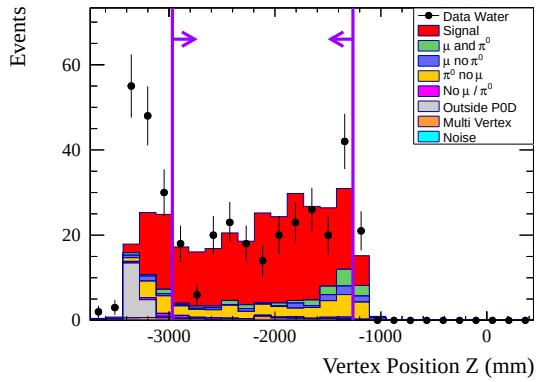

(e) Vertex Position Z Water Configuration

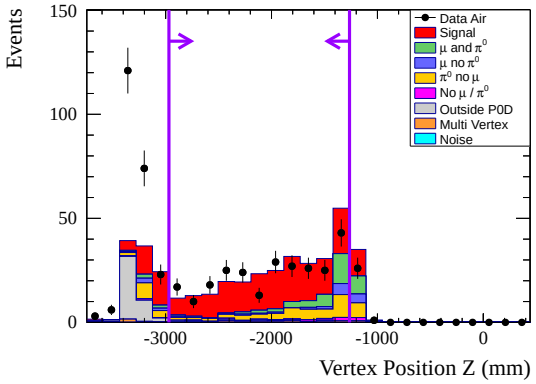

(f) Vertex Position Z Air Configuration

Figure 4.6: The N-1 plots of the fiducial volume selection that is split up in separated cuts for the X, Y, and Z direction. In each plot, the fiducial volume requirement has been applied to the other two dimensions. The plots are shown for the water and air PØD configuration with the MC POT-normalized to the data. The first and last bin contain the underflow and overflow bin, respectively. The cut values for the fiducial volume are shown as vertical lines.

better than the one for the candidate track. That is why the angle of the candidate shower is used to apply this particle direction cut. Figure 4.8 shows the area-normalized N-1 plot of the particle direction cut for the water and air configuration. The muon background event concentration around $\cos(\theta) \approx 0.3$ is caused by short high-angle events. As the muon hits several adjacent scintillator bars in a layer, the event passes the later described median width selection cuts.

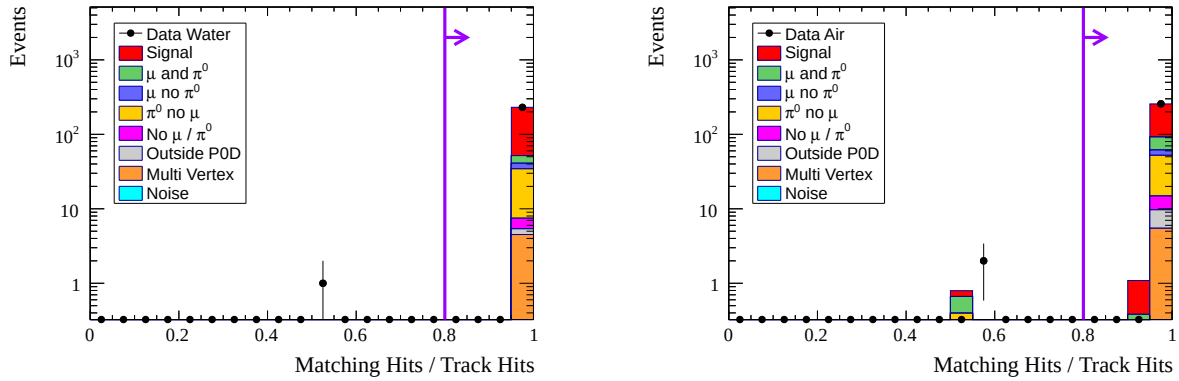

(a) Water Configuration **(b)** Air Configuration

Figure 4.7: The N-1 plot of the hit matching selection cut for the water and air configuration. The plots are area-normalized to emphasize shape differences between the data and MC. The cut value is set at 0.8 for both water and air configuration.

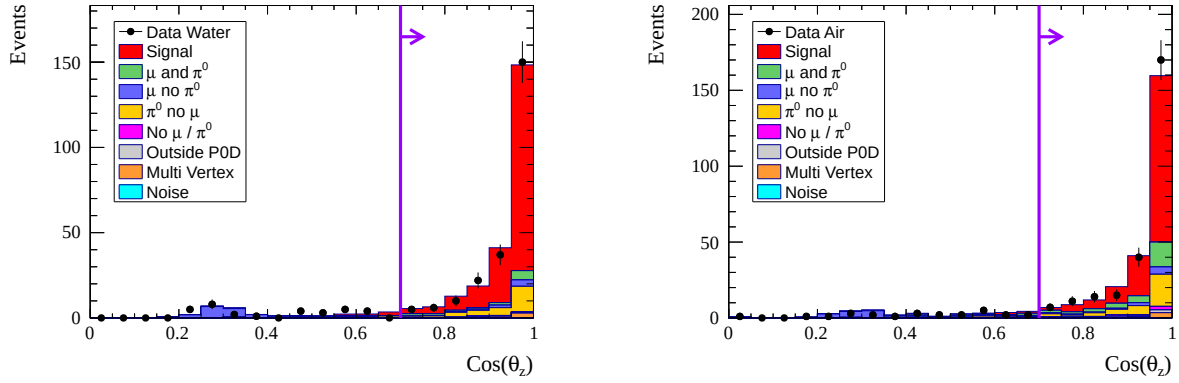

(a) Water Configuration **(b)** Air Configuration

Figure 4.8: The N-1 plot of the particle direction selection cut for the water and air configuration. The plots are area-normalized to emphasize shape differences between the data and MC. The cut value is set at 0.7 for both water and air configuration.

4.3.4 Neutrino Energy

Only events with reconstructed neutrino energy of 1.5 GeV or above are used for this analysis. In this energy region, the majority of the ν_e flux arises from kaon decays and the PØD detector shows high performance to distinguish electrons from other particles. The reconstructed neutrino energy is calculated using quasi-elastic approximation (4.1). As shown in Sec. 4.2, both the MC electron energy resolution and the MC angular resolution is significantly better when using shower reconstruction information. That's the reason why the shower angle and the shower energy is used to calculate the neutrino energy. Figure 4.9 shows the area-normalized N-1 plot of the neutrino energy cut for the water and air configuration. The neutrino energy selection cut removes a large fraction of the remaining background events, especially π^0 events.

4.3.5 Track Median Width

The design of the PØD detector with high density materials (brass and lead) causes electrons to develop electromagnetic shower. The reconstructed track of an electron is therefore typically wider than the reconstructed track of a muon. This feature can be used to distinguish muons and electrons with the median width of the reconstructed candidate track. In each scintillator layer, the energy-weighted standard deviation of the position of the hits reconstructed in the track is calculated as follows:

1. If the two hits with the highest deposited energy are in adjacent strips, replace them with a single hit. The new hit's position is at the energy-weighted average position of the two original hits, and its energy is the sum of the energies of the original hits. Any other hits in the layers are left unchanged. This procedure gives layers with minimum ionizing tracks very small (almost always zero) width.

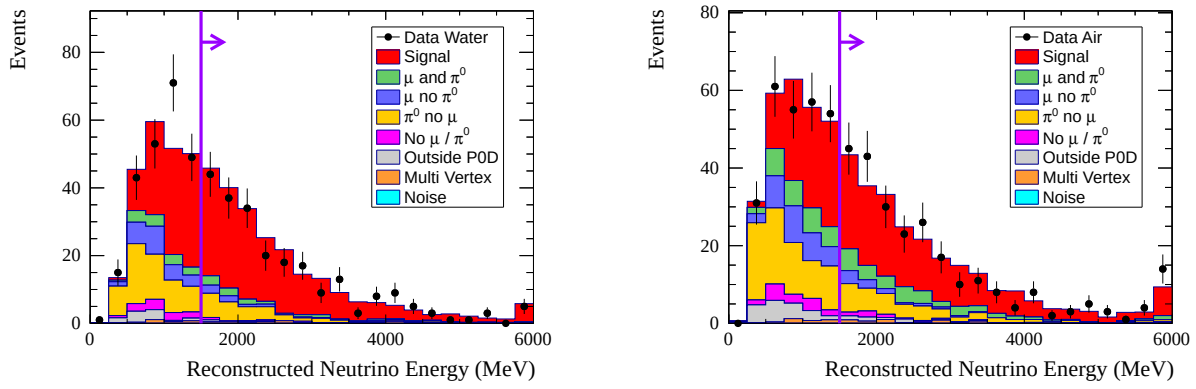

(a) Water Configuration **(b)** Air Configuration

Figure 4.9: The N-1 plot of the neutrino energy selection cut for the water and air configuration. The plots are area-normalized to emphasize shape differences between the data and MC. The last bin contains the overflow bin. The cut value is set at 1.5 GeV for both water and air configuration.

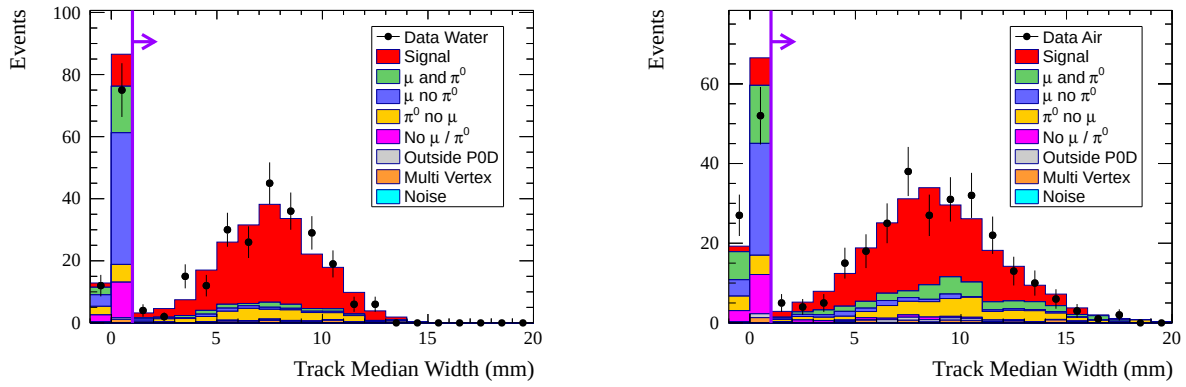

(a) Water Configuration

(b) Air Configuration

Figure 4.10: The N-1 plot of the track median width selection cut for the water and air configuration. The plots are area-normalized to emphasize shape differences between the data and MC. The first bin contains events that were too short to determine the median width while the last bin contains the overflow bin. The cut value is set at 1 mm for both water and air configuration.

2. The energy-weighted standard deviation of the hit positions is calculated for each layer.

3. Median width is the width of the middle layer after ordering by layer width.

Figure 4.10 shows the area-normalized N-1 plot of the track median width cut for the water and air configuration. The first bin contains events that were too short to determine the median width while the last bin contains the overflow bin. The cut value was chosen to be 1 mm to remove the narrow muon background events.

4.3.6 Shower Median Width

The PØDRecon shower reconstruction reanalyzes hits that are associated with electromagnetic-like tracks or are not used at the track reconstruction stage. The shower reconstruction looks for hits in a cone from the reconstructed vertex position and combines them in one or more showers. It can happen that hits from several particles are combined in one reconstructed shower, especially if they are almost overlapping. The PØD ν_e analysis looks for events with a single electron. Therefore, events with a very wide candidate shower are rejected as such events are more likely background events with several particles. The shower median width is calculated the same way as the track median width. Figure 4.11 shows the area-normalized N-1 plot of the shower median width for the PØD water and air configuration. The plots clearly show that events with a larger shower median width are most likely background events. Due to the different shapes of the event distributions, the optimal cut is expected to be at different values for the water and air configuration. The cut values are determined by optimizing $S/\sqrt{B}$ where S is the number of selected MC signal events while B is the number of selected MC background events. The cut values are found to be 18 mm for the water configuration and 27 mm for air configuration.

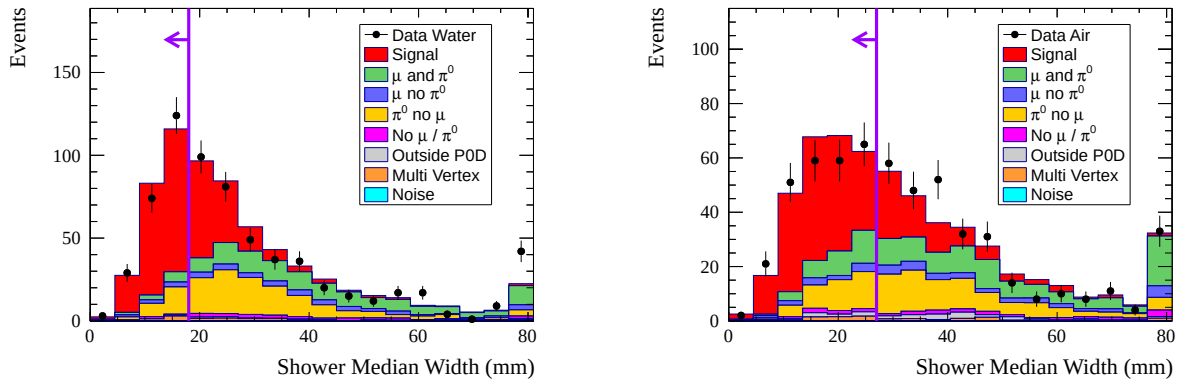

(a) Water Configuration

(b) Air Configuration

Figure 4.11: The N-1 plot of the shower median width selection cut for the water and air configuration. The plots are area-normalized to emphasize shape differences between the data and MC. The last bin contains the overflow bin and it also contains events that were too short to determine the median width. The cut value is set at 18 mm for the water and 27 mm for air configuration.

4.3.7 Shower Charge Fraction

To select quasi-elastic CCν_e events with a high purity, only events with most of the event charge contained in the candidate shower are selected. The obvious cut value would be at a shower charge fraction of 1.0 meaning that only events with a single shower and no muon-like tracks are selected. Figure 4.12 shows the area-normalized N-1 plot of the shower shower charge fraction cut for the PØD water and air configuration. The first bin contains the underflow bin while the last bin contains events with the entire charge contained in the candidate shower.

4.4 Selected Event Sample

This section looks into the data and MC events that pass all the selection criteria described in Sec. 4.3. For the remainder of this thesis, the term "selected events" will be used to define the sample of the data and MC events that pass all the selection criteria.

4.4.1 Number of Selected Events

The number of selected MC events normalized to the data POT for the PØD configurations water and air together with the number of selected data events are presented in Tab. 4.3. In addition, the water configuration MC events are split up into on-water and not-water events. On-water events are defined as events with true interaction vertex on the water targets while not-water events have the true interaction vertex not on water, i.e. on scintillator, lead, or bras. All events in the air configuration MC are not-water events as the water targets are

drained. The shown errors correspond to the statistical uncertainty due to the limited MC statistics.

The impact of each selection criterion is demonstrated with the N-1 plots presented in Sec. 4.3. The analysis procedure does not depend on the order in which the selection cuts are applied. Nevertheless, the effect on the selected data and MC events due to applying each cut in the order described in Sec. 4.3 is shown in Tab. 4.4 for both water and air configuration. As those numbers depend strongly on the order in which the cuts are applied, care should be taken in interpreting this table. However, the obtained numbers clearly show that the event selection favors signal events compared to background events.

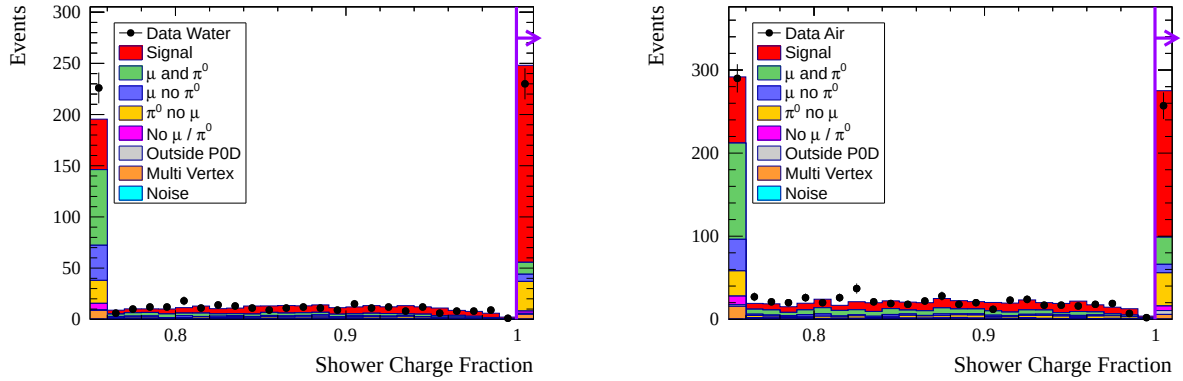

(a) Water Configuration

(b) Air Configuration

Figure 4.12: The N-1 plot of the shower charge fraction selection cut for the water and air configuration. The plots are area-normalized to emphasize shape differences between the data and MC. The first bin contains the underflow bin while the last bin contains events with the entire charge contained in the candidate shower. The cut value is set at 1.0 for both water and air configuration.

Table 4.3: The selected number of MC signal events S, MC background events B, and the total number of selected MC events $S+B$ normalized to the data POT for the water and air configuration are listed together with the selected data events D. In addition, the water configuration MC events are split up in on-water and not-water events. The errors correspond to the statistical uncertainty due to the limited MC statistics.

	MC Signal S	MC Background B	MC Total $S+B$	Data D
Water	196.1 ± 4.8	56.7 ± 2.7	252.8 ± 5.5	230
On-Water	60.2 ± 2.6	14.5 ± 1.3	74.7 ± 2.9	
Not-Water	135.9 ± 4.0	42.2 ± 2.3	178.2 ± 4.6	
Air	173.6 ± 4.6	97.4 ± 3.6	271.0 ± 5.8	257

Table 4.4: The number of the data and MC (total and signal) events passing the selection criteria when they are applied in the order described in Sec. 4.3. In addition, the relative efficiency with respect to the event sample passing the basic selection is presented. The MC is scaled to the data POT.

(a) Water Configuration

	Data (D)		MC Total ($S+B$)		MC Signal (S)	
Selection Criterion	Events	Rel. (%)	Events	Rel. (%)	Events	Rel. (%)
Basic Selection	73916	100.0	76310.6	100.0	2328.4	100.0
Hit Matching	47331	64.0	47987.2	62.9	1872.8	80.4
Particle Direction	24629	33.3	24733.7	32.4	1491.1	64.0
Neutrino Energy	8271	11.2	8054.0	10.6	998.8	42.9
Track Median Width	5866	7.9	5646.0	7.4	939.1	40.3
Shower Median Width	705	1.0	718.4	0.9	388.3	16.7
Shower Charge Fraction	230	0.3	252.8	0.3	196.1	8.4

(b) Air Configuration

	Data (D)		MC Total ($S+B$)		MC Signal (S)	
Selection Criterion	Events	Rel. (%)	Events	Rel. (%)	Events	Rel. (%)
Basic Selection	79322	100.0	81995.4	100.0	2211.0	100.0
Hit Matching	51098	64.4	51684.9	63.0	1729.3	78.2
Particle Direction	26794	33.8	26873.6	32.8	1380.5	62.4
Neutrino Energy	6777	8.5	6706.6	8.2	878.1	39.7
Track Median Width	4999	6.3	4929.8	6.0	829.6	37.5
Shower Median Width	1025	1.3	1009.5	1.2	465.1	21.0
Shower Charge Fraction	257	0.3	270.953	0.3	173.59	7.9

4.4.2 Efficiency and Purity

The efficiency ϵ and purity p of MC signal events are defined as

$$\epsilon = \frac{S}{T} \tag{4.2}$$

$$p = \frac{S}{S+B} \tag{4.3}$$

where S is the number of selected MC signal events and B is the number of selected MC background events. T is the number of true MC signal events with true vertex within the fiducial volume and true neutrino energy larger than 1.5 GeV, i.e. $E_\nu > 1.5\,\text{GeV}$. This means, The events in T contains only true MC information without any reconstruction applied. The values of T, the obtained efficiencies, and the calculated purities for the water and air configuration are listed in Tab. 4.5. Events of the PØD water configuration are split-up in events happening on-water and not-water (scintillator, bras, lead, etc.). As shown in Tab. 4.5, the value of the reconstruction efficiency of the not-water events is slightly larger than the value of the general water reconstruction efficiency. The reason is that the not-water signal events happening outside of the fiducial volume, mainly at the upstream and downstream end of the detector, migrate inside the fiducial volume. As there are no water targets outside the fiducial volume in Z direction, this migration affects only the not-water events.

The selection efficiency of signal events as a function of the true neutrino energy E_{true} for the PØD water and air configurations are shown in Fig. 4.13. The selection of low energy signal events is suppressed by the high neutrino energy cut of 1.5 GeV while the acceptance of high energy signal events is suppressed by the shower median width cut and the shower charge fraction cut.

Table 4.5: The number of true signal events T with true vertex within the fiducial volume and true neutrino energy larger than 1.5 GeV, the signal efficiencies ϵ and purities p are listed for the water and air configuration. The events of the PØD water configuration are split-up in events happening on-water and not-water (scintillator, bras, lead, etc.). The errors correspond to the statistical uncertainty due to the limited MC statistics.

	Truth T	Efficiency ϵ	Purity p
Water	1792.6 ± 14.7	$(10.9 \pm 0.3)\,\%$	$(77.6 \pm 2.5)\,\%$
On-Water	611.5 ± 8.5	$(9.8 \pm 0.4)\,\%$	$(80.6 \pm 4.7)\,\%$
Not-Water	1181.1 ± 12.0	$(11.5 \pm 0.4)\,\%$	$(76.3 \pm 3.0)\,\%$
Air	1573.1 ± 14.1	$(11.0 \pm 0.3)\,\%$	$(64.1 \pm 2.2)\,\%$

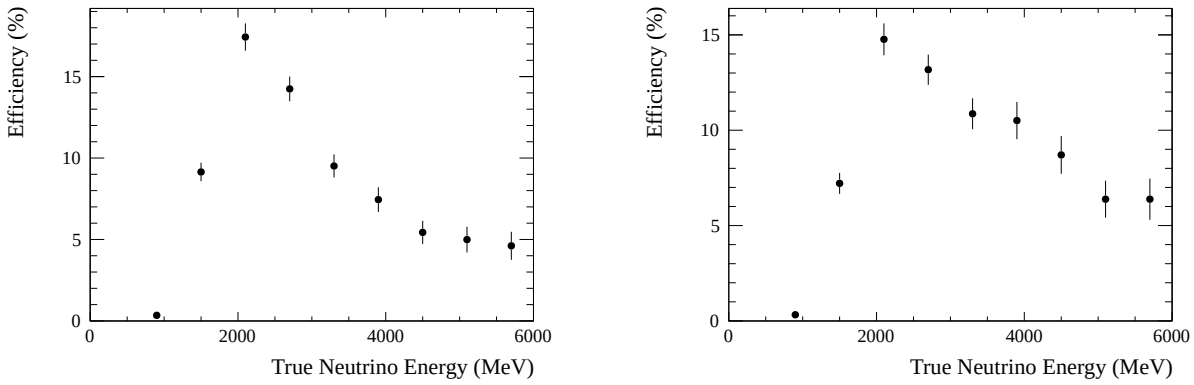

(a) Water Configuration **(b)** Air Configuration

Figure 4.13: Selection efficiency of signal events as a function of the true neutrino energy E_{true} for the water and air configuration. The error bars correspond to the uncertainties due to limited MC statistics.

4.4.3 Selected MC Sample

This section analyzes the composition of the selected MC sample and looks at the contribution from events of different interaction types. In addition, the selected MC sample broken down by neutrino type and parent particle is analyzed.

In both Tab. 4.3 and Tab. 4.4, the number of MC events passing the event selection are divided into signal events, i.e. CCν_e interactions, and background events. Table 4.7 shows the number of selected MC events for the PØD water and air configuration with the background events broken down by the event type. The MC events broken down by the same event type but only with the basic selection applied is shown in Tab. 4.6 for the reference. The table clearly shows that the majority of the remaining background events contain a π^0, namely 73 % for both the PØD water and air configuration. Table 4.8 shows the number of selected MC events broken down by the interaction types defined by NEUT for both the PØD configurations. The table shows the interaction type with the corresponding NEUT reaction codes and the relative contributions of neutral/charged-current background and signal events. The obtained numbers show that most of the background events come from ν_μ-induced deep inelastic scattering events and neutral-current coherent and resonant π^0 production. The MC event distributions broken down by the interaction type as a function of the reconstructed neutrino energy are shown in Fig. 4.14. The event distributions for the water and air configuration are separately shown for the signal and background events.

Table 4.8 shows that 63.0 % and 66.4 % of the selected signal events are quasi-elastic for the PØD configuration water and air, respectively.

The MC event distributions broken down by neutrino type, i.e. ν_e, $\bar{\nu}_e$, ν_μ and $\bar{\nu}_\mu$, as a function of the reconstructed neutrino energy are shown in Fig. 4.15. The event distributions for the water and air configuration are separately shown for signal and background events. The plots clearly show that all selected signal events are coming from ν_e or $\bar{\nu}_e$ interactions which is not surprising as a signal event is defined as electron neutrino or anti-neutrino

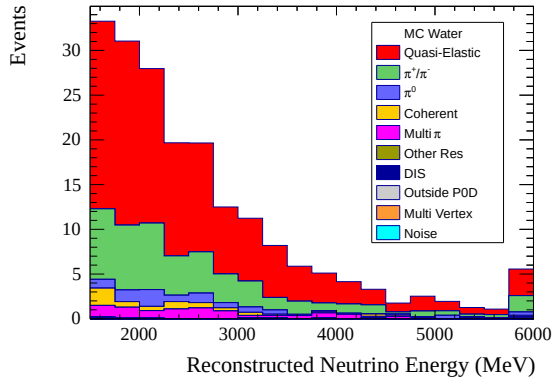

(a) Signal Events Water Configuration

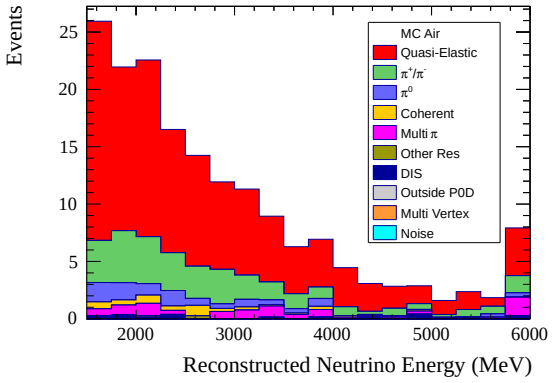

(b) Signal Events Air Configuration

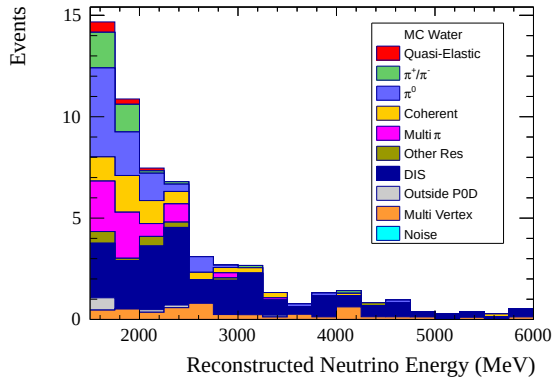

(c) Background Events Water Configuration

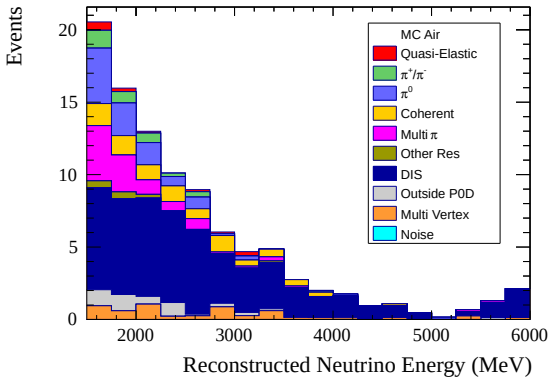

(d) Background Events Air Configuration

Figure 4.14: Distribution of the selected MC events broken down by the interaction type for the PØD water and air configuration. The distributions for signal ((a) and (b)) and background events ((c) and (d)) are shown separately.

interaction with an electron in the final state. Background events are mostly coming from ν_μ interactions, precisely with 88 % for both the PØD water and air configuration. The contribution of ν_e interactions to the background is approximately 8 % for both water and air configuration. Those events are not classified as signal events because they have the true interaction vertex outside the PØD detector, are multi vertex events, or have for some

Table 4.6: MC events broken down by the event type for the PØD configuration water and air, with only basic selection applied. The MC events are normalized to the data POT.

	MC Water		MC Air	
Event Type	Events	Rel. (%)	Events	Rel. (%)
Signal	2328.4	3.1	2211.0	2.7
μ and π^0	16096.2	21.1	15467.5	18.9
μ no π^0	35530.0	46.6	36286.5	44.3
π^0 no μ	7734.1	10.1	7303.7	8.9
No μ/π^0	6950.4	9.1	7235.8	8.8
Outside P0D	5105.5	6.6	10679.5	13.0
Multi Vertex	2566.0	3.4	2811.5	3.4
Noise	0.0	0.0	0.0	0.0
Total	76310.6	100.0	81995.4	100.0

Table 4.7: Selected MC events broken down by the event type for the PØD configuration water and air. The MC events are normalized to the data POT.

	MC Water		MC Air	
Event Type	Events	Rel. (%)	Events	Rel. (%)
Signal	196.1	77.6	173.6	64.1
μ and π^0	11.9	4.7	32.2	11.9
μ no π^0	7.1	2.8	10.1	3.7
π^0 no μ	29.5	11.7	39.3	14.5
No μ/π^0	2.3	0.9	5.4	2.0
Outside P0D	1.0	0.4	4.6	1.7
Multi Vertex	4.9	1.9	5.8	2.1
Noise	0.0	0.0	0.0	0.0
Total	252.8	100.0	271.0	100.0

Table 4.8: Selected signal and background MC events broken down by the interaction type, as defined by NEUT, for the PØD water and air configuration. The tables list the interaction type, the corresponding NEUT codes, and relative contributions of neutral-current (NC) and charged-current (CC) background (B) as well as signal events. The background percentages are relative to the total selected background events and the signal percentages are relative to the total predicted signal events.

(a) Water Configuration

Interaction	NEUT Code	NC B (%)	CC B (%)	Signal (%)
Quasi-Elastic	1/51-52	0.2	1.4	63.0
π^+/π^-	11/13/33-34	2.3	4.0	24.1
π^0	12/31-32	13.9	2.9	4.6
Coherent	16/36	10.5	0.5	3.0
Multi π	21/41	5.8	5.9	4.6
Other Res	17/22-23/38-39/42-45	1.3	1.7	0.3
DIS	26/46	21.6	17.6	0.4
Outside P0D	-	0.2	1.5	0.0
Multi Vertex	-	0.6	8.1	0.0
Total	-	56.5	43.5	100.0

(b) Air Configuration

Interaction	NEUT Code	NC B (%)	CC B (%)	Signal (%)
Quasi-Elastic	1/51-52	0.1	1.4	66.4
π^+/π^-	11/13/33-34	1.1	2.4	18.8
π^0	12/31-32	8.2	1.8	5.5
Coherent	16/36	8.7	0.2	2.6
Multi π	21/41	3.3	6.7	5.1
Other Res	17/22-23/38-39/42-45	0.9	0.5	0.2
DIS	26/46	23.5	30.6	1.4
Outside P0D	-	1.0	3.7	0.0
Multi Vertex	-	0.6	5.3	0.0
Total	-	47.5	52.5	100.0

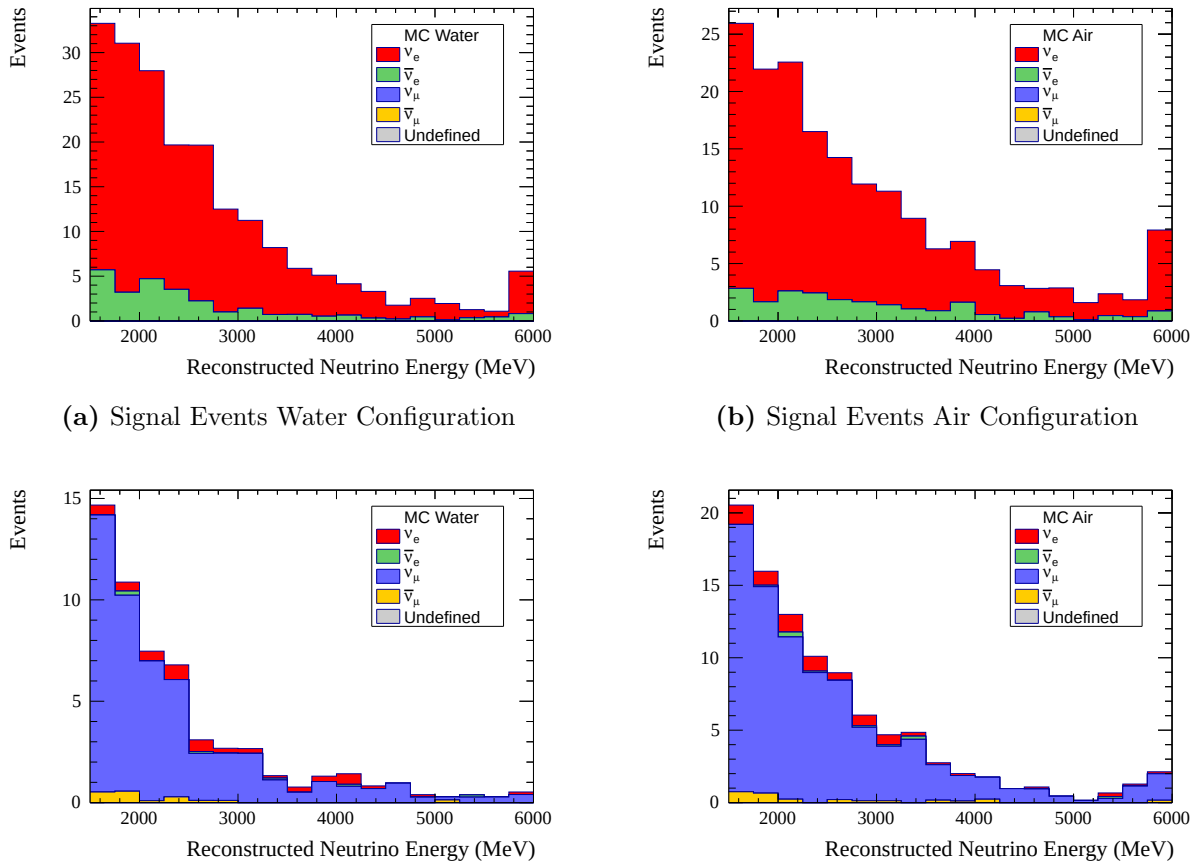

(a) Signal Events Water Configuration

(b) Signal Events Air Configuration

(c) Background Events Water Configuration

(d) Background Events Air Configuration

Figure 4.15: Distribution of the selected MC events broken down by neutrino type for the PØD water and air configuration. The distributions for signal and background events are shown separately.

reasons no electron in the final state.

The MC event distributions broken down by parent particle, i.e. $K^{+/-}$, K^0, and μ or π, as a function of the reconstructed neutrino energy are shown in Fig. 4.16. The event distributions for the water and air configuration are separately shown for signal and background events. The plots clearly show that most of the selected signal events, namely approximately 90 %, are coming from Kaon decays.

4.4.4 Selected Data Sample

This section looks at the selected data sample and the corresponding event distributions as a function of various kinematic variables. In addition, the data event distribution over time and the PØD detector are analyzed.

Inputs for the quasi-elastic formula to calculate the neutrino energy are the electron angle and the electron energy. Figure 4.17 shows the particle direction and energy of selected events

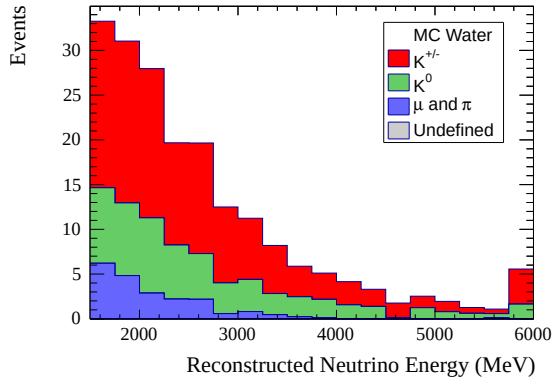

(a) Signal Events Water Configuration

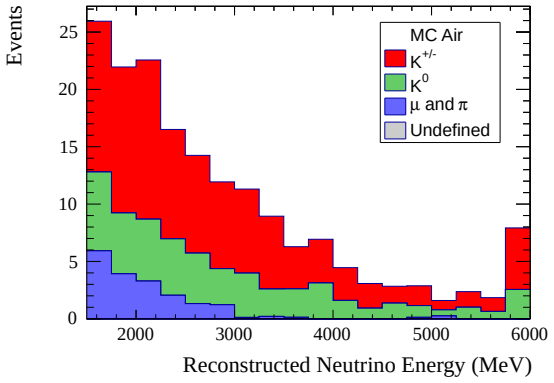

(b) Signal Events Air Configuration

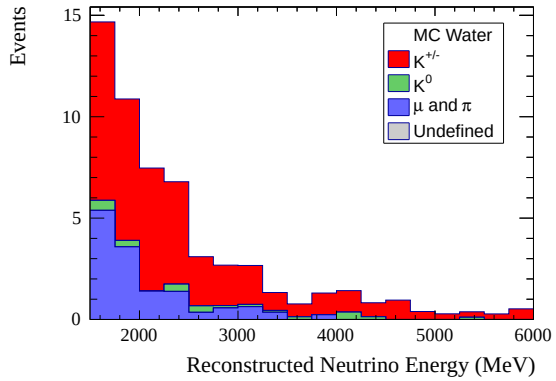

(c) Background Events Water Configuration

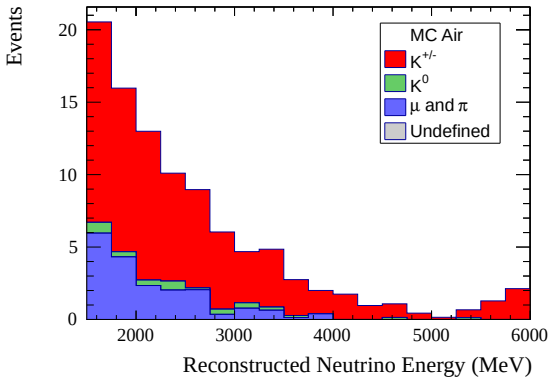

(d) Background Events Air Configuration

Figure 4.16: Distribution of the selected MC events broken down by parent particle type for the PØD water and air configuration. The distributions for signal and background events are shown separately.

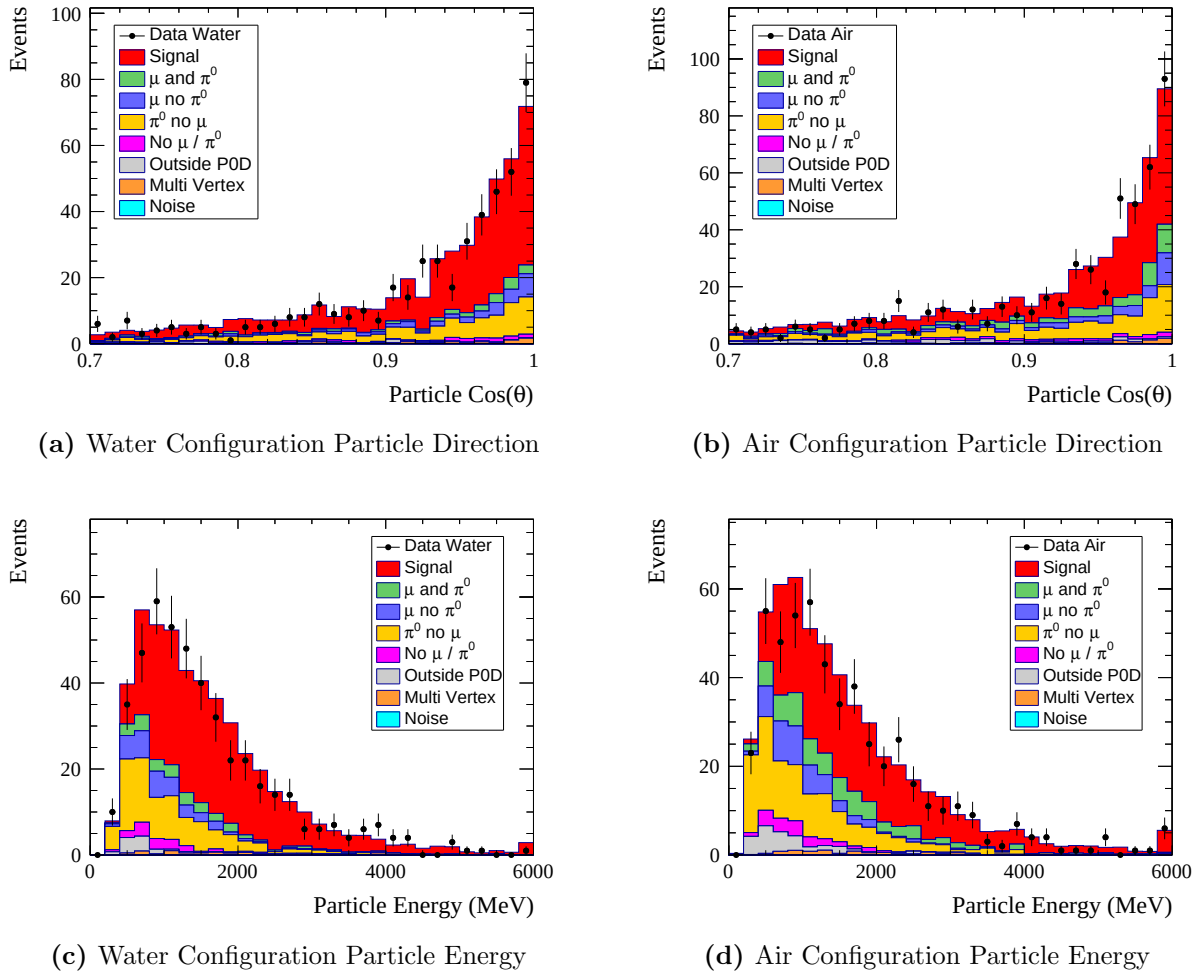

(a) Water Configuration Particle Direction

(b) Air Configuration Particle Direction

(c) Water Configuration Particle Energy

(d) Air Configuration Particle Energy

Figure 4.17: Events passing the event selection except Neutrino Energy cut, as a function of the particle direction and energy for the water and air configuration. The MC events are normalized to the data POT.

before Neutrino Energy cut, and Fig. 4.18 shows those of the selected events with all cuts for the water and air configuration with the MC events normalized to the data POT. The obtained reconstructed neutrino energy distributions are shown in Fig. 4.19. For comparison, both the area-normalized and the POT-normalized MC is shown.

Looking at the data events passing all selection criteria for each analyzed run period, results in the selected number of the data events presented in Tab. 4.9. The table also shows the summarized POT and selected data events collected during the water and air configurations. In total, 230 events were selected for the PØD water configuration and 257 events were selected for the PØD air configuration. Figure 4.20 shows the number of selected data events as a function of the accumulated POT for each PØD configuration. The plots also show the expected distribution for a constant event rate as straight line. A Kolmogorov-Smirnov test returns a maximum difference of 0.0613 (0.0371) resulting in a p-value of 35.4 %

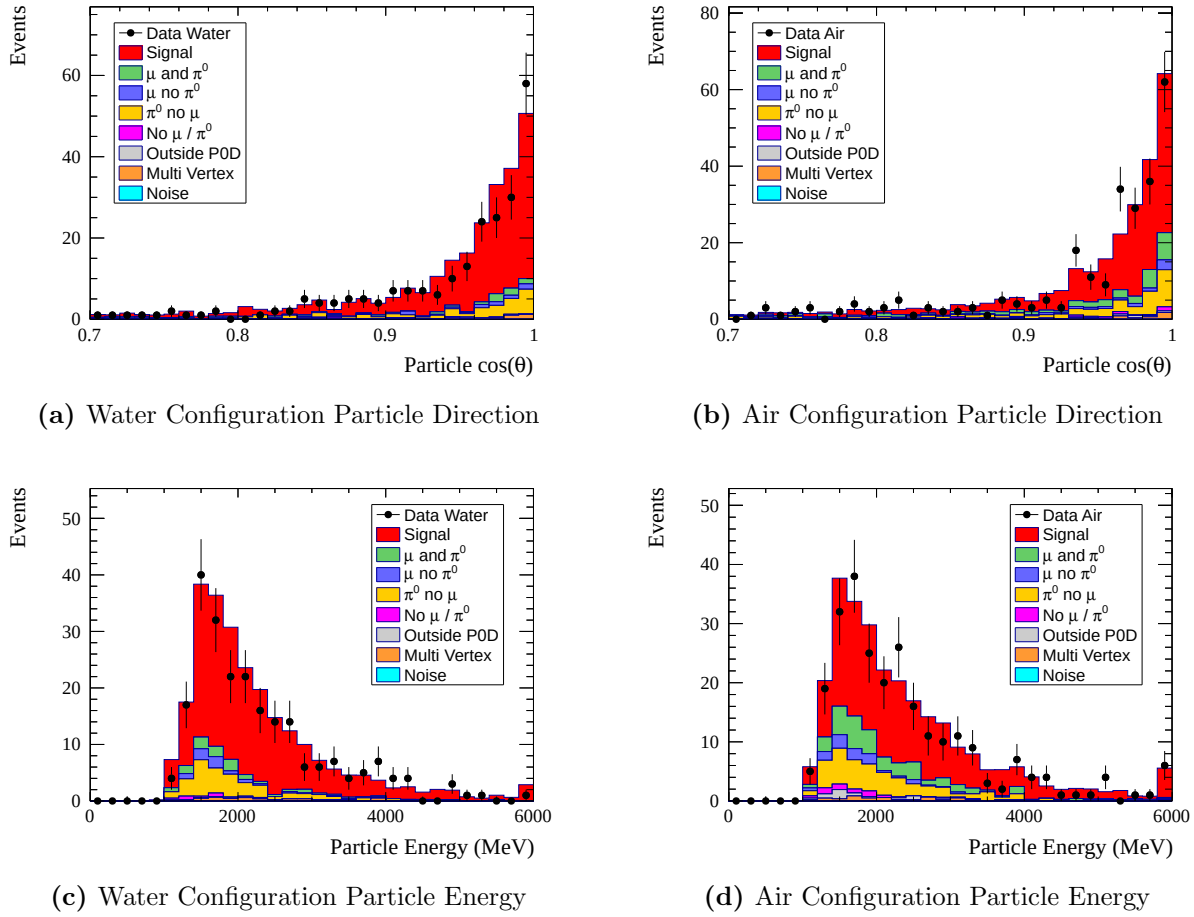

(a) Water Configuration Particle Direction

(b) Air Configuration Particle Direction

(c) Water Configuration Particle Energy

(d) Air Configuration Particle Energy

Figure 4.18: Events passing the event selection as a function of the particle direction and energy for the water and air configuration. The MC events are normalized to the data POT.

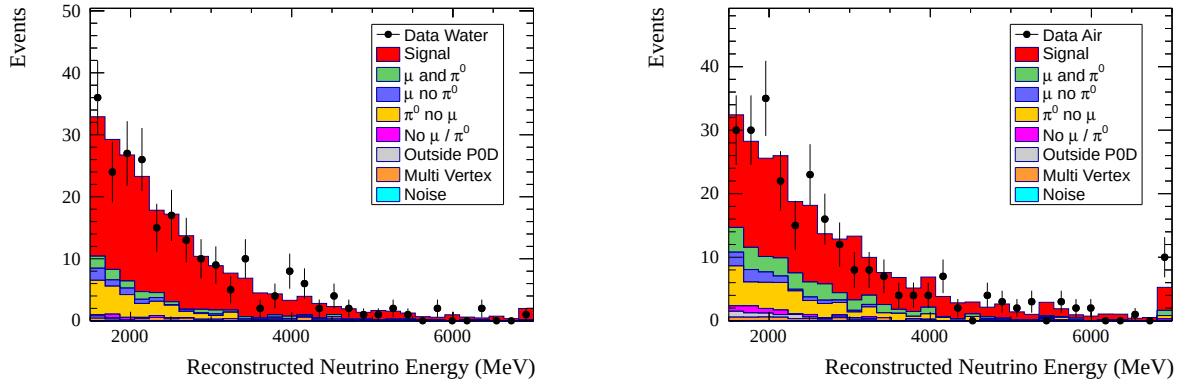

(a) Water Configuration Area Normalized

(b) Air Configuration Area Normalized

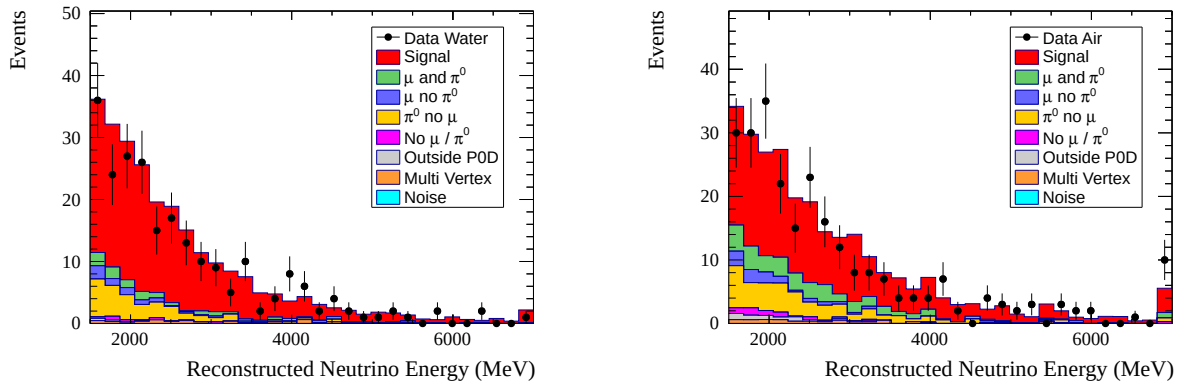

(c) Water Configuration POT Normalized

(d) Air Configuration POT Normalized

Figure 4.19: Events passing the event selection as a function of the reconstructed neutrino energy for the water and air configuration. The top plots are area-normalized to emphasize shape differences between the data and MC while the bottom plots are the data POT-normalized.

(87.0 %) for the water (air) configuration.

The time distribution of the selected data events for the PØD water and air run periods is shown in Fig. 4.21. The plots show that the beam bunch structure is as expected. The 1D and 2D distributions of the reconstructed vertex for selected data and MC events are shown in Fig. 4.22 and Fig. 4.23, respectively. The MC events are normalized to the data POT. The plots clearly show that the event distribution in X and Y coordinate is uniformly while the event distribution of the Z coordinate shows a higher event rate at the downstream end

Table 4.9: The number of the data events passing all selection criteria for each analyzed run period. The table shows the run number, the PØD configuration, the beam configuration, the collected POT, and the selected number of the data events. In addition, the summarized POT and selected data events collected during the water and air configurations are shown.

Run	PØD Configuration	Beam	Collected POT	Selected Events
1	Water	A	2.96×10^{19}	34
2	Water	B	6.96×10^{19}	62
2	Air	B	3.59×10^{19}	26
3	Air	C	1.35×10^{20}	108
4	Water	C	1.65×10^{20}	134
4	Air	C	1.78×10^{20}	123
1-4	Water	A-C	2.64×10^{20}	230
2-4	Air	B-C	3.49×10^{20}	257

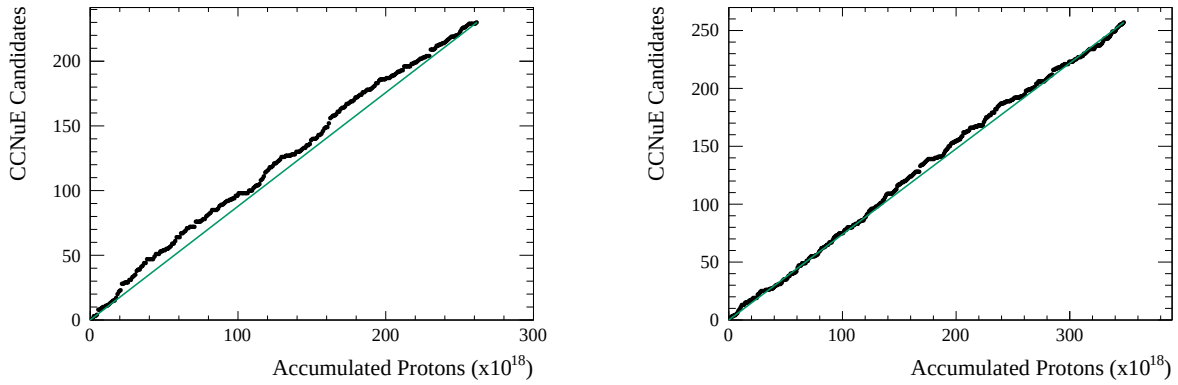

(a) Water Configuration **(b)** Air Configuration

Figure 4.20: Cumulative number of selected data events as a function of the accumulated POT. The data distribution is shown as black data points and the expected distribution for a constant event rate is shown as straight line.

of the fiducial volume of the PØD detector. The reason for the increased event rate at the downstream end of the fiducial volume are background events including a muon that pass the selection cuts with higher probability.

4.5 On-Water Event Extraction

A simple background subtraction method is performed to extract the CCν_e interactions from the data samples collected during the PØD water and air configuration periods and to determine the number of on-water CCν_e interactions.

The measured ν_e interactions that were collected during the PØD water and air configuration are compared with the number of ν_e interactions predicted by the PØD water and air configuration MC, respectively. For that purpose, the measured number of ν_e interactions are extracted by subtracting the predicted MC background B from the selected data events D:

$$N^{\text{Data}}_{\text{CC}\nu_e,\text{water}} = D_{\text{water}} - B_{\text{water}} \tag{4.4}$$

$$N^{\text{Data}}_{\text{CC}\nu_e,\text{air}} = D_{\text{air}} - B_{\text{air}} \tag{4.5}$$

The background subtracted data is then divided by the predicted MC signal S to obtain the data/MC ratios for the water and air configurations:

$$R_{\text{water}} = \frac{N^{\text{Data}}_{\text{CC}\nu_e,\text{water}}}{S_{\text{water}}} \tag{4.6}$$

$$R_{\text{air}} = \frac{N^{\text{Data}}_{\text{CC}\nu_e,\text{air}}}{S_{\text{air}}} \tag{4.7}$$

To extract the measured number of on-water charged current ν_e interactions, the measured CCν_e interactions with the PØD water and air configurations are compared by taking into account the different collected POT and the different reconstruction efficiencies for the water and the air data sample:

$$N^{\text{Data}}_{\text{CC}\nu_e,\text{on-water}} = (D_{\text{Water}} - B_{\text{Air}}) - \frac{\epsilon_{\text{not-water}} \cdot \text{POT}_{\text{water}}}{\epsilon_{\text{air}} \cdot \text{POT}_{\text{air}}} \cdot (D_{\text{air}} - B_{\text{air}}) \tag{4.8}$$

In this formula, $\text{POT}_{\text{water}}$ (POT_{air}) is the collected the data POT with the PØD water (air) configuration:

$$\text{POT}_{\text{water}} = 2.64 \times 10^{20} \tag{4.9}$$

$$\text{POT}_{\text{air}} = 3.49 \times 10^{20} \tag{4.10}$$

The efficiency ϵ_{air} is defined in Sec. 4.4.2 and describes the reconstruction efficiency of signal events for the PØD air configuration. The efficiency $\epsilon_{\text{not-water}}$ describes the PØD water configuration reconstruction efficiency of signal interactions happening not on the water targets, i.e. they interact on the scintillators, brass, or lead. This efficiency is therefore different

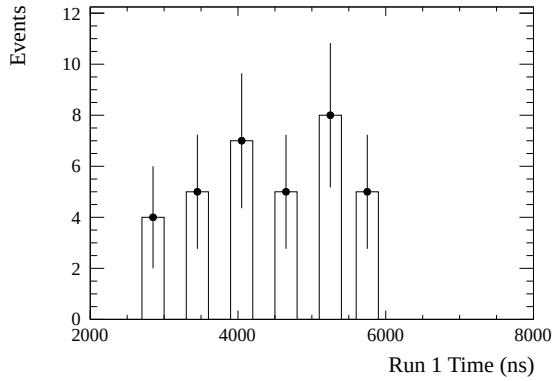

(a) Time Run 1 Water

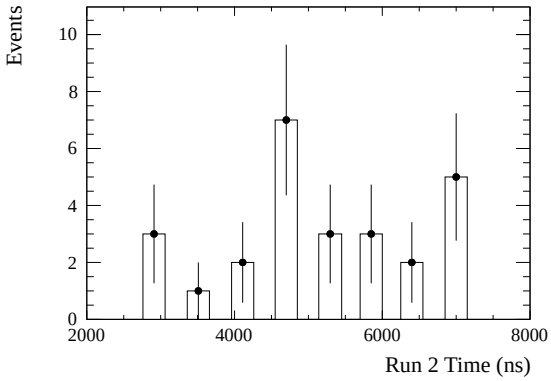

(b) Time Run 2 Air

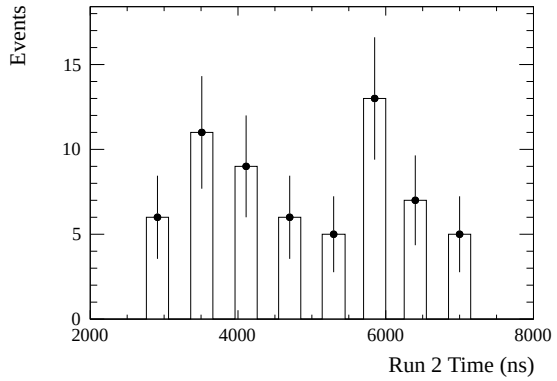

(c) Time Run 2 Water

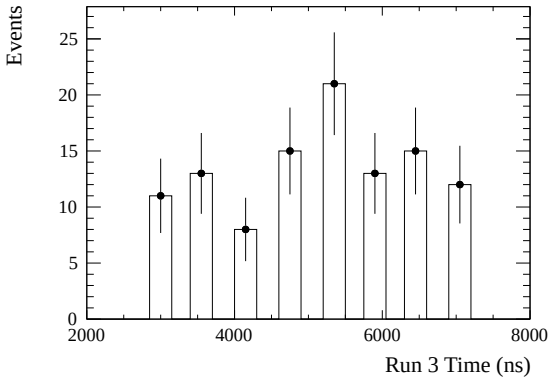

(d) Time Run 3 Air

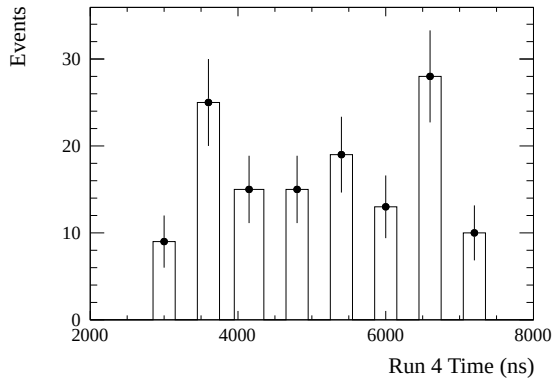

(e) Time Run 4 Water

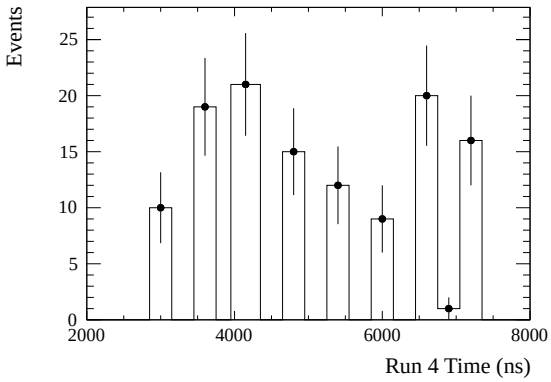

(f) Time Run 4 Air

Figure 4.21: Time distribution of the selected data events for the PØD water and air run periods to confirm the beam bunch structure.

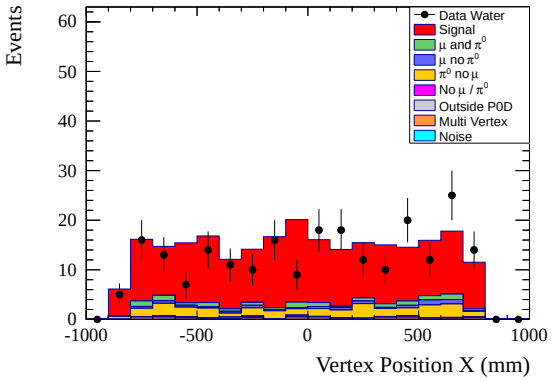

(a) Vertex Position X Water Configuration

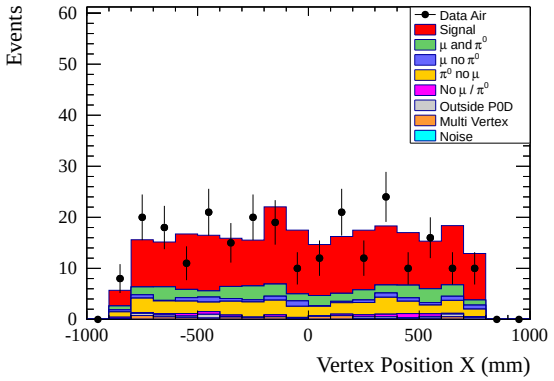

(b) Vertex Position X Air Configuration

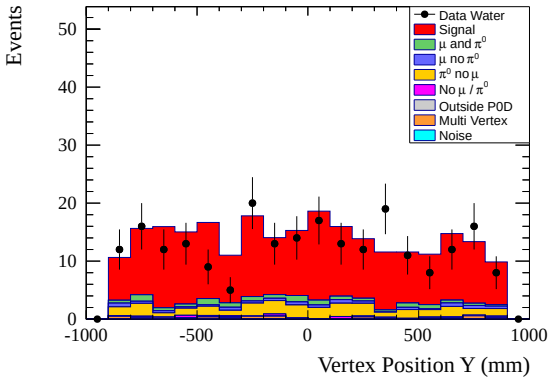

(c) Vertex Position Y Water Configuration

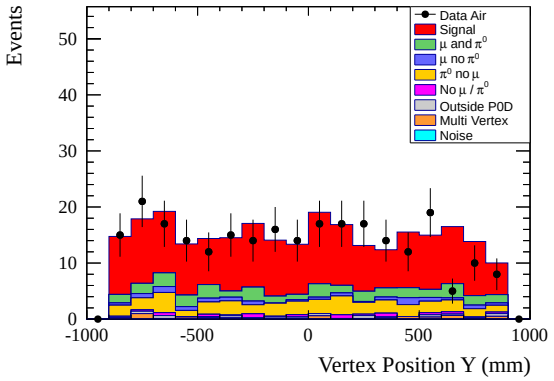

(d) Vertex Position Y Air Configuration

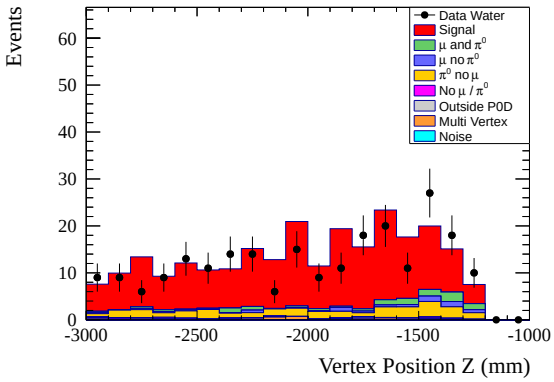

(e) Vertex Position Z Water Configuration

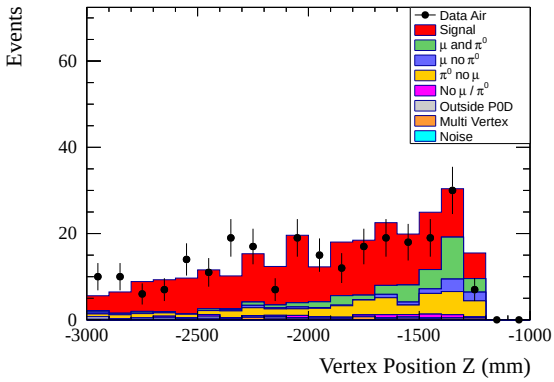

(f) Vertex Position Z Air Configuration

Figure 4.22: One dimensional vertex distributions of the selected data and MC events for the PØD water and air configuration. The MC events are normalized to the data POT.

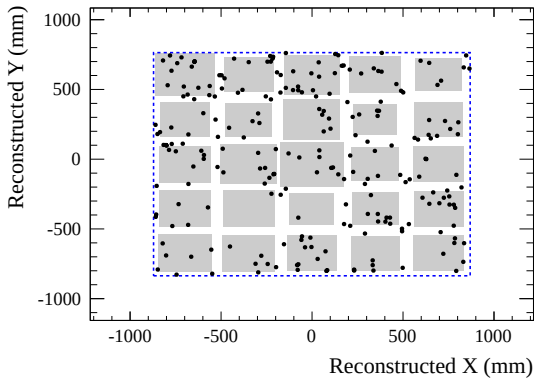

(a) Vertex Position XY Water Configuration

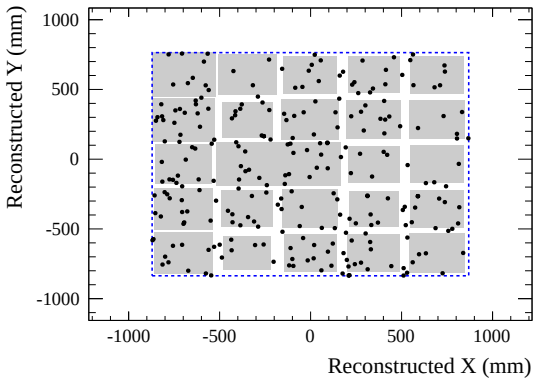

(b) Vertex Position XY Air Configuration

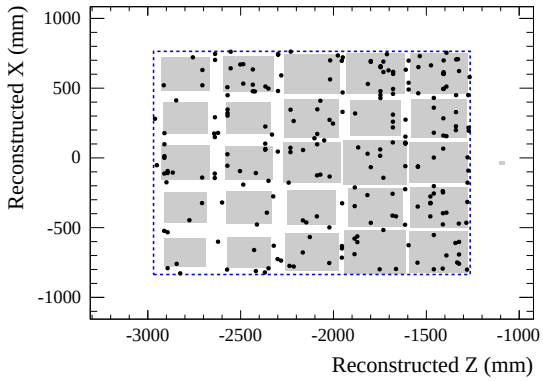

(c) Vertex Position XZ Water Configuration

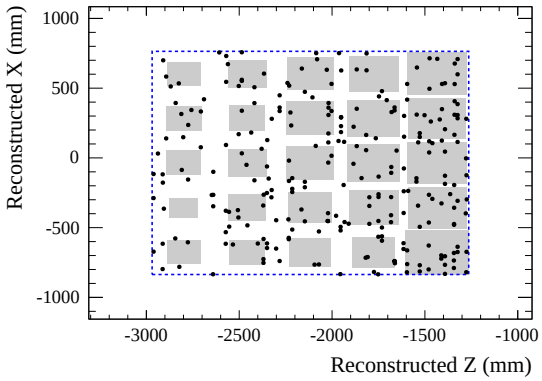

(d) Vertex Position XZ Air Configuration

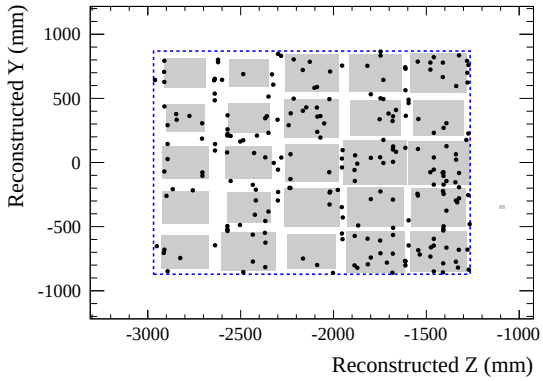

(e) Vertex Position YZ Water Configuration

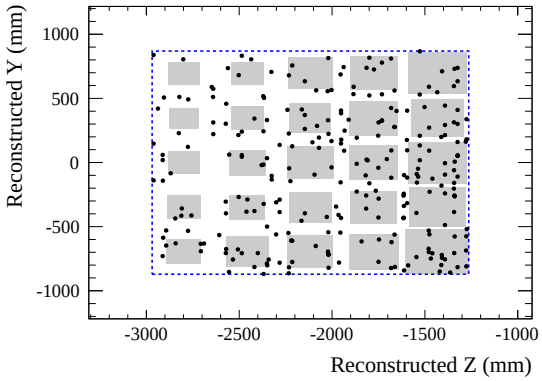

(f) Vertex Position YZ Air Configuration

Figure 4.23: Two dimensional vertex distributions of the selected data and MC events for the PØD water and air configuration. Data vertices are shown as black points while the relative vertex distribution of MC is indicated with gray squares. The larger a gray square the more MC vertices and vice versa. The boundaries of the PØD fiducial volume are indicated with dashed lines.

than the general reconstruction efficiency of signal events for the PØD water configuration as explained in Sec. 4.4.2. The values for the efficiencies are:

$$\epsilon_{\text{not-water}} = (11.5 \pm 0.4)\,\% \tag{4.11}$$

$$\epsilon_{\text{air}} = (11.0 \pm 0.3)\,\% \tag{4.12}$$

The errors correspond to the statistical uncertainty due to the limited MC statistics. The resulting data/MC ratio of on-water CCν_e interactions is given by:

$$R_{\text{on-water}} = \frac{N^{\text{Data}}_{\text{CC}\nu_e,\text{on-water}}}{S_{\text{on-water}}} \tag{4.13}$$

4.6 Systematic Uncertainties

The effect of detector, flux, and cross section systematic uncertainties on the results of the PØD ν_e analysis are discussed and estimated in this section. For many cases a simple Kolmogorov-Smirnov (KS) test [52, 53]is used for the systematic uncertainty tests, particularly where no deviation is indicated in the test.

4.6.1 PØD Geometry and Mass Uncertainties

This section estimates the systematic uncertainties coming from the PØD mass, the fiducial volume definition , and the PØD alignment.

Mass Uncertainty

The mass of the PØD fiducial volume is calculated previously [54] for both the water and the air configuration. The obtained as-built masses for Run 1 and 2 as well as the PØD mass in MC are listed in Tab. 3.2. The PØD mass is different for Run 1 and Run 2 because the entire water sensor system was replaced between those runs. At the time of writing this note, the information about the fiducial mass of the water for Run 4 was not available. It is therefore assumed to be the same as in Run 2. Most of the discrepancy between as-built mass and the mass in the MC is caused by the water target dead material which is not modeled in the MC.

The differences between as-built and MC masses is incorporated in the PØD ν_e analysis procedure by re-weighting MC events with the as-built over MC mass ratio. Only MC events with true vertex position inside the fiducial volume are re-weighted. The masses and their uncertainties for the PØD water and air configurations are not uncorrelated as the water configuration is composed of water and the dry mass which is identical with the PØD air configuration. The water mass and the dry mass of the PØD fiducial volume are presented in Tab. 4.10 and are extracted from the fiducial volume masses for the different PØD configurations listed in Tab. 3.2. Therefore, the MC events should be re-weighted with the corresponding mass correction according to their true interaction position. MC interactions in the water targets should be corrected with the water mass while MC events

Table 4.10: The as-built water and dry mass of the PØD fiducial volume for Run1 and 2 as well as the corresponding masses used in MC are listed.

	Water Mass (kg)	Dry Mass (kg)
As-Built Run 1	1902.00 ± 15.99	3558.86 ± 34.23
As-Built Run 2	1902.00 ± 16.01	3578.30 ± 33.80
MC	1924.08 ± 0.11	3469.14 ± 0.55

happening on other materials such as scintillator or bras should be corrected with the dry mass.

The systematic effect on the CCν_e data/MC ratios for the water (R_{water}), air (R_{air}), and on-water ($R_{\text{on-water}}$) coming from the PØD fiducial volume mass uncertainties are estimated by varying the water and dry mass according to the uncertainties. The water and dry mass are thrown 10,000 times and the MC events are re-weighted accordingly. Then, the PØD ν_e analysis is applied to the nominal data set and the re-weighted MC set of each mass throw. The CCν_e data/MC ratios R_{water}, R_{air}, and $R_{\text{on-water}}$ are calculated and plotted in a histogram. The obtained distributions are shown in Fig. 4.24 and they are fit with a Gaussian. The fitted widths for each distribution are presented in Tab. 4.11 and are considered to be the systematic uncertainty coming from the PØD mass uncertainty. The obtained uncertainty for the CCν_e data/MC ratio is 0.01 for each data sample (water, air, on-water).

Fiducial Volume

Whether or not an event passes the fiducial volume cut depends on its reconstructed vertex location. Varying the fiducial volume definition causes migration of events into and out of the fiducial volume that could be different for the data and MC events. To estimate if there is a general systematic impact of this effect on the data/MC ratio, a test sample of events is selected. Those events are required to pass the basic cuts and having no energy deposit in side bars. The first requirement ensures a good reconstruction quality and the second condition is chosen because the event selection described in Sec. 4.3 suppresses side

Table 4.11: PØD mass systematic uncertainties for the water (R_{water}), air (R_{air}), and on-water ($R_{\text{on-water}}$) CCν_e data/MC ratios.

CCν_e Data/MC Ratio	Uncertainty
R_{water}	0.01
R_{air}	0.01
$R_{\text{on-water}}$	0.01

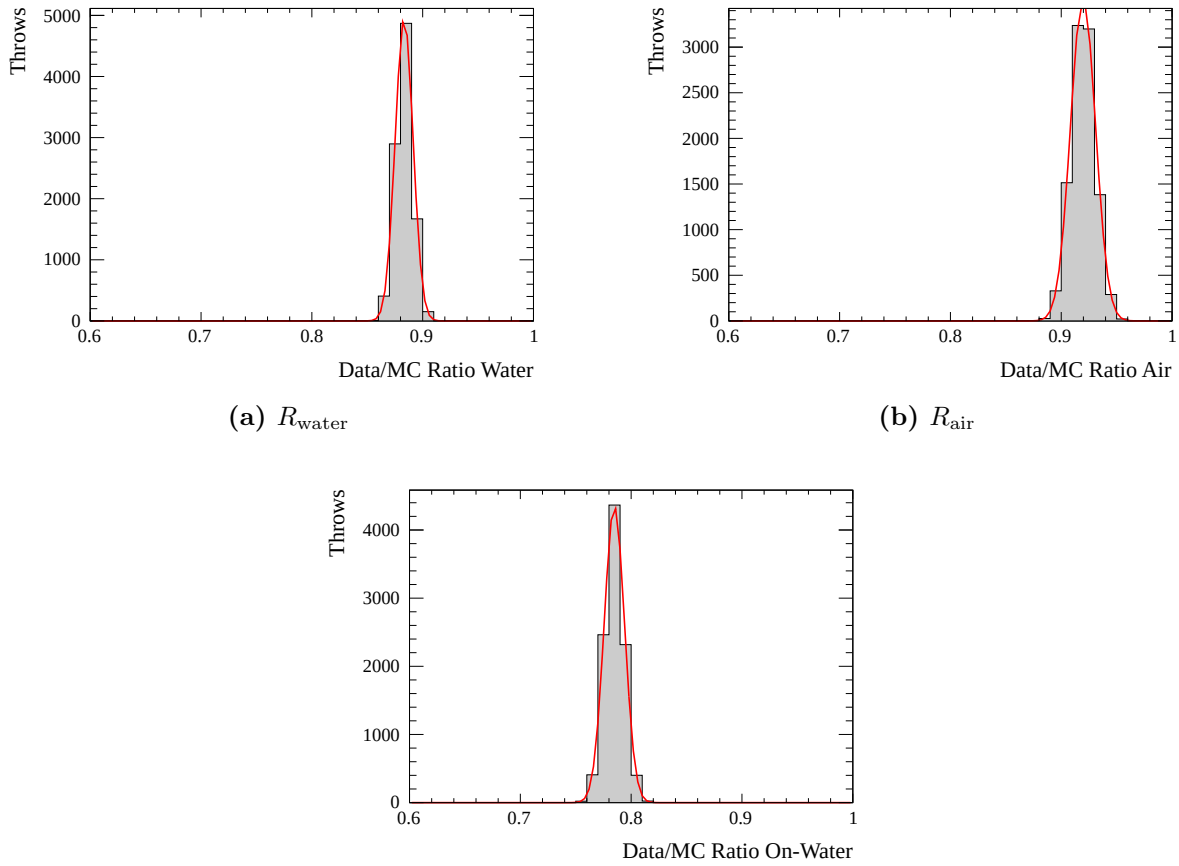

(a) R_{water} **(b)** R_{air}

(c) $R_{\text{on-water}}$

Figure 4.24: Data/MC ratios for the water (R_{water}), air (R_{air}), and on-water ($R_{\text{on-water}}$) varied within the PØD mass systematic uncertainties. The distributions are fit with a single Gaussian.

exiting events. Vertex distributions for the data and MC events passing those requirements are shown in Fig. 4.25 for the PØD configurations water and air. In each plot, the fiducial volume requirement has been applied to the other two dimensions. The Z distribution plot shows a data excess at the upstream PØD face due to sand muons.

To quantify the systematic error, the fiducial volume is varied separately in X, Y, and Z direction. The amount by which the fiducial volume should be varied in each direction is chosen to be the MC vertex resolution of selected events which is presented in Tab. 4.1. The boundaries are varied by $\pm 1\sigma$ and $\pm 2\sigma$. The relative ratio of the data events D' to MC events M' passing the varied fiducial volume cut is measured and compared to the relative ratio of the data events D and MC events M passing the original fiducial volume cut

$$V = \frac{D'/M'}{D/M}, \tag{4.14}$$

for each dimension (X, Y, Z), each fiducial edge variation (-2σ, -1σ, $+1\sigma$, $+2\sigma$), and each the PØD configuration (water, air). The obtained values are presented in Tab. 4.12. The

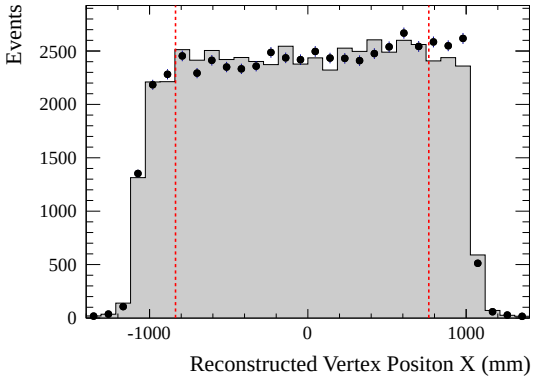

(a) Vertex Position X Water Configuration

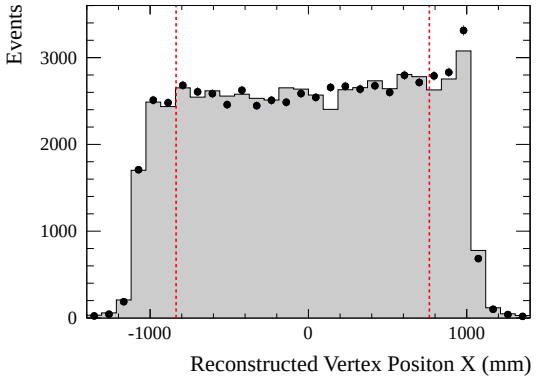

(b) Vertex Position X Air Configuration

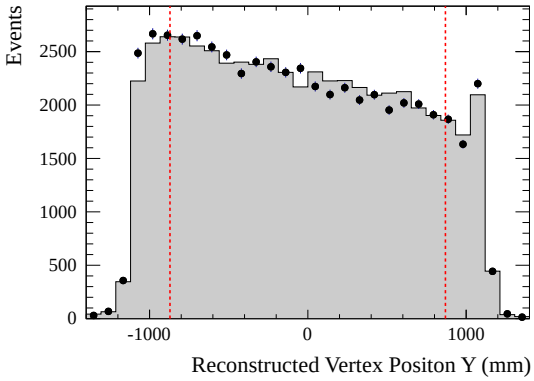

(c) Vertex Position Y Water Configuration

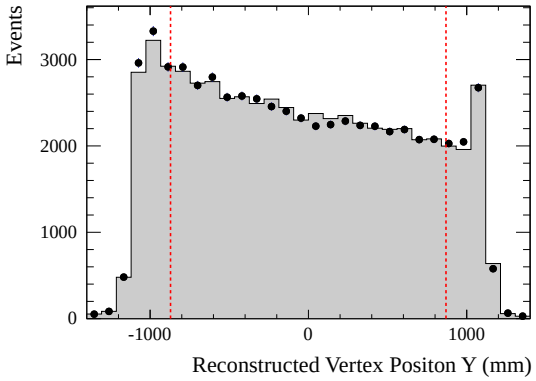

(d) Vertex Position Y Air Configuration

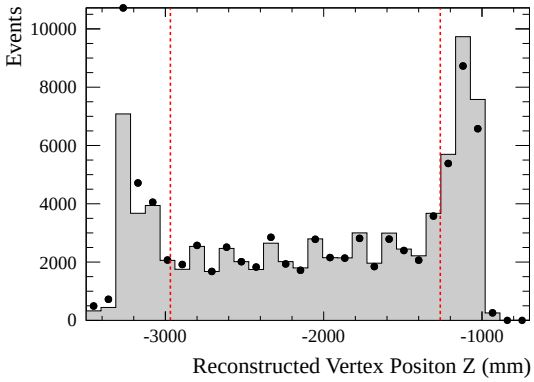

(e) Vertex Position Z Water Configuration

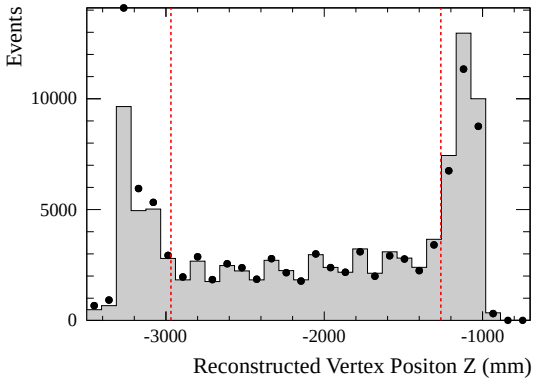

(f) Vertex Position Z Air Configuration

Figure 4.25: Distribution of vertices in X, Y, and Z of events passing the basic selection cuts and having no energy deposit in side bars. Data events are plotted as black points while the POT-normalized MC events are shown as filled histograms. The vertical lines represent the location of the fiducial volume boundaries defined in Tab. 3.1. In each plot, the fiducial volume requirement has been applied to the other two dimensions.

Table 4.12: Relative variation V of the total data/MC ratios for the test sample

(a) Relative Variation V Water

Dimension	-2σ	-1σ	$+1\sigma$	$+2\sigma$
X	1.0000 ± 0.0010	0.9996 ± 0.0007	1.0015 ± 0.0006	1.0029 ± 0.0009
Y	0.9993 ± 0.0010	1.0001 ± 0.0007	0.9998 ± 0.0007	1.0001 ± 0.0009
Z	0.9946 ± 0.0016	0.9977 ± 0.0011	1.0000 ± 0.0010	0.9967 ± 0.0016

(b) Relative Variation V Air

Dimension	-2σ	-1σ	$+1\sigma$	$+2\sigma$
X	0.9992 ± 0.0012	1.0001 ± 0.0009	1.0005 ± 0.0008	1.0031 ± 0.0011
Y	0.9983 ± 0.0012	0.9992 ± 0.0008	1.0000 ± 0.0008	1.0004 ± 0.0011
Z	1.0023 ± 0.0019	1.0019 ± 0.0011	0.9983 ± 0.0013	0.9934 ± 0.0019

shown uncertainties are the statistical uncertainties based on the difference of event numbers passing the original or varied fiducial volume cut. The table clearly shows that the impact on the data/MC ratio due to varying the fiducial volume is very small. Taking the $\pm 1\sigma$ values, the uncertainty

$$U = |V - 1| \tag{4.15}$$

can be calculated for each dimension and each fiducial edge variation. The obtained uncertainties are listed in Tab. 4.13 and show that the uncertainty from the fiducial volume on the total data/MC ratio for the test sample is always smaller than 0.01 for both water and air configuration. Therefore, it is concluded that the systematic effect coming from the fiducial volume definition is negligible.

Alignment

The PØDules of the PØD detector are shifted in X and Y direction according to the results of the alignment which is described in [54]. According to this note, the resolution of a hit in X direction is 2.46 mm and in Y direction it is 2.78 mm. To determine the impact of the alignment on the CCν_e data/MC ratios, the MC fiducial volume is shifted separately in X and Y direction with respect to the data fiducial volume. For each direction, the shift is thrown 10,000 times with the corresponding resolution as uncertainty. Then the analysis described in Sec. 4.5 is applied. The resulting CCν_e data/MC ratios for the water, air, and on-water are plotted in a histogram and fitted with a Gaussian. The resulting width is considered to be the systematic uncertainty from the alignment. The obtained uncertainties are smaller than 0.01 for all ratios therefore negligible.

Table 4.13: Fiducial volume uncertainty U for the total data/MC ratio for the test sample for both the PØD configurations water and air. Due to the very small uncertainties, it is concluded that the systematic uncertainty of the fiducial volume definition is also negligible (< 0.01) for all CCν_e data/MC ratios (water, air, on-water).

Dimension	Water	Air
X	0.001	0.000
Y	0.000	0.001
Z	0.002	0.002

4.6.2 Energy Scale

Possible systematic effects on the reconstructed electron energy are studied. The effects are investigated by looking at potential scaling factors of the reconstructed energy scale, then the difference in CCν_e data/MC ratio is calculated.

PØD Material Density and Thickness

The possible difference between MC geometry and the as-built detector can effect the energy scale systematic uncertainty. Three high Z materials, plastic of scintillator, and the water are considered here: the brass in the water target regions, the lead absorber in the ECals, the steel sheet covering the lead absorber, the polystyrene from the scintillator, and the water from the water bags in water-in configuration of the PØD.

For this study, samples of 1000 1 GeV electron particle gun starting at upstream water target and directed towards downstream along the beam axis are generated. The 1 GeV electrons are used as these electrons are closest in energy to those produced by 1.5 GeV neutrinos. We vary density and thickness of each materials by 1σ following [54], and nd280mc geometry is modified with the variation. The varied parameters are listed in Tab. 4.14 and Tab. 4.15, and the total variation of the materials are shown in Tab. 4.16. The reconstructed energies are fitted with Gaussian.

For the water density variation, the possible uncertainty is coming from the fact that the water bags are not straight and therefore the width of the water bag is not consistent. The possible maximum change in the width of the water bag is estimated by considering the 'settlement' of the water bag after the fill. By looking at water depth plots from GSC monitor, the average change in the water depth is 3 cm which leads to maximum change in water bag width 1.7 mm for each bag. This change is equivalent to 6 % water density change.

With these possible density variations, the percentage changes in the reconstructed energy are calculated for each materials. Some examples of reconstructed energy plots are shown in Fig. 4.26, and the result of the variation can be seen in Tab. 4.17.

Table 4.14: Variation of material density to study effect on the energy scale. All values are taken from the MC and [54].

Material	Default (g/cm^3)	-1σ (g/cm^3)	$+1\sigma$ (g/cm^3)
Brass	8.50	8.35	8.65
Steel	8.03	7.79	8.27
Lead	11.350	11.316	11.384
Polystyrene	1.050	1.049	1.051
Water	1.00	0.94	1.06

Table 4.15: Variation of material thickness to study effect on the energy scale. All values are taken from [54].

Material	Default (mm)	-1σ (mm)	$+1\sigma$ (mm)
Brass	1.28	1.25	1.31
Steel	0.45	0.40	0.50
Lead	3.45	3.40	3.50
Polystyrene	1.375	1.250	1.500

Table 4.16: Total variation of geometry parameters to study effect on the energy scale.

Material	Default (g/cm^3)	Minimum (g/cm^3)	Maximum (g/cm^3)
Brass	8.50	8.15	8.85
Steel	8.03	6.90	9.16
Lead	11.350	11.297	11.403
Polystyrene	1.050	0.954	1.146
Water	1.00	0.94	1.06

Variation in PØD Response with Time

The PØD charge deposit response varies over time even though most of the variation is removed at the calibration stage. The PØD response over time has been studied previously [54]. According to this study, the residual time variation after correction is 0.5 % for both water and air configurations, as which the systematic uncertainty on the energy scale from this source is taken.

Table 4.17: The percentage change in the reconstructed energy of 1 GeV electrons, for different material densities. In each material, the geometry is varied by 1σ.

Configuration		Brass (%)	Steel (%)	Lead (%)	Polystyrene (%)	Water (%)
Water	-1σ	$+0.6 \pm 0.3$	$+0.2 \pm 0.2$	$+0.1 \pm 0.3$	$+0.3 \pm 0.3$	$+1.4 \pm 0.3$
	$+1\sigma$	-0.5 ± 0.2	-0.2 ± 0.3	-0.1 ± 0.3	$+0.0 \pm 0.3$	-2.0 ± 0.3
Air	-1σ	$+0.9 \pm 0.4$	$+0.5 \pm 0.4$	$+0.2 \pm 0.4$	$+0.8 \pm 0.4$	0.0 ± 0.4
	$+1\sigma$	-0.8 ± 0.4	-0.6 ± 0.4	-1.1 ± 0.4	-0.5 ± 0.4	0.0 ± 0.4

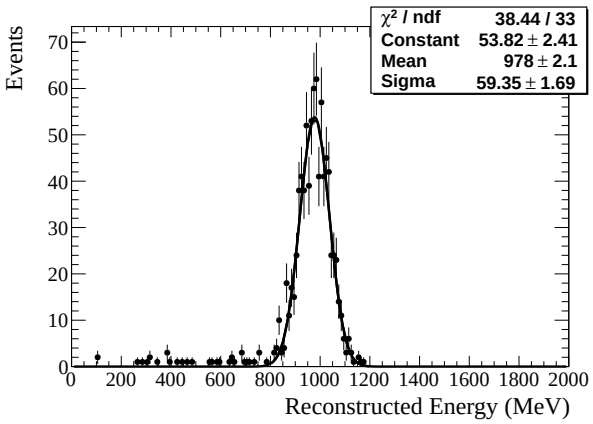

(a) Reconstructed Energy, Nominal

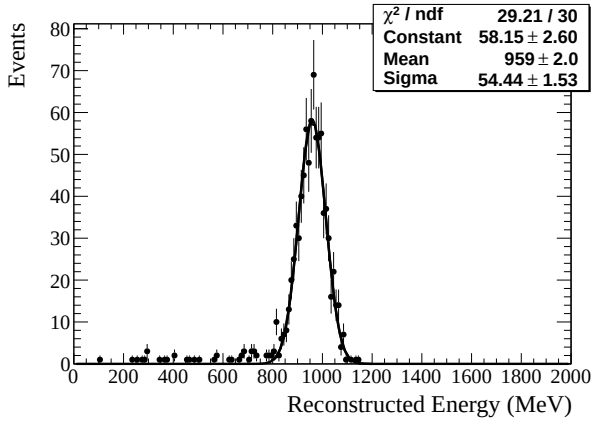

(b) Reconstructed Energy, Water Density Maximum

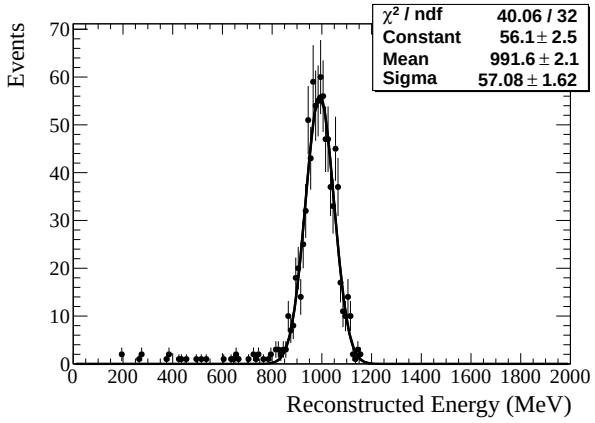

(c) Reconstructed Energy, Water Density Minimum

Figure 4.26: Example plots of reconstructed energy of 1 GeV MC electron particle gun for the nominal, water density maximum, and water density minimum settings in water configuration. Peaks of the plots are fitted with Gaussian.

GEANT4 Uncertainty

The ND280 software uses GEANT4 simulation, hence GEANT4 uncertainty on electron energy deposition enters energy scale uncertainty. Even though there are no exact values for

our particular particle/configuration, the uncertainty for the general case can be estimated. In various papers from GEANT4 collaboration [48, 49, 50, 51], the error is 2 % at the largest. We take the value 2 % for the safe assumption.

Total Effect on CCν_e Data/MC Ratio

By summing all potential systematic uncertainties shown in Tab. 4.18 in quadrature, the maximum energy uncertainties are estimated, 3.01 % for the water and 2.75 % for air. We assume material density uncertainty due to other materials than water are correlated between water and air configurations, where water density uncertainty is uncorrelated. To estimate the systematic impact of the energy scale on the background subtracted data/MC ratio, the reconstructed particle energy by the uncertainties given by Tab. 4.18 is smeared, then the event selection for these smeared events is processed. Gaussian distribution with 10,000 throws were applied. Then the quadrature addition of shifted data/MC ratio to the nominal ratio and the width of distribution will be our systematic uncertainty. The data/MC ratio plots with smeared reconstructed particle energy are shown in Fig. 4.27. Table 4.19 presents energy scale systematics results.

Table 4.18: The Total uncertainties in reconstructed energy scale. The total uncertainties are calculated by summing up all the uncertainties in quadrature. We assume material density uncertainty of other materials than water are correlated between water and air configurations

	Water (%)	Air (%)
PØD Response over Time	±0.50	± 0.50
PØD Material Density: Water	±2.00	0.00
PØD Material Density: Rest of the Materials	±0.74	±1.76
GEANT4	±2.00	±2.00
Total	±2.96	±2.71

Table 4.19: Energy scale systematic uncertainties for the water (R_{water}), air (R_{air}), and on-water ($R_{\text{on-water}}$) CCν_e data/MC ratios.

CCν_e Data/MC Ratio	Uncertainty
R_{water}	0.05
R_{air}	0.05
$R_{\text{on-water}}$	0.10

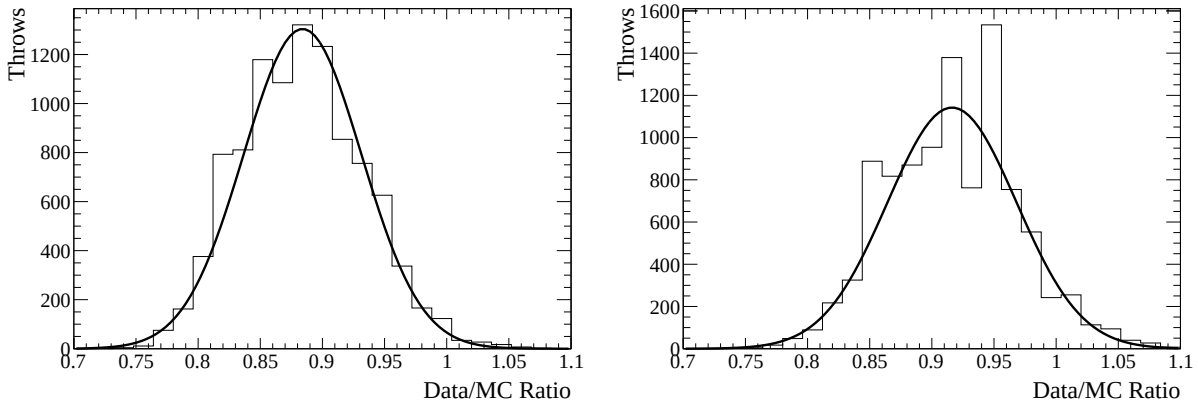

(a) R_{water}

(b) R_{air}

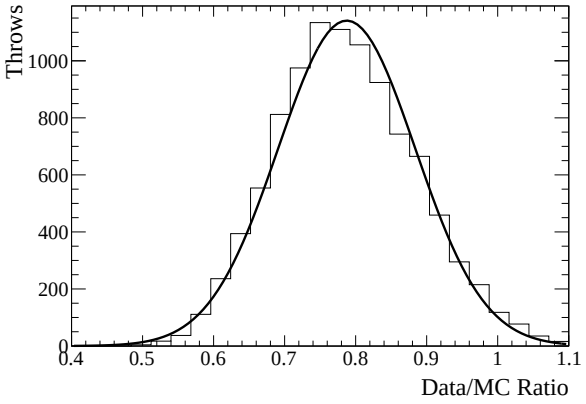

(c) $R_{\text{on-water}}$

Figure 4.27: Data/MC ratio for the water (R_{water}), air (R_{air}), and on-water ($R_{\text{on-water}}$) with maximum energy uncertainties and smearing. The distributions are fit with a single Gaussian

4.6.3 Reconstruction Systematics

The systematics uncertainties coming from the reconstruction of events in the PØD are investigated in this section.

Matching Hits of Candidate Track and Candidate Shower

To combine the results of the PØDRecon track reconstruction and the shower reconstruction, it is necessary to confirm that the candidate track and the candidate shower belong to the same particle. For this purpose, the event selection requires that 80 % of the hits associated with the candidate track are also used for the candidate shower as described in Sec. 4.3.2. This selection criteria is a safety condition to avoid that reconstruction failures are selected. Because the other event selection criteria are looking for a very clear signal pattern in the PØD, the hit matching condition has almost no impact on the number of selected events

Table 4.20: A confusion matrix for the PID at the tracking stage for the water configuration.

	True Muon	True Electron	True Proton
Raw Count			
Reconstructed Light Track	1361381	18624	311993
Reconstructed EM	447099	1064310	689316
Reconstructed Heavy Track	370509	25057	535913
Percentages			
Reconstructed Light Track	62.5%	1.7%	20.3%
Reconstructed EM	20.5%	96.1%	44.8%
Reconstructed Heavy Track	17.0%	2.3%	34.9%

as shown in the N-1 plots in Fig. 4.7. Only one data event collected during PØD water configuration and two events collected during PØD air configuration fail this selection criteria. The systematic uncertainty coming from the hit matching selection criterion is therefore negligible.

Track PID

It was already shown in the previous section that setting the hit matching cut to 80 % has a negligible impact on the CCν_e data/MC ratios. However, one needs to keep in mind that only hits associated with a reconstructed track that is classified as electromagnetic track (`kEM`, typically electrons or photons) or other track (`kOther`) are forwarded to the PØDRecon shower stage. All hits associated with a track that is classified as light track (`kLightTrack`, typically muons) or a heavy track (`kHeavyTrack`, typically protons) are not forwarded to the PØDRecon shower stage and cannot be reconstructed as shower. The classification of the reconstructed tracks is based on the PØD PID, therefore differences in the PID for the data and MC might cause systematic uncertainties for the CCν_e data/MC ratios. Those systematic uncertainties are estimated in this section.

Previously a PID study with stopping muons in the PØD has been performed [54], which is described below.

There is a certain efficiency for a particle to be reconstructed as a shower, see Tab. 4.20 and Tab. 4.21. Using the information provided in Tab. 4.20 and Tab. 4.21 as the nominal, the goal is to quantify the difference in the data through a simple map. The map was constructed by looking at a data ample of stopping muon and comparing it to a particle gun of stopping muons. Using each track PID parameter, a map is created between distributions of the Monte Carlo to the data by mapping the values extracted from the same quantile in the Monte Carlo to data. The likelihood is recalculated and a new PID is assigned based on these mapped parameters and shown in Tab. 4.22 and Tab. 4.23.

Table 4.21: A confusion matrix for the PID at the tracking stage for the air configuration.

	True Muon	True Electron	True Proton
Raw Count			
Reconstructed Light Track	403149	8866	102480
Reconstructed EM	253524	496189	371301
Reconstructed Heavy Track	197261	14247	343162
Percentages			
Reconstructed Light Track	47.2%	1.7%	12.5%
Reconstructed EM	29.7%	95.5%	45.5%
Reconstructed Heavy Track	23.1%	2.7%	42.0%

Table 4.22: For the water configuration, the track-by-track rates of the mapped PID.

	True Muon	True Electron	True Proton
Raw Count			
Reconstructed Light Track	1112131	8876	238387
Reconstructed EM	564760	1083166	778480
Reconstructed Heavy Track	502098	15949	520355
Percentages			
Reconstructed Light Track	51.0%	0.08%	15.5%
Reconstructed EM	25.9%	97.8%	50.6%
Reconstructed Heavy Track	23.0%	1.4%	33.8%

Table 4.23: For the air configuration, the track-by-track rates of the mapped PID.

	True Muon	True Electron	True Proton
Raw Count			
Reconstructed Light Track	361716	5129	100355
Reconstructed EM	296773	504353	421055
Reconstructed Heavy Track	195445	9820	295533
Percentages			
Reconstructed Light Track	42.4%	1.0%	12.3%
Reconstructed EM	34.8%	97.1%	51.5%
Reconstructed Heavy Track	22.9%	1.9%	36.2%

Using the information in Tables Tab. 4.22 and Tab. 4.23, the difference between the default and mapped PID can be examined. Looking at events reconstructed as EM tracks, the muon misidentification shows a difference of approximately 5 % between the default and the mapped PID while the electron identification shows a difference of approximately 2 %. It should be pointed out again that the mapping was done with a stopping muon sample and not with electrons since such a control sample does not exist.

To estimate the impact of the track PID uncertainty on the CCν_e data/MC ratios, the MC background and the MC signal of the selected MC events are weighted according to the corresponding uncertainty while the data set is fixed. The systematics are thrown 10,000 times assuming that the water and air samples are uncorrelated and also the signal and background uncertainties are uncorrelated. The analysis chain is then applied to the data set and the weighted MC and the resulting CCν_e data/MC are plotted in a histogram. The obtained distributions are fit with a Gaussian and the resulting sigma is considered to be the systematic uncertainty coming from the track PID. To determine the impact of the background uncertainty caused by the track PID separately, the uncertainty on the signal was set to 0 %. The results are shown in the first columns of Tab. 4.24. The uncertainty for the air configuration is larger than for the water configuration because the purity is higher for the latter. Using a background uncertainty of 5 % and a signal uncertainty of 2 % results in the uncertainties for the CCν_e data/MC ratios shown in the central column of that table. However, using 2 % as uncertainty for signal events requires to assume that the PID mapping derived from muons is equivalent for electrons. A very conservative approach is therefore to assume also a 5 % uncertainty for the signal events. The corresponding results are listed in the right columns of Tab. 4.24 and the corresponding histograms are shown in Fig. 4.28. Those values will be used for the track PID systematic uncertainties.

Table 4.24: Track PID systematic uncertainties for the water (R_{water}), air (R_{air}), and on-water ($R_{\text{on-water}}$) CCν_e data/MC ratios for different uncertainty configurations for signal (sig) and background (bkg) events.

CCν_e Data/MC Ratio	Bkg 5 % — Sig 0 %	Bkg 5 % — Sig 2 %	Bkg 5 % — Sig 5 %
R_{water}	0.01	0.02	0.05
R_{air}	0.03	0.03	0.05
$R_{\text{on-water}}$	0.08	0.08	0.09

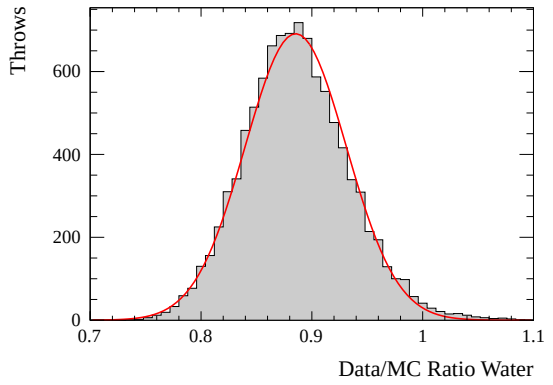

(a) R_{water}

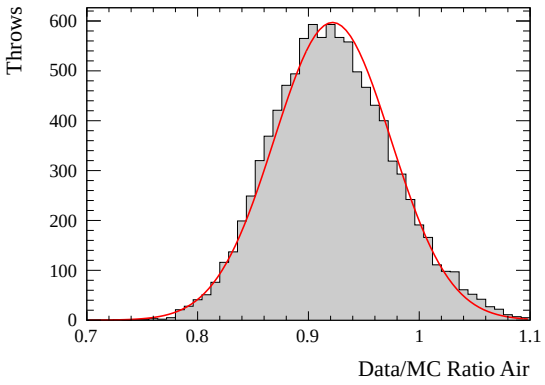

(b) R_{air}

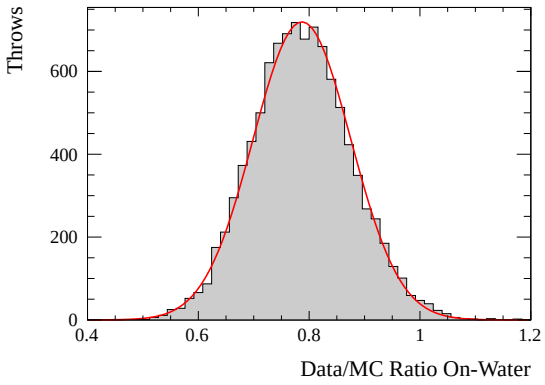

(c) $R_{\text{on-water}}$

Figure 4.28: Data/MC ratios for the water (R_{water}), air (R_{air}), and on-water ($R_{\text{on-water}}$) varied within the Track PID systematic uncertainties. The distributions are fit with a single Gaussian.

Energy Resolution

In Sec. 4.6.2 the maximum possible energy uncertainties due to potential factors of the detector and the software is estimated. In order to get an uncertainties coming from the energy

resolution, the possible broadening of the resolution due to the energy scale uncertainty needs to be calculated. Monte Carlo electron energy resolution is already studied in Sec. 4.2, which gives us 15.5 % for the water and 16.2 % for air configuration. With particle energy uncertainty obtained from Sec. 4.6.2, the energy resolution is broadened to 16.0 % and 16.4 % for the water and air configuration, respectively. The differences in resolutions will be the smearing factors, which are applied to MC with 10,000 Gaussian random throws. Then the data/MC ratio differences and the width of distribution will be the uncertainties coming from the electron energy resolution. The total effect on background-subtracted data/MC ratio is smaller than 0.01 for both water and air configurations, and 0.01 for on-water ratio. Shifted data/MC ratio plots with random throws are shown in Fig. 4.29.

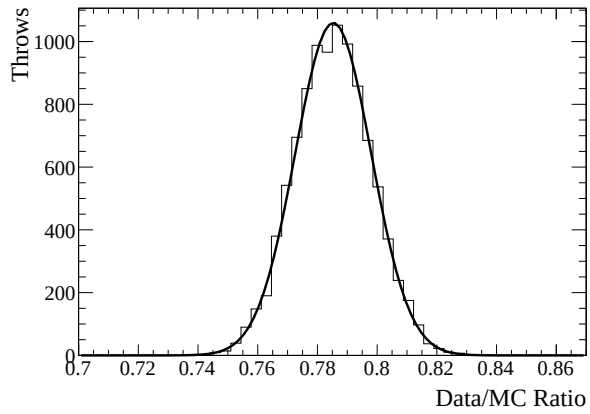

Figure 4.29: On-water Data/MC ratio ($R_{\text{on-water}}$) with energy resolution broadening. The distributions are fit with a single Gaussian.

Angular Resolution

As well as electron energy resolution, angular resolution for selected events is calculated in Sec. 4.2.2. Smearing factors will be the angular resolution itself, applied to MC only with 10,000 Gaussian random throws. The uncertainty will be the shift of the background-subtracted data/MC from the nominal value. The uncertainty of the CCν_e data/MC ratio due to MC angular resolution is smaller than 0.01 for both water and air configurations, and 0.01 for on-water ratio. The shifted on-water data/MC ratio plots after the random throws are shown in Fig. 4.30.

Median Width

Here, the systematic uncertainties coming from the track median width described in Sec. 4.3.5 and the shower median width described in Sec. 4.3.6 are estimated.

To estimate the systematic uncertainty caused by the track median width, the N-1 plots presented in Fig. 4.10 are integrated and a Kolmogorov-Smirnov test is performed to test if the data and the MC event distribution are consistent. The integrated and normalized event

distributions are shown in Fig. 4.31 and the Kolmogorov-Smirnov test returns a p-value of 91.2 % for the water and 92.2 % for air. There are no hints of a shift between the data and MC event distributions or a unknown scaling factor between them. In addition, the event selection cut is at 1 mm and therefore at the beginning of the event distribution. Even if a scaling factor is applied to the MC, it has only little impact on the result. Therefore, it is concluded that the systematic uncertainties of the track median width are negligible for this analysis.

The shower median width cut is placed in a width region with a large number of events. Therefore, a systematic uncertainty on the measured shower median width will have larger impact on the CCν_e data/MC ratios than the track median width uncertainty does. To estimate the systematic uncertainty caused by the shower median width, the N-1 plots

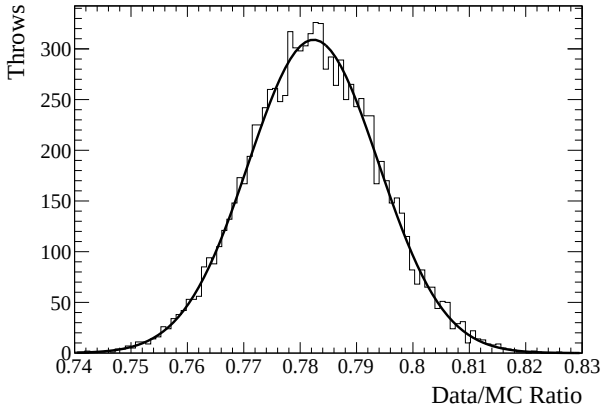

Figure 4.30: On-water Data/MC ratio ($R_{\text{on-water}}$) with angular resolution broadening. The distributions are fit with a single Gaussian.

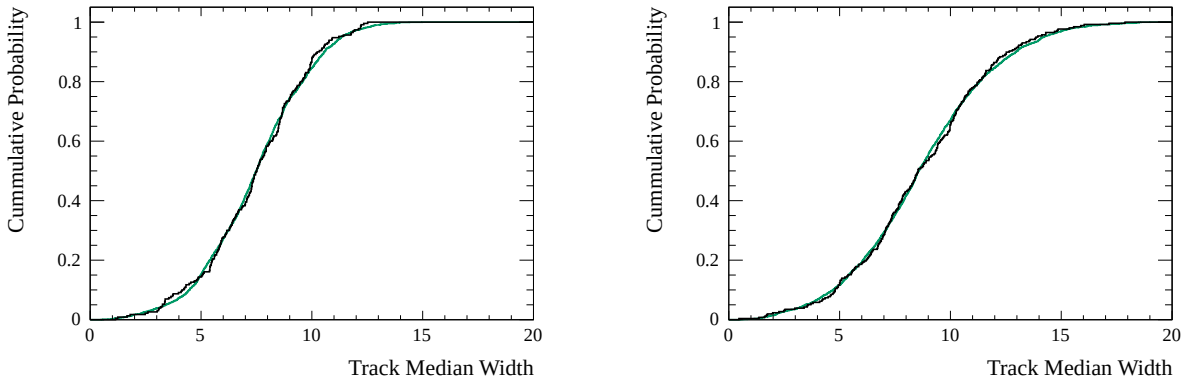

(a) Water Configuration **(b)** Air Configuration

Figure 4.31: The integrated and normalized N-1 plots of the track median width for the water and the air configuration. The data is shown as black solid line while MC is plotted as green solid line.

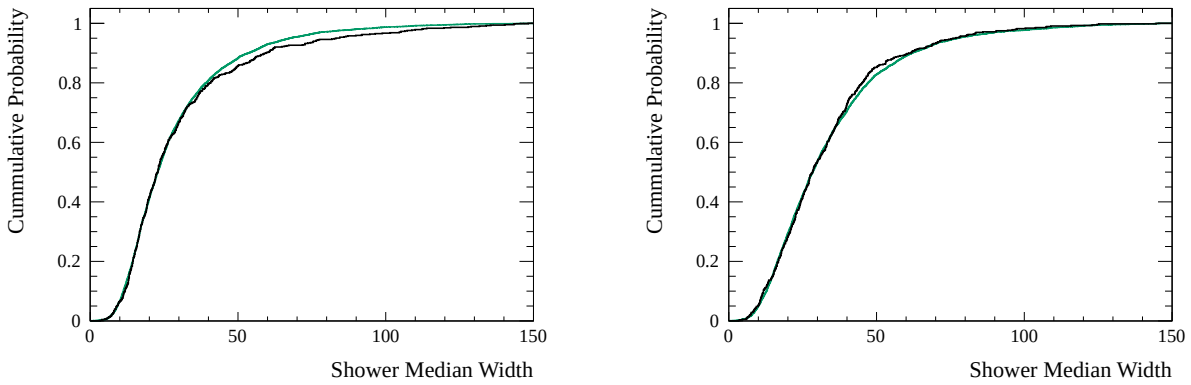

(a) Water Configuration **(b)** Air Configuration

Figure 4.32: The integrated and normalized N-1 plots of the shower median width for the water and the air configuration. Data is shown as black solid line while MC is plotted as green solid line.

presented in Fig. 4.11 are integrated and a Kolmogorov-Smirnov test is performed to test if the data and the MC event distribution are consistent. The integrated and normalized event distributions are shown in Fig. 4.32 and the Kolmogorov-Smirnov test returns a p-value of 50.0 % for the water and 65.9 % for air. The plots show that there might be an indication of a hidden scaling factor applied to MC, i.e. the factor to be applied to the MC median width distribution to obtain the data distribution. but the distributions are still consistent within statistical uncertainties. To determine a reasonable scaling factor range, different scaling factors from 0.9 to 1.1 were applied to MC and the resulting p-values were plotted. Placing a line at 68 % of the p-value peak height results in a scaling factor range from 0.98 to 1.02.

The systematic effect on the CCν_e data/MC ratios for the water (R_{water}), air (R_{air}), and on-water ($R_{\text{on-water}}$) coming from the shower median width are estimated by varying the scaling factor that is applied to the MC shower median width according to the previously mentioned uncertainty. The scaling factor is thrown 10,000 times assuming that the scaling factors for the water and the air configuration are uncorrelated. Then, the PØD ν_e analysis is applied to the nominal data set and the modified MC set for each throw. The CCν_e data/MC ratios R_{water}, R_{air}, and $R_{\text{on-water}}$ are calculated, and plotted in a histogram. The obtained distributions are shown in Fig. 4.33 and they are fit with a Gaussian. The fitted widths for each distribution are presented in Tab. 4.25 and are considered to be the systematic uncertainty coming from the shower median width.

Shower Charge Fraction

To estimate the possible impact of systematic effects of the shower charge fraction on the PØD ν_e analysis, the event distributions of the shower median width sideband (events passing all cuts but fail the shower median width cut) are analyzed. The distributions of the data and MC events as a function of the shower charge fraction are shown in Fig. 4.34. In order to find the best fit between the data and MC event distributions, different shower charge fraction scaling factors are applied to the MC events where a shower charge fraction of 1.0

is defined to be the reference point. With a Kolmogorov-Smirnov test, it was found that the shape agreement between the data and MC is maximized when applying a scaling factor of 1.03 to the water MC events and 1.05 to the air MC events. The systematic effect on the

Table 4.25: Shower median width uncertainties for the water (R_{water}), air (R_{air}), and on-water ($R_{\text{on-water}}$) CCν_e data/MC ratios.

CCν_e Data/MC Ratio	Uncertainty
R_{water}	0.04
R_{air}	0.04
$R_{\text{on-water}}$	0.08

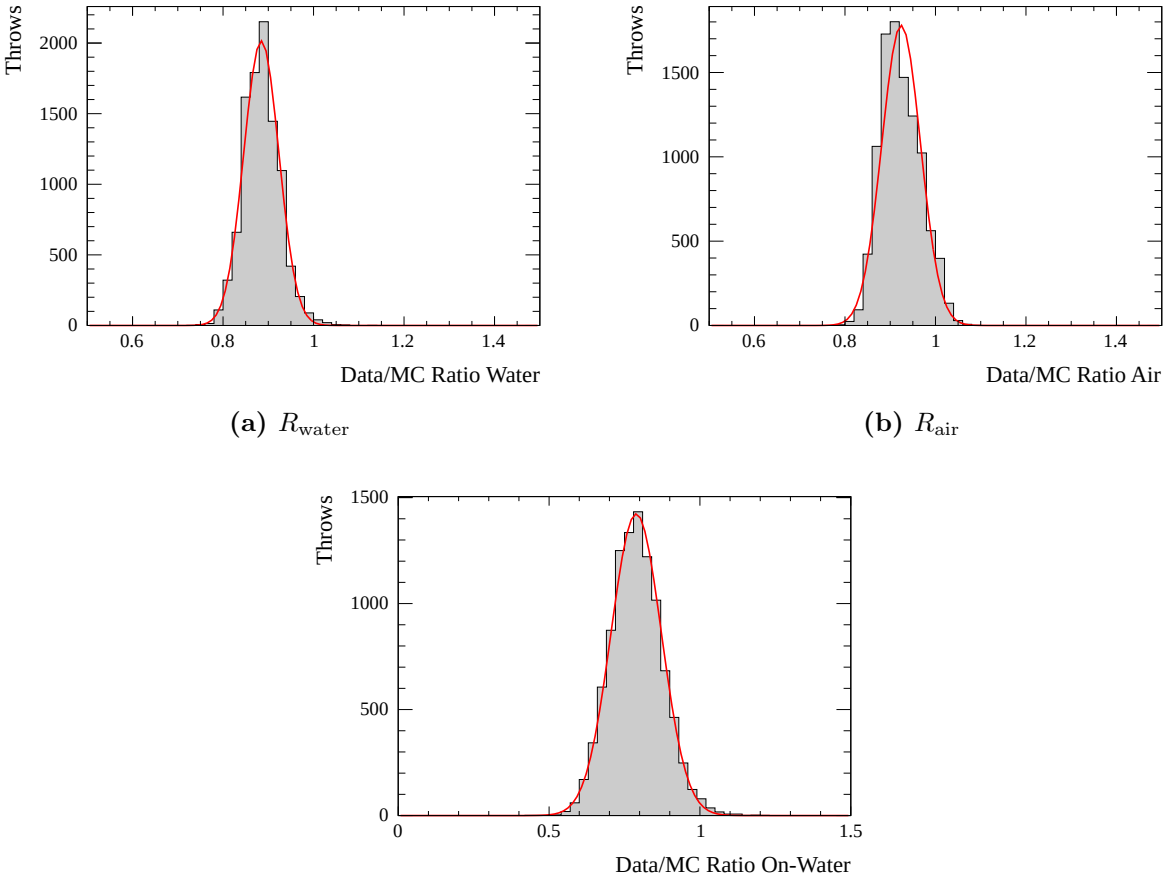

(a) R_{water} **(b)** R_{air}

(c) $R_{\text{on-water}}$

Figure 4.33: Data/MC ratios for the water (R_{water}), air (R_{air}), and on-water ($R_{\text{on-water}}$) varied within the shower median width systematic uncertainties. The distributions are fit with a single Gaussian.

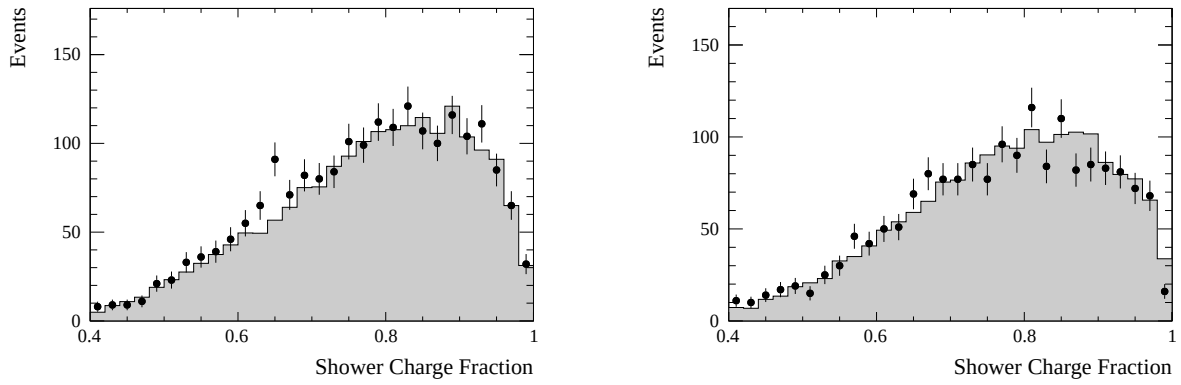

(a) Water Configuration **(b)** Air Configuration

Figure 4.34: Data and MC events in the shower median width sideband are shown as a function of the shower charge fraction. Data events are plotted as black points while the POT-normalized MC events are shown as filled histograms. Events with a shower charge fraction of 1.0 are not shown in these plots.

Table 4.26: Shower charge fraction uncertainties for the water (R_{water}), air (R_{air}), and on-water ($R_{\text{on-water}}$) CCν_e data/MC ratios.

CCν_e Data/MC Ratio	Uncertainty
R_{water}	0.01
R_{air}	0.04
$R_{\text{on-water}}$	0.04

CCν_e data/MC ratios for the water (R_{water}), air (R_{air}), and on-water ($R_{\text{on-water}}$) coming from the shower charge fraction scaling factors are estimated by varying the scaling factor that is applied to the MC according to the uncertainty mentioned before. The scaling factor is thrown 10,000 times assuming that the scaling factors for the water and the air configuration are uncorrelated. The obtained ratios are fitted with a Gaussian and the width is considered to be the systematic uncertainty which results in a uncertainty of 0.01, 0.04, and 0.04 for the water, air, and on-water, respectively. The obtained distributions for the CCν_e data/MC ratios are shown in Fig. 4.35 and the fitted widths, i.e. the uncertainties, are presented in Tab. 4.26.

4.6.4 Flux and Cross Section Systematic Uncertainties

For the inclusion of the flux and cross section systematic uncertainties in the PØD ν_e analysis, the T2KReWeight framework is used. T2KReWeight package provides reweighting values according to the uncertainties of the flux and cross section parameters which are correlated

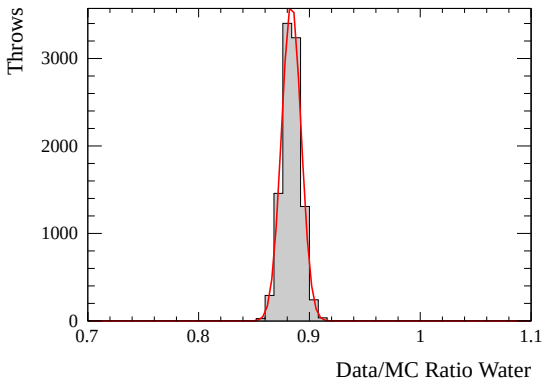

(a) R_{water}

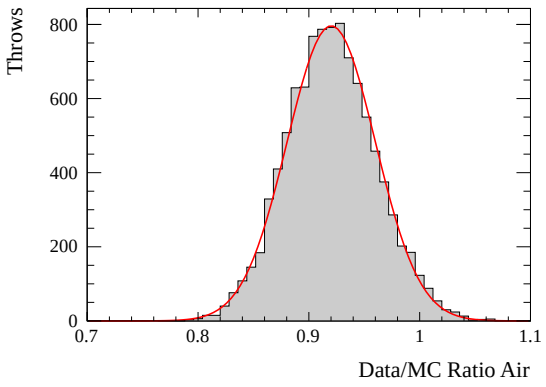

(b) R_{air}

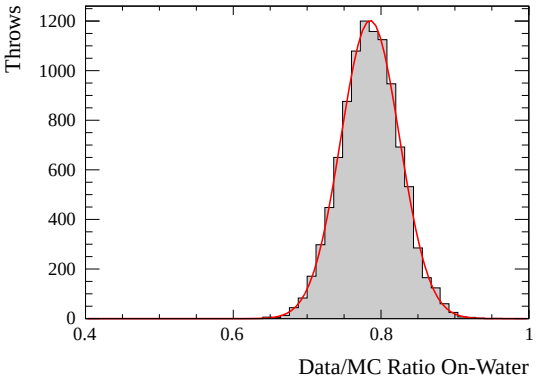

(c) $R_{\text{on-water}}$

Figure 4.35: Data/MC ratios for the water (R_{water}), air (R_{air}), and on-water ($R_{\text{on-water}}$) varied within the shower charge fraction systematic uncertainties. The data/MC ratios obtained are shown. The distributions are fit with a single Gaussian.

among each other, and reweights each analyzed MC event accordingly.

The parameter values and uncertainties are provided by different external measurements such as NA61 and the Neutrino Interaction Working Group (NIWG). Those parameters are used as input for the BANFF (Beam And Nd280 Flux measurement task Force) fit. The ν_e and ν_μ come from the same pion to muon to electron decay chain, and lepton universality allows the expected rate of ν_e to be constrained by measuring the much larger flux of ν_μ. Details concerning the T2K beam flux measurement by BANFF, and further information on recent measurements of ν_μ interactions in the near detectors, can be found in Ref. [55].

For this analysis, the newest version of the BANFF output file among 2013 oscillation analysis, is used. This file contains the values and the covariance matrix of all parameters before and after the BANFF fit. In total, there are 46 parameters included in the PØD ν_e analysis [56]:

- 25 flux parameters

- 6 final state interaction parameters
- 2 NEUT parameters
- 13 NIWG parameters

The flux systematic parameters reweight each MC event depending on it's neutrino flavor and it's true neutrino energy. In the 2013 T2K oscillation analyses there are 11 parameters re-weighting the ν_μ-flux, 5 parameters re-weighting the $\bar{\nu}_\mu$-flux, 7 parameters reweighting the ν_e-flux, and 2 parameters re-weighting the $\bar{\nu}_e$-flux, i.e. in total 25 flux parameters. Each parameter corresponds to a true neutrino energy bin as shown in Tab. 4.27. The BANFF pre-fit parameters and the corresponding uncertainties are extracted from external measurements like NA61 and other hadronic production measurements. Those parameters are then fitted to ND280 data resulting in the BANFF post-fit parameters and uncertainties. The flux systematic parameters cannot be negative physically, therefore only the positive region is allowed. The flux systematic parameters and their uncertainties are summarized in Tab. 4.28, the covariance matrix is shown in Fig. 4.36, and the BANFF pre/post-fit uncertainties are shown in Fig. 4.37. This plot clearly shows, that the BANFF post-fit uncertainties are smaller than the pre-fit uncertainties.

The BANFF pre- and post-fit cross section systematics, including 6 FSI parameters, 2 NEUT parameters, and 13 NIWG parameters, are summarized in Tab. 4.29, the covariance matrix is shown in Fig. 4.36, and the BANFF pre/post-fit uncertainties are shown in Fig. 4.37. The re-weighting factors for CCQE and CC1π neutrino interactions depend on the true neutrino energy. The energy binning for those interactions is shown in Tab. 4.29.

All the flux and cross section systematic parameters mentioned before re-weight each MC event depending on its interaction and neutrino energy resulting in four possible MC configurations:

- Raw MC: Output of the ND280 reprocessing based on 11a neutrino fluxes.
- Flux Re-Weighted MC: Raw MC re-weighted with 11b-v3.2 neutrino fluxes (if not stated otherwise, this MC configuration is used for the results and plots shown in this note).

Table 4.27: True neutrino energy binning for the ν_μ, $\bar{\nu}_\mu$, ν_e, and $\bar{\nu}_e$ flux systematic parameters used for the 2013 T2K oscillation analyses.

Flavor	Bins	True Neutrino Energy Binning (GeV)
ν_μ	11	0 - 0.4 - 0.5 - 0.6 - 0.7 - 1.0 -1.5 - 2.5 - 3.5 - 5.0 - 7.0 - 30.0
$\bar{\nu}_\mu$	5	0 - 0.7 - 1.0 - 1.5 - 2.5 - 30.0
ν_e	7	0 - 0.5 - 0.7 - 0.8 - 1.5 - 2.5 - 4.0 - 30.0
$\bar{\nu}_e$	2	0 - 2.5 - 30.0

Table 4.28: Systematic flux parameters for the ν_μ, $\bar{\nu}_\mu$, ν_e, and $\bar{\nu}_e$ flux used for the 2013 T2K oscillation analyses.The table shows the parameter names, their indices, the BANFF pre-fit parameter values and uncertainties, and the corresponding BANFF post-fit values.

Parameter	Index	BANFF Pre-Fit	BANFF Post-Fit
ν_μ-flux E0	0	1.000 ± 0.122	1.027 ± 0.085
ν_μ-flux E1	1	1.000 ± 0.128	1.012 ± 0.086
ν_μ-flux E2	2	1.000 ± 0.120	0.994 ± 0.079
ν_μ-flux E3	3	1.000 ± 0.118	0.965 ± 0.078
ν_μ-flux E4	4	1.000 ± 0.124	0.934 ± 0.081
ν_μ-flux E5	5	1.000 ± 0.121	0.972 ± 0.079
ν_μ-flux E6	6	1.000 ± 0.102	1.027 ± 0.069
ν_μ-flux E7	7	1.000 ± 0.100	1.059 ± 0.071
ν_μ-flux E8	8	1.000 ± 0.107	1.039 ± 0.068
ν_μ-flux E9	9	1.000 ± 0.147	0.980 ± 0.073
ν_μ-flux E10	10	1.000 ± 0.196	0.960 ± 0.076
$\bar{\nu}_\mu$-flux E0	11	1.000 ± 0.145	1.030 ± 0.114
$\bar{\nu}_\mu$-flux E1	12	1.000 ± 0.126	1.010 ± 0.098
$\bar{\nu}_\mu$-flux E2	13	1.000 ± 0.115	0.997 ± 0.094
$\bar{\nu}_\mu$-flux E3	14	1.000 ± 0.115	1.015 ± 0.096
$\bar{\nu}_\mu$-flux E4	15	1.000 ± 0.161	1.039 ± 0.140
ν_e-flux E0	16	1.000 ± 0.124	1.024 ± 0.094
ν_e-flux E1	17	1.000 ± 0.135	1.020 ± 0.096
ν_e-flux E2	18	1.000 ± 0.138	0.988 ± 0.107
ν_e-flux E3	19	1.000 ± 0.109	0.995 ± 0.078
ν_e-flux E4	20	1.000 ± 0.109	1.015 ± 0.075
ν_e-flux E5	21	1.000 ± 0.121	0.997 ± 0.066
ν_e-flux E6	22	1.000 ± 0.167	0.947 ± 0.075
$\bar{\nu}_e$-flux E0	23	1.000 ± 0.182	1.014 ± 0.167
$\bar{\nu}_e$-flux E1	24	1.000 ± 0.139	0.953 ± 0.078

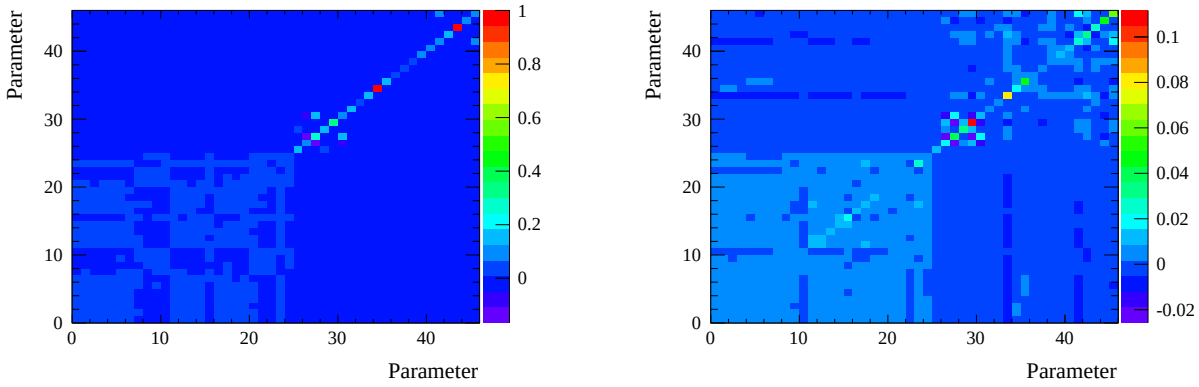

(a) BANFF Pre-Fit Covariance

(b) BANFF Post-Fit Covariance

Figure 4.36: BANFF pre- and post-fit covariance matrix of the flux and cross section systematic parameters used in this analysis (ν_μ-flux (0-10), $\bar{\nu}_\mu$-flux (11-15), ν_e-flux (16-22), $\bar{\nu}_e$-flux (23-24), FSI (25-30), NEUT (31-32), NIWG (33-45)).

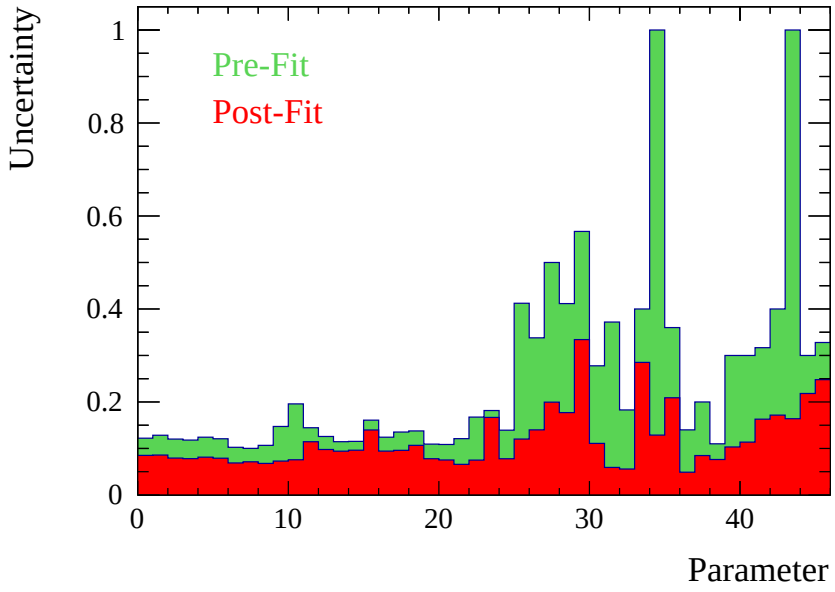

Figure 4.37: BANFF pre- and post-fit uncertainties of the flux and cross section systematic parameters used in this analysis (ν_μ-flux (0-10), $\bar{\nu}_\mu$-flux (11-15), ν_e-flux (16-22), $\bar{\nu}_e$-flux (23-24), FSI (25-30), NEUT (31-32), NIWG (33-45)). To demonstrate that the BANFF post-fit uncertainties are smaller than the pre-fit uncertainties, the histograms are not stack.

- BANFF Pre-Fit Re-Weighted MC: BANFF pre-fit flux and cross section systematic parameters applied to the flux re-weighted MC, i.e. this MC configuration is based on the work of the NIWG on the MiniBooNE data.

Table 4.29: Systematic cross section parameters used for the 2013 T2K oscillation analyses.The table shows the parameter names, their indices, the BANFF pre-fit parameter values and uncertainties, and the corresponding BANFF post-fit values.

Parameter	Index	BANFF Pre-Fit	BANFF Post-Fit
FSI Inel. Low	25	0.000 ± 0.412	0.118 ± 0.120
FSI Inel. High	26	0.000 ± 0.338	0.445 ± 0.140
FSI π Prod.	27	0.000 ± 0.500	-0.685 ± 0.200
FSI π Abs.	28	0.000 ± 0.412	-0.270 ± 0.177
FSI CEX Low	29	0.000 ± 0.567	0.360 ± 0.334
FSI CEX High	30	0.000 ± 0.278	-0.381 ± 0.111
M_A^{QE}	31	1.000 ± 0.372	1.025 ± 0.059
M_A^{RES}	32	1.163 ± 0.183	0.797 ± 0.056
CC Other Shape	33	0.000 ± 0.400	0.225 ± 0.285
Spectral Function	34	0.000 ± 1.000	0.240 ± 0.129
E_b	35	1.000 ± 0.360	1.236 ± 0.209
P_F	36	1.000 ± 0.140	1.227 ± 0.049
π-less Δ decay	37	0.000 ± 0.200	0.006 ± 0.085
CCQE E0	38	1.000 ± 0.110	0.966 ± 0.076
CCQE E1	39	1.000 ± 0.300	0.931 ± 0.103
CCQE E2	40	1.000 ± 0.300	0.852 ± 0.114
CC1π E0	41	1.154 ± 0.317	1.265 ± 0.163
CC1π E1	42	1.000 ± 0.400	1.122 ± 0.172
CC Coherent	43	1.000 ± 1.000	0.449 ± 0.164
NC Other	44	1.000 ± 0.300	1.410 ± 0.218
NC1π^0	45	0.963 ± 0.328	1.135 ± 0.248

Table 4.30: True neutrino energy binning for the CCQE and CC1π cross section systematic parameters used for the 2013 T2K oscillation analyses.

Interaction	Bins	True Neutrino Energy Binning (GeV)
CCQE	3	0 - 1.5 - 3.5 - 30.0
CC1π	2	0 - 2.5 - 30.0

- BANFF Post-Fit Re-Weighted MC: BANFF post-fit flux and cross section systematic parameters applied to the flux re-weighted MC, i.e. this MC configuration contains the current knowledge about T2K.

Applying the PØD ν_e analysis described in Sec. 4.5 to the flux re-weighted MC results in a measurement of the intrinsic ν_e beam and the on-water cross section that is independent of the NIWG and BANFF results while applying it to the BANFF post-fit re-weighted MC shows if the PØD ν_e measurement is consistent with other T2K measurements.

Figure 4.38 shows the selected data events as a function of the reconstructed neutrino energy for the PØD water and air configuration. In addition, the selected MC events are shown for flux, BANFF pre-fit, and BANFF post-fit re-weighting where all MC sets are POT-normalized. Figure 4.39 and Fig. 4.40 are the plots for the reconstructed particle energy and angle, respectively. The plots show that applying the BANFF pre- or post-fit parameters has only little impact on the selected MC shape. The number of MC events normalized to the data POT for flux, BANFF pre-fit, and BANFF post-fit re-weighting are listed in Tab. 4.31 for the event selection.

To obtain the flux and cross section systematic uncertainties for the water, air, and on-water CCν_e data/MC ratios, the T2KReWeight framework and the 2013 BANFF pre- and post-fit covariance matrices are used. The systematic parameters are thrown 1000 times according to the covariance matrix and the PØD ν_e analysis described in Sec. 4.5 is then applied to each throw. This procedure is done twice, namely first using the BANFF pre-fit covariance matrix and second using the BANFF post-fit covariance matrix. Figure 4.41 shows the selected number of signal and background events varied within the BANFF pre- and post-fit flux and cross section systematic uncertainties for both the water and air configuration. The CCν_e data/MC ratio distributions for the water (R_{water}), air (R_{air}), and on-water ($R_{\text{on-water}}$) obtained are shown in Fig. 4.42. The distributions are fit with single Gaussians and the resulting sigma is considered to be the flux and cross section systematic

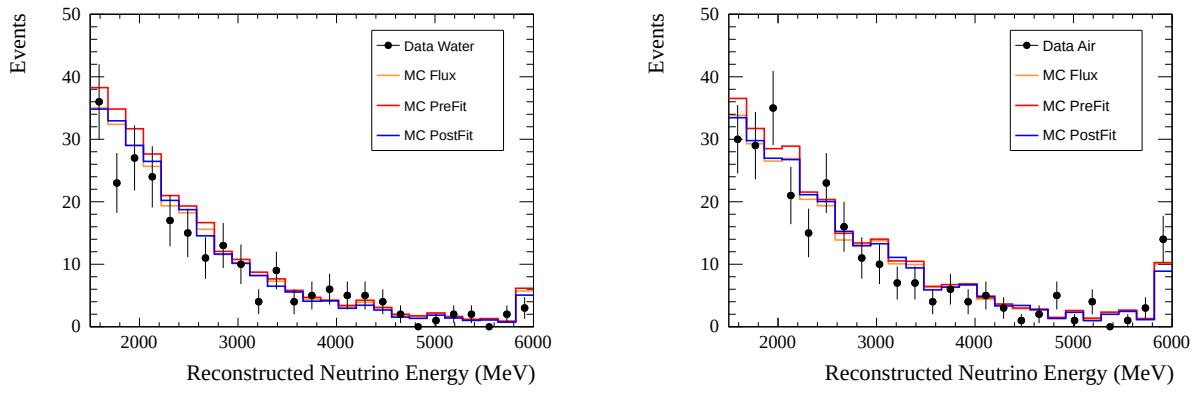

(a) Water Configuration **(b)** Air Configuration

Figure 4.38: Selected data events as a function of the reconstructed neutrino energy. In addition, the selected MC events are shown for flux, BANFF pre-fit, and BANFF post-fit re-weighting. The MC sets are POT-normalized.

uncertainties for the PØD ν_e analysis. The results for all data/MC ratios and for all analysis methods are shown in Tab. 4.32. As expected, the plots and numbers clearly show that the flux and cross section systematic uncertainties are significantly smaller if the BANFF post-fit parameter values are used. In addition, the numbers also show that the uncertainty for the PØD water configuration is better than the one for the PØD air configuration which is a consequence of the more pure selected event sample.

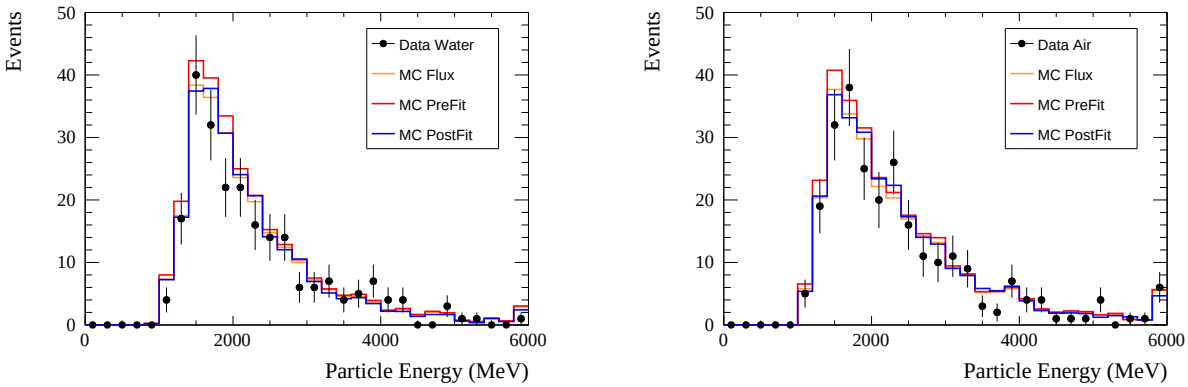

(a) Water Configuration **(b)** Air Configuration

Figure 4.39: Selected data events as a function of the reconstructed particle energy. In addition, the selected MC events are shown for flux, BANFF pre-fit, and BANFF post-fit re-weighting. The MC sets are POT-normalized.

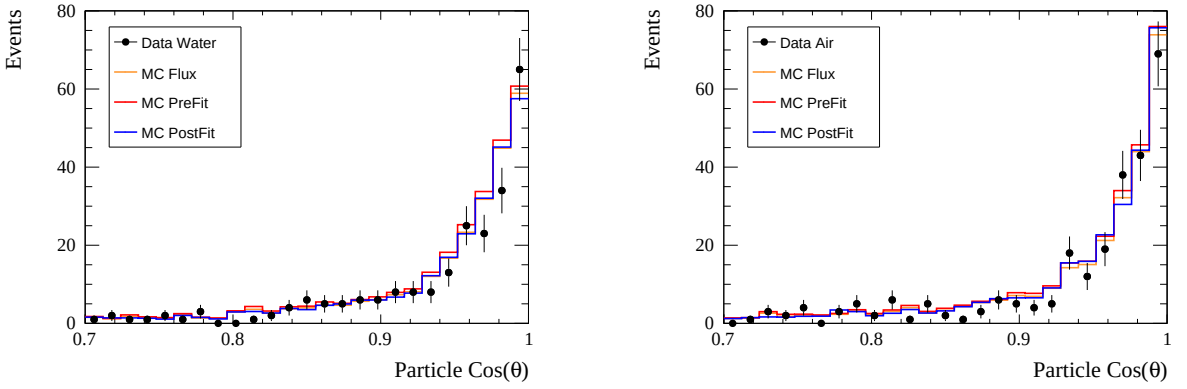

(a) Water Configuration **(b)** Air Configuration

Figure 4.40: Selected data events as a function of the reconstructed particle direction. In addition, the selected MC events are shown for flux, BANFF pre-fit, and BANFF post-fit re-weighting. The MC sets are POT-normalized.

Table 4.31: The selected number of MC signal events S, MC background events B, and the total number of selected MC events $S+B$ normalized to the data POT for the water and air configuration are listed for flux, BANFF pre-fit, and BANFF post-fit re-weighting.

	Re-Weighting	MC Total $S+B$	MC Signal S	MC Background B
Water	Flux	252.8	196.1	56.7
	Pre-Fit	271.3	208.8	62.5
	Post-Fit	250.0	182.9	67.2
Air	Flux	271.0	173.6	97.4
	Pre-Fit	287.1	182.3	104.7
	Post-Fit	272.5	158.7	113.7

Table 4.32: Flux and cross section systematic uncertainties for the water (R_{water}), air (R_{air}), and on-water ($R_{\text{on-water}}$) CCν_e data/MC ratios.

CCν_e Data/MC Ratio	BANFF Pre-Fit	BANFF Post-Fit
R_{water}	0.22	0.07
R_{air}	0.26	0.09
$R_{\text{on-water}}$	0.17	0.06

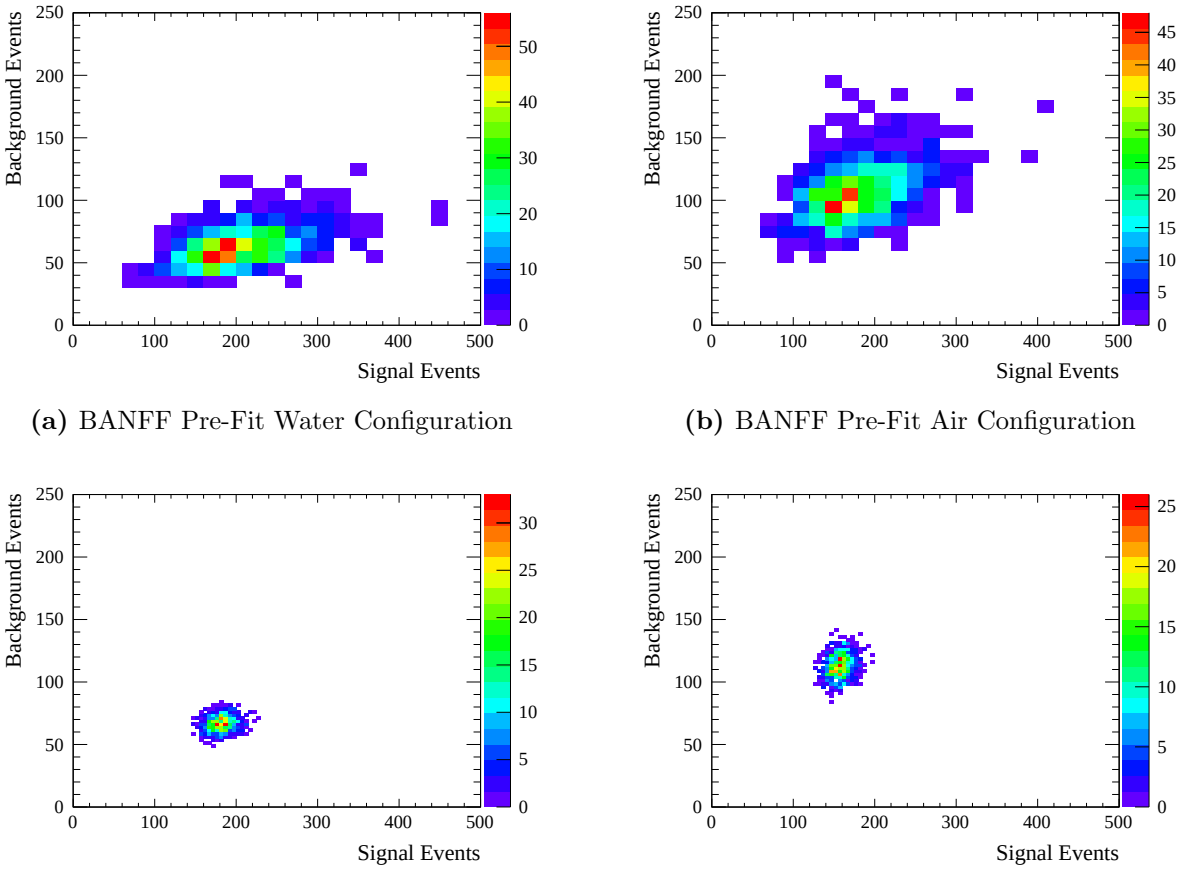

(a) BANFF Pre-Fit Water Configuration

(b) BANFF Pre-Fit Air Configuration

(c) BANFF Post-Fit Water Configuration

(d) BANFF Post-Fit Air Configuration

Figure 4.41: Selected number of signal vs background events varied within the BANFF pre- and post-fit flux and cross section systematic uncertainties for the PØD water and air configuration.

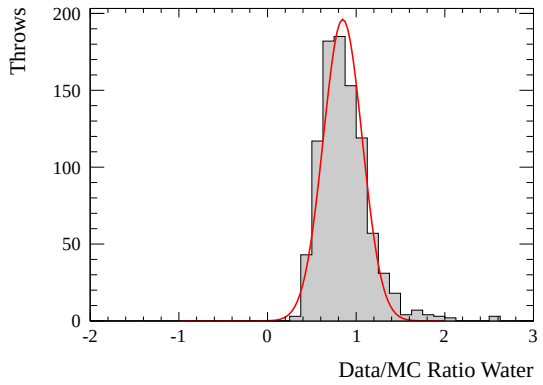

(a) R_{water} BANFF Pre-Fit

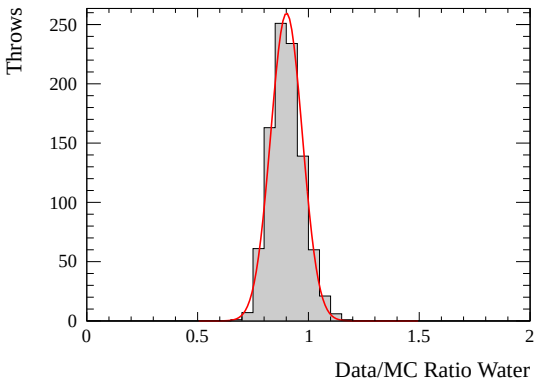

(b) R_{water} BANFF Post-Fit

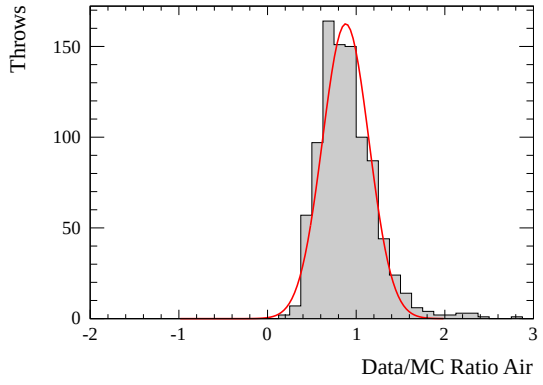

(c) R_{air} BANFF Pre-Fit

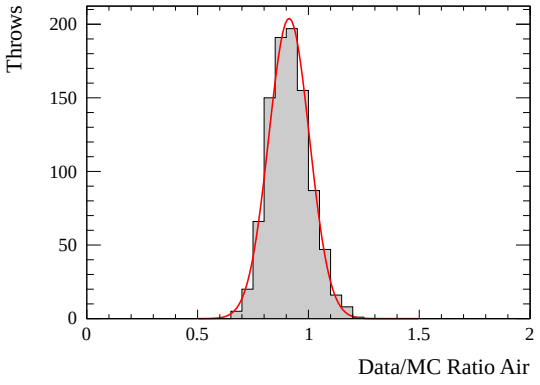

(d) R_{air} BANFF Post-Fit

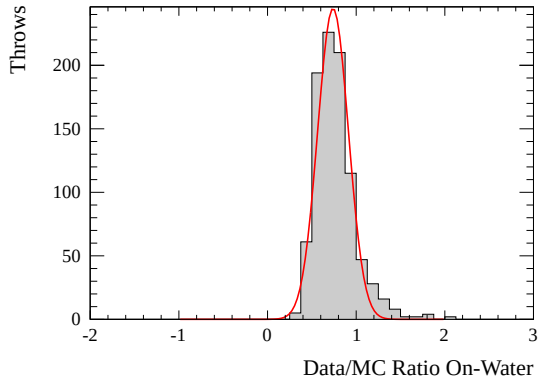

(e) $R_{\text{on-water}}$ BANFF Pre-Fit

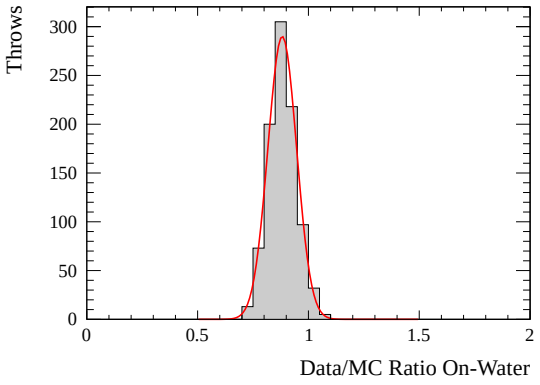

(f) $R_{\text{on-water}}$ BANFF Post-Fit

Figure 4.42: Data/MC ratios for the water (R_{water}), air (R_{air}), and on-water ($R_{\text{on-water}}$) varied within the BANFF pre- and post-fit flux and cross section systematic uncertainties. The distributions are fit with a single Gaussian.

4.6.5 Systematics Summary

All systematic uncertainties on the CCν_e data/MC ratios for the water (R_{water}), air (R_{air}), and on-water ($R_{\text{on-water}}$) that were estimated in the previous sections are summarized in Tab. 4.33. In addition, the tables show the total systematic uncertainty.

Table 4.33: Summary of systematic uncertainties on the CCν_e data/MC ratios for the water (R_{water}), air (R_{air}), and on-water ($R_{\text{on-water}}$)

Systematic Uncertainty for CCν_e Data/MC Ratio	R_{water}	R_{air}	$R_{\text{on-water}}$
MC Statistics	0.03	0.04	0.12
Bias Analysis Method	0.00	0.00	0.02
PØD Mass	0.01	0.01	0.01
PØD Fiducial Volume	< 0.01	< 0.01	< 0.01
PØD Alignment	< 0.01	< 0.01	< 0.01
Energy Scale	0.05	0.05	0.10
Hit Matching	< 0.01	< 0.01	< 0.01
Track PID	0.05	0.05	0.09
Energy Resolution	< 0.01	< 0.01	0.01
Angular Resolution	< 0.01	< 0.01	0.01
Track Median Width	< 0.01	< 0.01	< 0.01
Shower Median Width	0.04	0.04	0.08
Shower Charge Fraction	0.01	0.04	0.04
Flux and Cross Sections Pre-Fit	0.22	0.26	0.17
Flux and Cross Sections Post-Fit	0.07	0.09	0.06
Total with Pre-Fit	0.24	0.28	0.27
Total with Post-Fit	0.11	0.13	0.21

4.7 Result

Applying the event selection that was developed for the PØD ν_e analysis to the full Run 1 to Run 4 data results in 230 selected data events during the PØD water configuration and 257 selected data events during the PØD air configuration. The analysis described in Sec. 4.5 to obtain the background subtracted CCν_e data/MC ratios for the water (R_{water}), air (R_{air}), and on-water ($R_{\text{on-water}}$) events was performed.

Our primary result of the analysis uses the BANFF post-fit weighted MC. The back-

ground subtracted data/MC ratio R is:

$$R_{\text{water}} = 0.89 \pm 0.08 \text{ (stat.)} \pm 0.11 \text{ (sys.)} \tag{4.16}$$
$$R_{\text{air}} = 0.90 \pm 0.09 \text{ (stat.)} \pm 0.13 \text{ (sys.)} \tag{4.17}$$
$$R_{\text{on-water}} = 0.87 \pm 0.33 \text{ (stat.)} \pm 0.21 \text{ (sys.)} \tag{4.18}$$

The distribution of selected events for the reconstructed particle energy, angle, and the neutrino energy are shown in Fig. 4.43.

For the cross check and future reference, the results using differently weighted MC are presented.

Using the flux weighted MC results in:

$$R_{\text{water}} = 0.88 \pm 0.08 \text{ (stat.)} \pm 0.24 \text{ (sys.)} \tag{4.19}$$
$$R_{\text{air}} = 0.92 \pm 0.09 \text{ (stat.)} \pm 0.28 \text{ (sys.)} \tag{4.20}$$
$$R_{\text{on-water}} = 0.79 \pm 0.33 \text{ (stat.)} \pm 0.27 \text{ (sys.)} \tag{4.21}$$

Using the BANFF pre-fit weighted MC results in:

$$R_{\text{water}} = 0.80 \pm 0.08 \text{ (stat.)} \pm 0.23 \text{ (sys.)} \tag{4.22}$$
$$R_{\text{air}} = 0.84 \pm 0.09 \text{ (stat.)} \pm 0.28 \text{ (sys.)} \tag{4.23}$$
$$R_{\text{on-water}} = 0.71 \pm 0.33 \text{ (stat.)} \pm 0.27 \text{ (sys.)} \tag{4.24}$$

This result is published in *Phys. Rev. D* [57], and the script of the paper can be found in Appendix A.

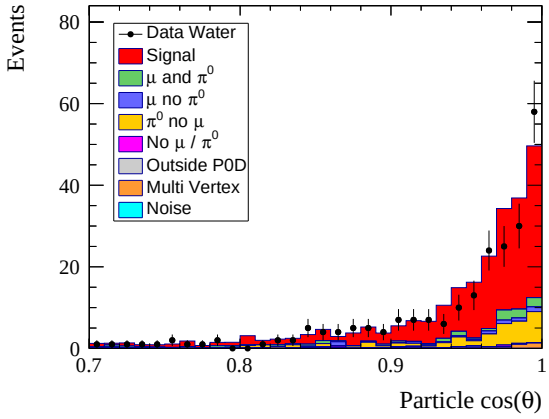

(a) Water Configuration Particle Direction

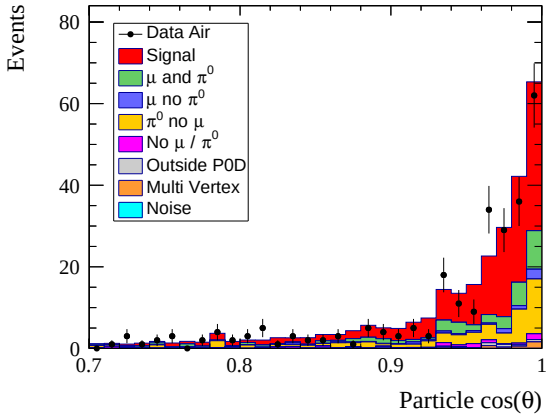

(b) Air Configuration Particle Direction

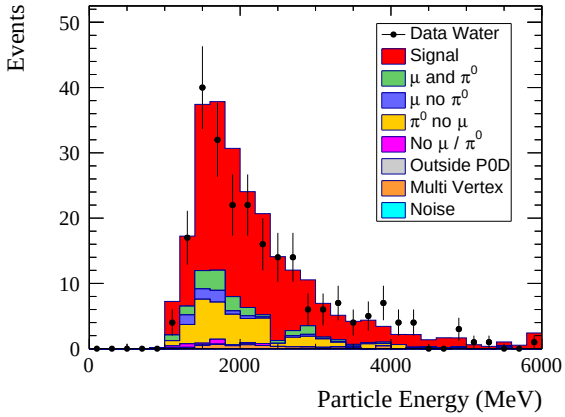

(c) Water Configuration Particle Energy

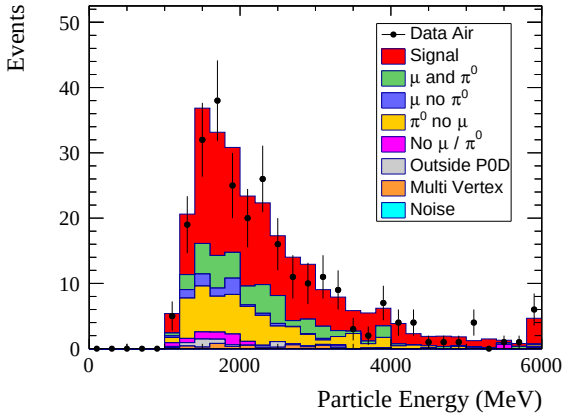

(d) Air Configuration Particle Energy

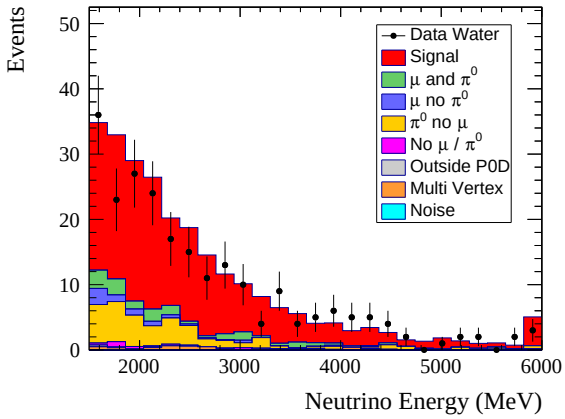

(e) Water Configuration Neutrino Energy

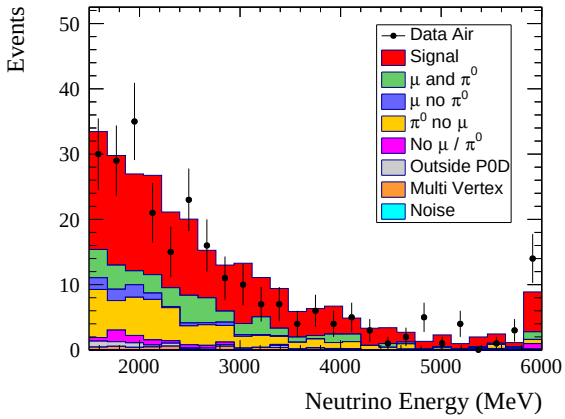

(f) Air Configuration Neutrino Energy

Figure 4.43: Events passing the event selection as a function of the particle direction, particle energy and the neutrino energy for the water and air configuration. The MC events are normalized to the data POT, and with BANFF post-fit.

Chapter 5

CCν_e Interaction Rate Measurement

The limitation of the previous high energy ν_e analysis (Chap.4) is the existence of the energy threshold. To provide useful physics information outside T2K as well as to measure cross section of ν_e on water, a study on ν_e interaction rate in all energy spectrum is required.

The analysis uses the same data sets as the previous high energy analysis, but the software has been updated with better reconstruction algorithm. Without the energy threshold and therefore with large low energy background events introduced, new sets of selection criteria are applied and optimized.

5.1 Analysis Overview

The data sets used in this analysis is same as the previous analysis, the full data collected between Jan. 2010 and May. 2013 except for small Run 3 data. The summary of the data POT is shown in Tab.2.1. The MC POT corresponds to ten times the data POT.

The software has been updated from the previous analysis (ND280 Software Production5G v10r11) to improved version (Production6B v11r13). The change in the PØD aspect is mainly improvements of the shower reconstruction. We also use a newer version of neutrino generator, NEUT, version 5.3.2.

The event type definition is the same as before, refer to Sec. 4.1. Also the new neutrino flux reweighting is applied in this analysis (version 13a-v1.1).

5.2 Reconstruction Resolution

The general description of the reconstruction algorithm of the PØDRecon is given in Sec. 3.3. In this section, the vertex and the energy resolution of the analysis is studied. The method is the same as Chap. 4, but some differences in the resolution are expected as the software and the event selection has changed.

5.2.1 Vertex Resolution

The MC reconstruction resolutions of the vertex position are obtained by selecting MC events passing all selection cuts described later in Sec. 5.3 and comparing the true vertex position with the reconstructed vertex position. The distributions obtained with the track PØDRecon information are shown in Fig. 5.1 together with the 16 % and 84 % quantiles.

The MC reconstruction resolution is found by taking half the distance from the 16 % and 84 % quantiles which is equivalent to 1σ of a Gaussian fit. The resolutions obtained from both the track and shower reconstruction stage are summarized in Tab. 4.1. The table shows that the vertex position resolution obtained by using track reconstruction information is slightly better compared to the resolutions obtained by using shower stage information. As a consequence, the vertex information coming from the track reconstruction is used for vertex related selection criteria (described in Sec. 5.3). Compared to the high energy ν_e analysis vertex resolution (Sec. 4.2), no significant change can be observed.

Table 5.1: MC resolutions for the vertex position reconstruction if using vertex reconstruction information from the track stage. The tables show the shift (obtained from the median value) and the resolutions (obtained from the 16 % and 84 % quantiles) for all three dimensions and for the PØD configurations water and air.

(a) Vertex Resolutions with Track Stage Information

	Vertex Position X (cm)		Vertex Position Y (cm)		Vertex Position Z (cm)	
	Shift	Resolution	Shift	Resolution	Shift	Resolution
Water	0.0	1.7	0.0	1.8	-0.5	3.4
Air	0.0	2.2	0.0	2.1	0.1	3.5

(b) Vertex Resolutions with Shower Stage Information

	Vertex Position X (cm)		Vertex Position Y (cm)		Vertex Position Z (cm)	
	Shift	Resolution	Shift	Resolution	Shift	Resolution
Water	0.0	2.7	0.0	2.8	0.0	4.7
Air	0.1	3.4	0.0	3.3	0.4	5.2

5.2.2 Energy Resolution

In addition to the vertex position resolution, the MC reconstruction resolutions for electron are examined. For that purpose, MC signal events that pass all selection criteria described in Sec. 5.3 are studied.

The reconstructed neutrino energy is calculated from the reconstructed electron energy E_e and the reconstructed electron angle θ_e using the quasi-elastic approximation.

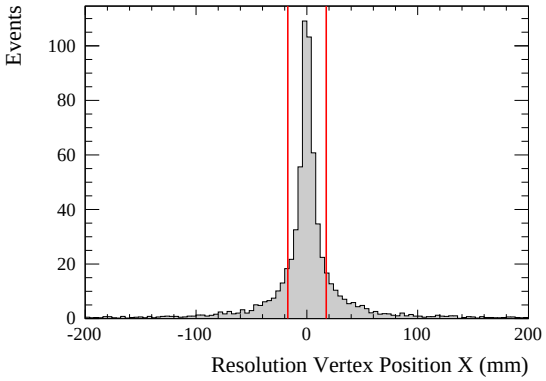

(a) Vertex Position X Water Configuration

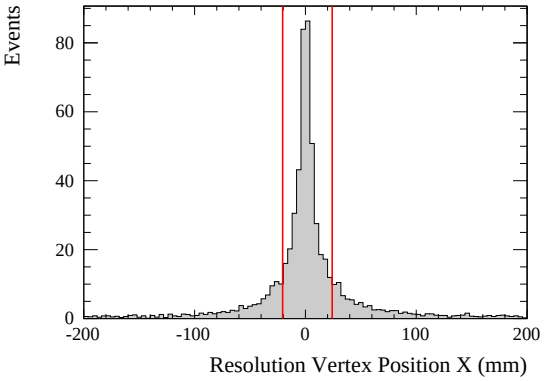

(b) Vertex Position X Air Configuration

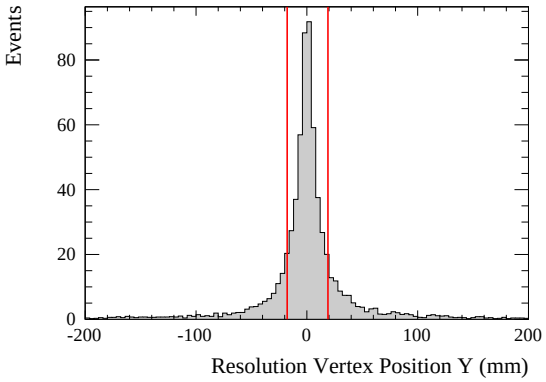

(c) Vertex Position Y Water Configuration

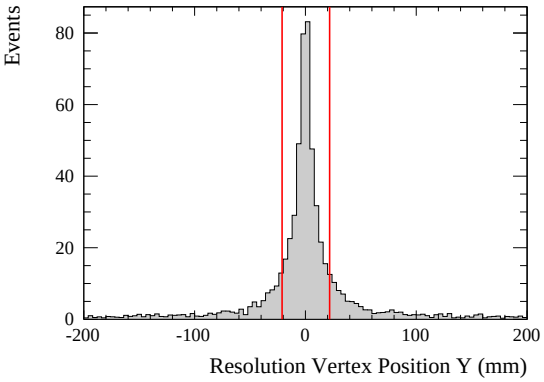

(d) Vertex Position Y Air Configuration

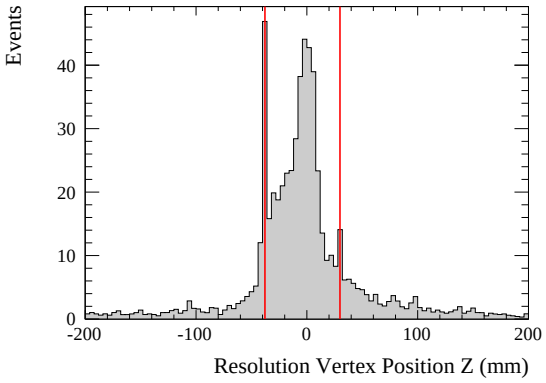

(e) Vertex Position Z Water Configuration

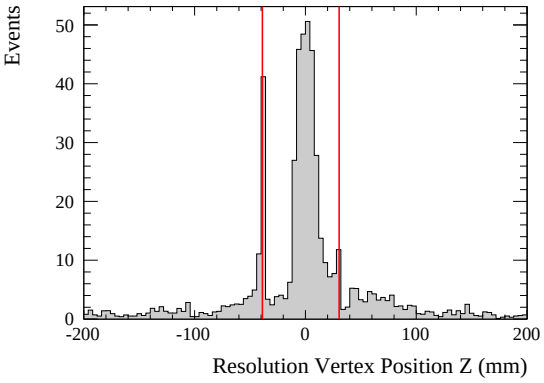

(f) Vertex Position Z Air Configuration

Figure 5.1: MC vertex position resolutions for the PØD water and air configuration. Reconstruction information from the track stage of the PØDRecon is used for these plots. The vertical lines correspond to the 16 % and 84 % quantiles.

The distribution of the difference between true and reconstructed electron angle in units of π for both the water and air PØD configuration are shown in Fig. 5.2a and Fig. 5.2b, respectively. The distribution of the relative difference between reconstructed and true electron energy for the water and air PØD configuration are shown in Fig. 5.2c and Fig. 5.2d. While the corresponding distributions of the relative difference between reconstructed and true neutrino energy are shown in Fig. 5.2e and Fig. 5.2f. All those plots are obtained by using reconstruction information from the PØDRecon shower stage and are shown together with the 16 % and 84 % quantiles.

The resolutions are found by taking half the distance from those quantiles which is equivalent to 1σ of a Gaussian fit. The MC resolutions obtained from both the track and shower reconstruction stage are summarized in Tab. 5.2. The table shows that both the electron energy resolution and the angular resolution is better if it is obtained from the PØDRecon shower stage. As a consequence, the particle angle and energy related selection cuts are applied to reconstruction information coming from the shower stage of the PØDRecon. Compared to the high energy ν_e analysis energy resolution (Sec. 4.2), no significant change is observed.

Table 5.2: MC reconstruction resolutions for the electron angle, the electron energy, and the neutrino energy if using reconstruction information from the track stage or the shower stage. The tables show the shift (obtained from the median value) and the resolutions (obtained from the 16 % and 84 % quantiles) for the PØD configurations water and air.

(a) Electron and Neutrino Resolutions with Track Stage Information

	Electron Angle (π)		Relative Electron Energy		Relative Neutrino Energy	
	Shift	Resolution	Shift	Resolution	Shift	Resolution
Water	-0.008	0.022	0.034	0.172	-0.023	0.219
Air	-0.008	0.021	0.006	0.178	-0.049	0.219

(b) Electron and Neutrino Resolutions with Shower Stage Information

	Electron Angle (π)		Relative Electron Energy		Relative Neutrino Energy	
	Shift	Resolution	Shift	Resolution	Shift	Resolution
Water	-0.004	0.010	0.029	0.162	-0.036	0.178
Air	-0.005	0.011	-0.008	0.161	-0.068	0.176

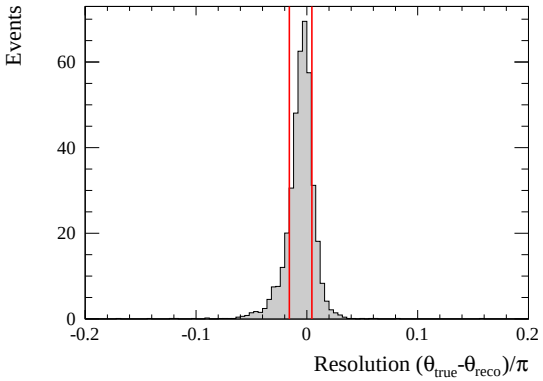

(a) Electron Angle Water Configuration

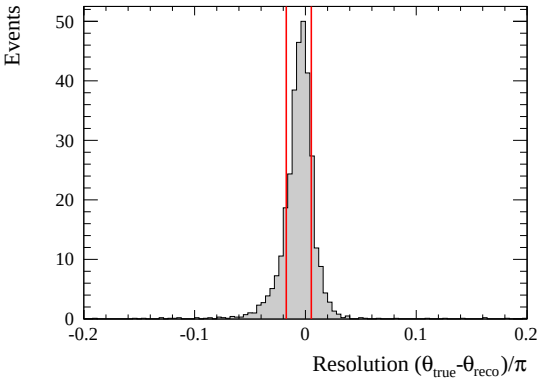

(b) Electron Angle Air Configuration

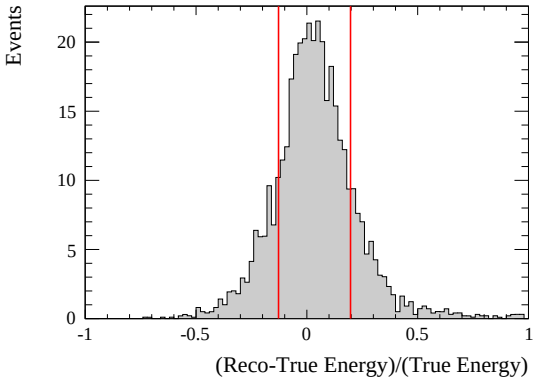

(c) Electron Energy Water Configuration

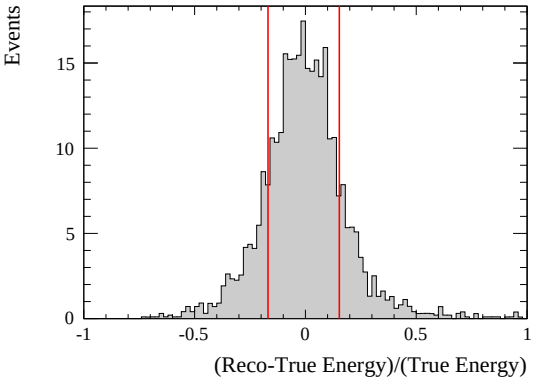

(d) Electron Energy Air Configuration

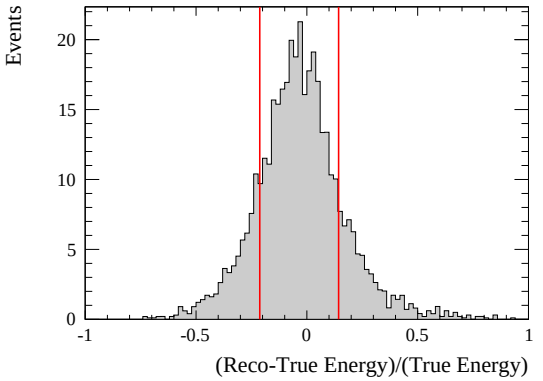

(e) Neutrino Energy Water Configuration

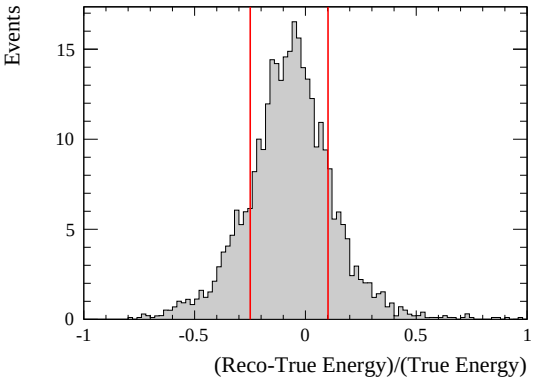

(f) Neutrino Energy Air Configuration

Figure 5.2: MC reconstruction resolutions for the electron angle, the electron energy, and the neutrino energy for the PØD configurations water and air. Reconstruction information from the shower stage of the PØDRecon is used for these plots. The vertical lines correspond to the 16 % and 84 % quantiles.

5.3 Event Selection

The event selection for the analysis follows the similar selections of the previous high energy ν_e analysis (Sec. 4.3). However due to removal of the neutrino energy cut and decrease of the purity, a new selection criteria is applied. Also the tunable selections, i.e. shower median width, shower charge fraction, and vertex Z position cuts, have been tuned by maximizing $S/\sqrt{B}$.

5.3.1 Basic Selection, Hit Matching, Particle Direction

As a pre-selection of the analysis, the basic selection, hit matching selection, and the particle direction cut are required to ensure a good reconstruction quality. For the basic selection, valid 3D vertex, valid 3D track, and valid 3D shower are required.

The fiducial volume cut is also applied with the fiducial volume definition shown in Tab. 3.1, and the hit matching selection and particle direction cut are applied with the same methods described in Sec. 4.3.2 and Sec. 4.3.3. The N-1 plots of the hit matching selection is shown in Fig. 5.3, and it is clearly seen that the almost all events pass the selection criteria.

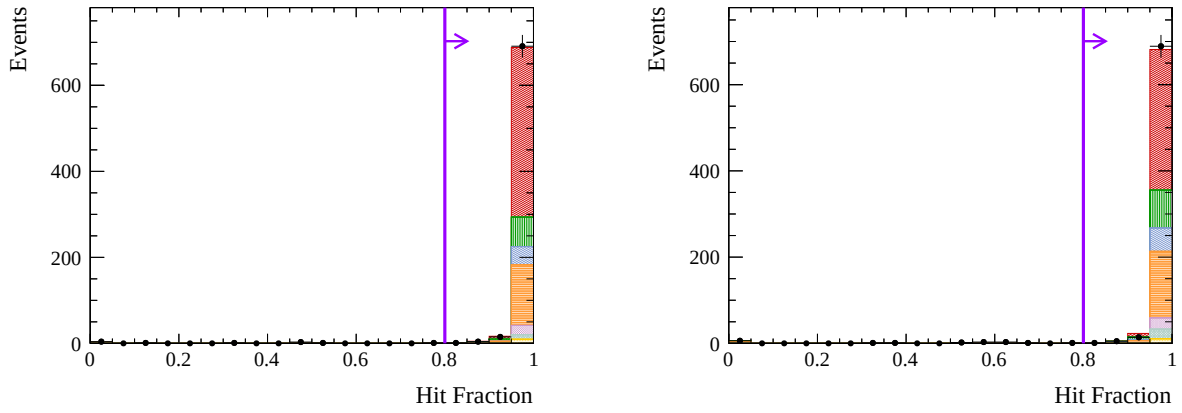

(a) Water Configuration **(b)** Air Configuration

Figure 5.3: The N-1 plot of the hit matching selection cut for the water and air configuration. The plots are area-normalized to emphasize shape differences between the data and MC.

5.3.2 Track Median Width

As the reconstructed track of an electron is typically wider than the reconstructed track of muon, the energy-weighted standard deviation of the position of the hits in the track, the track median width, is calculated (Sec. 4.3.5) and used as a selection.

Figure 5.4 shows the area-normalized N-1 plot of the track median width cut for the water and air configuration. The first bin contains the events that were too short to determine the median width. The cut value was chosen to be 1 mm to remove the narrow muon background events.

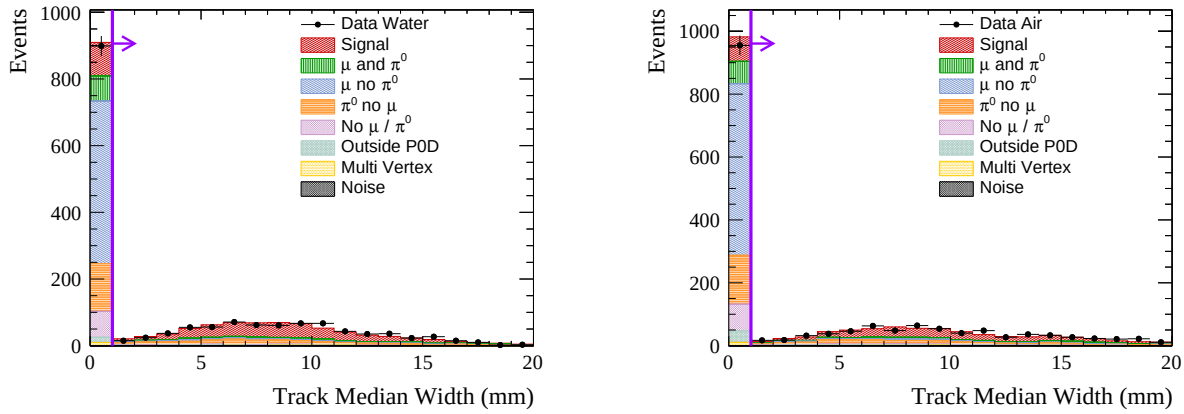

(a) Water Configuration

(b) Air Configuration

Figure 5.4: The N-1 plot of the track median width selection cut for the water and air configuration. The plots are area-normalized to emphasize shape differences between the data and MC.

5.3.3 Shower Median Width

When more than one showers overlap each other, such as π^0 events, the PØDRecon sometimes mis-reconstruct those showers with a single shower. These mis-reconstructed background events will have wider shower than the signal event, which is with a single electron, and this feature can be used to distinguish background events from the signal. The shower median width variable is calculated the same way as the track median width.

Figure 5.5 shows the area-normalized N-1 plot of the shower median width for the PØD water and air configuration. The plots clearly show that events with a larger shower median width are most likely background events. The cut values are determined by optimizing $S/\sqrt{B}$ where S is the number of selected MC signal events while B is the number of selected MC background events. The cut values are found to be 23 mm for the water configuration and 31 mm for air configuration.

5.3.4 Shower Charge Fraction

To select signal events with a high purity, events with most of the event charge contained in the candidate shower are selected. The cut values were chosen to maximize $S/\sqrt{B}$, and they are found to be 0.9 for both water and air configuration. Figure 5.6 shows the area-normalized N-1 plot of the shower charge fraction cut for the PØD water and air configuration.

5.3.5 Track Vertex Z Position

With increase of the background events due to removal of the energy threshold, an additional variable was investigated to improve purity of the selected sample. When an event is reconstructed at the downstream edge of the the PØD, it will have relatively short track

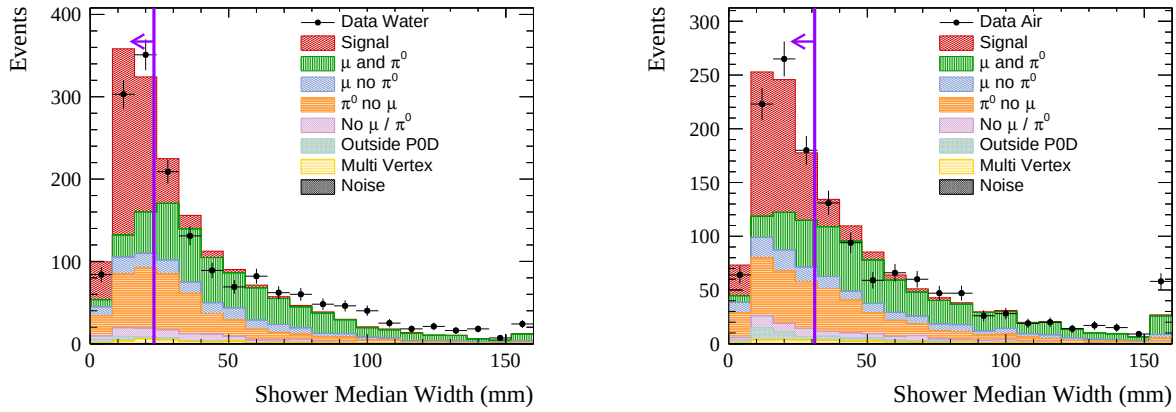

(a) Water Configuration **(b)** Air Configuration

Figure 5.5: The N-1 plot of the shower median width selection cut for the water and air configuration. The plots are area-normalized to emphasize shape differences between the data and MC.

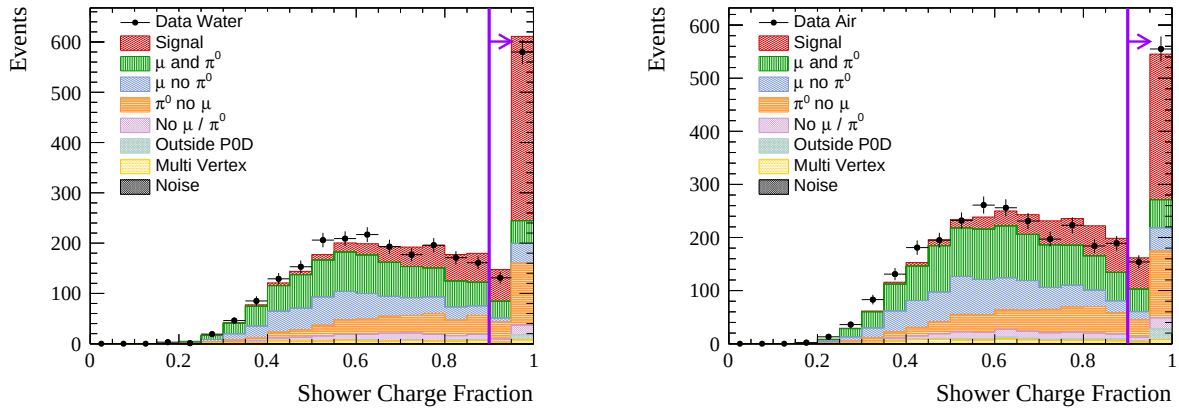

(a) Water Configuration **(b)** Air Configuration

Figure 5.6: The N-1 plot of the shower charge fraction selection cut for the water and air configuration. The plots are area-normalized to emphasize shape differences between the data and MC.

length. These short track events, generally low energy muon events, is not well removed by track median width cut as it will likely to be mis-reconstructed due to short length.

Figure 5.7 shows the area-normalized N-1 plot of the track vertex Z position for the PØD water and air configuration. The cut values were optimized with $S/\sqrt{B}$, and they are found to be -1541 mm for the water configuration and -1529 mm for the air configuration.

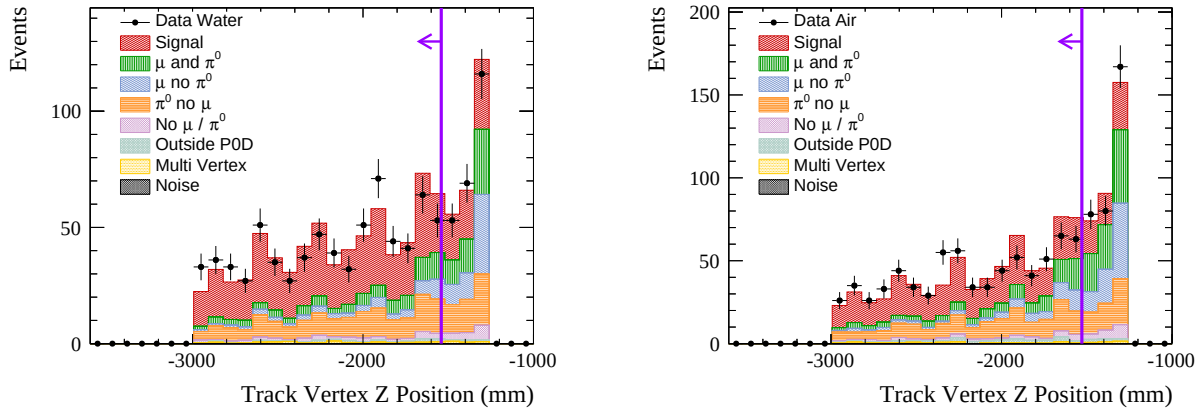

(a) Water Configuration **(b)** Air Configuration

Figure 5.7: The N-1 plot of the track vertex Z position selection cut for the water and air configuration. The plots are area-normalized to emphasize shape differences between the data and MC.

5.4 Selected Event Sample

5.4.1 Number of Selected Events

The number of selected MC events normalized to the data POT for the PØD configurations water and air together with the number of selected data events are presented in Tab. 5.3. In addition, the water configuration MC events are split up into on-water and not-water events. On-water events are defined as events with true interaction vertex on the water targets while not-water events have the true interaction vertex not on water, i.e. on scintillator, lead, or bras. All events in the air configuration MC are not-water events as the water targets are drained. The shown errors correspond to the statistical uncertainty due to the limited MC statistics. The impact of each selection criterion is demonstrated with the N-1 plots presented in Sec. 5.3.

Table 5.3: The selected number of MC signal events S, MC background events B, and the total number of selected MC events $S+B$ normalized to the data POT for the water and air configuration are listed together with the selected data events D. In addition, the water configuration MC events are split up in on-water and not-water events. The errors correspond to the statistical uncertainty due to the limited MC statistics.

	MC Signal S	MC Background B	MC Total $S+B$	Data D
Water	447.6 ± 7.1	343.2 ± 6.4	790.8 ± 9.6	711
On-Water	152.7 ± 4.1	100.7 ± 3.4	253.4 ± 5.3	
Not-Water	294.9 ± 5.8	242.5 ± 5.4	537.4 ± 7.9	
Air	355.6 ± 6.3	399.7 ± 6.9	755.3 ± 9.4	709

5.4.2 Efficiency and Purity

The efficiency ϵ and purity p of MC signal events are defined as

$$\epsilon = \frac{S}{T} \tag{5.1}$$

$$p = \frac{S}{S+B} \tag{5.2}$$

where S is the number of selected MC signal events and B is the number of selected MC background events. T is the number of true MC signal events with the true vertex within the fiducial volume. Note that there is no requirement on true neutrino energy larger than 1.5 GeV as in the high energy CCν_e analysis.

The values of T, the obtained efficiencies, and the calculated purities for the water and air configuration are listed in Tab. 5.4. Events of the PØD water configuration are split-up in events happening on-water and not-water (scintillator, bras, lead, etc.).

Table 5.4: The number of true signal events T with true vertex within the fiducial volume, the signal efficiencies ϵ and purities p are listed for the water and air configuration. Events of the PØD water configuration are split-up in events happening on-water and not-water (scintillator, bras, lead, etc.). The errors correspond to the statistical uncertainty due to the limited MC statistics.

	Truth T	Efficiency ϵ	Purity p
Water	2459.0 ± 16.7	$(18.2 \pm 0.5)\,\%$	$(56.6 \pm 3.1)\,\%$
On-Water	819.3 ± 9.5	$(18.6 \pm 0.6)\,\%$	$(60.3 \pm 5.3)\,\%$
Not-Water	1639.6 ± 13.7	$(18.0 \pm 0.5)\,\%$	$(54.9 \pm 3.9)\,\%$
Air	2200.2 ± 15.8	$(16.2 \pm 0.5)\,\%$	$(47.1 \pm 3.4)\,\%$

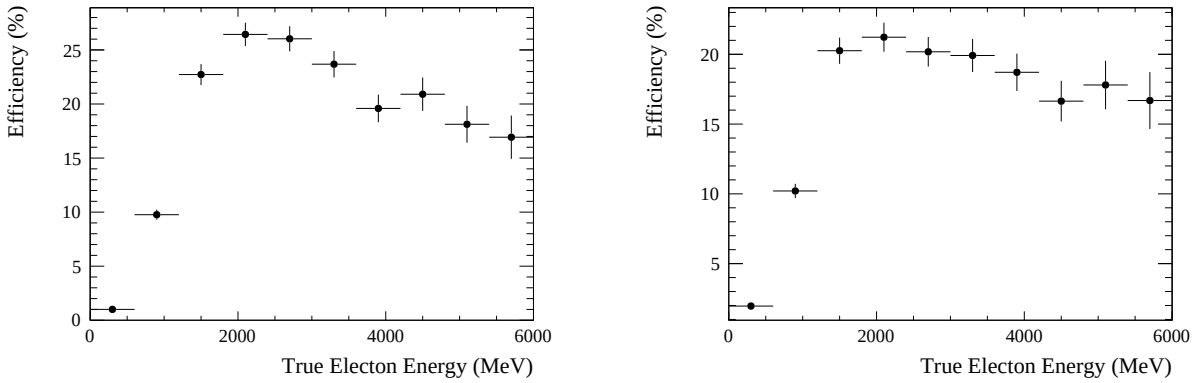

(a) Water Configuration **(b)** Air Configuration

Figure 5.8: Selection efficiency of signal events as a function of the true neutrino energy E_{true} for the water and air configuration. The error bars correspond to the uncertainties due to limited MC statistics.

The selection efficiency of signal events as a function of the true neutrino energy E_{true} for the PØD water and air configurations are shown in Fig. 5.8. The selection of high energy signal events is somewhat suppressed by the shower median width cut and the shower charge fraction cut. Compared to the previous high energy CCν_e analysis, one can see that the high energy suppression is weaker in the current analysis. This is because the shower charge fraction cut is relaxed (Shower charge fraction > 0.9) compared to the previous cut (Shower charge fraction $= 1$).

5.4.3 Selected MC/Data Sample

Table 5.5 shows the number of selected MC events for the PØD water and air configuration with the background events broken down by the event type. The table clearly shows that

the majority of the remaining background events contain a π^0.

Figure 5.9 shows the particle direction and energy of selected events with all cuts for the water and air configuration, with the MC events normalized to the data POT.

5.5 Systematic Uncertainties

The effect of detector, flux, and cross section systematic uncertainties on the results of the analysis are discussed and estimated in this section. Unless noted otherwise, all the methods of the estimation are shared with the previous high energy CCν_e analysis, Sec. 4.6. It should be pointed out that the energy scale uncertainty, which was discussed in Sec. 4.6.2, does not play a significant role in this analysis. This is mainly because there does not exist the neutrino energy cut anymore, and also because the fact that the energy scale have minimal impact on the event selection. The energy scale uncertainty will have small correlation with the cut values of other selection such as shower median width, but as the shower median width uncertainty will be taking care of the change itself with fairly large uncertainty, the energy scale uncertainty will have negligible impact on the uncertainty of other selections.

5.5.1 PØD Geometry and Mass Uncertainties

As stated in Sec. 4.6.1, he difference of the PØD mass fiducial volume between as-built mass and MC mass can cause systematic uncertainty, as well as uncertainties of the fiducial volume and the detector alignment.

Table 5.5: Selected MC events broken down by the event type for the PØD configuration water and air. The MC events are normalized to the data POT.

	MC Water		MC Air	
Event Type	Events	Rel. (%)	Events	Rel. (%)
Signal	447.6	56.6	355.6	47.1
μ and π^0	82.0	10.4	101.9	13.5
μ no π^0	49.8	6.3	62.7	8.3
π^0 no μ	162.9	20.6	169.9	22.5
No μ/π^0	25.6	3.2	29.4	3.9
Outside P0D	11.9	0.4	24.4	3.2
Multi Vertex	11.0	1.5	11.5	1.5
Noise	0.0	0.0	0.0	0.0
Total	790.8	100.0	755.3	100.0

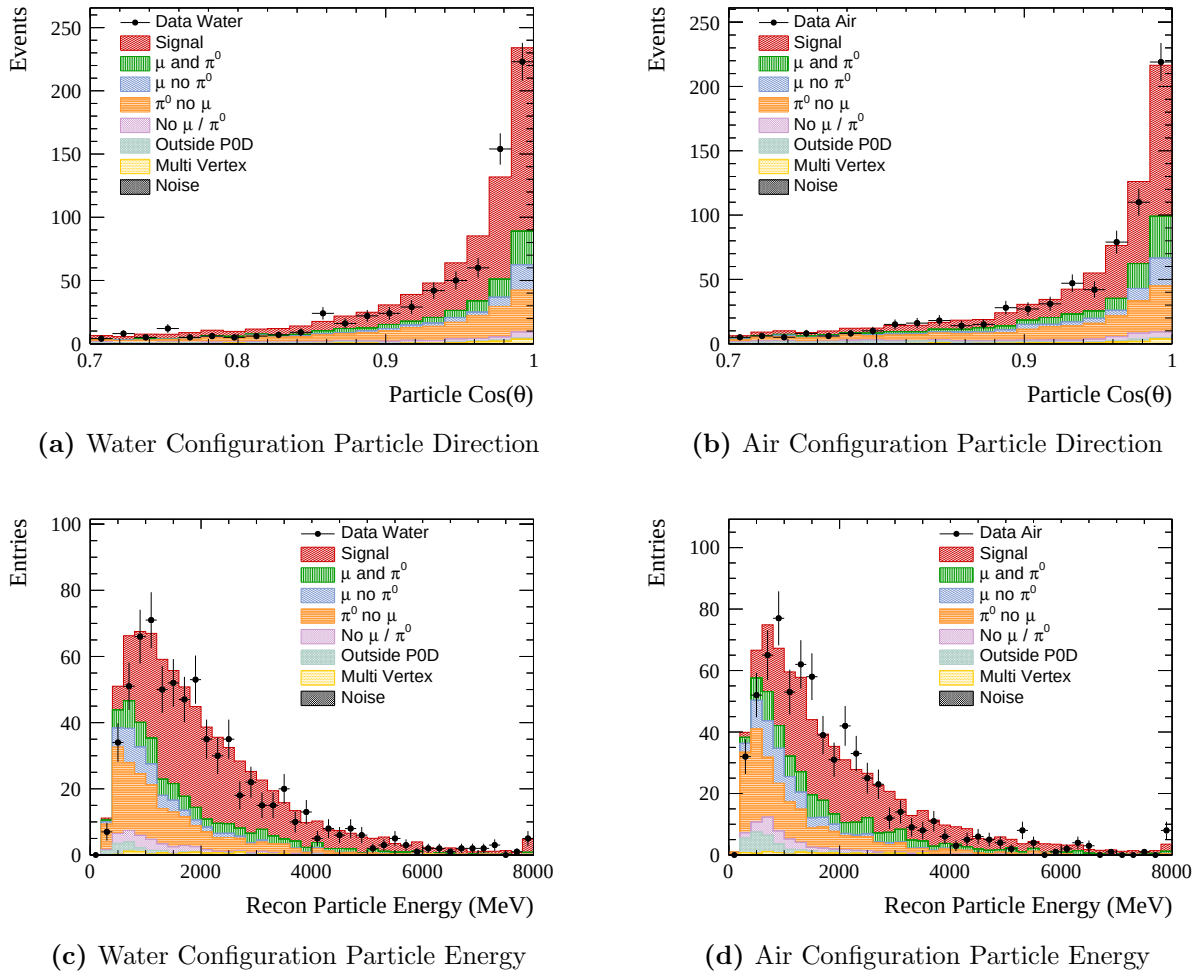

(a) Water Configuration Particle Direction

(b) Air Configuration Particle Direction

(c) Water Configuration Particle Energy

(d) Air Configuration Particle Energy

Figure 5.9: Events passing the event selection as a function of the particle direction and energy for the water and air configuration. The MC events are normalized to the data POT.

Mass Uncertainty

The PØD fiducial volume mass used in Production 6 MC is the same as that of Production 5 MC. Therefore the discrepancy between as-built mass and the mass in MC is the same as the previous analysis.

The systematic effect on the CCν_e data/MC ratios for the water (R_{water}), air (R_{air}), and on-water ($R_{\text{on-water}}$) coming from the PØD fiducial volume mass uncertainties are estimated by varying the water and dry mass according to the uncertainties. The water and dry mass are thrown 10,000 times and the MC events are re-weighted accordingly. Then, the analysis chain is applied to the nominal data set and the re-weighted MC set of each mass throw. The CCν_e data/MC ratios R_{water}, R_{air}, and $R_{\text{on-water}}$ are calculated and plotted in a histogram. The obtained distributions are shown in Fig. 5.10 and they are fit with a Gaussian. The fitted widths for each distribution are presented in Tab. 5.6 and are considered to be the systematic uncertainty coming from the PØD mass uncertainty. The obtained uncertainty

Table 5.6: PØD mass systematic uncertainties for the water (R_{water}), air (R_{air}), and on-water ($R_{\text{on-water}}$) CCν_e data/MC ratios.

CCν_e Data/MC Ratio	Uncertainty
R_{water}	0.01
R_{air}	0.02
$R_{\text{on-water}}$	0.01

for the CCν_e data/MC ratio is 0.01 for each data sample (water, air, on-water).

Fiducial Volume

We use the same method stated in Sec. 4.6.1, but with different variation of the fiducial volume due to different MC vertex resolution. The MC vertex resolution in this analysis is presented in Tab. 5.1. Following the same procedure as Sec. 4.6.1, the uncertainty from the fiducial volume on the total data/MC ratio is always smaller than 0.01 for both water and air configuration. Therefore, it is concluded that the systematic effect coming from the fiducial volume definition is negligible.

Alignment

To determine the impact of the alignment on the CCν_e data/MC ratios, the MC fiducial volume is shifted separately in X and Y direction with respect to the data fiducial volume, by the resolution of a hit in X direction of 2.46 mm and in Y direction of 2.78 mm. For each direction, the shift is thrown 10,000 times with the corresponding resolution as uncertainty. The resulting CCν_e data/MC ratios for the water, air, and on-water target are plotted in a histogram and fitted with a Gaussian. The resulting width is considered to be the systematic uncertainty from the alignment. The obtained uncertainties are smaller than 0.01 for all ratios therefore negligible.

5.5.2 Reconstruction Systematics

Matching Hit

As stated in Sec. 5.3, the event selection requires that 80 % of the hits associated with the candidate track are also used for the candidate shower. Because the other event selection criteria look for a very clear signal pattern in the PØD, the hit matching condition has almost no impact on the number of selected events as shown in the N-1 plots in Fig. 5.3 and zoomed-in plots in Fig. 5.11. Only 11 data event collected during the PØD water configuration and 16 events collected during the PØD air configuration fail this selection criteria, and only 1

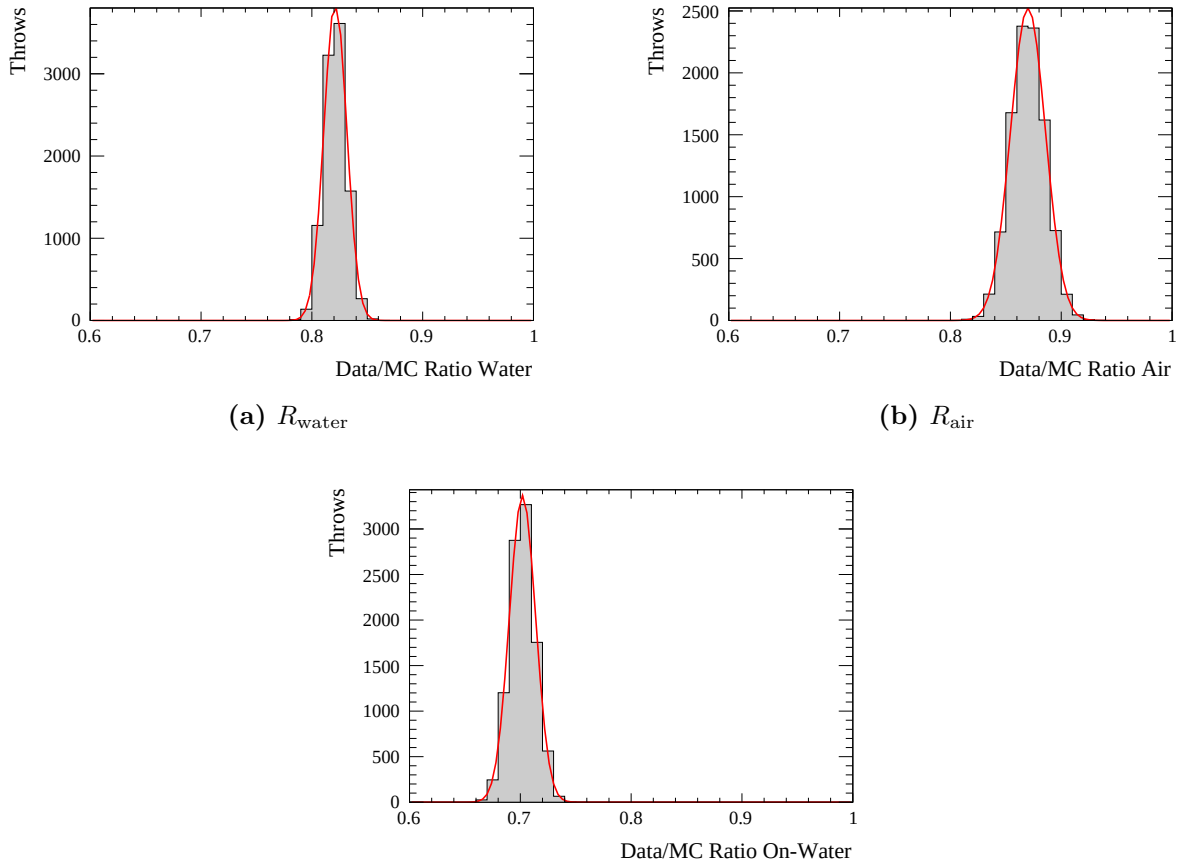

(a) R_{water} **(b)** R_{air}

(c) $R_{\text{on-water}}$

Figure 5.10: Data/MC ratios for the water (R_{water}), air (R_{air}), and on-water ($R_{\text{on-water}}$) varied within the PØD mass systematic uncertainties. The distributions are fit with a single Gaussian.

event for both configuration near the cut value (0.8). The systematic uncertainty coming from the hit matching selection criterion is therefore negligible.

Track PID

The systematic uncertainty coming from the PID difference between Data and MC has been studied by following the same methodology stated in Sec. 4.6.3. But using the new software used in this analysis. 10,000 stopping muon sample were created for the mapping procedure.

The map is constructed by looking at a data sample of stopping muon and comparing it to a particle gun of stopping muons. Using each track PID parameters, a map is created between distributions of the Monte Carlo to the data by mapping the values extracted from the same quantile in MC to data.

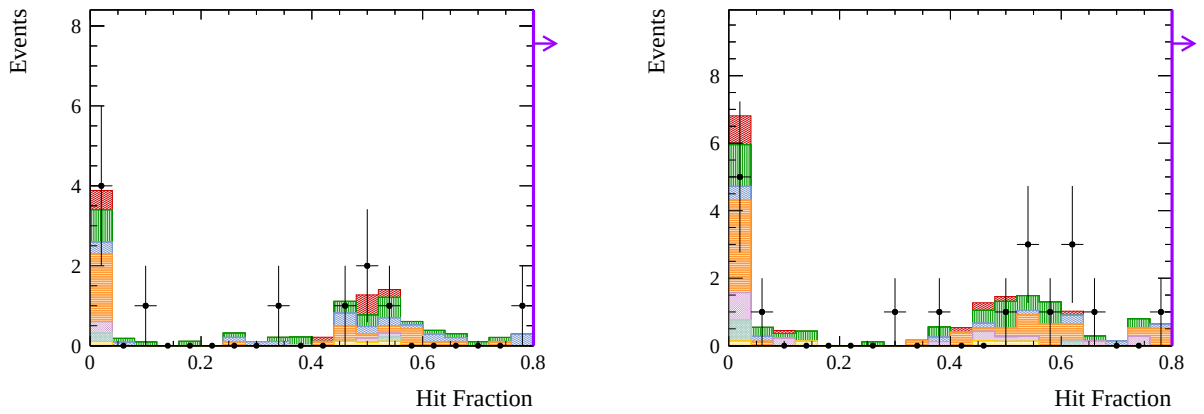

(a) Water Configuration **(b)** Air Configuration

Figure 5.11: The zoomed-in N-1 plot of the hit matching selection cut for the water and air configuration. The plots are area-normalized to emphasize shape differences between the data and MC.

The default PID efficiency is shown in Tab. 5.7 and Tab. 5.8, and the mapped PID efficiency is in Tab. 5.9 and Tab. 5.10. The comparison between the default and mapped PID differences, the muon misidentification shows a difference of approximately 4% while the electron identification shows a difference of approximately 2%.

As discussed in Sec. 4.6.3, because the stopping muon sample is used for the mapping and non-electron control samples. Therefore 4% as the uncertainty for signal events is taken as a very conservative approach. The corresponding results are shown in Tab. 5.11 and in the histograms in Fig. 5.12.

Angular Resolution

The angular resolution for selected events is calculated in Sec. 5.2. Smearing factors will be the angular resolution itself, applied to MC only with 10,000 Gaussian random trials. The uncertainty will be the shift of the background-subtracted data/MC from the nominal value. The uncertainty of the CCν_e data/MC ratio due to MC angular resolution is smaller than 0.01 for both water and air configurations as well for on-water ratio. Therefore it is concluded that the systematic uncertainty coming from the angular resolution is negligible. The shifted on-water data/MC ratio plots after the random throws are shown in Fig. 5.13.

Median Width

As described in Sec. 4.6.3, as the event selection cut is very tight (at 1 mm) for the track median width cut and therefore scaling MC with the possible uncertainty will not effect the event selection of the cut. Here estimation of the systematic uncertainty caused by the shower median width is discussed.

Table 5.7: A confusion matrix for the PID at the tracking stage for the water configuration.

	True Muon	True Electron	True Proton
Raw Count			
Reconstructed Light Track	983727	17178	267467
Reconstructed EM	302492	780521	446854
Reconstructed Heavy Track	248768	15552	428273
Percentages			
Reconstructed Light Track	64.0%	2.1%	23.4%
Reconstructed EM	19.7%	96.0%	39.1%
Reconstructed Heavy Track	16.3%	1.9%	37.5%

Table 5.8: A confusion matrix for the PID at the tracking stage for the air configuration.

	True Muon	True Electron	True Proton
Raw Count			
Reconstructed Light Track	359729	8155	72961
Reconstructed EM	181772	489860	261814
Reconstructed Heavy Track	159794	13957	294737
Percentages			
Reconstructed Light Track	51.3%	1.6%	11.6%
Reconstructed EM	25.9%	95.7%	41.6%
Reconstructed Heavy Track	25.6%	2.7%	46.8%

Table 5.9: For the water configuration, the track-by-track rates of the mapped PID.

	True Muon	True Electron	True Proton
Raw Count			
Reconstructed Light Track	911138	5183	171930
Reconstructed EM	365894	798097	525170
Reconstructed Heavy Track	257955	9971	445494
Percentages			
Reconstructed Light Track	59.4%	0.6%	15.0%
Reconstructed EM	23.8%	98.1%	46.0%
Reconstructed Heavy Track	16.8%	1.3%	39.0%

Table 5.10: For the air configuration, the track-by-track rates of the mapped PID.

	True Muon	True Electron	True Proton
Raw Count			
Reconstructed Light Track	282341	5632	93761
Reconstructed EM	210796	499337	315574
Reconstructed Heavy Track	208156	7003	220177
Percentages			
Reconstructed Light Track	40.3%	1.1%	14.9%
Reconstructed EM	30.0%	97.5%	50.1%
Reconstructed Heavy Track	29.7%	1.4%	35.0%

Table 5.11: Track PID systematic uncertainties for the water (R_{water}), air (R_{air}), and on-water ($R_{\text{on-water}}$) CCν_e data/MC ratios.

CCν_e Data/MC Ratio	Bkg 4 % — Sig 4 %
R_{water}	0.03
R_{air}	0.05
$R_{\text{on-water}}$	0.10

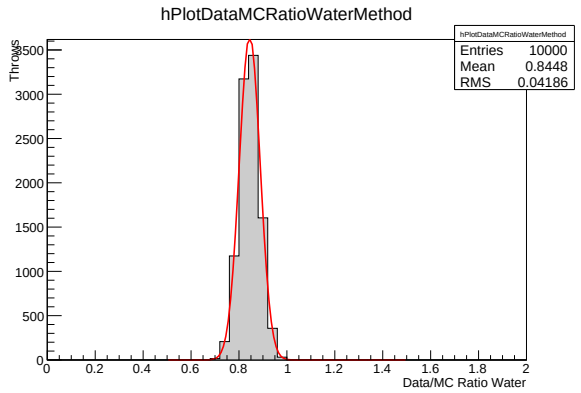

(a) R_{water}

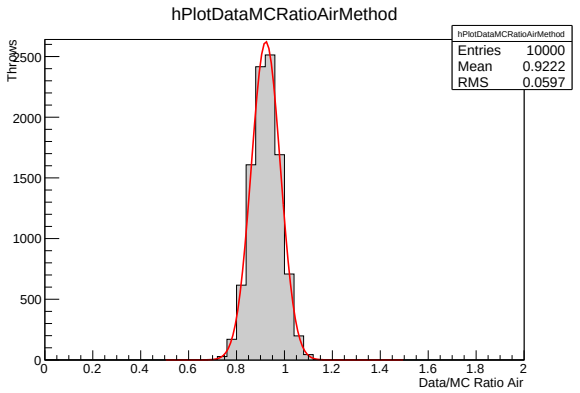

(b) R_{air}

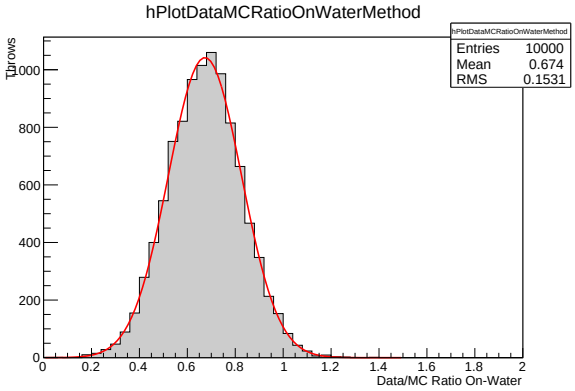

(c) $R_{\text{on-water}}$

Figure 5.12: Data/MC ratios for the water (R_{water}), air (R_{air}), and on-water ($R_{\text{on-water}}$) varied within the Track PID systematic uncertainties. The distributions are fit with a single Gaussian.

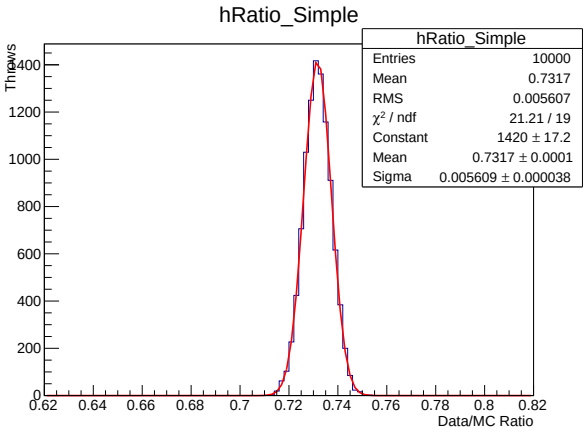

Figure 5.13: On-water Data/MC ratio ($R_{\text{on-water}}$) with angular resolution broadening. The distributions are fit with a single Gaussian.

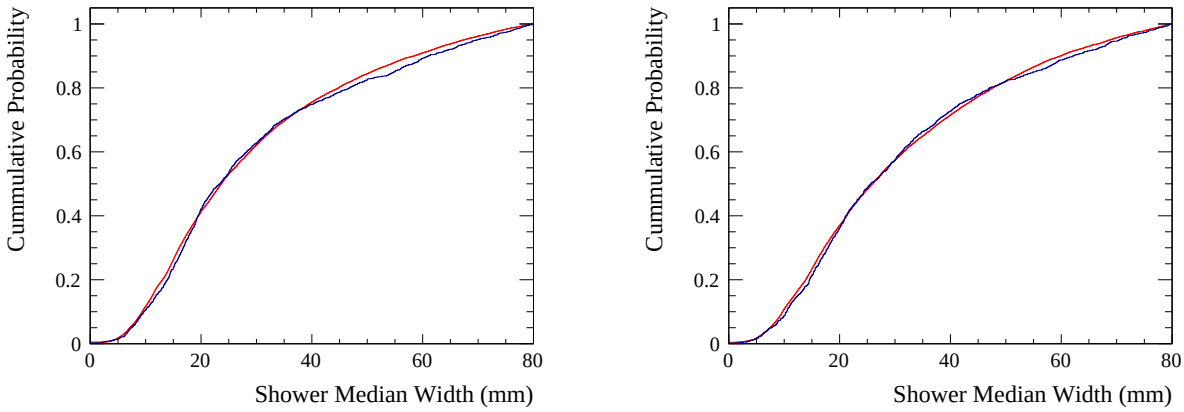

(a) Water Configuration **(b)** Air Configuration

Figure 5.14: The integrated and normalized N-1 plots of the shower median width for the water and air configuration. The data is shown as black solid line while MC is plotted as red solid line.

To estimate the systematic uncertainty caused by an uncertainty in the shower median width, the N-1 plots presented in Fig. 5.5 are integrated and a Kolmogorov-Smirnov test is performed to test if the data and the MC event distribution are consistent. The integrated and normalized event distributions are shown in Fig. 5.14 and the Kolmogorov-Smirnov test returns a p-value of 28.5 % for the water and 42.2 % for air. The plots show that there might be an indication of a unknown scaling factor applied to MC, i.e. the factor to be applied to the MC median width distribution to obtain the data distribution. but the distributions are still consistent within statistical uncertainties. To determine a reasonable scaling factor range, different scaling factors from 0.9 to 1.1 were applied to MC and the resulting p-values were plotted. Placing a line at 68 % of the p-value peak height results in a scaling factor range from 0.97 to 1.03.

The systematic effect on the CCν_e data/MC ratios for the water (R_{water}), air (R_{air}), and on-water ($R_{\text{on-water}}$) coming from the shower median width are estimated by varying the scaling factor that is applied to the MC shower median width according to the previously mentioned uncertainty. The scaling factor is thrown 10,000 times with Gaussian distribution assuming that the scaling factors for the water and the air configuration are uncorrelated. Then, the PØD ν_e analysis is applied to the nominal data set and the modified MC set for each throw. The CCν_e data/MC ratios R_{water}, R_{air}, and $R_{\text{on-water}}$ are calculated, and plotted in a histogram. The obtained distributions are shown in Fig. 5.15 and they are fit with a Gaussian. The fitted widths for each distribution are presented in Tab. 5.12 and are considered to be the systematic uncertainty coming from the shower median width.

Shower Charge Fraction

To estimate the possible impact of systematic effects of the shower charge fraction on the PØD ν_e analysis, the event distributions of the shower charge fraction sideband are analyzed. The distributions of the data and MC events as a function of the shower charge fraction are

Table 5.12: Shower median width uncertainties for the water (R_{water}), air (R_{air}), and on-water ($R_{\text{on-water}}$) CCν_e data/MC ratios.

CCν_e Data/MC Ratio	Uncertainty
R_{water}	0.06
R_{air}	0.05
$R_{\text{on-water}}$	0.14

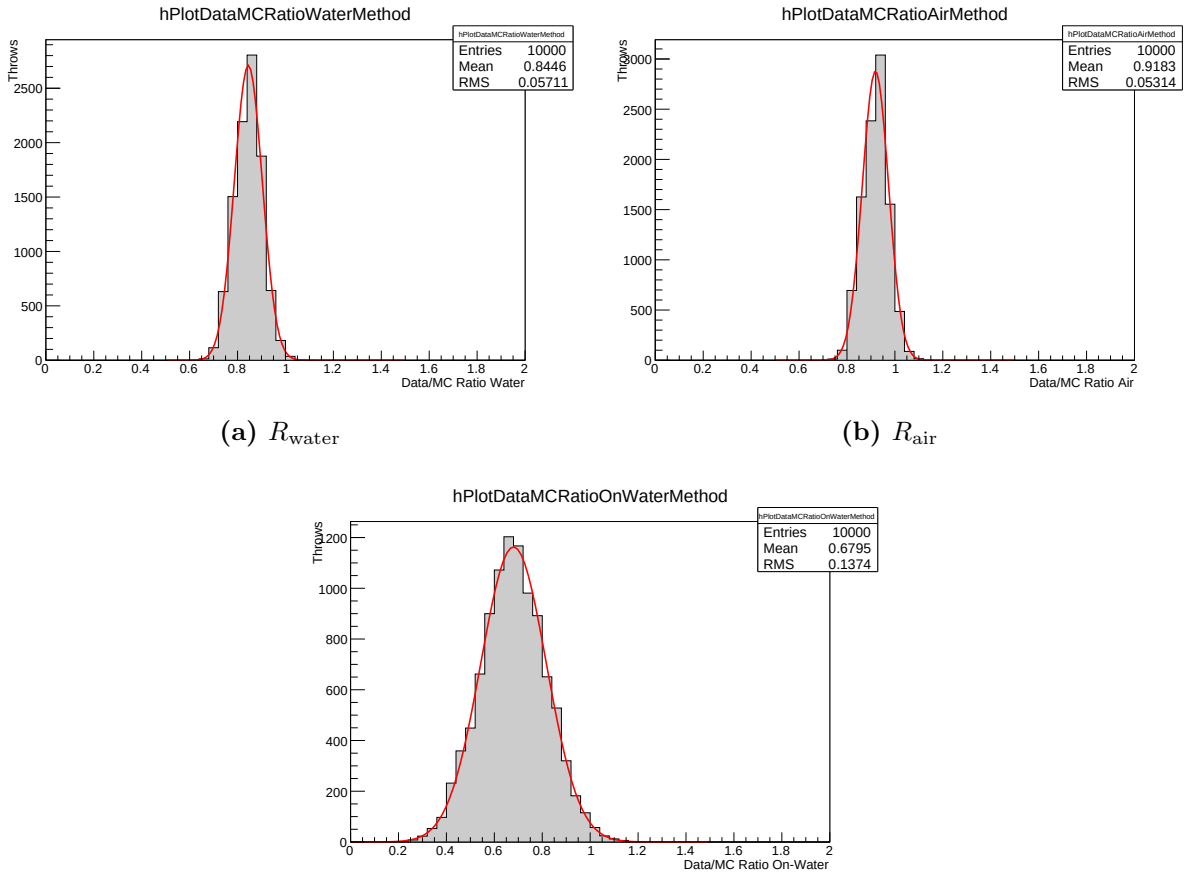

(a) R_{water} **(b)** R_{air}

(c) $R_{\text{on-water}}$

Figure 5.15: Data/MC ratios for the water (R_{water}), air (R_{air}), and on-water ($R_{\text{on-water}}$) varied within the shower median width systematic uncertainties. The distributions are fit with a single Gaussian.

shown in Fig. 5.16. In order to find the best fit between the data and MC event distributions, different shower charge fraction scaling factors are applied to the MC events where a shower charge fraction of 1.0 is defined to be the reference point. With a Kolmogorov-Smirnov test, it was found that the shape agreement between data and MC is maximized when applying a

scaling factor of 1.04 to the water MC events and 1.05 to the air MC events. The systematic effect on the CCν_e data/MC ratios for the water (R_{water}), air (R_{air}), and on-water ($R_{\text{on-water}}$) coming from the shower charge fraction scaling factors are estimated by varying the scaling factor that is applied to the MC according to the uncertainty mentioned before. The scaling factor is thrown 10,000 times assuming that the scaling factors for the water and the air configuration are uncorrelated. The obtained ratios are fitted with a Gaussian and the width is considered to be the systematic uncertainty which results in a uncertainty of 0.03, 0.05, and 0.09 for the water, air, and on-water, respectively. The obtained distributions for the CCν_e data/MC ratios are shown in Fig. 5.17 and the fitted widths, i.e. the uncertainties, are presented in Tab. 5.13.

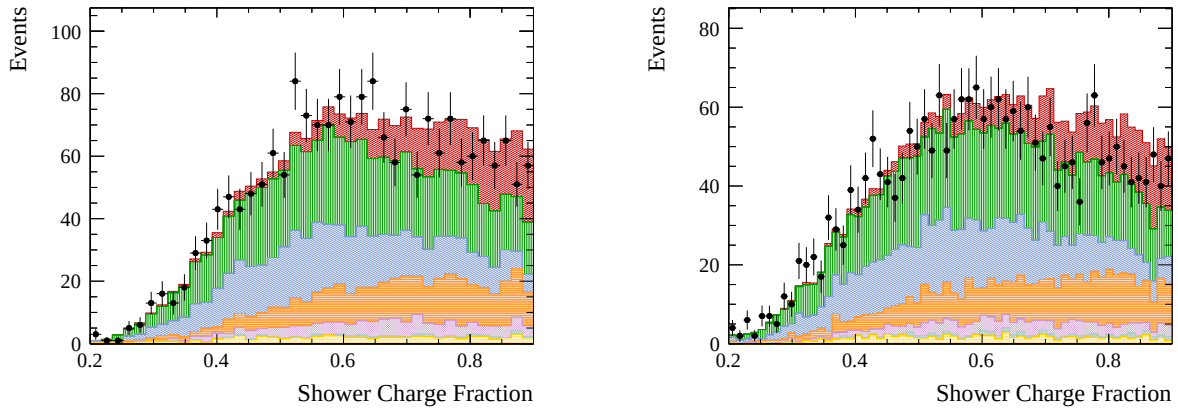

(a) Water Configuration **(b)** Air Configuration

Figure 5.16: Data and MC events in the shower charge fraction sideband are shown as a function of the shower charge fraction. Data events are plotted as black points while the POT-normalized MC events are shown as filled histograms. Events with a shower charge fraction of 1.0 are not shown in these plots.

Table 5.13: Shower charge fraction uncertainties for the water (R_{water}), air (R_{air}), and on-water ($R_{\text{on-water}}$) CCν_e data/MC ratios.

CCν_e Data/MC Ratio	Uncertainty
R_{water}	0.03
R_{air}	0.05
$R_{\text{on-water}}$	0.09

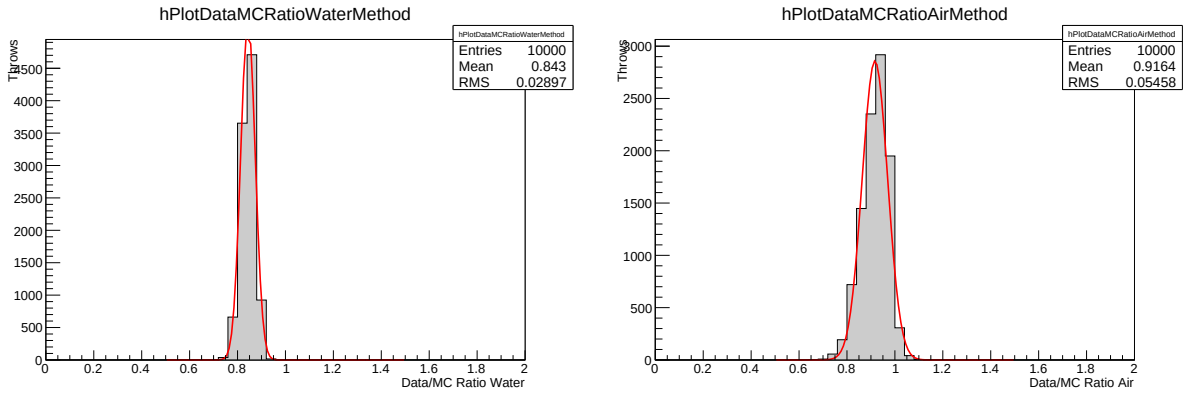

(a) R_{water}

(b) R_{air}

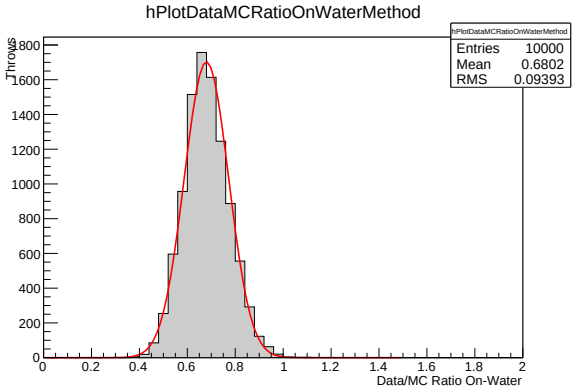

(c) $R_{\text{on-water}}$

Figure 5.17: Data/MC ratios for the water (R_{water}), air (R_{air}), and on-water ($R_{\text{on-water}}$) varied within the shower charge fraction systematic uncertainties. The data/MC ratios obtained are shown. The distributions are fit with a single Gaussian.

5.5.3 Flux and Cross Section Systematic Uncertainties

For the flux and cross section systematic uncertainty estimation, the T2KReWeight package is used, with the same method applied in Sec. 4.6.4. The same BANFF output file, the newest version among the T2K 2013 oscillation analysis, is used and 46 parameters are considered. For the details of the True energy binning, systematic flux and cross parameters, and covariance matrices refer to Sec. 4.6.4.

The number of MC events normalized to the data POT for flux and BANFF post-fit reweighting are listed in Tab. 5.14. To obtain the flux and cross section systematic uncertainties for CCν_e data/MC ratios, the T2KReWeight framework and 2013 BANFF post-fit covariance matrix is used. The systematic parameters are thrown 1000 times according the the covariance matrix. Figure 5.18 shows the CCν_e data/MC ratio distributions for the water, air and on-water obtained. The distributions are fit with single Gaussians and the resulting sigma is considered to be the flux and cross section systematic uncertainties for the

analysis and the results are shown in Tab. 5.15.

Table 5.14: The selected number of MC signal events S, MC background events B, and the total number of selected MC events $S+B$ normalized to the data POT for the water and air configuration are listed for flux and BANFF post-fit re-weighting.

	Re-Weighting	MC Total $S+B$	MC Signal S	MC Background B
Water	Flux	790.8	447.6	343.2
	Post-Fit	785.2	435.5	349.7
Air	Flux	755.3	355.6	399.7
	Post-Fit	753.7	341.1	412.6

Table 5.15: Flux and cross section systematic uncertainties for the water (R_{water}), air (R_{air}), and on-water ($R_{\text{on-water}}$) CCν_e data/MC ratios.

CCν_e Data/MC Ratio	BANFF Post-Fit
R_{water}	0.11
R_{air}	0.13
$R_{\text{on-water}}$	0.10

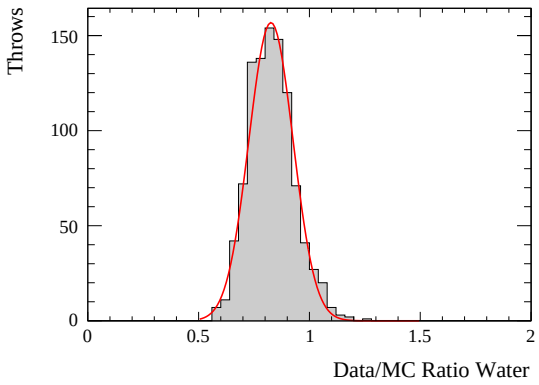

(a) R_{water} BANFF Post-Fit

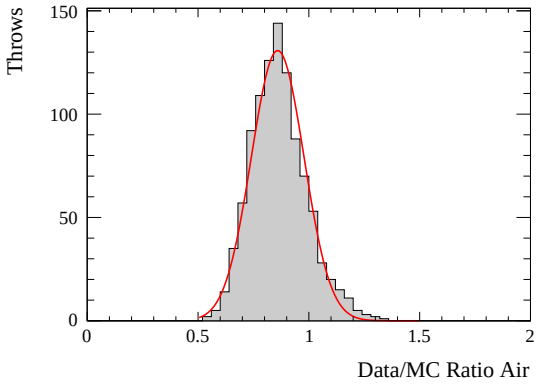

(b) R_{air} BANFF Post-Fit

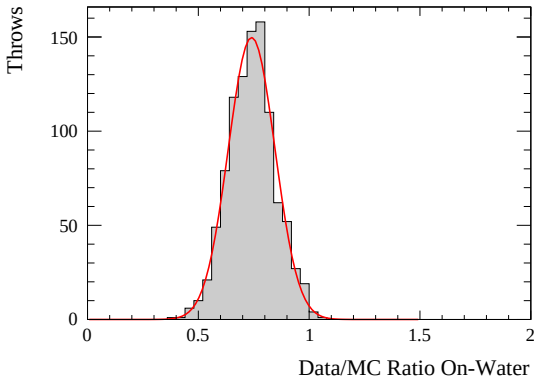

(c) $R_{\text{on-water}}$ BANFF Post-Fit

Figure 5.18: Data/MC ratios for the water (R_{water}), air (R_{air}), and on-water ($R_{\text{on-water}}$) varied within the BANFF post-fit flux and cross section systematic uncertainties. The distributions are fit with a single Gaussian.

5.5.4 Systematics Summary

All systematic uncertainties on the CCν_e data/MC ratios for the water (R_{water}), air (R_{air}), and on-water ($R_{\text{on-water}}$) that were estimated in the previous sections are summarized in Tab. 5.16. In addition, the tables show the total systematic uncertainty.

Table 5.16: Summary of systematic uncertainties on the CCν_e data/MC ratios for the water (R_{water}), air (R_{air}), and on-water ($R_{\text{on-water}}$)

Systematic Uncertainty for CCν_e Data/MC Ratio	R_{water}	R_{air}	$R_{\text{on-water}}$
MC Statistics	0.03	0.03	0.10
PØD Mass	0.01	0.02	0.01
PØD Fiducial Volume	< 0.01	< 0.01	< 0.01
PØD Alignment	< 0.01	< 0.01	< 0.01
Hit Matching	< 0.01	< 0.01	< 0.01
Track PID	0.03	0.05	0.10
Angular Resolution	< 0.01	< 0.01	0.01
Track Median Width	< 0.01	< 0.01	< 0.01
Shower Median Width	0.06	0.05	0.14
Shower Charge Fraction	0.03	0.05	0.09
Flux and Cross Sections Post-Fit	0.11	0.13	0.10
Total with Post-Fit	0.14	0.16	0.24

5.6 Result

Applying the event selection to the full Run 1 to Run 4 data results in 711 selected data events during the PØD water configuration and 709 selected data events during the PØD air configuration. The analysis described in Sec. 4.5 to obtained the background subtracted CCν_e data/MC ratios for the water (R_{water}), air (R_{air}), and on-water ($R_{\text{on-water}}$) events was performed.

Our primary result of the analysis uses the BANFF post-fit weighted MC. The background subtracted data/MC ratio R is:

$$R_{\text{water}} = 0.83 \pm 0.05\ (\text{stat.}) \pm 0.14\ (\text{sys.}) \tag{5.3}$$

$$R_{\text{air}} = 0.86 \pm 0.06\ (\text{stat.}) \pm 0.16\ (\text{sys.}) \tag{5.4}$$

$$R_{\text{on-water}} = 0.76 \pm 0.23\ (\text{stat.}) \pm 0.24\ (\text{sys.}) \tag{5.5}$$

The distribution of selected events for the reconstructed particle energy and the particle direction are shown in Fig. 5.19.

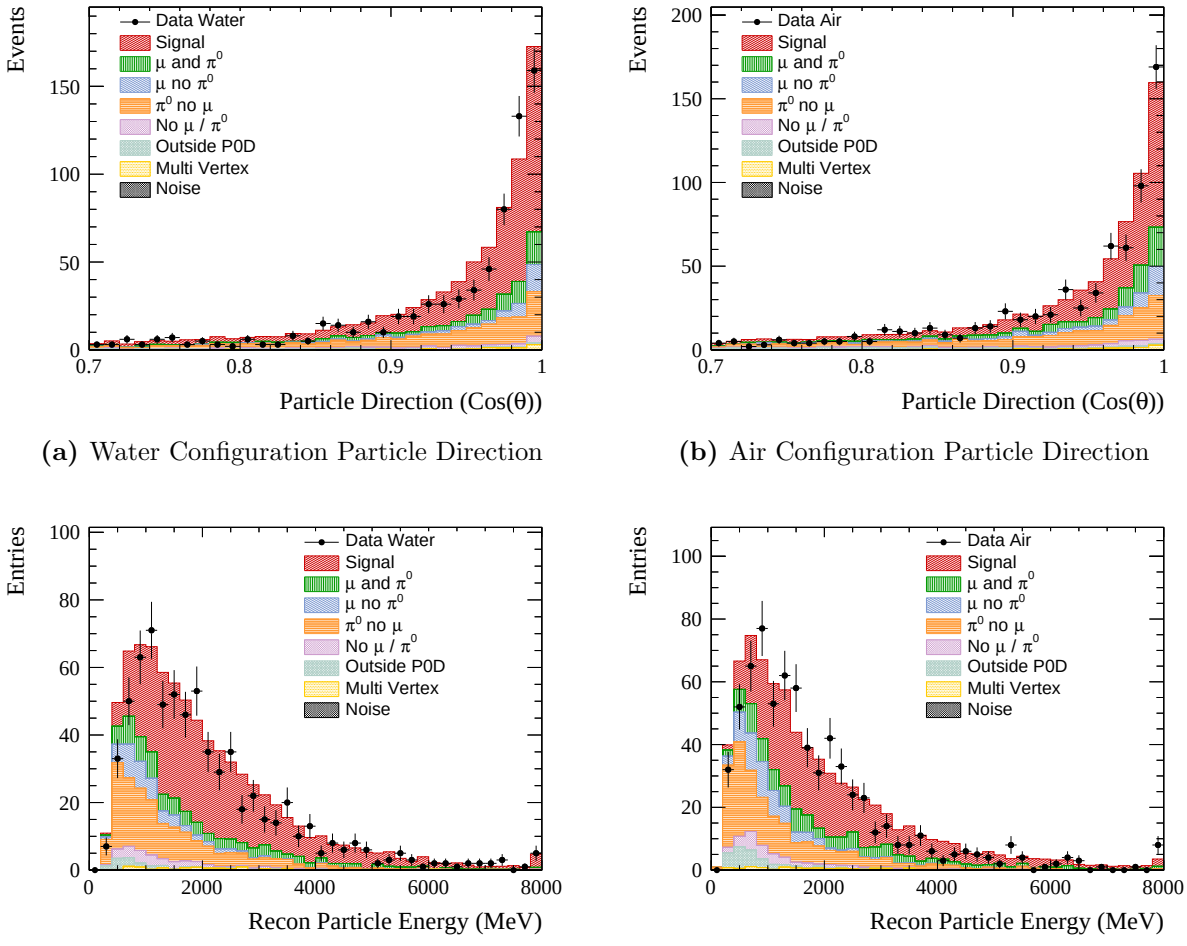

(a) Water Configuration Particle Direction

(b) Air Configuration Particle Direction

(c) Water Configuration Particle Energy

(d) Air Configuration Particle Energy

Figure 5.19: Events passing the event selection as a function of the particle direction and particle energy for the water and air configuration. The MC events are normalized to the data POT, and with BANFF post-fit.

Chapter 6

CC$\bar{\nu}_e$ Interaction Rate Measurement

Since May 2014, T2K has been taking data with anti-neutrino beam mode. The goal is to measure $\bar{\nu}_\mu$ disappearance and $\bar{\nu}_e$ appearance, which are necessary steps toward the future CP-violation searches. In this chapter, a preliminary result of $\bar{\nu}_e$ interaction rate measurement with the PØD is described.

6.1 Analysis Overview

In this analysis anti-neutrino run data of the T2K Run 5 and Run 6, are used. All the data were taken with the PØD air configuration. The summary of the data used in the analysis can be found in Tab. 2.2. Run 6 data files, however, are not fully processed yet and are with only preliminary calibration constants. In order to get the first idea of $\bar{\nu}_e$ result, results with these files will be shown, but one needs to keep in mind that the final result can change with the fully-calibrated Run 6 files.

Unlike the previous ν_e analyses, one needs to distinguish between neutrino and anti-neutrino interactions. While anti-neutrino contribution is negligible in ν_e analyses, neutrino contribution in $\bar{\nu}_e$ analysis is fairly large. This is because of the fact that neutrino flux component is non-negligible in anti-neutrino beam. Figure 6.1 shows the ND280 flux prediction for both neutrino and anti-neutrino beam mode, which clearly show that the neutrino portion in anti-neutrino beam is much larger than anti-neutirno portion in neutrino beam, especially at higher neutrino energy region.

However, unlike tracker part of the ND280, the PØD is not capable of discriminating ν_e interactions from $\bar{\nu}_e$ interactions. For track-like events, such as μ events, one can study the curvature of the track due to the magnetic field and distinguish μ events from $\bar{\mu}$ events. For electron events, however, study of the difference in shower development is required, which is much more challenging. Moreover, Super-Kamiokande also does not have event-by-event discrimination power between anti-neutrino and neutrino[1]. Hence the analysis aim to select both ν_e and $\bar{\nu}_e$ event: the signal definition will be charged current ν_e or charged current $\bar{\nu}_e$ interactions in the PØD.

[1]Statistically, SK distinguishes between neutrino and anti-neutrino.

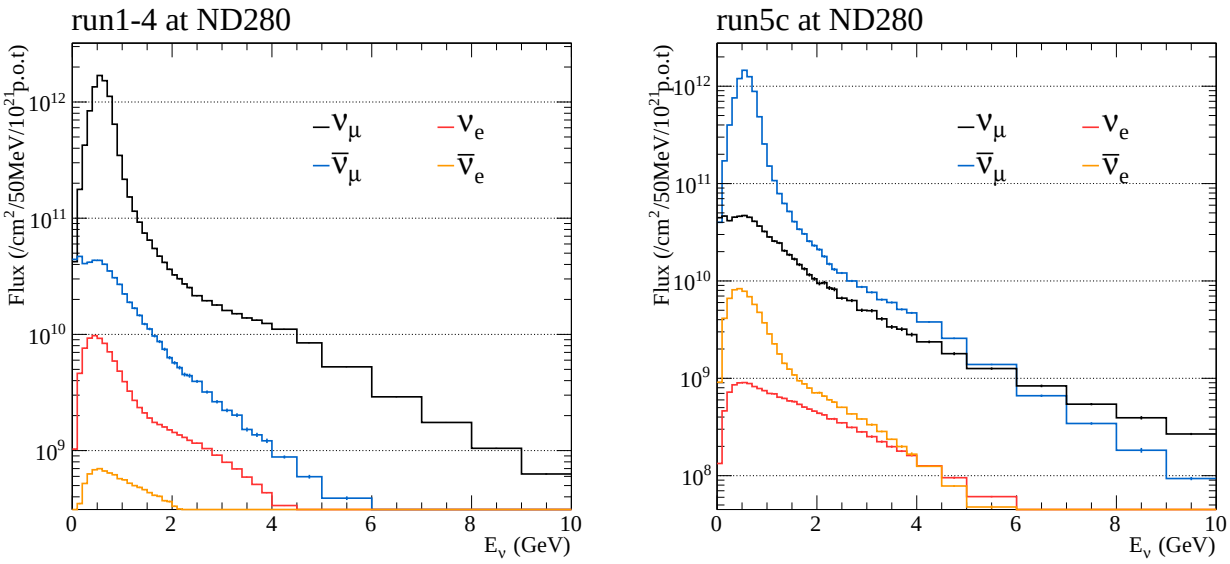

Figure 6.1: The ND280 flux prediction for Runs 1-4 (horns operating in 250 kA mode) and for Run 5c (horns operating in -250 kA mode). All plots are normalized to 1×10^{21} POT.

6.2 Event Selection

The $\bar{\nu}_e$ analysis shares the same sets of selection criteria with the CCν_e analysis, Sec.4.3. We optimize tunable cuts, shower median width and vertex Z position cut, by maximizing $S/\sqrt{B}$, with signal definition as $\nu_e + \bar{\nu}_e$.

6.3 Selected Event Sample

The number of selected MC events normalized to the data POT, together with the number of selected data events are presented in Tab. 6.1.

The efficiency ϵ and the purity p of MC signal events are defined as same as the ν_e analysis without energy threshold (Sec. 5.4.2). The values of T, the number of true MC

Table 6.1: The selected number of MC signal events S, MC background events B, and the total number of selected MC events $S + B$ normalized to the data POT are listed together with the selected data events D. The errors correspond to the statistical uncertainty due to the limited MC statistics.

	MC Signal S	MC Background B	MC Total $S + B$	Data D
Air	118.2 ± 2.78	65.6 ± 2.3	183.8 ± 3.6	199

Table 6.2: The number of true signal events T with true vertex within the fiducial volume, the signal efficiencies ϵ and purities p are listed. The errors correspond to the statistical uncertainty due to the limited MC statistics.

	Truth T	Efficiency ϵ	Purity p
Air	858.7 ± 8.1	$(13.8 \pm 0.2)\,\%$	$(64.3 \pm 1.3)\,\%$

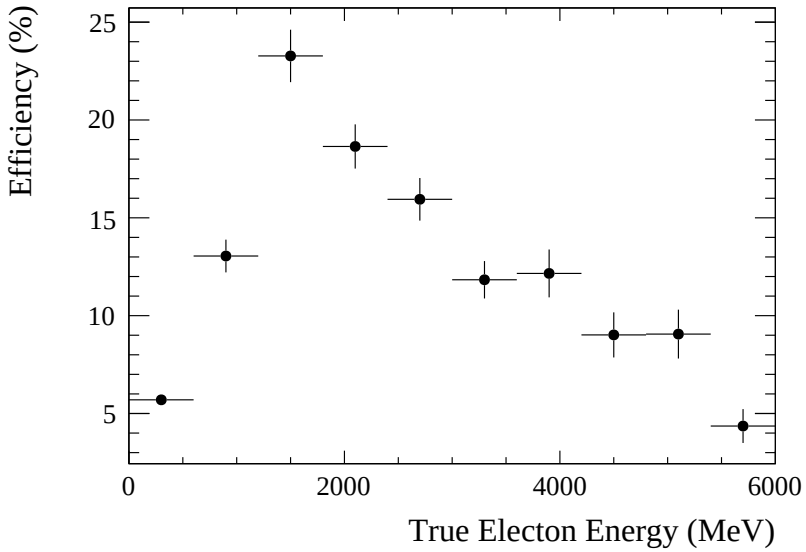

Figure 6.2: Selection efficiency of signal events as function of the true neutrino energy. The error bars correspond to the uncertainties due to limited MC statistics.

signal events with true vertex within the fiducial volume, namely the obtained efficiencies, and the calculated purities are listed in Tab. 6.2.

The selection efficiency of signal events as function of the true neutrino energy E_{true} is shown in Fig. 6.2. The selection of high energy signal events is suppressed by the shower median width cut and the shower charge fraction cut. Table 6.3 shows the number of selected MC events with the background events broken down by event type. The table clearly shows that the majority of the background events contain a π^0. Figure 6.3 shows the reconstructed particle direction and the reconstructed particle energy of selected events, with the MC events normalize to the data POT.

The background subtracted data/MC ratio is R is:

$$R_{air} = 1.13 \pm 0.12(stat.) \tag{6.1}$$

Table 6.3: Selected MC events broken down by the event type. The MC events are normalized to the data POT.

Event Type	Events	Rel. (%)
CC$\bar{\nu}_e$	73.8	40.1
CCν_e	44.4	24.2
μ and π^0	8.7	4.7
μ no π^0	11.4	6.2
π^0 no μ	34.5	18.8
No μ/π^0	4.5	2.4
Outside P0D	6.2	3.4
Multi Vertex	0.4	0.2
Noise	0.0	0.00
Total	183.8	100.0

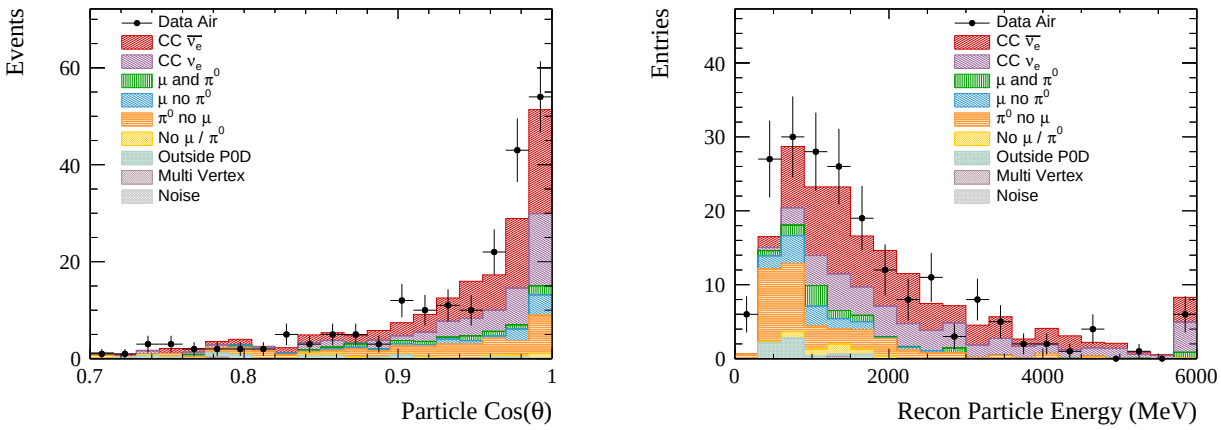

Figure 6.3: Events passing the event selection as a function of the particle direction and particle energy. The MC events are normalized to the data POT.

6.4 Prospect

In this thesis, the event selection and the analysis strategy for $\bar{\nu}_e$ interaction rate measurement is completed but the systematic study has not been done yet. The preliminary study shows promising results with fairly good agreement between the data and MC, along with relatively high purity and efficiency. In the near future, more detailed study of systematic uncertainties will be performed. This is currently the only ND280 analysis that can provide $\bar{\nu}_e$ information with sufficient statistics; hence important for future T2K anti-neutrino oscillation analysis.

Chapter 7

Conclusion

In this thesis, measurement of charged Current ν_e and $\bar{\nu}_e$ interactions using the T2K PØD have been made. The PØD includes fillable water targets which allows separate measurement for the water and air configurations of the ND280 PØD as well as the measurements of $\nu_e/\bar{\nu}_e$ on-water interactions in a predominantly ν_μ beam.

The analyses used Run 1 through Run 4 data of neutrino beam, with 2.64×10^{20} POT for PØD water configuration and 3.49×10^{20} POT for PØD air configuration. The anti-neutrino beam data (Run 5 through Run 6) of 2.83×10^{20} POT with PØD air configuration is also used for $\bar{\nu}_e$ analysis.

For the ν_e interaction measurements, the study were performed in two parts: Firstly, it was studied above the neutrino energy above 1.5 GeV, where ∼85% of the selected sample comes from the decay of kaons. The simulation expects 182.9 signal events for the water configuration and 158.7 signal events for air configuration. The resulting background-subtracted data to MC ratios for the water, air and on-water configuration are:

$$R_{\text{water}} = 0.89 \pm 0.08\ (\text{stat.}) \pm 0.11\ (\text{sys.}) \tag{7.1}$$
$$R_{\text{air}} = 0.90 \pm 0.09\ (\text{stat.}) \pm 0.13\ (\text{sys.}) \tag{7.2}$$
$$R_{\text{on-water}} = 0.87 \pm 0.33\ (\text{stat.}) \pm 0.21\ (\text{sys.}) \tag{7.3}$$

Then with the newly updated software and new sets of event selection, the measurement in all energy spectrum has been made. Due to removal of the neutrino energy threshold, although the purity has decreased, the statistics is higher. According to the MC simulation it is expected that there are 435.5 signal events for the water configuration and 341.1 signal events for the air configuration. The resulting background-subtracted data to MC ratios for the water, air and on-water configuration are:

$$R_{\text{water}} = 0.83 \pm 0.05\ (\text{stat.}) \pm 0.14\ (\text{sys.}) \tag{7.4}$$
$$R_{\text{air}} = 0.86 \pm 0.06\ (\text{stat.}) \pm 0.16\ (\text{sys.}) \tag{7.5}$$
$$R_{\text{on-water}} = 0.76 \pm 0.23\ (\text{stat.}) \pm 0.24\ (\text{sys.}) \tag{7.6}$$

For the $\bar{\nu}_e$ interaction measurement, only the preliminary study was performed. The event selection has been updated from the ν_e analyses, and the signal definition is $\nu_e + \bar{\nu}_e$ events as PØD is not capable of distinguish $\bar{\nu}_e$ from ν_e. The simulation expects 118.2 signal events for air configuration. The resulting background-subtracted data to MC ratio for air with only statistical error is:

$$R_{air} = 1.13 \pm 0.12(stat.) \tag{7.7}$$

For all analyses, the observed number of selected events is in good agreement with the prediction for the water configuration, the air configuration, and for the on-water subtraction sample. The measurement is statistically limited, especially for on-water. However, it will be improved in the future since collection of 10 times more data is planned in the coming years.

These are the first $\nu_e/\bar{\nu}_e$ interaction rate measurements on water in the few GeV energy region. Interaction of $\nu_e/\bar{\nu}_e$ on water are of particular interest for long-baseline neutrino experiments using water Cherenkov detectors with the aim to measure CP violation in the lepton sector.

Bibliography

[1] W. Pauli. *Letter to L. Metner and her colleagues*. 1930.

[2] F. Reines, C. L. Cowan, et al. *Phys. Rev.*, 117, 1960.

[3] G. Danby et al. *Phys. Rev. Lett*, 9, 1962.

[4] F. J. Hasert et al. (Gargamelle Collaboration). *Phys. Lett. B*, 46, 2012.

[5] K. Kodama et al. (DONUT Collaboration). *Phys. Lett. B*, 504, 2001.

[6] S. Schael et al. *Phys. Rept.*, 427, 2006.

[7] G. Aad et al. (ATLAS Collaboration). *Phys. Lett. B*, 716, 2012.

[8] S. Chatrchyan et al. (CMS Collaboration). *Phys. Lett. B*, 716, 2012.

[9] A. Sunyar M. Goldhaber, L. Grodzins. *Physical review*, 109(3), 1958.

[10] B. Pontecorvo. *Zh. Eksp. Teor. Fiz.*, 33, 1957.

[11] B. Pontecorvo. *Zh. Eksp. Teor. Fiz.*, 34, 1958.

[12] S. Sakata Z. Maki, M. Nakagawa. *Prog. Theor. Phys.*, 28, 1962.

[13] K. A. Olve et al. (Particle Data Group). *Chin. Phys. C*, 38, 2014.

[14] C. F. von Weizsacker. *Physikalische Zeitschrift*, 39, 1938.

[15] H. A. Bethe. *Phys. Rev.*, 55, 1939.

[16] K. C. Hoffman J. Davis, D. S. Harmer. *Phys. Rev. Lett.*, 20, 1968.

[17] R. L. Sears. *Astrophys. J*, 140, 1964.

[18] Q. R. Ahmad et al. (SNO COllaboration). *Phys. Rev. Lett.*, 87, 2001.

[19] Y. Fukuda et al. (Super-Kamiokande Collaboration). *Phys. Rev. Lett.*, 81, 1998.

[20] K. Abe et al. (T2K Collaboration). *Phys. Rev. Lett.*, 107, 2011.

[21] F. An et al. (DAYA-BAY Collaboration). *Phys. Rev. Lett.*, 108, 2012.

[22] J. Ahn et al. (RENO Collaboration). *Phys. Rev. Lett.*, 108, 2012.

[23] Y. Abe et al. (Double Chooz Collaboration). *Phys. Rev. D*, 86, 2012.

[24] R. E. Shrock and L. L. Wang, 1978.

[25] J. A. Formaggio and G. P. Zeller. *Rev. Mod. Phys.*, 84, 2012.

[26] D. Casper. *Nucl. Phys. (Proc. Supp.)*, 112, 2002.

[27] K. Abe et al. (T2K Collaboration). *Nucl.Instrum.Meth.*, A659:106–135, 2011.

[28] Y. Yamazaki et al. *KEK-Report*, 2002-13, 2003.

[29] S. Assylbekov et al. *Nucl.Instrum.Meth.*, A686(0):48 – 63, 2012.

[30] N. Abgrall et al. *Nucl. Instrum. Methods Phys. Res., Sect. A*, 637:25–46, 2011.

[31] P. A. Amaudruz et al. *Nucl. Instrum. Meth.*, A696, 2012.

[32] D. Allan et al. *Journal of Instrum.*, 8, 2013.

[33] S. Aoki et al. *Nucl.Instrum.Meth.*, A698:135–146, 2013.

[34] M. Otani et al. *Nucl. Instrum. Methods Phys. Res. Sect. A*, 623(1):368 – 370, 2010.

[35] S. Fukuda et al. *Nucl.Instrum.Meth*, A501:418 – 462, 2003.

[36] K. Abe et al. (T2K Collaboration). *Phys. Rev. Lett.*, 112, 2014.

[37] K. Abe et al. (T2K Collaboration). *Phys. Rev. D*, 85, 2012.

[38] K. Abe et al. (T2K Collaboration). *Phys. Rev. Lett.*, 111, 2013.

[39] K. Abe et al. (T2K Collaboration). *Phys. Rev. D*, 87, 2013.

[40] K. Abe et al. *Phys. Rev. Lett.*, 112, 2014.

[41] G. Gran et al. *Phys. Rev. D*, 74, 2006.

[42] C. Mariani et al. *Phys. Rev. D*, 83, 2011.

[43] A. Rodriguez et al. *Phys. Rev. D*, 78, 2008.

[44] S. Nakayama et al. *Phys. Rev. Lett.*, 619, 2005.

[45] M. Hasegawa et al. *Phys. Rev. Lett.*, 95, 2005.

[46] M. Yokoyama et al. *Nucl. Instrum. Meth.*, A610, 2009.

[47] Y. Hayato. *Nucl. Phys. B, Proc. Suppl.*, 112, 2002.

[48] Andreas Schalicke et al. *J. Phys: Conf. Ser.*, 331, 2011.

[49] O. Kadri et al. *Nucl. Instrum. Meth*, B258:381–387, 2007.

[50] D. L. Sawkey and B. A. Faddegon. *Med Phys.*, 36(3):698–707, 2009.

[51] V. N. Ivanchenko. Geant4 toolkit for simulation of hep experiments. *Nucl. Instrum. Meth*, A502:666–668, 2003.

[52] A. Kolmogorov. *G. Ist. Ital. Attuari*, 4:8391, 1933.

[53] N. Smirnov. *Annals of Mathematical Statistics*, 19:279281, 1948.

[54] K. Gilje. *PhD thesis*, Stony Brook University, 2014.

[55] M. Day and K. S. McFarland. *Phys. Rev. D*, 86, 2012.

[56] K. Abe et al. *Phys. Rev. D*, 89, 2014.

[57] K. Abe et al. (T2K Collaboration). *Phys. Rev. D*, 91, 2015.

Appendix A

Publication

The high energy ν_e interaction rate measurement on water, based on the analysis of this thesis, was published in Physical Review D. In the following pages we reproduced the article published.

Measurement of the electron neutrino charged-current interaction rate on water with the T2K ND280 π^0 detector

K. Abe,[1] J. Adam,[2] H. Aihara,[3,4] C. Andreopoulos,[5,6] S. Aoki,[7] A. Ariga,[8] S. Assylbekov,[9] D. Autiero,[10] M. Barbi,[11] G. J. Barker,[12] G. Barr,[13] P. Bartet-Friburg,[14] M. Bass,[9] M. Batkiewicz,[15] F. Bay,[16] V. Berardi,[17] B. E. Berger,[9,4] S. Berkman,[18] S. Bhadra,[19] F. d. M. Blaszczyk,[20] A. Blondel,[21] S. Bolognesi,[22] S. Bordoni,[23] S. B. Boyd,[12] D. Brailsford,[24] A. Bravar,[21] C. Bronner,[4] N. Buchanan,[9] R. G. Calland,[4] J. Caravaca Rodríguez,[23] S. L. Cartwright,[25] R. Castillo,[23] M. G. Catanesi,[17] A. Cervera,[26] D. Cherdack,[9] N. Chikuma,[3] G. Christodoulou,[6] A. Clifton,[9] J. Coleman,[6] S. J. Coleman,[27] G. Collazuol,[28] K. Connolly,[29] L. Cremonesi,[30] A. Dabrowska,[15] R. Das,[9] S. Davis,[29] P. de Perio,[31] G. De Rosa,[32] T. Dealtry,[33,13] S. R. Dennis,[12,5] C. Densham,[5] D. Dewhurst,[13] F. Di Lodovico,[30] S. Di Luise,[16] S. Dolan,[13] O. Drapier,[34] K. Duffy,[13] J. Dumarchez,[14] S. Dytman,[35] M. Dziewiecki,[36] S. Emery-Schrenk,[22] A. Ereditato,[8] L. Escudero,[26] T. Feusels,[18] A. J. Finch,[33] G. A. Fiorentini,[19] M. Friend,[37,*] Y. Fujii,[37,*] Y. Fukuda,[38] A. P. Furmanski,[12] V. Galymov,[10] A. Garcia,[23] S. Giffin,[11] C. Giganti,[14] K. Gilje,[2] D. Goeldi,[8] T. Golan,[39] M. Gonin,[34] N. Grant,[33] D. Gudin,[40] D. R. Hadley,[12] L. Haegel,[21] A. Haesler,[21] M. D. Haigh,[12] P. Hamilton,[24] D. Hansen,[35] T. Hara,[7] M. Hartz,[4,41] T. Hasegawa,[37,*] N. C. Hastings,[11] T. Hayashino,[42] Y. Hayato,[1,4] R. L. Helmer,[41] M. Hierholzer,[8] J. Hignight,[2] A. Hillairet,[43] A. Himmel,[44] T. Hiraki,[42] S. Hirota,[42] J. Holeczek,[45] S. Horikawa,[16] F. Hosomi,[3] K. Huang,[42] A. K. Ichikawa,[42] K. Ieki,[42] M. Ieva,[23] M. Ikeda,[1] J. Imber,[34] J. Insler,[46] T. J. Irvine,[47] T. Ishida,[37,*] T. Ishii,[37,*] E. Iwai,[37] K. Iwamoto,[48] K. Iyogi,[1] A. Izmaylov,[26,40] A. Jacob,[13] B. Jamieson,[49] M. Jiang,[42] S. Johnson,[27] J. H. Jo,[2] P. Jonsson,[24] C. K. Jung,[2,†] M. Kabirnezhad,[50] A. C. Kaboth,[24] T. Kajita,[47,†] H. Kakuno,[51] J. Kameda,[1] Y. Kanazawa,[3] D. Karlen,[43,41] I. Karpikov,[40] T. Katori,[30] E. Kearns,[20,†] M. Khabibullin,[40] A. Khotjantsev,[40] D. Kielczewska,[52] T. Kikawa,[42] A. Kilinski,[50] J. Kim,[18] S. King,[30] J. Kisiel,[45] P. Kitching,[59] T. Kobayashi,[37,*] L. Koch,[53] T. Koga,[3] A. Kolaceke,[11] A. Konaka,[41] A. Kopylov,[40] L. L. Kormos,[33] A. Korzenev,[21] Y. Koshio,[54,†] W. Kropp,[55] H. Kubo,[42] Y. Kudenko,[40,‡] R. Kurjata,[36] T. Kutter,[46] J. Lagoda,[50] I. Lamont,[33] E. Larkin,[12] M. Laveder,[28] M. Lawe,[33] M. Lazos,[6] T. Lindner,[41] C. Lister,[12] R. P. Litchfield,[12] A. Longhin,[28] J. P. Lopez,[27] L. Ludovici,[56] L. Magaletti,[17] K. Mahn,[57] M. Malek,[25] S. Manly,[48] A. D. Marino,[27] J. Marteau,[10] J. F. Martin,[31] P. Martins,[30] S. Martynenko,[40] T. Maruyama,[37,*] V. Matveev,[40] K. Mavrokoridis,[6] E. Mazzucato,[22] M. McCarthy,[19] N. McCauley,[6] K. S. McFarland,[48] C. McGrew,[2] A. Mefodiev,[40] C. Metelko,[6] M. Mezzetto,[28] P. Mijakowski,[50] C. A. Miller,[41] A. Minamino,[42] O. Mineev,[40] S. Mine,[55] A. Missert,[27] M. Miura,[1,†] S. Moriyama,[1,†] Th. A. Mueller,[34] A. Murakami,[42] M. Murdoch,[6] S. Murphy,[16] J. Myslik,[43] T. Nakadaira,[37,*] M. Nakahata,[1,4] K. G. Nakamura,[42] K. Nakamura,[4,*] S. Nakayama,[1,†] T. Nakaya,[42,4] K. Nakayoshi,[37,*] C. Nantais,[18] C. Nielsen,[18] M. Nirkko,[8] K. Nishikawa,[37,*] Y. Nishimura,[47] J. Nowak,[33] H. M. O'Keeffe,[33] R. Ohta,[37,*] K. Okumura,[47,4] T. Okusawa,[58] W. Oryszczak,[52] S. M. Oser,[18] T. Ovsyannikova,[40] R. A. Owen,[30] Y. Oyama,[37,*] V. Palladino,[32] J. L. Palomino,[2] V. Paolone,[35] D. Payne,[6] O. Perevozchikov,[46] J. D. Perkin,[25] Y. Petrov,[18] L. Pickard,[25] E. S. Pinzon Guerra,[19] C. Pistillo,[8] P. Plonski,[36] E. Poplawska,[30] B. Popov,[14,§] M. Posiadala-Zezula,[52] J.-M. Poutissou,[41] R. Poutissou,[41] P. Przewlocki,[50] B. Quilain,[34] E. Radicioni,[17] P. N. Ratoff,[33] M. Ravonel,[21] M. A. M. Rayner,[21] A. Redij,[8] M. Reeves,[33] E. Reinherz-Aronis,[9] C. Riccio,[32] P. A. Rodrigues,[48] P. Rojas,[9] E. Rondio,[50] S. Roth,[53] A. Rubbia,[16] D. Ruterbories,[9] A. Rychter,[36] R. Sacco,[30] K. Sakashita,[37,*] F. Sánchez,[23] F. Sato,[37] E. Scantamburlo,[21] K. Scholberg,[44] S. Schoppmann,[53] J. D. Schwehr,[9] M. Scott,[41] Y. Seiya,[58] T. Sekiguchi,[37,*] H. Sekiya,[1,†] D. Sgalaberna,[16] R. Shah,[5,13] A. Shaikhiev,[40] F. Shaker,[49] D. Shaw,[33] M. Shiozawa,[1,4] S. Short,[30] Y. Shustrov,[40] P. Sinclair,[24] B. Smith,[24] M. Smy,[55] J. T. Sobczyk,[39] H. Sobel,[55,4] M. Sorel,[26] L. Southwell,[33] P. Stamoulis,[26] J. Steinmann,[53] Y. Suda,[3] A. Suzuki,[7] K. Suzuki,[42] S. Y. Suzuki,[37,*] Y. Suzuki,[4] R. Tacik,[11,41] M. Tada,[37,*] S. Takahashi,[42] A. Takeda,[1] Y. Takeuchi,[7,4] H. K. Tanaka,[1,†] H. A. Tanaka,[18,‖] M. M. Tanaka,[37,*] D. Terhorst,[53] R. Terri,[30] L. F. Thompson,[25] A. Thorley,[6] S. Tobayama,[18] W. Toki,[9] T. Tomura,[1] C. Touramanis,[6] T. Tsukamoto,[37,*] M. Tzanov,[46] Y. Uchida,[24] A. Vacheret,[13] M. Vagins,[4,55] G. Vasseur,[22] T. Wachala,[15] K. Wakamatsu,[58] C. W. Walter,[44] D. Wark,[5,13] W. Warzycha,[52] M. O. Wascko,[24] A. Weber,[5,13] R. Wendell,[1,†] R. J. Wilkes,[29] M. J. Wilking,[2] C. Wilkinson,[25] Z. Williamson,[13] J. R. Wilson,[30] R. J. Wilson,[9] T. Wongjirad,[44] Y. Yamada,[37,*] K. Yamamoto,[58] C. Yanagisawa,[2,¶] T. Yano,[7] S. Yen,[41] N. Yershov,[40] M. Yokoyama,[3,†] J. Yoo,[46] K. Yoshida,[42] T. Yuan,[27] M. Yu,[19] A. Zalewska,[15] J. Zalipska,[50] L. Zambelli,[37,*] K. Zaremba,[36] M. Ziembicki,[36] E. D. Zimmerman,[27] M. Zito,[22] and J. Żmuda[39]

(T2K Collaboration)

[1]*University of Tokyo, Institute for Cosmic Ray Research, Kamioka Observatory, Kamioka, Japan*
[2]*State University of New York at Stony Brook, Department of Physics and Astronomy, Stony Brook, New York 11794, USA*
[3]*University of Tokyo, Department of Physics, Tokyo, Japan*
[4]*Kavli Institute for the Physics and Mathematics of the Universe (WPI), Todai Institutes for Advanced Study, University of Tokyo, Kashiwa, Chiba, Japan*

[5]*STFC, Rutherford Appleton Laboratory, Harwell Oxford, and Daresbury Laboratory, Warrington, United Kingdom*
[6]*University of Liverpool, Department of Physics, Liverpool, United Kingdom*
[7]*Kobe University, Kobe, Japan*
[8]*University of Bern, Albert Einstein Center for Fundamental Physics, Laboratory for High Energy Physics (LHEP), Bern, Switzerland*
[9]*Colorado State University, Department of Physics, Fort Collins, Colorado 80523, USA*
[10]*Université de Lyon, Université Claude Bernard Lyon 1, IPN Lyon (IN2P3), Villeurbanne, France*
[11]*University of Regina, Department of Physics, Regina, Saskatchewan, Canada*
[12]*University of Warwick, Department of Physics, Coventry, United Kingdom*
[13]*Oxford University, Department of Physics, Oxford, United Kingdom*
[14]*UPMC, Université Paris Diderot, CNRS/IN2P3, Laboratoire de Physique Nucléaire et de Hautes Energies (LPNHE), Paris, France*
[15]*H. Niewodniczanski Institute of Nuclear Physics PAN, Cracow, Poland*
[16]*ETH Zurich, Institute for Particle Physics, Zurich, Switzerland*
[17]*INFN Sezione di Bari and Università e Politecnico di Bari, Dipartimento Interuniversitario di Fisica, Bari, Italy*
[18]*University of British Columbia, Department of Physics and Astronomy, Vancouver, British Columbia, Canada*
[19]*York University, Department of Physics and Astronomy, Toronto, Ontario, Canada*
[20]*Boston University, Department of Physics, Boston, Massachusetts 02215, USA*
[21]*University of Geneva, Section de Physique, DPNC, Geneva, Switzerland*
[22]*IRFU, CEA Saclay, Gif-sur-Yvette, France*
[23]*Institut de Fisica d'Altes Energies (IFAE), Bellaterra (Barcelona), Spain*
[24]*Imperial College London, Department of Physics, London, United Kingdom*
[25]*University of Sheffield, Department of Physics and Astronomy, Sheffield, United Kingdom*
[26]*IFIC (CSIC & University of Valencia), Valencia, Spain*
[27]*University of Colorado at Boulder, Department of Physics, Boulder, Colorado 80309, USA*
[28]*INFN Sezione di Padova and Università di Padova, Dipartimento di Fisica, Padova, Italy*
[29]*University of Washington, Department of Physics, Seattle, Washington 98195, USA*
[30]*Queen Mary University of London, School of Physics and Astronomy, London, United Kingdom*
[31]*University of Toronto, Department of Physics, Toronto, Ontario, Canada*
[32]*INFN Sezione di Napoli and Università di Napoli, Dipartimento di Fisica, Napoli, Italy*
[33]*Lancaster University, Physics Department, Lancaster, United Kingdom*
[34]*Ecole Polytechnique, IN2P3-CNRS, Laboratoire Leprince-Ringuet, Palaiseau, France*
[35]*University of Pittsburgh, Department of Physics and Astronomy, Pittsburgh, Pennsylvania 15260, USA*
[36]*Warsaw University of Technology, Institute of Radioelectronics, Warsaw, Poland*
[37]*High Energy Accelerator Research Organization (KEK), Tsukuba, Ibaraki, Japan*
[38]*Miyagi University of Education, Department of Physics, Sendai, Japan*
[39]*Wroclaw University, Faculty of Physics and Astronomy, Wroclaw, Poland*
[40]*Institute for Nuclear Research of the Russian Academy of Sciences, Moscow, Russia*
[41]*TRIUMF, Vancouver, British Columbia, Canada*
[42]*Kyoto University, Department of Physics, Kyoto, Japan*
[43]*University of Victoria, Department of Physics and Astronomy, Victoria, British Columbia, Canada*
[44]*Duke University, Department of Physics, Durham, North Carolina 27708, USA*
[45]*University of Silesia, Institute of Physics, Katowice, Poland*
[46]*Louisiana State University, Department of Physics and Astronomy, Baton Rouge, Louisiana 70803, USA*
[47]*University of Tokyo, Institute for Cosmic Ray Research, Research Center for Cosmic Neutrinos, Kashiwa, Japan*
[48]*University of Rochester, Department of Physics and Astronomy, Rochester, New York 14627, USA*
[49]*University of Winnipeg, Department of Physics, Winnipeg, Manitoba, Canada*
[50]*National Centre for Nuclear Research, Warsaw, Poland*
[51]*Tokyo Metropolitan University, Department of Physics, Tokyo, Japan*
[52]*University of Warsaw, Faculty of Physics, Warsaw, Poland*
[53]*RWTH Aachen University, III. Physikalisches Institut, Aachen, Germany*
[54]*Okayama University, Department of Physics, Okayama, Japan*
[55]*University of California, Irvine, Department of Physics and Astronomy, Irvine, California 92697, USA*
[56]*INFN Sezione di Roma and Università di Roma "La Sapienza," Roma, Italy*

[57]Michigan State University, Department of Physics and Astronomy, East Lansing, Michigan 48824, USA
[58]Osaka City University, Department of Physics, Osaka, Japan
[59]University of Alberta, Centre for Particle Physics, Department of Physics, Edmonton, Alberta, Canada
(Received 30 March 2015; revised manuscript received 8 May 2015; published 19 June 2015)

This paper presents a measurement of the charged current interaction rate of the electron neutrino beam component of the beam above 1.5 GeV using the large fiducial mass of the T2K π^0 detector. The predominant portion of the ν_e flux (~85%) at these energies comes from kaon decays. The measured ratio of the observed beam interaction rate to the predicted rate in the detector with water targets filled is $0.89 \pm 0.08(\text{stat}) \pm 0.11(\text{sys})$, and with the water targets emptied is $0.90 \pm 0.09(\text{stat}) \pm 0.13\,(\text{sys})$. The ratio obtained for the interactions on water only from an event subtraction method is $0.87 \pm 0.33(\text{stat}) \pm 0.21(\text{sys})$. This is the first measurement of the interaction rate of electron neutrinos on water, which is particularly of interest to experiments with water Cherenkov detectors.

DOI: 10.1103/PhysRevD.91.112010 PACS numbers: 13.15.+g

I. INTRODUCTION

This paper reports a measurement of the ratio of the charged current ν_e event rate relative to the simulation with NEUT [1] event generator, version 4.1.4.2, for neutrino energies above 1.5 GeV in the T2K beam. The interaction rate of electron neutrinos on water has never been measured at the neutrinos energies above 1.5 GeV, or at any other energies. The mean reconstructed energy of the selected neutrinos in the analysis presented in this paper is 2.7 GeV. The ν_e cross section has been measured on a liquid freon target for energies between 1.5 and 8 GeV by Gargamelle [2] and on ^{12}C for energies around 32 MeV at LANSCE [3]. Also at lower energies, the antielectron neutrino interactions have been measured by experiments near nuclear reactors. A review of neutrino cross section measurements can be found in [4].

The T2K experiment [5] was built with the primary goals of precisely determining the oscillation parameter θ_{13} via electron neutrino appearance, and of the parameters θ_{23} and Δm^2_{32} via muon neutrino disappearance. The predominantly ν_μ beam for these measurements is produced at the Japan Proton Accelerator Research Complex (J-PARC) in Tokai. The neutrinos from this beam are observed at a near detector, ND280, which is located 280 m downstream from the production target, where the neutrinos are not expected to have been affected by oscillations. The T2K far detector, Super-Kamiokande (SK), then measures the muon and electron neutrinos (and antineutrinos) after they have undergone a near maximal oscillation.

The oscillation probability for $\nu_\mu \to \nu_e$ depends on the mixing parameter, θ_{13}, and on subleading effects that depend on the charge parity (CP)-violating phase, δ_{CP}, and on the mass hierarchy [6]. T2K has already observed the appearance of 28 ν_e candidate events at the far detector with a 7.3σ significance over a background expectation of 4.92 ± 0.55 events for $\theta_{13} = 0$ [7]. The largest irreducible background for the appearance measurement comes from the predicted 3.2 intrinsic ν_e beam events.

In T2K the ν_e are expected to represent about 1.2% of the total neutrino flux [8]. The T2K ν_μ beam is produced by magnetic focusing of pions and kaons produced by the interaction of a proton beam with a graphite target. The unavoidable ν_e component comes from the decay of muons from pion decay, and from kaon decay. In any long-baseline neutrino experiment proposed to measure CP violation and precisely measure neutrino oscillation parameters, the ν_e component of the beam will be the main source of background [9–11].

The measurement of the beam ν_e charged current (CCν_e) interactions on a plastic scintillator and water target using ND280 tracker, was reported in [12]. This paper reports a direct measurement of this component of the charged current (CC) neutrino interactions in the ND280 π^0 detector (PØD) [13], which is located just upstream of the tracker. In this selection, the majority of the electron neutrinos were produced in kaon decay, and have energies above 1.5 GeV. The PØD detector has water targets that can be filled or emptied. Data were taken both with the targets filled to create a water target (water configuration), and empty to leave just air in place of the water target (air configuration). With data in the two configurations a subtraction analysis obtained the interaction rate just on water.

[*]Also at J-PARC, Tokai, Japan.
[†]Affiliated member at Kavli IPMU (WPI), the University of Tokyo, Japan.
[‡]Also at Moscow Institute of Physics and Technology and National Research Nuclear University "MEPhI," Moscow, Russia.
[§]Also at JINR, Dubna, Russia.
[‖]Also at Institute of Particle Physics, Canada.
[¶]Also at BMCC/CUNY, Science Department, New York, New York, USA.

Similar to the subtraction analysis presented here, a ratio analysis has been conducted by the Minerva collaboration for 2–20 GeV ν_μ on C, Fe, and Pb compared to CH [14]. A subtraction analysis of the Minerva data is presented in the thesis of Tice [15]. Apart from the Minerva measurements, this appears to be the only other use of the subtraction analysis to date in neutrino scattering experiments.

The ν_e and ν_μ come from the same pion to muon to electron decay chain, and lepton universality allows the expected rate of ν_e to be constrained by measuring the much larger flux of ν_μ. Details concerning the T2K beam flux measurement, and further information on recent measurements of ν_μ interactions in the near detectors, can be found in Ref. [16].

One of the systematic uncertainties in long-baseline neutrino oscillation measurements using water Cherenkov detectors comes from model uncertainties in the meson exchange current for C versus for O. Having measurements of neutrino interaction rates on water is therefore important. For a recent review of ν_μ cross section measurements on various nuclear targets refer to the PDG [17]. The only measurements of ν_μ neutrino interactions on water were reported by the K2K experiment for quasielastic interactions [18], and for reactions resulting in pions in the final state [19–22].

The paper is organized as follows. In Sec. II the PØD detector, used to do the measurement, is described. The electron selection, and expected backgrounds are then described in Sec. III. The particle identification (PID) to select electrons from muons in the PØD is a key component of this measurement, and will be described further in the section on event selection. The water subtraction method is then described in IV. The detector, reconstruction, flux and cross section systematic uncertainties in the measurement are reviewed in Sec. V. Finally the results of the rate measurement are presented in Sec. VI and a summary is in Sec. VII.

II. ND280 π^0 DETECTOR

The T2K ND280 π^0 Detector (PØD) is a scintillator based tracking calorimeter optimized to measure neutral current π^0 in the momentum range that contributes to backgrounds for ν_e appearance [13]. Refer to Fig. 4 of [13] for a picture of the PØD detector. The PØD is composed of layers of plastic scintillator alternating with water targets and brass sheets or lead sheets. The PØD sits in front of a tracking detector made up of two fine grain scintillator modules which serve as active targets placed between three time projection chambers. Both the PØD and tracking detector are surrounded by electromagnetic calorimeters and are in a 0.2 T magnetic field.

The PØD is constructed using 40 scintillator modules, each module is constructed with two perpendicular arrays of triangular scintillating bars and is approximately 38 mm thick. The scintillator modules are arranged in three regions. The most upstream and downstream regions of the detector are composed of seven modules interleaved with 4.5 mm thick sheets of stainless steel-clad lead that function as 4.9 radiation length electromagnetic calorimeters to improve the containment of photons and electrons. The central region serves as a target containing water. It has 25 water target layers that are 28 mm thick sandwiched between 26 scintillator modules and 1.3 mm brass sheets, positioned in between water targets and scintillator layers. The target region has a fiducial mass of approximately 1900 kg of water and 3570 kg of other materials.

The energy resolution of the PØD can be estimated from Monte Carlo studies by calculating the difference between true and reconstructed energy for many events. The energy resolution for electrons, after the selections described in III, is 16%.

III. EVENT SELECTION

A. Overview

In this analysis, all the data collected between January 2010 and May 2013 except for a very small fraction of run III data, due to the magnetic horn current decrease which caused a failure in good spill preselection, are used. The data are subdivided into different run periods and PØD configurations as shown in Table I. The simulated data used in this analysis corresponds to 10 times the protons on target (POT) of the data, and reproduces the various experimental conditions of the different data-taking periods.

Neutrino interactions in ND280 are simulated with the NEUT [1] event generator, version 5.1.4.2. The generator covers a range of neutrino energy from several tens of MeV to hundreds of TeV and simulates all the nuclear targets present in ND280. In the simulated data, neutrino interactions are generated outside and within the full ND280 volume including all active and inactive material, providing information to understand the signal and backgrounds from interactions outside the ND280 fiducial volume. The details of the simulation process are described in [23].

TABLE I. Summary of T2K runs and the number of protons on target (POT) used in the analysis.

T2K run	PØD configuration	Beam power (kW)	POT ($\times 10^{19}$)
Run I	Water	50	2.96
Run II	Water	120	6.96
Run II	Air	120	3.59
Run III	Air	178	13.5
Run IV	Water	178	16.5
Run IV	Air	178	17.8
Total	Water		26.4
	Air		34.9

Simulation of products of the neutrino interactions in the PØD is done using a GEANT 4.9.4 simulation [24–27]. The standard GEANT physics list for electromagnetic interactions is used in the simulation.

The analysis uses two reconstructed objects, a track and a shower. Within the PØD reconstruction algorithm, hits in the PØD scintillator layer associated with a reconstructed track classified as an electromagnetic track (typically electrons or photons) are forwarded to the shower reconstruction stage. Hits associated with a track that are classified as a light track (typically muon) or a heavy track (typically proton) are not forwarded to the shower reconstruction stage and cannot be reconstructed as a shower.

The signal events for the analysis are the charged current ν_e interactions in the PØD. A cut-based event selection using known reconstruction characteristics was tuned to maximize the product of efficiency and purity. To avoid bias, the selection strategy was developed based on Monte Carlo (MC) samples. Event displays of a typical CCν_e candidate and a π^0 background event selected in the analysis are shown in Fig. 1.

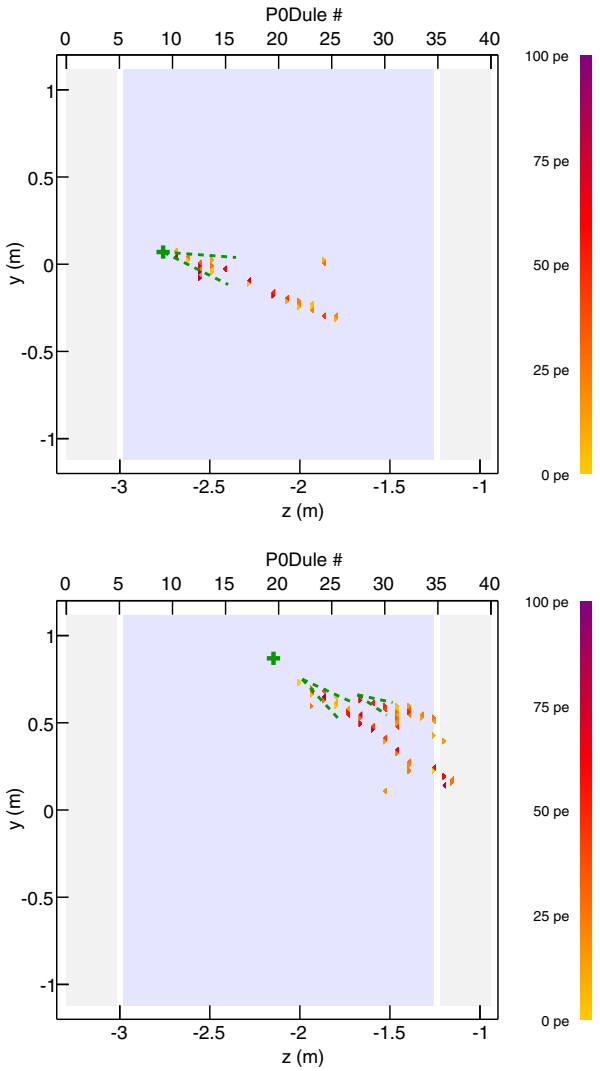

FIG. 1 (color online). Side view of a CCν_e event (top) and a π^0 background event (bottom) reconstructed in the PØD. Triangles are hits colored by the charge deposited, the green cross symbol shows the reconstructed shower vertex, and the green dashed lines show the cones of reconstructed showers.

B. Selection cuts

The event selection strategy focuses on identifying single high-energy electron shower events with a vertex in the PØD. As a preselection, the reconstructed shower in the PØD must be in time with the beam bunch time. The PØD reconstruction searches for both tracks and showers with two independent algorithms, and the highest energy track and the highest energy shower are used in the analysis. The reconstruction algorithm builds tracks and showers from hits, but as the shower reconstruction occurs after the track reconstruction the algorithm needs to make sure that the hits shower reconstruction uses are the same hits the track reconstruction uses, for each single event. Therefore 80% of the hits associated with the track and shower are required to be the same.

In addition, events are selected where the angle of the reconstructed shower with respect to the z-axis, which is approximately the beam axis, is less than 45°. The scintillator bars of the PØD have a triangular profile with angles of approximately 45°. Particles with an angle of more than 45° with respect to the beam axis would therefore hit more than two adjacent bars in a layer. The PØD reconstruction algorithm currently only handles up to two adjacent bar hits in a layer, causing reconstruction failures for higher angle tracks.

For this analysis, only events with a reconstructed neutrino energy of 1.5 GeV or more are selected. Reconstructed neutrino energy is calculated from the reconstructed electron energy and the electron angle using the quasielastic approximation. In this energy region, the majority of the ν_e flux arises from kaon decays and the PØD shows good performance to distinguish electrons from other particles. In addition, using a high neutrino energy cut improves the purity of the electron sample.

To reject muons, the median width of the selected track is used. In each scintillator layer, the energy-weighted standard deviation of the position of the hits reconstructed in the track is calculated as follows:

(1) If the two hits with the highest deposited energy are in adjacent strips, replace them with a single hit. The new hit's position is at the energy-weighted average position of the two original hits, and its energy is the sum of the energies of the original hits. Any other hits in the layers are left unchanged. This procedure gives layers with minimum ionizing tracks very small (almost always zero) width.

(2) The energy-weighted standard deviation of the hit positions is calculated for each layer.

(3) Median width is the width of the middle layer after ordering by layer width.

The design of the PØD with layers of high density materials (brass and lead) causes electrons to shower. The reconstructed track of an electron is therefore typically wider than the reconstructed track of a muon. This feature can be used to distinguish muons and electrons with the median width of the reconstructed candidate track.

The track median width for events which pass all the selection criteria with the exception of the track median width cut is shown in Fig. 2 and indicates that most of the background muon events are rejected by this cut.

Similarly, to reject background events that contain neutral pions, a cut is applied to the median width of the selected shower. The shower reconstruction looks for hits in a cone from the reconstructed vertex position and combines them in one or more showers. It can happen that hits from several particles are combined in one reconstructed shower, especially when they are almost overlapping. The PØD ν_e analysis looks for events with a single electron. Events with a very wide candidate shower are rejected, because such events are more likely background events with several particles. The shower median width is calculated the same way as the track median width. Distributions of events which pass all the selection criteria with the exception of the shower median width cut is shown in Fig. 3. It shows many π^0 background events are rejected with this cut.

Finally, a cut is applied to the fraction of the event's charge that is contained in the selected shower. To select CCν_e events with a high purity, the fraction of the event's charge contained in the candidate shower of exactly 1.0 is required, which selects only events with a single shower and without muonlike tracks in the final state.

C. Selected event samples

The selected number of events passing all cuts predicted by the simulation, both when the PØD is configured to contain water and air, together with the number of selected data events are presented in Table II. The water configuration simulation events are separated into on-water and

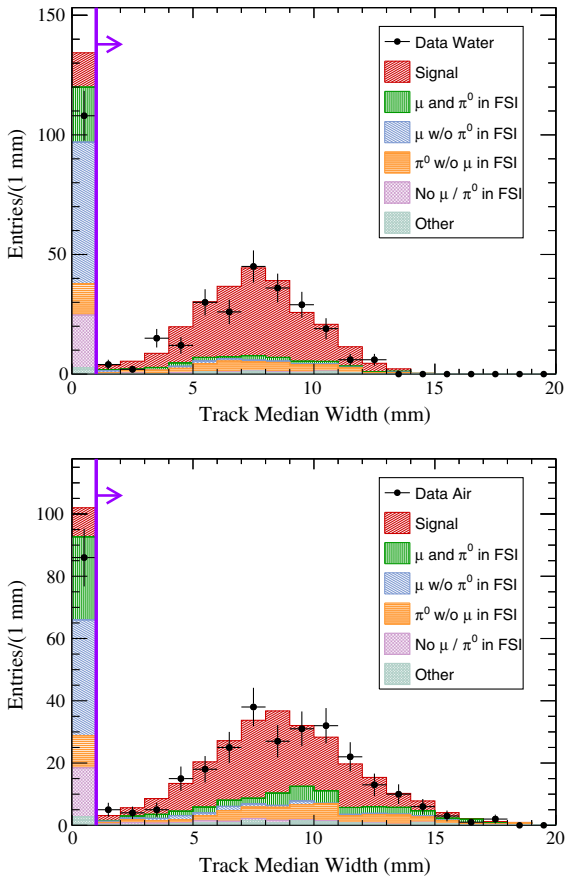

FIG. 2 (color online). Distribution of events which pass all the selection criteria with the exception of the track median width cut, for water (top) and air configuration (bottom). The vertical line shows the cut value used (1 mm). A sudden drop of events above 11 mm is an effect of shower median width cut.

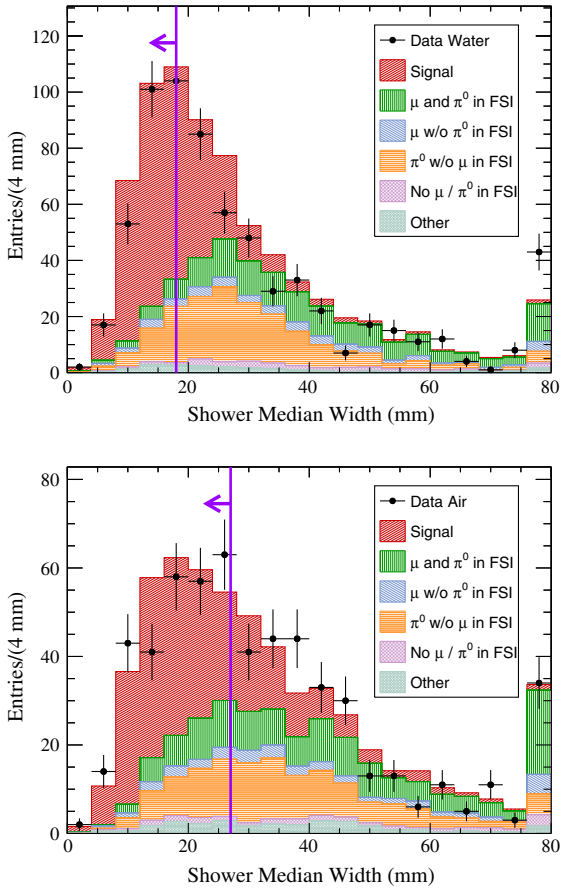

FIG. 3 (color online). Distribution of events which pass all the selection criteria with the exception of the shower median width cut, for water (top) and air configuration (bottom). The vertical line shows the applied cuts which are optimized for each configuration.

TABLE II. The selected number of MC signal events, MC background events, and the total number of selected MC events normalized to data POT for water and air configuration are listed together with the selected data events. In addition, the water configuration MC events are split up in on-water and not-water events. The errors correspond to the statistical uncertainty due to the limited MC statistics.

	MC signal	MC background	MC total	Data
Water	196.1 ± 4.8	56.7 ± 2.7	252.8 ± 5.5	230
On-water	60.2 ± 2.6	14.5 ± 1.3	74.7 ± 2.9	
Not-water	135.9 ± 4.0	42.2 ± 2.3	178.2 ± 4.6	
Air	173.6 ± 4.6	97.4 ± 3.6	271.0 ± 5.8	257

TABLE III. The signal efficiencies ϵ and purities p are listed for water and air configuration. Events of the PØD water configuration are split into events happening on-water and not-water. The errors correspond to the statistical uncertainty due to the limited MC statistics.

	Efficiency ϵ	Purity p
Water	$(10.9 \pm 0.3)\%$	$(77.6 \pm 2.5)\%$
On-water	$(9.8 \pm 0.4)\%$	$(80.6 \pm 4.7)\%$
Not-water	$(11.5 \pm 0.4)\%$	$(76.3 \pm 3.0)\%$
Air	$(11.0 \pm 0.3)\%$	$(64.1 \pm 2.2)\%$

not-water events. On-water events are defined as events with true interaction vertex in the water, and not-water events have the true interaction vertex on scintillator, lead, brass, or other materials besides water. All events in the air configuration MC are not-water events as the water targets are drained.

D. Efficiency and purity

The efficiency ϵ and purity p of the simulated electron neutrino signal events, for water and air configurations, are summarized in Table III. In the PØD water configuration, events are split into events happening on water (on-water) and events on scintillator, brass, and lead (not-water).

The selection efficiency of signal events as function of the true neutrino energy E_{true} for PØD water and air configurations are shown in Fig. 4. The selection of low energy signal events is suppressed by the high neutrino energy cut at 1.5 GeV while the selection of high energy signal events is suppressed by the shower median width cut and the shower charge fraction cut.

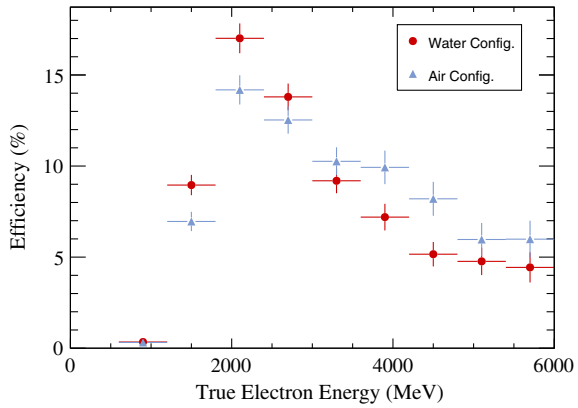

FIG. 4 (color online). Selection efficiency of signal events as a function of the true neutrino energy E_{true} for water and air configuration. The error bars correspond to the uncertainties due to limited MC statistics.

IV. WATER SUBTRACTION METHOD

The measured ν_e interactions that were collected during PØD water and air configuration running are compared with the number of ν_e interactions predicted by the PØD water and air configuration MC, respectively. The measured number of ν_e interactions are extracted by subtracting the predicted MC background B from the selected data events D, resulting in

$$N^{\text{Data}}_{\text{CC}\nu_e,\text{water}} = D_{\text{water}} - B_{\text{water}}, \quad \text{and} \tag{1}$$

$$N^{\text{Data}}_{\text{CC}\nu_e,\text{air}} = D_{\text{air}} - B_{\text{air}}. \tag{2}$$

The background subtracted data are then divided by the predicted Monte Carlo signal S to obtain the data/MC ratios for the water and air configurations:

$$R_{\text{water}} = \frac{N^{\text{Data}}_{\text{CC}\nu_e,\text{water}}}{S_{\text{water}}}, \quad \text{and} \tag{3}$$

$$R_{\text{air}} = \frac{N^{\text{Data}}_{\text{CC}\nu_e,\text{air}}}{S_{\text{air}}}. \tag{4}$$

To extract the measured number of on-water charged current ν_e interactions, the measured CCν_e interactions with PØD water and air configurations are compared by taking into account the different collected POT and the different reconstruction efficiencies for the water and the air data sample using

$$N^{\text{Data}}_{\text{CC}\nu_e,\text{on-water}} = (D_{\text{water}} - B_{\text{water}}) - \frac{\epsilon_{\text{not-water}} \cdot \text{POT}_{\text{water}}}{\epsilon_{\text{air}} \cdot \text{POT}_{\text{air}}} \cdot (D_{\text{air}} - B_{\text{air}}). \tag{5}$$

In this formula, $\text{POT}_{\text{water}} = 2.64 \times 10^{20}$ ($\text{POT}_{\text{air}} = 3.49 \times 10^{20}$) is the collected data POT for the PØD water (air) configuration. The resulting data/MC ratio for on-water CCν_e interactions is given by

$$R_{\text{on-water}} = \frac{N^{\text{Data}}_{\text{CC}\nu_e,\text{on-water}}}{S_{\text{on-water}}}. \tag{6}$$

V. SYSTEMATIC UNCERTAINTIES

The systematic uncertainties in the measurements are divided into three categories: detector, reconstruction, and neutrino flux/cross section uncertainties. Control sample events to study systematic effects in the measurement have been studied, but often the events in these control samples are not used for the final systematic uncertainty evaluation. The control sample events were found to be too similar to the signal events, or did not have the same background as the signal events. For this reason a simple Kolmogorov Smirnov (KS) test is used for several of the systematic uncertainty tests, particularly where no deviation is indicated in the test.

A. Detector systematic uncertainties

The detector's as-built mass and its mass in the Monte Carlo are different. The masses for water and air configurations as well as different run periods also vary. These differences are incorporated in the analysis procedure by reweighting MC events with mass uncertainties estimated to be 0.01 for all configurations. Similarly, the fiducial volume and the alignment of the PØD is considered. Varying the fiducial volume by the MC vertex resolution and shifting in PØD alignment provides an estimate of the systematic uncertainties in data/MC ratios. The uncertainties obtained are smaller than 0.01 for all ratios making them negligible in this measurement.

Possible systematic effects on the reconstructed electron energy are also studied. The effects are investigated by changing the reconstructed energy scale to observe the differences in CCν_e data/MC ratios. The possible effects are as follows: 1. PØD material density and thickness, 2. drifts in the PØD response over time, and 3. the simulation (GEANT4) uncertainty in the electron energy deposition. It is assumed the water and air configuration are correlated for the PØD material density and thickness only. The resulting systematic uncertainties for water (R_{water}), air (R_{air}), and on-water ($R_{\text{on-water}}$) are 0.05, 0.05, and 0.10 respectively.

B. Reconstruction systematic uncertainties

1. Track PID

As described earlier at the beginning of Sec. III, the classification of the reconstructed tracks is based on the PØD PID. Differences in the PID between data and MC can therefore cause systematic uncertainties in the CCν_e data/MC ratios.

A PID study with stopping muons in the PØD was performed to estimate this uncertainty, and a map of mis-PID between a data sample and a simulation of stopping muons was constructed. To estimate the impact of the track PID uncertainty on the CCν_e data/MC ratios, the MC signal and background was weighted according to the uncertainty of the map. The systematic parameter values were randomly varied assuming that the water and air samples are uncorrelated and also that the signal and background uncertainties are uncorrelated. The uncertainties for water (R_{water}), air (R_{air}), and on-water ($R_{\text{on-water}}$) were determined to be 0.05, 0.05, and 0.09 respectively.

2. Track and shower median width

To estimate the systematic uncertainty caused by the track median width, the plots with all selection criteria applied but failing the track median width cut (the N-1 plots) are integrated, and a Kolmogorov-Smirnov test is performed to test if the data and the Monte Carlo event distributions are consistent [28,29]. The Kolmogorov-Smirnov test returns a p-value of 91.2% for water and 92.2% for air configuration indicating that there are no significant evidence for a shift between the data and MC event distributions. The systematic uncertainty due to the track median width cut is therefore negligible for this analysis.

The threshold of the shower median width cut is placed in a region with a large number of events. The systematic uncertainty on the measured shower median width therefore has a larger impact on the CCν_e data/MC ratios than the track median width uncertainty does. To estimate the systematic uncertainty caused by the shower median width, the N-1 plots are integrated, and a Kolmogorov-Smirnov test is performed. The Kolmogorov-Smirnov test returns a p-value of 50.0% for water and 65.9% for air configuration. To determine a reasonable scaling factor range for Monte Carlo, different scaling factors from 0.9 to 1.1 were applied to Monte Carlo and the resulting p-values were studied. For a p-value of 68%, the peak scaling factor ranged from 0.98 to 1.02. The systematic effect on the CCν_e data/MC ratios for R_{water}, R_{air}, and $R_{\text{on-water}}$ coming from the shower median width are estimated by varying the scaling factor that is applied to the MC shower median width. The uncertainties obtained for R_{water}, R_{air}, and $R_{\text{on-water}}$ are 0.04, 0.04, and 0.08 respectively.

3. Shower charge fraction

To estimate the possible impact of systematic effects of the shower charge fraction on the analysis, additional reconstructed objects with low energy are studied. Such additional tracks or showers would cause an event to fail the shower charge fraction selection criteria. Looking at the event distribution of these events, the only hint for a systematic difference between data and MC appears in the highest bin of the air configuration. Events with a shower charge fraction between 0.98 and 1.00 which pass all other selection criteria are analyzed to estimate the systematic uncertainty. The data/MC difference in this region is considered to be the uncertainty on the MC events in the signal region, resulting in the systematic uncertainties for R_{water}, R_{air}, and $R_{\text{on-water}}$ of 0.01, 0.04, and 0.04 respectively.

TABLE IV. Summary of systematic uncertainties on the CCν_e data/MC ratios for water (R_{water}), air (R_{air}), and on-water ($R_{\text{on-water}}$).

Systematic uncertainty	R_{water}	R_{air}	$R_{\text{on-water}}$
MC statistics	0.03	0.04	0.12
PØD mass	0.01	0.01	0.01
PØD fiducial volume	<0.01	<0.01	<0.01
PØD alignment	<0.01	<0.01	<0.01
Energy scale	0.05	0.05	0.10
Hit matching	<0.01	<0.01	<0.01
Track PID	0.05	0.05	0.09
Energy resolution	<0.01	<0.01	0.01
Angular resolution	<0.01	<0.01	0.01
Track median width	<0.01	<0.01	<0.01
Shower median width	0.04	0.04	0.08
Shower charge fraction	0.01	0.04	0.04
Flux and cross sections	0.07	0.09	0.06
Total	0.11	0.13	0.21

C. Flux and cross section systematic uncertainties

For the inclusion of the flux and cross section systematic uncertainties in the analysis, each analyzed MC event is reweighted according to the uncertainties of the flux and cross section parameters which are correlated. The parameter values and uncertainties are provided by different external measurements such as NA61 and other hadronic production experiments, and these parameters are then fitted to ND280 data from TPC and FGD, the other subdetectors of ND280 than PØD. The systematic parameters and their uncertainties obtained from the fit to the ND280 data, which includes 25 flux parameters, 6 FSI parameters, 2 NEUT parameters, and 13 neutrino interaction parameters, has been studied in Ref. [23].

To obtain the flux and cross section systematic uncertainties, the systematic parameters are thrown according to the covariance matrix and the analysis described in Sec. IV is then applied to each throw. The distributions are fit with single Gaussians and the resulting width is considered to be the flux and cross section systematic uncertainty for the analysis. The uncertainties obtained for water (R_{water}), air (R_{air}), and on-water ($R_{\text{on-water}}$) are 0.07, 0.09, and 0.06 respectively.

D. Summary of the systematic uncertainties

All systematic uncertainties on the CCν_e data/MC ratios for water (R_{water}), air (R_{air}), and on-water ($R_{\text{on-water}}$) that were estimated in the previous sections are summarized in Table IV. This table also shows the total systematic uncertainty.

VI. RESULTS

The results obtained for the background subtracted data/MC ratio (R) for water configuration, air configuration, and on-water are

$$R_{\text{water}} = 0.89 \pm 0.08(\text{stat}) \pm 0.11(\text{sys}), \quad (7)$$

$$R_{\text{air}} = 0.90 \pm 0.09(\text{stat}) \pm 0.13(\text{sys}), \quad \text{and} \quad (8)$$

$$R_{\text{on-water}} = 0.87 \pm 0.33(\text{stat}) \pm 0.21(\text{sys}). \quad (9)$$

The ratios are consistent with 1, within statistical and systematic uncertainties. For the on-water ratio, uncertainties are relatively large due to limited statistics and the impact of the subtraction method.

For the selected events, the distribution of the reconstructed particle directions is shown in Fig. 5 and the distribution of particle energies is shown in Fig. 6. This result indicates that the beam ν_e component in high energy region measured in the data is consistent with expectations after including constraints from the ND280 data for all configurations.

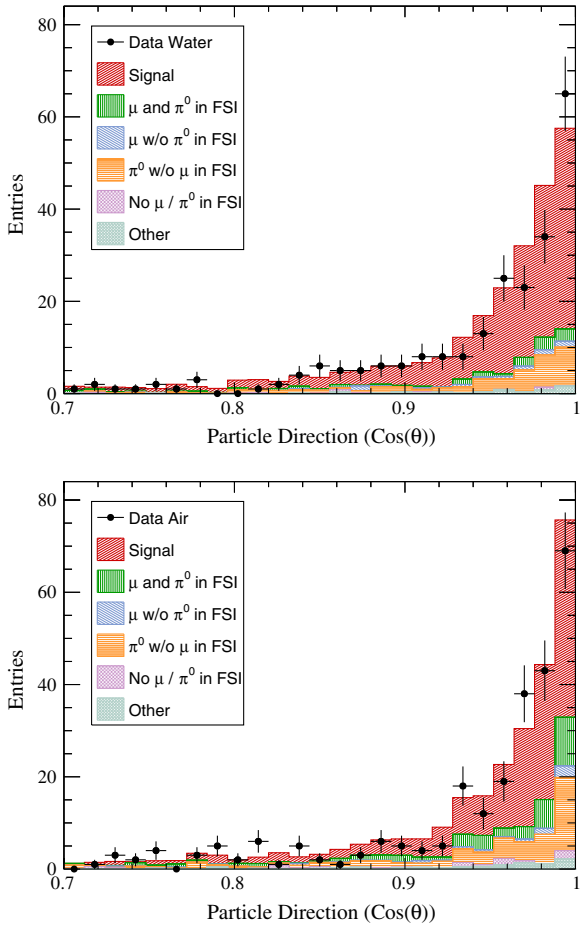

FIG. 5 (color online). Events passing the event selection as a function of the particle direction for water (top) and air configuration (bottom). The MC events are normalized to data POT, and the fit results from ND280 are applied.

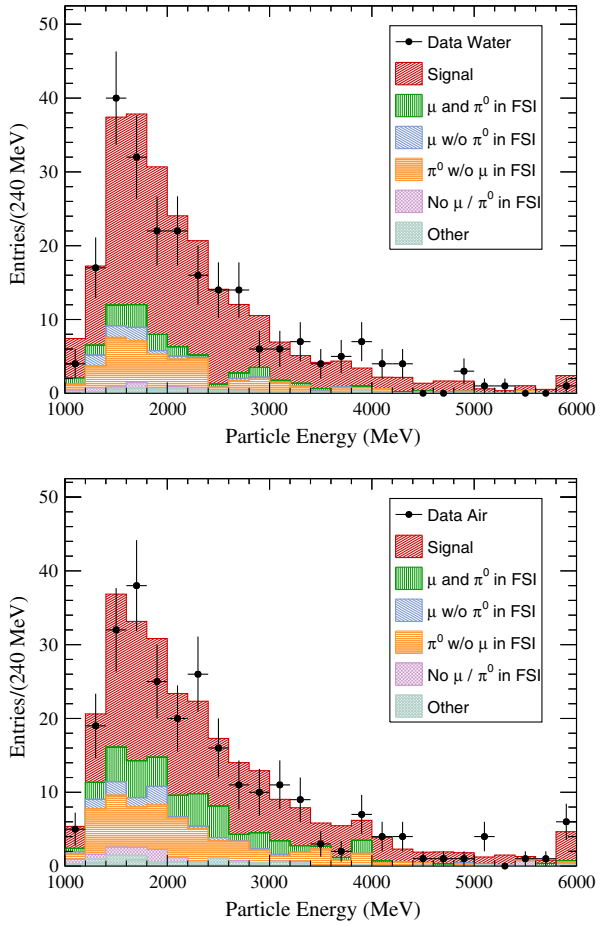

FIG. 6 (color online). Events passing the event selection as a function of the particle energy for water (top) and air configuration (bottom). The MC events are normalized to data POT, and the fit results from ND280 are applied.

VII. CONCLUSION

In conclusion, measurements of CCν_e interactions using the ND280 PØD have been made. The PØD includes fillable water targets which allows separate measurements for the water and air configurations of the ND280 PØD as well as the measurement of ν_e on-water interactions above 1.5 GeV in a predominantly ν_μ beam. About ~85% of the selected sample comes from the decay of kaons.

The 230 (257) water configuration (air configuration) electron neutrino candidate events selected in the data are in good agreement with the prediction for the water configuration, the air configuration, and for the on-water subtraction samples respectively. The measurement is statistically limited, especially for on-water, but it will be improved in the future, since collection of 10 times more data is planned in the coming years. Furthermore, studies and improvements to the reconstruction algorithms are being investigated to lower the energy threshold, which will lead to the measurement of the ν_e cross section on water.

This is the first ν_e interaction rate measurement on water in the few GeV energy region. Interactions of ν_e on water are of particular interest for long-baseline neutrino oscillation experiments, and atmospheric neutrino experiments using water Cherenkov detectors with the aim to measure *CP* violation in the lepton sector.

ACKNOWLEDGMENTS

We thank the J-PARC staff for superb accelerator performance and the CERN NA61 collaboration for providing valuable particle production data. We acknowledge the support of MEXT, Japan; NSERC, NRC and CFI, Canada; CEA and CNRS/IN2P3, France; DFG, Germany; INFN, Italy; National Science Centre (NCN), Poland; RSF, RFBR and MES, Russia; MINECO and ERDF funds, Spain; SNSF and SER, Switzerland; STFC, U.K.; and DOE, U.S.A. We also thank CERN for the UA1/NOMAD magnet, DESY for the HERA-B magnet mover system, NII for SINET4, the WestGrid and SciNet consortia in Compute Canada, GridPP, U.K. In addition participation of individual researchers and institutions has been further supported by funds from: ERC (FP7), EU; JSPS, Japan; Royal Society, U.K.; DOE Early Career program, U.S.A.

[1] Y. Hayato, Nucl. Phys. B, Proc. Suppl. **112**, 171 (2002).
[2] J. Blietschau *et al.* (Gargamelle Collaboration), Nucl. Phys. **B133**, 205 (1978).
[3] L. B. Auerbach *et al.* (LSND Collaboration), Phys. Rev. D **63**, 112001 (2001).
[4] J. A. Formaggio and G. P. Zeller, Rev. Mod. Phys. **84**, 1307 (2012).
[5] K. Abe *et al.* (T2K Collaboration), Nucl. Instrum. Methods Phys. Res., Sect. A **659**, 106 (2011).
[6] J. Arafune, M. Koike, and J. Sato, Phys. Rev. D **56**, 3093 (1997).
[7] K. Abe *et al.* (T2K Collaboration), Phys. Rev. Lett. **112**, 061802 (2014).
[8] K. Abe *et al.* (T2K Collaboration), Phys. Rev. D **87**, 012001 (2013).
[9] K. Abe *et al.*, arXiv:1109.3262.
[10] C. Adams *et al.* (LBNE Collaboration), arXiv:1307.7335.
[11] A. Stahl *et al.*, Report No. CERN-PH-EP-2012-021, SPSC-EOI-007, 2012.
[12] K. Abe *et al.* (T2K Collaboration), Phys. Rev. D **89**, 099902 (2014).

[13] S. Assylbekov *et al.* (T2K ND280 P0D Collaboration), Nucl. Instrum. Methods Phys. Res., Sect. A **686**, 48 (2012).
[14] B. G. Tice *et al.* (Minerva Collaboration), Phys. Rev. Lett. **112**, 231801 (2014).
[15] B. Tice, Ph.D. thesis, Rutgers University, 2014.
[16] M. Day and K. S. McFarland, Phys. Rev. D **86**, 053003 (2012).
[17] K.A. Olive *et al.* (Particle Data Group), Chin. Phys. C **38**, 090001 (2014).
[18] G. Gran *et al.*, Phys. Rev. D **74**, 052002 (2006).
[19] C. Mariani *et al.*, Phys. Rev. D **83**, 054023 (2011).
[20] A. Rodriguez *et al.*, Phys. Rev. D **78**, 032003 (2008).
[21] S. Nakayama *et al.*, Phys. Rev. Lett. **619**, 255 (2005).
[22] M. Hasegawa *et al.*, Phys. Rev. Lett. **95**, 252301 (2005).
[23] K. Abe *et al.* (T2K Collaboration), Phys. Rev. D **89**, 092003 (2014).
[24] A. Schalicke, A. Bagulya, Ø. Dale, F. Dupertuis, V. Ivanchenko, O. Kadri, A. Lechner, M. Maire, M. Tsagri, and L. Urban, J. Phys. Conf. Ser. **331**, 032029 (2011).
[25] O. Kadri, V. N. Ivanchenko, F. Gharbi, and A. Trabelsi, Nucl. Instrum. Methods Phys. Res., Sect. B **258**, 381 (2007).
[26] D. L. Sawkey and B. A. Faddegon, Med. Phys. **36**, 698 (2009).
[27] V. N. Ivanchenko, Nucl. Instrum. Methods Phys. Res., Sect. A **502**, 666 (2003).
[28] A. N. Kolmogorov, G. Ist. Ital. Attuari **4**, 83 (1933).
[29] N. Smirnov, Ann. Math. Stat. **19**, 279 (1948).